SHEAR CAPACITY OF FIBER REINFORCED POLYMER STRENGTHENED REINFORCED CONCRETE BEAMS

A DISSERTATION
SUBMITTED TO THE SCHOOL OF
CIVIL AND ENVIRONMENTAL ENGINEERING
UNIVERSITY OF ADELAIDE
FOR THE DEEGREE OF
DOCTOR OF PHILOSOPHY

By

Raizal Saifulnaz Muhammad Rashid

January 10, 2007

ABSTRACT

Plating using Fiber Reinforced Plastic (FRP) is one of the latest ways of retrofitting. Two of the most popular types of plating available are Externally Bonded (EB) and Near Surface Mounted (NSM) plating. EB plating (pultruded or wet lay up) is easy to apply but it debonds at low strain which limits the ductility, however, NSM plating, although slightly more difficult to apply debonds at higher strains. Both of these FRP plating systems are included in this research.

The major contribution of this thesis is towards the shear capacity and shear failure mechanism of reinforced concrete beams with adhesively bonded transverse NSM FRP plates. In shear strengthening, there are two forms of plate debonding that interact with each other consisting of Intermediate Crack (IC) debonding that is governed by the axial forces in the plates, and Critical Diagonal Crack plate debonding, where axial forces in the plate are induced by shear deformations. This research considers both forms of debonding and in particular their interaction.

Thirty eight pull tests with different types of plates, plate orientations and plate numbers were carried out on concrete prism and along with results from other researchers used in deriving a generic equation that can be used to predict the Intermediate Crack (IC) debonding resistance in plated beams. Furthermore, 8 beams tests were also carried out on simply supported beams strengthen with NSM plating to identify the plating contributions towards the shear capacity.

STATEMENT OF ORIGINALITY

This work contains no material which has been accepted for the award of any other degree or diploma in any university or other tertiary institution and, to the best of my knowledge and belief, contains no material previously published or written by another person, except where due to reference has been made in the text.

I give consent to this copy of my thesis, when deposited in the University Library, being available for load and photocopying.

10/01/2007

Raizal Saifulnaz Muhammad Rashid — Date

LIST OF PUBLICATIONS

The following papers were written based on the work presented in this thesis.

Journal Papers

1. Seracino, R., Raizal Saifulnaz M.R. and Oehlers, D.J. (2006). "Generic intermediate crack debonding resistance of EB and NSM plate-to-concrete joints". ASCE Composites. In press, October 2006.
2. Raizal Saifulnaz M.R., Oehlers, D.J. and Seracino, R. (2006). "IC debonding of FRP NSM and EB retrofitted concrete: plate and cover interaction test", submitted ASCE Composites Journal.
3. Oehler, D.J., Raizal Saifulnaz M.R. and Seracino, R. (2006). "IC debonding resistance of groups of FRP NSM strips in reinforced concrete beams", submitted Construction and Building Materials.
4. Seracino, R., Raizal Saifulnaz M.R. and Oehlers, D.J. (2006). "Contribution of concrete, internal shear reinforcement and FRP plate to the shear capacity" In preparation in Journal Publication.
5. Oehler, D.J., Raizal Saifulnaz M.R. and Seracino, R. (2006). "Shear capacity of NSM FRP plated beams" In preparation in Journal Publication.

Symposium Papers

1. Seracino, R., Oehlers, D.J. and Raizal Saifulnaz M.R. (2005). "Towards a generic model of the intermediate crack debonding resistance of plates adhesively bonded to concrete". Proceeding of the International Symposium on Bond Behaviour of FRP in Structures (BBFS 2005).

ACKNOWLEDGEMENT

The work described in this thesis was carried out at the University of Adelaide in the Department of Civil and Environmental Engineering under the supervision of Associate Professor Deric Oehlers and Dr. Rudolf Seracino.

I would like to express my deepest gratitude to Associate Professor Deric Oehlers and Dr. Rudolf Seracino for their excellent guidance, enthusiastic supervision and tolerant throughout this research. Their dedication and contribution gave me tremendous help in completion of this research and the publication of the papers. I would also like to thank them for their commitment to this research especially in organising weekly meeting which was with valuable discussion and ideas.

Also a special thank you to Dr. M.S. Mohamed Ali Sahib for his guidance and assistance on the fundamental understanding on shear strengthening which helps in this research.

I am very thankful for the help from all the laboratory technicians in the Civil Engineering department, especially to David Hale for his professional advises and patience throughout the experimental program.

Lastly to my family, Nor Asilah Wati Abdul Hamid and Muhammad Haziq Raizal Saifulnaz for their love, encouragement and continual support throughout the years doing this research.

TABLE OF CONTENTS

TABLE OF FIGURES

TABLE OF TABLES

Chapter

1 INTRODUCTION

1.1 Background

The need to rehabilitate or retrofit infrastructure is becoming a major and urgent problem facing the world. In contrast with the traditional methods of structural rehabilitation such as introducing additional beams and externally bonded steel plates, the use of fiber reinforced polymers (FRP) as externally bonded reinforcement has gained widespread acceptance all over the world as an excellent method for the maintenance, rehabilitation and upgrading of existing concrete structures. This is due to the fact that FRP has many beneficial characteristics such as high strength and stiffness to weight ratio, high corrosion resistance, electromagnetic neutrality, inherent tailorability and ease of application in the field. Many studies [Khalifa A, et al. (1998),Triantafillou (1998),Mohamed Ali (2000),Triantafillou and Antonopoulos (2000),Teng, et al. (2002),Teng and Chen (2003)] have shown that significant increase in stiffness, strength and also seismic capacities can be achieved by this technique. Recent studies have also observed a wide variety of failure modes, which may limit these gains, such as crushing of concrete, shear failure, FRP rupture, and peeling-off or debonding of FRP at the adhesive-concrete interface.

1.2 Forms of Adhesive Plating

FRP plates adhesively bonded to the concrete surface are referred to as Externally Bonded (EB) plates. The plates can be placed on any surface of the beams and can be in any shape such as flat plates, channels or angle section as shown in Figure 1.2.1. In contrast NSM plating as shown in Figure 1.2.2, require grooves to be made on any surface of the beams before inserting a rod, bar or strips of FRP and gluing it in with epoxy adhesive.

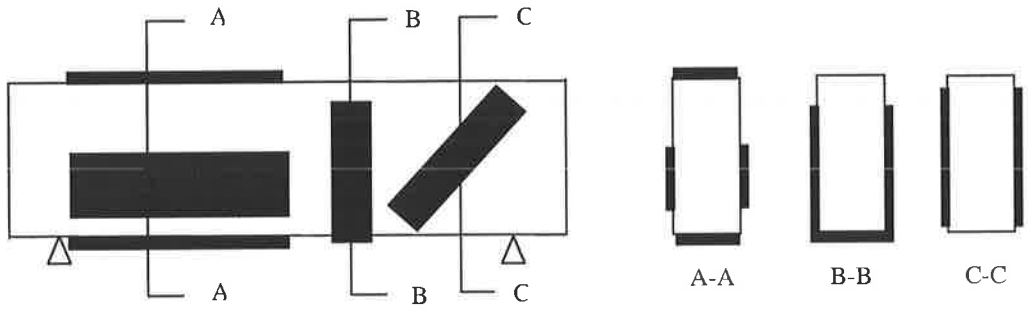

Figure 1.2.1: Longitudinal and transverse externally bonded plates.

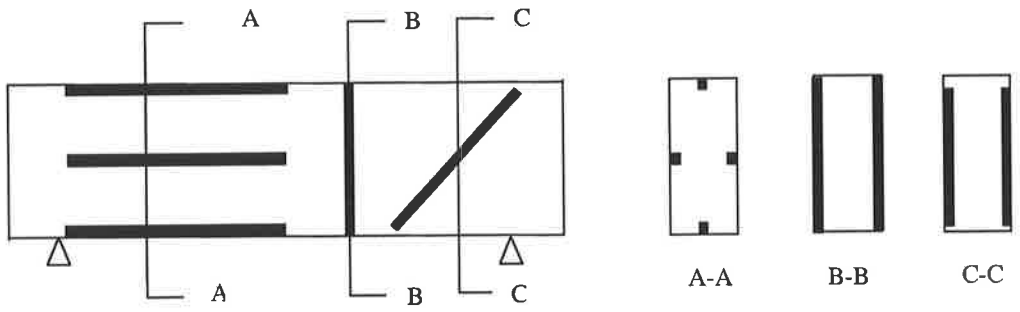

Figure 1.2.2: Longitudinal and transverse NSM plates.

1.3 Debonding Mechanisms

Previous researchers [Mohamed Ali (2000),Teng, et al. (2002),Oehlers and Seracino (2004)] have identified 2 different forms of debonding mechanism in shear strengthening; intermediate crack debonding and critical diagonal crack debonding. These 2 debonding mechanisms usually occurs at the concrete surface adjacent to the adhesive as the adhesive strength is much greater that the tensile strength of the adjacent concrete.

1.3.1 Intermediate Crack (IC) Debonding

An intermediate crack can be a flexural, shear and flexural/shear crack. An IC intercepting the plate induces interface intermediate cracks as shown in Figure 1.3.1. Interface intermediate cracks generally have a slight impact on the overall beam strength. In shear strengthening, intermediate crack debonding is associated with the formation of critical diagonal cracks that intercept the plates inducing interface intermediate cracks that reduce the strain in the plate. The propagation of interface intermediate cracks towards the plate end is called IC debonding. Knowing IC debonding is difficult to prevent, it is the failure mode that engineers design for when retrofitting beams.

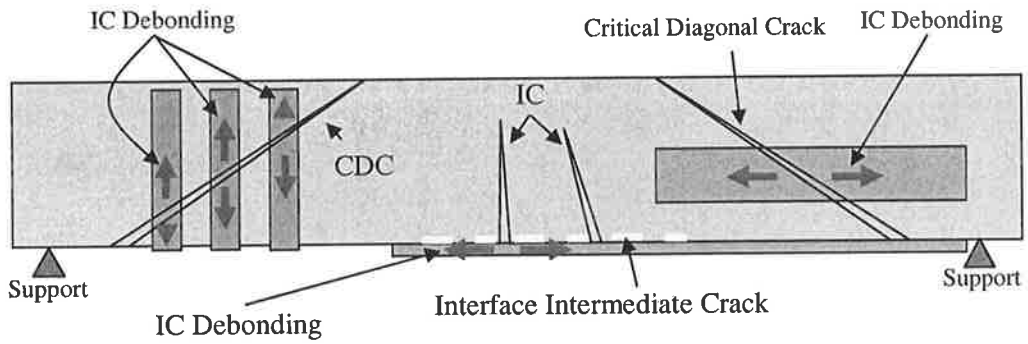

Figure 1.3.1: Intermediate crack debonding mechanism.

1.3.2 Critical Diagonal Crack (CDC) Debonding

A Critical Diagonal Crack is a single inclined crack in a shear span across which rigid body displacement occurs. It is also know as vertical shear debonding. As the critical diagonal crack forms, sliding and rotation action occurs across the crack causing the plate to separate from the beam by debonding crack propagation due to interception of the diagonal crack as shown in Figure 1.3.2.

CDC debonding is a sudden failure with no visual warning and the presence of stirrups has little or no effect on CDC debonding. Hence beams are prone to CDC debonding failure when the shear load exceeds the concrete shear capacity of the beam. Several models have been developed in analysing the problem such as Mohamed Ali's critical diagonal crack debonding model ([Mohamed Ali (2000)]. CDC debonding can be prevented by altering the plate geometries and the beam cross section at design stage [Oehlers and Seracino (2004)].

It can be seen that CDC debonding is associated with IC debonding of a plate induced by the shear deformations across the CDC.

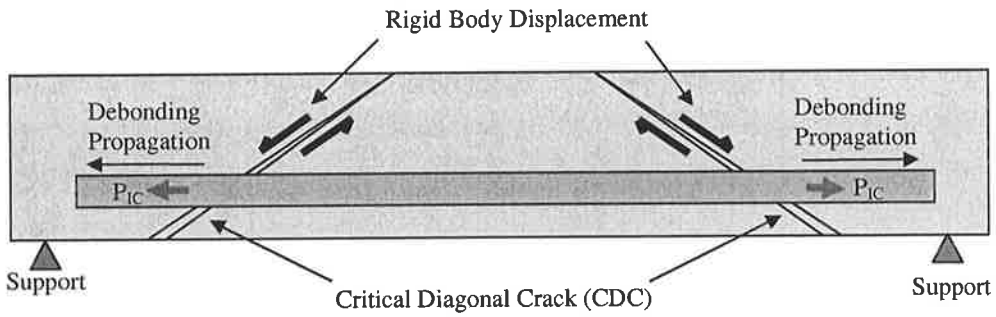

Figure 1.3.2: Critical Diagonal debonding mechanism.

1.4 Scope and Objectives

This research will look into the shear capacity and failure mechanism of reinforced concrete beams with adhesively bonded transverse NSM FRP plates. Much research has been conducted in flexural strengthening but not much in shear strengthening. Therefore, there is a need for more research into shear strengthening and the outcomes will be useful for developing design equations.

1.5 Thesis Outline

The thesis begins with an introduction in Chapter 1 which includes a general background on reinforced concrete beams with adhesively bonded plates, and a discussion on the scope and objective of this research.

Chapter 2 consist literature review and also describing CDC analysis used in this thesis which requires the IC debonding resistance of plates. The IC debonding resistance is determined in Chapter 3 for plates that fall between externally bonded plated and near surface mounted strips. The results from Chapter 3 was used in Chapter 4 to developed a lower bound Intermediate Crack (IC) debonding resistance and behaviour for any given plate dimension and type of plates, with any degree of embedment for the plate which can be used in design to suit the requirement of retrofitting for strength or ductility and serviceability. The IC debonding resistance allowing for the interaction between pairs of plates and the interaction of the plate with cover for NSM plates are determine in Chapter 5 followed by Chapter 6 covering the analysis of results in Chapter 5.

In Chapter 7, the generic equation derived in Chapter 4 was used in the prediction of the increase in shear capacity for beams with Carbon Fiber Reinforced Polymer (CFRP) Near Surface Mounted (NSM) plates. Parameters varied in these test were the plate orientation (longitudinal, inclined and vertical) and the presence of internal steel stirrups within the shear span. The behaviour of the plated beams is also compared with that of the corresponding unplated beam.

Finally, the thesis is concluded in Chapter 8 with a summary of all the findings in this research.

1.6 References

1. Khalifa A, Gold W.J., NanniA and M.I., A. A. (1998). "Contribution of Externally Bonded FRP to Shear Capcity of Flexural Members." Composites for Construction **2**(4): 195-203.

2. Mohamed Ali, M. S. (2000). Peeling of Plates Adhesively Bonded to Reinforced Concrete Beams. Department of Civil and Environmental Engineering. Adelaide, University of Adelaide: 593.

3. Oehlers, D. J. and Seracino, R. (2004). "Design of FRP and Steel Plated RC Structures." 222.

4. Teng, J. G. and Chen, J. F. (2003). "Shear Capacity of FRP-strengthened RC beams : FRP debonding." Construction and Building Material **17**: 27-41.

5. Teng, J. G., Chen, J. F. and Smith, S. T. (2002). FRP Strengthened RC Structures. England, John Wiley & Sons, Ltd.

6. Triantafillou, T. C. (1998). "Shear Strengthening of Reinforced Concrete Beams Using Epoxy-Bonded FRP Composites." ACI Structural Journal **95**(2): 107-115.

7. Triantafillou, T. C. and Antonopoulos, C. P. (2000). "Design of Concrete Flexural Members Strengthened in Shear with FRP." Journal of Composites for Construction **4**(4): 198-204.

Chapter

2 SHEAR CAPACITY ANALYSIS

2.1 Introduction

This chapter covers the shear failure mechanism and shear capacity of unstrengthened and strengthened Reinforced Concrete (RC) beams with Externally Bonded (EB) and Near Surface Mounted (NSM) plating. The literature is presented and the aims of this research will be clearly stated.

2.2 Literature Review

In RC beams, there are two components that contribute to the total shear capacity; the concrete shear capacity (V_c) and the contribution of the internal steel stirrups (V_s). Both of these components can be calculated using any international design codes. However, the shear failure (ie. failure load) of reinforced concrete beams with and without internal steel stirrups is significantly different from each other and this has an effect on the contribution of the FRP to the total shear capacity.

2.2.1 Shear Capacity of beams without internal stirrups

ASCE-ACI Committee 426 Report identified four mechanisms of shear transfer: shear stress in the uncracked region of the concrete; interface shear transfer well known as "aggregate interlock" or "crack friction"; dowel action of the longitudinal reinforcing bars; and arching action. Following that, ASCE-ACI Committee 445 Report highlighted a new mechanism, the residual tensile stress, which is transmitted directly across the cracks. Opinions vary about the importance of each mechanism in the total shear capacity, resulting in many different models available for predicting the shear strength of beams without internal stirrups. In the next section one of the reliable models, known as Zhang's approach, is described and with this, two international design codes are also presented for comparison.

2.1.1.1 Zhang's Iterative approach

One of the better models is an ingenious crack sliding model that was developed at the Technical University of Denmark by Zhang [Zhang (1994),Zhang (1997)] for predicting the position and strength of the critical diagonal crack that causes shear failure for non-shear reinforced concrete beams.

Zhang's iterative approach, also known as Critical Diagonal Crack (CDC) analysis, is a lower bound approach and can predict the weakest or critical diagonal crack that will give V_c as well as the angle of the shear crack. In this approach the vertical shear to cause crack sliding which is $(V_{dat})_{cr}$ and vertical shear to cause crack sliding $(V_{dat})_u$ are determined using equilibrium of a free body diagram. It is necessary to determine the shear load at datum point $(V_{dat})_{cr}$, that will cause the diagonal crack at an angle θ to form, that is the vertical shear to cause cracking. The following equation based on rotational equilibrium of stress resultants about point O in Figure 2.2.1, is used to plot the variation of the shear load to cause cracking $(V_{dat})_{cr}$ as a function of crack orientation, x (refer to figure 2.2.3).

$$(V_{dat})_{cr} = \frac{\left(\left(x^2 + h^2\right)\left(\frac{b_c f_{tef}}{2}\right)\right) + \left(F_{ps} d_{ps}\right)}{L_o + K_M - K_W e} \qquad (2.2.1)$$

where

$$f_{tef} = 0.156 f_c^{2/3}\left(\frac{h}{100}\right)^{-0.3} \quad \text{[N and mm]} \qquad (2.2.2)$$

x is the inclination θ of the diagonal crack,

h is the total depth of the beam or slab,

b_c is the width of the slab or the width of the web of a beam,

f_{tef} is the effective tensile strength of the concrete,

F_{ps} is the prestressing force,

d_{ps} is the lever arm of the prestressing force from the compression face,

L_o is the length of the free body,

K_M is the moment factor, and

K_W is the load factor.

In Figure 2.2.1, the beam is assumed to be prestressed with prestressing tendon at a vertical distance d_{ps} from the focal point and a prestressing force of F_{ps}. The axial force in the longitudinal reinforcement is ignored as prior to cracking the stresses in the reinforcing bars are negligible. The shear load at datum point to cause cracking $(V_{dat})_{cr}$ is our reference stress resultant. $(M_{dat})_{cr}$ is the moment at datum point when $(V_{dat})_{cr}$ is acting. Therefore $(M_{dat})_{cr}$ is a function of $(V_{dat})_{cr}$, that is $(M_{dat})_{cr} = K_M(V_{dat})_{cr}$. Furthermore, $(W_{dat})_{cr}$ is the resultant of the

applied loads acting on the free body of length L_o when $(V_{dat})_{cr}$ is acting and it is also proportional to $(V_{dat})_{cr}$ making $(W_{dat})_{cr} = K_W(V_{dat})_{cr}$. The resultant applied load $(W_{dat})_{cr}$ acts at a distance e from the focal point.

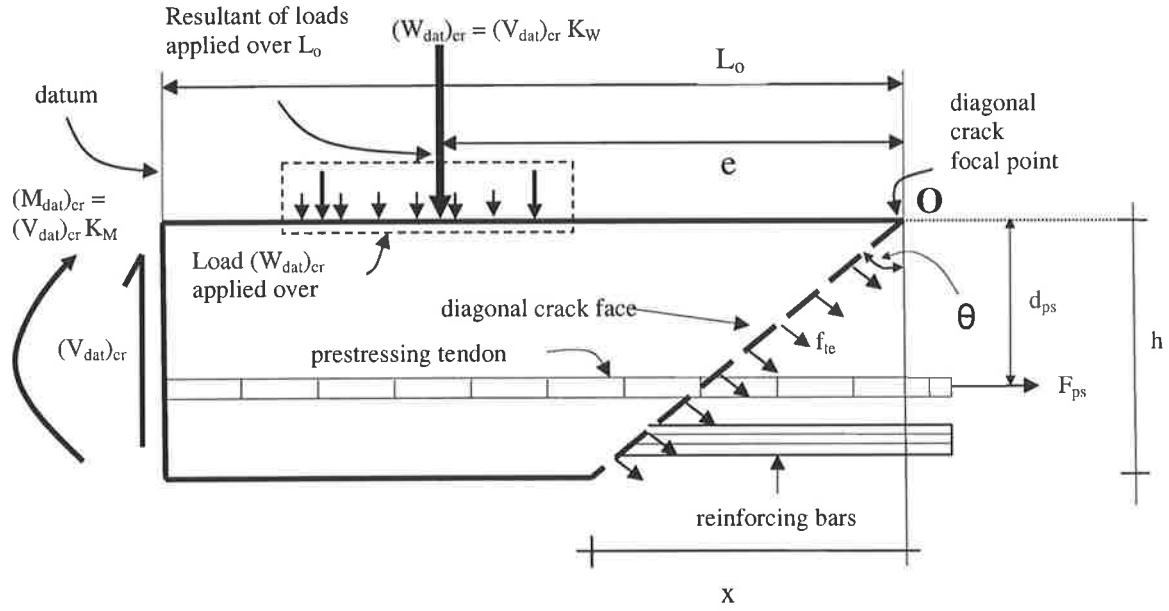

Figure 2.2.1: Shear load to cause cracking.

Meanwhile, for shear load at datum to cause failure after a diagonal crack has formed can be determined from vertical equilibrium in Figure 2.2.2, and is used to plot the line of the shear load to cause crack sliding which is $(V_{dat})_u$ given by the following (shown in figure 2.2.3). The applied load $(W_{dat})_u$ acts over the length L_o of the free body when $(V_{dat})_u$ is acting. Hence, $(W_{dat})_u$ is a function of $(V_{dat})_u$, that is $(W_{dat})_u = (V_{dat})_u K_W$. The vertical shear resistance across the diagonal crack is V_u (Figure 2.2.2).

$$(V_{dat})_u = \frac{0.4\left(f_1(f_c)f_2(h)f_3(\rho)f_4\left(\frac{\sigma_{ps}}{f_c}\right)\right)f_c b_c h\left(\sqrt{1+\sqrt{\left(\frac{x}{h}\right)^2}}-\frac{x}{h}\right)}{1-K_w} \qquad (2.2.3)$$

where, the concrete strength is accounted for by

$$f_1(f_c) = \frac{3.5}{\sqrt{f_c}} \text{ [N and mm]} \quad 5 < f_c < 60\ MPa \qquad (2.2.4)$$

the size effect by

$$f_2(h) = 0.27\left(1+\frac{1}{\sqrt{h}}\right) \qquad 0.08 < h < 0.7 \text{ [m]} \tag{2.2.5}$$

and the contribution of longitudinal reinforcement by

$$f_3(\rho) = 0.15\rho + 0.58 \qquad \rho = \frac{A_s}{b_c h}\, x\, 100 < 4.5 \tag{2.2.6}$$

where A_s is the cross-section area of all the longitudinal reinforcement crossing the critical diagonal crack and it is suggested those within the beam web (b_c). The contribution of prestressing is given by

$$f_4\left(\frac{\sigma_{ps}}{f_c}\right) = 1 + 2\frac{\sigma_{ps}}{f_c} \qquad \text{where } \sigma_{ps} = \frac{F_{ps}}{b_c h} \tag{2.2.7}$$

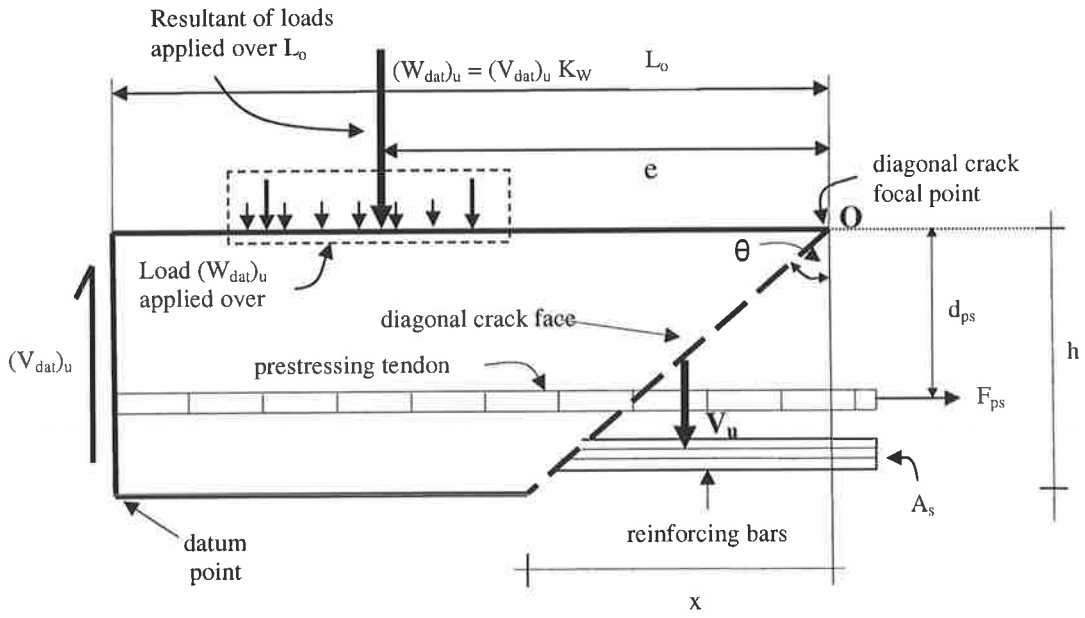

Figure 2.2.2: Vertical loads to cause crack sliding at failure

With both the shear load to cause cracking and vertical loads to cause crack sliding equations explained, now the Critical Diagonal Crack (CDC) analysis is described. Three possible

critical diagonal cracks in an unplated RC beam is shown in Figure 2.2.3. Let us consider crack O-B, the shear load $(V_{dat})_{cr}$, at the point of contraflexure, required to induce the diagonal crack is shown as point E1. The shear load $(V_{dat})_u$ to overcome the shear resistance of the crack is at point F1. Hence, when the beam is gradually loaded, the diagonal crack will first form at $(V_{dat})_{cr}$ = E1, but the diagonal crack will not fail until the shear has increased to $(V_{dat})_u$ = F1. This shows that there is warning of failure, so it is called soft failure. Next, let us consider the diagonal crack O-D in Figure 2.2.3, the shear load to cause cracking is E2 and the shear load to overcome the shear resistance of that diagonal crack is F2. Hence, for the diagonal crack O-D, nothing will happen until the shear crack forms at $(V_{dat})_{cr}$ = E2 and immediately there will be a catastrophic failure as the shear load at the datum point required to cause sliding given by $(V_{dat})_u$ = F2 is less that that to cause cracking.

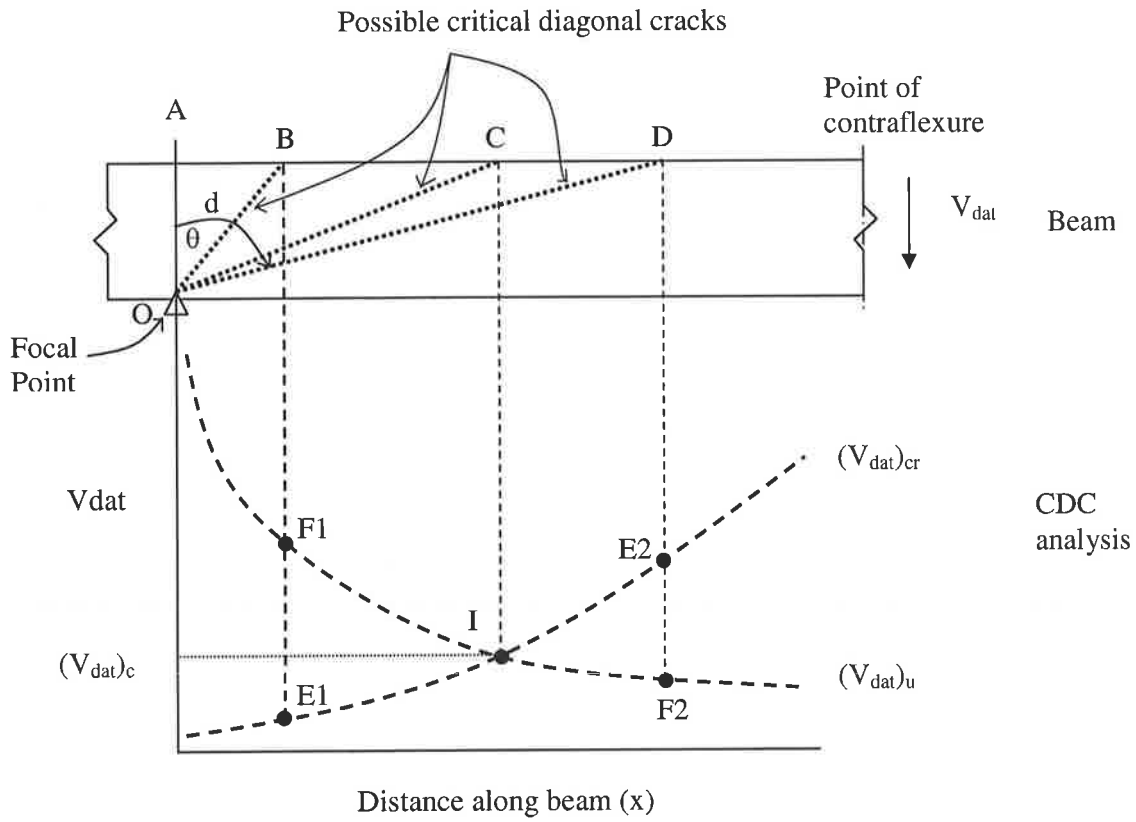

Figure 2.2.3: CDC analysis of RC beam without stirrups

The interception of $(V_{dat})_u$ and $(V_{dat})_{cr}$ at point I in Figure 2.2.3 gives the weakest strength and hence, the shear load at the datum point to cause shear failure in a beam without stirrups

$(V_{dat})_c$. It also gives the position of the critical diagonal crack. However, for beams with internal shear reinforcement, V_c is not the failure load, but the shear load at the critical diagonal crack which is also the shear load at which CDC debonding of plates occurs.
Meanwhile for longitudinal plated beam the following equation is used to plot the shear load at datum point to cause cracking for longitudinal plated beam, $(V_{dat})_{cr\ (plated)}$

$$(V_{dat})_{cr\ (plated)} = \frac{\left(\left(x^2+h^2\right)\left(\frac{b_c f_{tef}}{2} + \frac{f_t \sum (m_p A_{rect} L_{rect})}{h^2}\right)\right) + \left(F_{ps} d_{ps}\right)}{L_o \pm K_M\ \mu\ K_W e} \qquad (2.2.8)$$

where,

f_t is the tensile strength of concrete, $0.4\sqrt{f_c}$,

m_p is the modular ratio of the plate and concrete, $\frac{E_p}{E_c}$,

A_{rect} is the cross-sectional area of rectangular section of the plate,

L_{rect} is the lever arm from the centroid of the rectangular section to the compression face,

The shear load at the datum to cause failure after a diagonal crack has formed is given by

$$(V_{dat})_{u\,(plated)} = \frac{0.4 f_c b_c \left(1 + \frac{2F_{ps} + 4\sum P_{axial}}{f_c b_c h}\right)\left(\sqrt{1+\left(\frac{x}{h}\right)^2} - \frac{x}{h}\right) f_1(f_c) f_2(h) f_3(\rho)}{1 \pm K_w} \qquad (2.2.9)$$

The interception of these two lines (Eq. 2.2.8 and 2.2.9) will gives the weakest strength and the shear load at the datum point to cause shear failure, as well as the position of the critical diagonal crack. Figure 2.2.4 shows the curves plotted for unplated and plated beams for comparison. It shows the increase of $(V_{dat})_{cr}$ and $(V_{dat})_u$ due to plating and the increase of concrete shear capacity, ΔV_c. It can be seen that both Eq. 2.2.8 and 2.2.9 can be used to determine the shear load at the datum point to cause cracking for unplated beam $(V_{dat})_{cr}$ and $(V_{dat})_u$ by substituting $m_p A_{rect} L_{rect} = 0$ (Eq. 2.2.8) and $P_{axial} = 0$ (Eq. 2.2.9). It is worth also noting that in Eq 2.2.8 and 2.2.9 the '±' sign is for the stress resultant depending on hogging or sagging region.

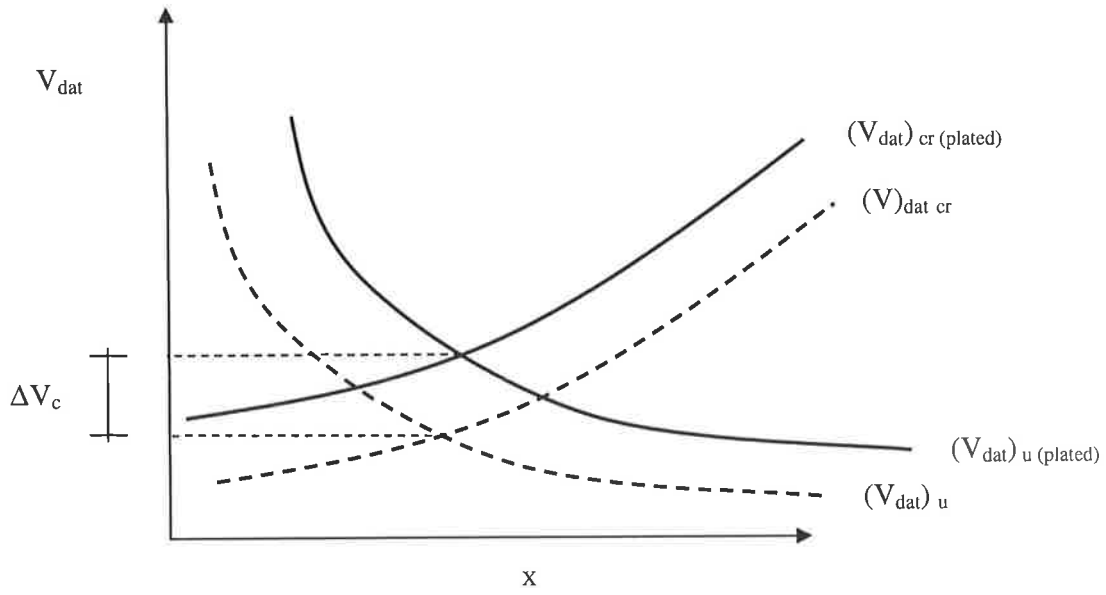

Figure 2.2.4: CDC analysis of unplated and plated beams.

In the next section, all the code models for predicting concrete shear capacity with and without steel stirrups will be elaborate for comparison with the CDC analysis.

2.1.1.2 Concrete Code Models

Australian Code AS3600-2001

The ultimate shear strength of a RC beam, not including the contribution of internal stirrups, is calculated from the following equation:

$$V_{uc} = \beta_1\beta_2\beta_3\, b_v d_o \left(\frac{A_{st}\, f'_c}{b_v d_o}\right)^{1/3} \qquad (2.2.10)$$

where

$$\beta_1 = 1.1(1.6 - d_o/1000) \geq 1.1 \qquad (2.2.11)$$

$\beta_2 = 1$; or

$= 1-(N^*/3.5A_g) \geq 0$ for members subject to significant axial tension: or

$= 1+(N^*/14A_g)$ for members subject to significant axial compression

$\beta_3 = 1$; or maybe taken as

$= 2d_o / a_v$ but not greater than 2, provided that the applied loads and the support are oriented so as to create diagonal compression over the length a_v,

a_v is the distance from the section at which shear is being considered to the face of nearest support,

d_o is the distance from extreme compression fibre of concrete to the centroid of the outermost layer of tensile reinforcement or tendons, but for prestressed concrete members not less a 0.8D,

A_{st} is the cross-sectional area of longitudinal reinforcement provided in the tension zone and fully anchored at the cross-section under consideration,

f'_c is the characteristic compressive cylinder strength of concrete at 28 days,

b_v is the effective width of web for shear

N^* is the axial compressive and tensile force on a cross-section

A_g is the gross cross-sectional area of a member

V_{uc} is in Newtons

Next, the Eurocode 2 equation for predicting concrete shear capacity will be elaborate.

Eurocode 2 (ENV 1992: Revised Final Draft)

The final version of the new draft of Eurocode 2 presents a different shear procedure than the previous version of this code (Eurocode 2) and it can be use for high concrete strength up to 100 MPa. The design value for the shear resistance in non-prestressed members is given by:

$$V_{Rd,c} = \left[\frac{0.18}{\gamma_c} k(100\rho_l f_{ck})^{1/3} + 0.15\sigma_{cp} \right] b_w d \qquad (2.2.12)$$

with a minimum of

$$V_{Rd,\min} = \lfloor 0.035 k^{3/2} f_{ck}^{1/2} \rfloor b_w d \qquad (2.2.13)$$

where

f_{ck} is the characteristic compressive cylinder strength of concrete at 28 days. [MPa]

$f_{ck} \leq 100$ MPa

$k \quad 1+\sqrt{\frac{200}{d}} \le 2.0$, where d is in mm, (2.2.14)

$\rho_l = \frac{A_{sl}}{b_w d} \le 0.02$, (2.2.15)

A_{sl} is the area of the anchored tensile reinforcement,

b_w is the smallest width of the cross-section in the tensile area (in mm),

$\sigma_{cp} = N_{Ed} / A_c < 0.2 f_{cd}$ [Mpa].

N_{Ed} is the axial force in the cross-section due to loading or presstressing in Newtons ($N_{Ed} > 0$ for compression). The influence of imposed deformation on N_E can be ignored,

A_c is the area of concrete cross section (mm^2), and

V_{Rd} is in Newtons

Next, beams shear capacity for AS3600 and Eurocode 2 with internal stirrups is elaborate.

2.2.2 Shear Capacity of beams with internal stirrups

The reason for shear reinforcement in RC beams is to ensure that shear failure does not occur before flexural failure. The shear reinforcement does not inhibit the shear crack from forming. The function of shear reinforcement is to transfer the tensile stresses once the shear crack has formed. Next, the code equation for shear capacity steel stirrups will be described.

2.1.2.1 Shear capacity contribution from internal stirrups

Australian Code AS3600-2001

The contribution to the ultimate shear strength by shear reinforcement in a beam is determined from the following equation:

$$V_{us} = \left(\frac{A_{sv} f_{sy.f} d_o}{s} \right) \cot \theta_v \quad (2.2.16)$$

where

A_{sv} is the cross-sectional area of shear reinforcement,

$f_{sy.f}$ is the yield strength of shear reinforcement,

s is the centre-to-centre spacing of shear reinforcement, measured parallel to the longitudinal axis of the member,

θ_v is the angle between the axis of the concrete compression strut and the longitudinal axis of the member, taken conservatively as 45°

Eurocode2 (ENV 1992: Revised Final Draft)

The contribution of vertical shear reinforcement is given by the following equations and should be taken as the lesser of

$$V_{Rd,s} = \frac{A_{sw}}{s} z f_{ywd} \cot\theta \qquad (2.2.17)$$

or

$$V_{Rd,mas} = \frac{\alpha_c b_w z v f_{cd}}{(\cot\theta + \tan\theta)} \qquad (2.2.18)$$

where recommended limiting values for $\cot\theta$ is $1 \le \cot\theta \le 2.5$ and

A_{sw} is the cross-sectional area of the shear reinforcement,

s is the spacing of the stirrups,

z is the lever arm of internal forces, where z = 0.9d,

d is the effective depth of beam or slab,

f_{ywd} is the yield strength of the shear reinforcement,

v may be taken to be 0.6 for $f_{ck} \le 60$ MPa, and (0.9-f_{ck} / 200) for high-strength concrete and,

α_c = 1, for non-prestressed structures,

At this stage, existing to predict the shear capacity of beams with and without internal shear reinforcement has been presented. In the following section the passive prestress approach is presented.

2.2.3 Passive Prestress approach

The passive prestress approach is based on the increase in the shear resistance to crack sliding after a diagonal has formed. In other words, the "passive prestress" which is the axial tensile force in the plate will only develop once the crack has formed. National codes determine the prestressed shear capacity of concrete beams in a few ways. But basically the stress due to prestressing is considered in the shear strength of the concrete, which is the same principle adopted by the passive prestress approach. However, not all national models can be used for the passive prestress approach. Comparisons done by [Oehlers and Seracino (2004)] between the ACI and the EC2 approach show that using the ACI approach, based on principal stresses, cannot be use for predicting shear capacity of unprestressed beams. Meanwhile, the EC2 approach can be use for both prestressed and unprestressed beams and because of this it suitable for the passive prestress approach.

For the passive prestress approach the EC2 models and the modified Zhang's Iterative approach, or CDC analysis (explained section 2.1.1.1), are used to determine the contribution of longitudinal plates to the shear capacity of the concrete. The EC2 approach gives:

$$V_{Eurocode2} = \left(\tau_{Rd} (1.6 - d)(1.2 + \frac{40A_{st}}{b_c d}) + 0.15\sigma_{ps} \right) b_c d \qquad (2.2.19)$$

where

τ_{Rd} is the basic design shear strength.

d is the effective depth of beam or slab,

b_c is the rectangular cross section of width beam or slab,

A_{st} is the cross-sectional area of tension reinforcing bars, and

σ_{ps} is the compressive prestress in the concrete due to prestressing force.

From Eq. 2.2.19, the increase in the shear capacity due to prestress is $0.15\sigma_{ps} b_c d \approx 0.15 F_{ps}$.

It can be assumed that the increase in the shear capacity due to the passive prestressed P_{plate} is $0.15P_{plate}$, that is 15% of P_{plate}.

This passive prestress approach concludes the literature review on shear capacity with and without internal shear reinforcement. In the next section of this literature review, explanation regarding shear strengthening with EB and NSM plates are discussed in detail with all the failure mechanisms known.

2.3 Shear Strengthening of Reinforced Concrete Beams

There are two types of strengthening available for shear strengthening, longitudinal (side plating) and transverse plating. Longitudinal plating consists of four possible plate positions; on the tension face, compression face, side plating (beams only) and combination of side and tension face, or angle plates as shown in Figure 2.3.1. For transverse plating on the sides of beams, plates may be inclined and vertical (on side only) , vertical U jackets, inclined U jackets and fully wrapped which may also be vertical and inclined [Sato, et al. (1997),Khalifa A, et al. (1998),Triantafillou (1998),Khalifa A and Nanni A (2000),Taljsten and Elfgren (2000),Hassan and Rizkalla (2003),Li, et al. (2003),Taljsten (2003)] Figure 2.3.1. There are two methods of bonding the plates, EB and NSM as shown in Figure 2.3.1 and Figure 2.3.2. The plate materials may be FRP or metallic plates, but in this research only FRP plates will be considered.

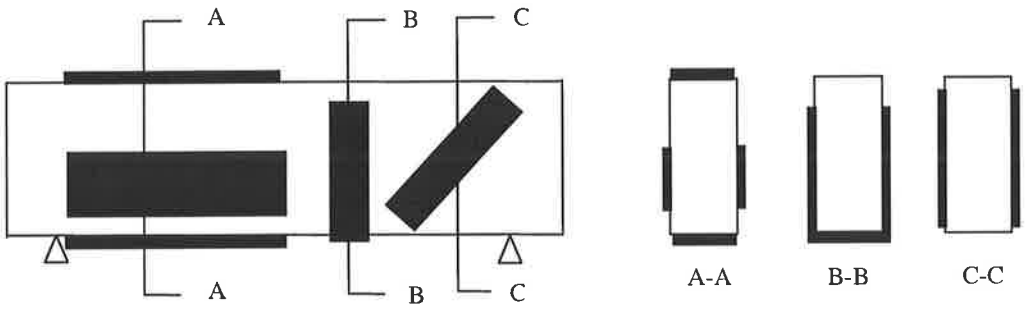

Figure 2.3.1: Longitudinal and transverse EB plates.

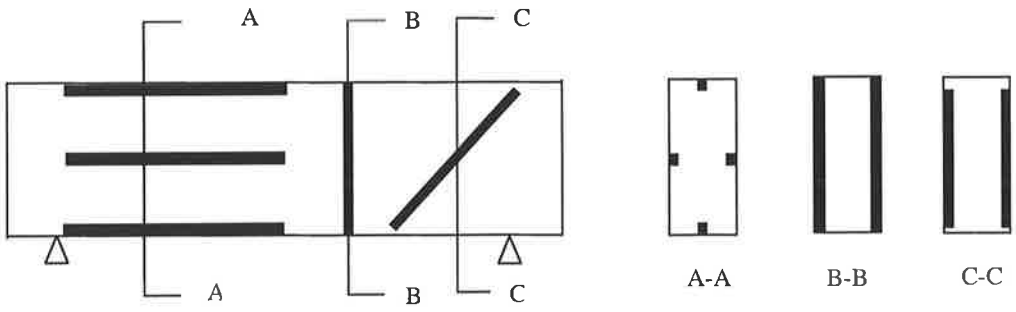

Figure 2.3.2: Longitudinal and transverse NSM plates.

2.4 Externally Bonded FRP

Steel plates bonded to the surfaces of RC structural elements have been used widely to strengthen existing RC members for several decades. However, steel plates have a few disadvantages, such as: deterioration of the bonding between the steel and concrete interface due to steel corrosion; and difficulty in handling the plates on the construction site because of the weight. Therefore, there are advantages in using light and easy to handle materials such as FRP.

FRP sheets are normally made of continuous carbon, aramid, or glass fibres that have a diameter in the range of 5-25 μm in one (unidirectional) or two perpendicular directions (pseudo-isotropic or bi-directional) and they are bonded together with a matrix such as epoxy or polyester resins. A useful general background on the composition of these materials and their mechanical properties can be found in ACI 440R-96 (1996). The resulting FRP material possesses superior structural tailorability, excellent corrosion resistance and high resistance to environmental degradation. The density of FRP is only 20% that of steel, but it possesses high tensile strength of the order 1000-3000 MPa. There is also a wide range of Young's modulus in the direction of fibre orientation, typically in the order of 50, 120 and 160-300 GPa for unidirectional FRPs with glass, aramid and carbon fibres respectively. Unlike mild steel, FRP materials are brittle and linear elastic up to failure strains of about 10000-20000 microstrain for carbon fibre and 25000-30000 microstrain for other fibres [Triantafillou and Plevris (1992),Meier (1995),Triantafillou (1998),Triantafillou and Antonopoulos (2000)]. Although FRP materials are more expensive than mild steel, they are often cost-effective as FRP plates have a high strength-to-weight ratio and the costs involved such as in transportation, labour and handling are less. In this regard, Meier (1995) suggests that FRP plates have the advantage in applications such as bridges, multi-storey parking spaces, railway stations and specialised industrial structures where corrosion, length of strengthening component (more than 8m) and handling on construction site plays an important role.

2.4.1 Debonding mechanisms of longitudinal EB plates

The FRP and concrete are glued together with the use of a strong adhesive. The adhesive is much stronger than the tensile strength of the concrete hence debonding or peeling usually occurs on the concrete surface. Cracks in the RC beams that intercept a plate will induce some amount of debonding to relieve stress concentrations. This is referred to as

intermediate crack (IC) interface cracking and has no effect on the strength of the structure as a whole. With increasing applied loads interface cracks spread and eventually join together reducing the strains in the plate. This is referred to as IC debonding [Oehlers and Seracino (2004),Liu (2005)]. Another type of debonding is caused by the rigid body shear displacement or critical diagonal crack (CDC) which occurs in RC members (beams and slabs) with or without the existence of internal steel stirrups (section 2.1.1.1). This is referred to as CDC debonding [Mohamed Ali (2000),Oehlers and Seracino (2004)]. The curvature in a flexural member may result in another form of debonding known as plate end (PE) debonding where debonding cracks propagate inwards. Although not a common type of debonding, it is good practise to make sure that the interface shear stress or shear flow between the plate and concrete does not cause failure of the concrete. This is referred as $\frac{VAy}{Ib}$ debonding [Oehlers and Seracino (2004)].

To conclude the discussion on debonding mechanism, IC debonding is associated with the strains in the plate, CDC debonding with the rigid body shear displacement along a diagonal shear crack and finally, PE debonding is associated with the curvature in a beam.

2.4.2 Debonding mechanism of transverse external bonded plates

Appendix A [Bousselham and Chaallal (2004)] shows that numerous tests have been done on shear strengthened beams with externally bonded FRP. The outcomes of these studies show that there are numerous parameters that influence the shear behaviour of RC beams. Unfortunately, the choice of parameters studied is often questionable. For example, the shear resistance mechanism, such as the interaction between the internal steel stirrups and the external bonded plates has not been investigated. Hence, this shows that there is still a need for more research with parameters that allow a better understanding of the behaviour of transverse EB plates.

From all of the models in the literature review [Adebar, et al. (1996),Triantafillou (1998),Deniaud and Cheng (2001),Teng, et al. (2002),Diagana, et al. (2003),Taljsten (2003),Teng and Chen (2003)], the Chen and Teng's (2003) approach is the one that is used in this analysis to calculate the contribution of the FRP to the shear capacity because it is accurate, reliable and up-to-date. Chen and Teng's (2003) approach considers the bond length and strength, concrete strength, ratio of plate area to concrete, stresses and stress distribution in the FRP that intercept the shear crack. In the next section, explanation

regarding the shear failure of transverse externally bonded plates is presented along with Chen and Teng's approach.

2.1.2.2 Chen and Teng's approach

Chen and Teng's calculation for the contribution of the FRP to the shear strength is given by,

$$V_{frp} = 2 f_{frp,e} t_{frp} w_{frp} \frac{h_{frp,e}(\cot\theta + \cot\beta)\sin\beta}{s_{frp}} \quad (2.4.1)$$

where the geometric are given in Figure 2.4.1 and effective height of the FRP is expressed as

$$h_{frp,e} = z_b - z_t \quad (2.4.2)$$

where z_t and z_b are the coordinates of the top and bottom ends of the effective FRP respectively given by

$$z_t = (0.1d + d_{frp,t}) - 0.1d = d_{frp,t} \quad (2.4.3)$$

$$z_b = [d-(h-d_{frp})] - 0.1d \quad (2.4.4)$$

where

$d_{frp,t}$ is the distance from the compression face to the top edge of the FRP ($d_{frp,t}$ = 0 for wrapping)

h is the beam height, and

d_{frp} is the distance from the compression face to the lower edge of the FRP.

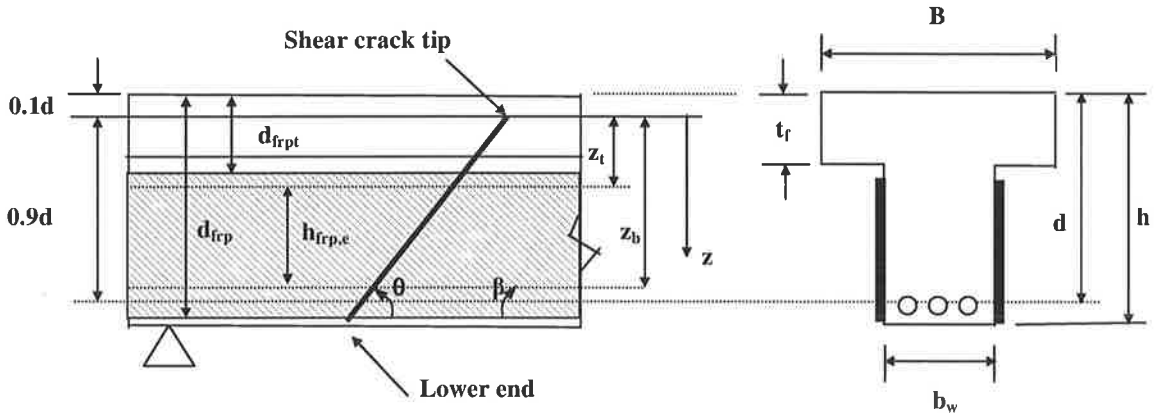

Figure 2.4.1: Notation for a general shear strengthening scheme.

Chen and Teng stated that stress distribution in the FRP along a shear crack is nonuniform at the ultimate limit state for both FRP rupture and FRP debonding. The average stress in the FRP intersected by the shear crack at the ultimate limit state $f_{frp,e}$ can be written as

$$f_{frp,e} = D_{frp}\sigma_{frp,max} \tag{2.4.5}$$

where $\sigma_{frp,max}$ is the maximum stress that can be reached in the FRP, intersect by the shear crack and D_{frp} is the stress distribution factor which defined as

$$D_{frp} = \frac{\int_{zl}^{zo} \sigma_{frp,z}\, d_z}{h_{frp,e}\sigma_{frp,max}} \tag{2.4.6}$$

The values of $\sigma_{frp,max}$ and D_{frp} depend on whether the failure is controlled by FRP rupture or FRP debonding. Meanwhile, $\sigma_{frp,z}$ is the stress in the FRP at the ultimate limit state at the location where the intersecting critical shear crack is at a coordinate z (Figure 2.4.1).

In derivation of Eq. 2.4.6, it was assumed that discrete FRP strips can be treated as an equivalent FRP continuous sheet/plate. As a result, this model is applicable for beams strengthened with either discrete strips or continuous sheet/plates and the continuous sheets/plates being a special case of discrete strips. The approach for strips involves some simplification, which for it to have reasonable accuracy, a strip spacing limitation is applied.

2.4.3 Shear Failure Controlled by FRP Rupture (FRP wrapping)

From the literature review, experiments show that most FRP rupture failures occur in beams strengthened by FRP wrapping (Figure 2.4.2). The stress (strain) in the FRP is approximately proportional to the width of the shear crack, closely represented by a linear variation increasing from zero at the crack tip for most of such shear failures.

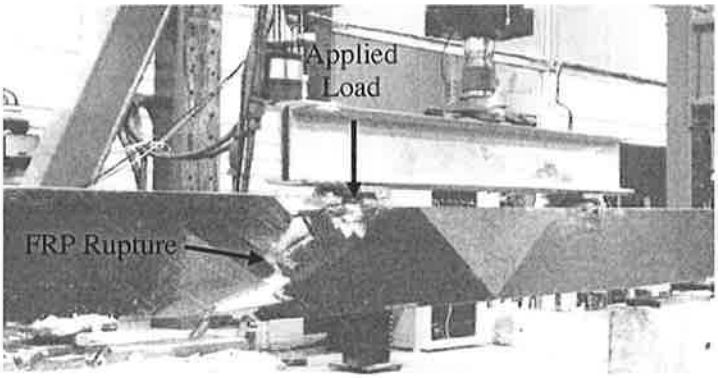

Figure 2.4.2: FRP Rupture of fully wrapped sheet.

A simple and conservative model based on a linear stress distribution was recommended by Chen and Teng for practical use. Hence, the stress distribution factor is expressed as

$$D_{frp} = \frac{1+\varsigma}{2}, \tag{2.4.7}$$

where $\varsigma = \frac{z_t}{z_b}$

For FRP that is bonded over the full height of the sides (e.g. wrapping), $\varsigma = 0$ and $D_{frp} = 0.5$. The FRP starts to rupture if the maximum stress, which occurs at the lower end of the FRP, intersected by the shear crack, reaches its ultimate tensile strength. Thus, the maximum stress in the FRP is

$$\sigma_{frp,max} = f_{frp} \tag{2.4.8}$$

Eq. 2.4.8 cannot be used in cases where the ultimate shear strength of the beam is reached before FRP rupture. The maximum stress in the FRP can be obtained from

$$\sigma_{frp,max} = \begin{cases} 0.8\ frp / \gamma_{frp} & if\ f_{frp} / E_{frp} \le \varepsilon_{\max} \\ 0.8\ \varepsilon_{\max} E_{frp} / \gamma_{frp} & if\ f_{frp} / E_{frp} < \varepsilon_{\max} \end{cases} \tag{2.4.9}$$

where γ_{frp} = partial safety factor which is 1.25 based on Chen and Teng's judgement to give safe and consistent design.

The factor of 0.8 in Eq. 2.4.9 was introduced by Chen and Teng to account for factors not considered in their strength models, for example, the effect of the corners of beams on the tensile strength of the FRP, if the corners are not properly rounded. Eq. 2.4.9 also includes a limit on the maximum usable strain of the FRP to control the width of shear crack for design use.

However, insufficient information is available in the literature to determine a suitable value for this maximum usable strain. Hence, further research is needed to clarify this. A value of ε_{max} = 1.5% may be used until an exact value is available. [Chen and Teng (2003)]

2.4.4 Shear Failure Controlled by FRP Debonding (U jackets and side bonded)

From the literature, the shear strength of beams with U jackets or side bonded FRP is typically controlled by the bond strength between the FRP and the concrete (Figure 2.4.3). An important aspect of this bond behaviour is that there exists an effective bond length beyond which extending the bonded length will not increase the bond strength. This is a fundamental difference between externally bonded reinforcement and internal reinforcement. Provided there is a sufficient concrete cover a long bond length can always be found so that the full tensile strength of the internal steel reinforcement can be achieved.

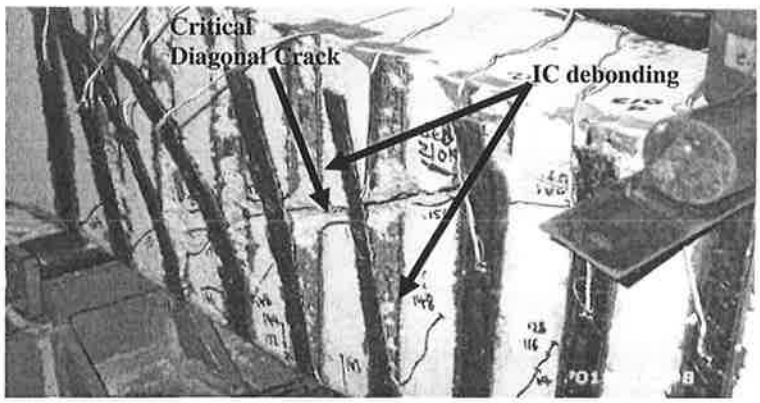

Figure 2.4.3: FRP debonding due to U jacketing.

Based on simple pull tests, Chen and Teng developed a model for predicting the bond strength and the effective bond length [Teng and Chen (2003)]. The maximum stress in the

FRP occurs at the location where the FRP has the longest bond length. The maximum stress in the FRP ($\sigma_{frp,max}$) is limited by the ultimate tensile strength of the FRP (rupture strength) as given by:

$$\sigma_{frp,\max} = \min \begin{cases} f_{frp} \\ 0.427\ \beta_w \beta_L \sqrt{\dfrac{E_{frp}\sqrt{f'_c}}{t_{frp}}} \end{cases} \tag{2.4.10}$$

where β_L reflects the effect of bond length and β_w the effect of FRP-to-concrete width ratio. For shear strengthening considered here, they can be expressed as

$$\beta_L = \begin{cases} 1 & if\ \lambda \geq 1 \\ \sin(\pi\lambda/2) & if\ \lambda < 1 \end{cases} \tag{2.4.11}$$

$$\beta_w = \sqrt{\frac{2 - w_{frp}/(s_{frp}\sin\beta)}{1 + w_{frp}/(s_{frp}\sin\beta)}} \tag{2.4.12}$$

where

w_{frp} is the width of the FRP plate,

s_{frp} is the spacing of the FRP,

$\beta = \dfrac{\sqrt{2}}{2}$ for continuous sheet/plates.

The normalised maximum bond length λ, the maximum bond length L_{max} and the effective bond length L_e are given by

$$\lambda = \frac{L_{\max}}{L_e} \tag{2.4.13}$$

$$L_{\max} = \begin{cases} h_{frp,e}/\sin\beta & for\ U\ jackets \\ h_{frp,e}/(2\sin\beta) & for\ side\ plates \end{cases} \tag{2.4.14}$$

$$L_e = \sqrt{\frac{E_{frp}t_{frp}}{\sqrt{f'_c}}} \tag{2.4.15}$$

Figure 2.4.3 has the maximum bond length for U jacketing and for side plates, the fibre in the middle of the shear crack has the maximum bond length. This is why the number 2 appears in the denominator for side plates (Eq. 2.4.14).

Because the FRP-to-concrete bonded joint generally continues to slip after reaching the ultimate bond strength (i.e. pseudo-plastic behaviour), Chen and Teng [Teng, et al. (2002)] assumed that all the FRP intersected by the shear crack develops its bond strength fully. It is worth noting that the bond strength of a particular part or strip depends on where the shear crack is located relative to the ends of the part or strip. Under this assumption, they derived the following stress distribution factor for debonding failure

$$D_{frp} = \begin{cases} \frac{2}{\pi\lambda}\frac{1-\cos(\pi/2)\lambda}{\sin(\pi/2)\lambda} & if\ \lambda \le 1 \\ 1-\frac{\pi-2}{\pi\lambda} & if\ \lambda > 1 \end{cases} \qquad (2.4.16)$$

The average stress in the FRP along the shear crack is calculated using Eq. 2.4.5. Eq. 2.4.14 is applicable to both U jackets and side strips/plates. However, the actual calculated values are different for these two cases even if the bond geometry is the same on the beam sides. This is because the maximum bond length L_{max} for U jackets is twice that for side strips/plates. For the same bonding geometry on the sides of a beam, D_{frp} is larger for U jacketing than for side bonding, because of the difference in the values of λ. This reflects the fact that U jacketing is more effective in shear strengthening than side bonding.

Shear failure is controlled by FRP debonding when the FRP at failure is controlled by the ultimate bond strength between the FRP and the concrete and both $\sigma_{frp,max}$ and D_{frp} are related to this bond strength. This bond behaviour between FRP and concrete in RC beams shear strengthened with bonded FRP are presented by simple pull tests. This shear tests is referring to pull tests for IC debonding. Meanwhile, when failure is controlled by FRP rupture, the failure process begins when the most highly stressed point in the FRP intersected by the shear crack reaches its ultimate tensile strength. The adjacent FRP then starts to rupture as the FRP needs to take over the forces released by the ruptured FRP. This shows that when the FRP starts to fail in rupture, rupture will propagate rapidly along the shear crack demonstrating that the FRP intersected by a shear crack is not stressed to the same ultimate tensile strength just prior to failure.

2.5 Near Surface Mounted FRP

Steel also has disadvantages in NSM plating. If it is to achieve the same amount of strengthening as FRP, a large area of steel is required and this is unsuitable as it will require large groove size which is difficult to do on site. The preparation includes cutting a groove in the surface of the concrete but the depth is limited to the cover of the concrete. The FRP (rod, bar or strip) is then inserted to the groove and glued to the concrete with an epoxy adhesive.

To compare the bond strength of NSM with EB FRP (with the same area of plating), NSM can achieve much higher debonding stress because of the large bonded area. It has been shown experimentally [Hassan and Rizkalla (2003)] that the maximum tensile strength of the plate (ie. rupture) can be achieved and hence, the material is used to its full capacity. Figure 2.5.1 shows that the maximum achievable strain for NSM increases with the bond length and may be limited by rupture. This increase due to more confinement of the plate compared to EB. Meanwhile, for externally bonded plate, the strain does not increase with the bond length and it fails by debonding.

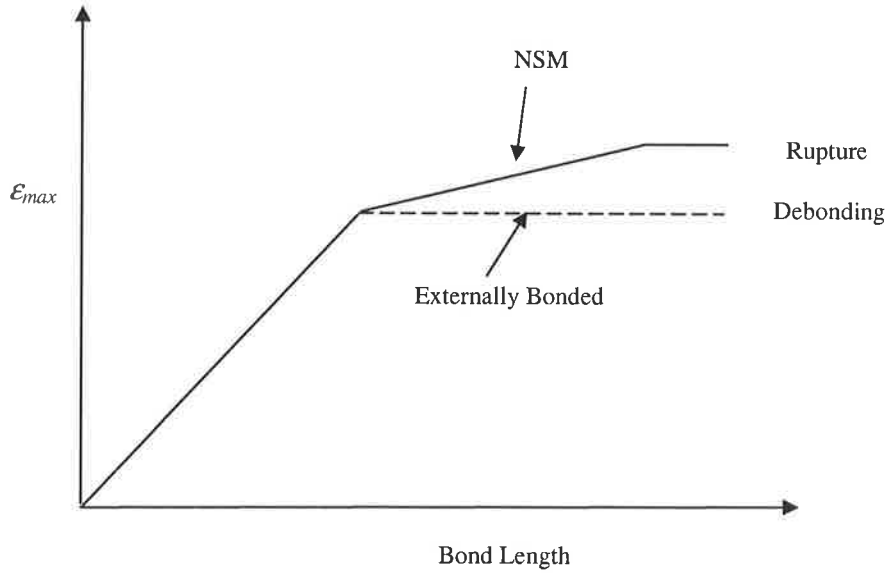

Figure 2.5.1: Comparison of EB and NSM strain and bond length relationship.

2.5.1 Debonding mechanism in NSM plates.

Because the NSM technique is a relatively new approach, there is not much understanding of the debonding mechanism. However, one test provides evidence of the failure mechanism of

NSM plates (by Hassan and Rizkalla 2003) where PE and rupture failure of the FRP strip were observed.

Hassan and Rizkalla found that beams with NSM reinforcement with short embedment length failed due to a cracks propagating from the cut-off points as well as from the flexural cracks. This is assumed to be PE debonding. Therefore, test results should differ from those found by a pull test, which is a simulation of the IC induced failure mechanism. Meanwhile, for longer embedment lengths, failure occurred when the strips ruptured. This shows that the shear to cause rupture was less than the shear to cause CDC failure which means, premature failure cause by the CDC did not occur. Hence, one of the aims of this research is to better understand the debonding mechanisms of NSM plates.

2.6 Analysis of the contribution of Concrete, Internal Shear Reinforcement and FRP to the Shear Capacity

Previous researchers have found that EB FRP increases the shear capacity of RC beams. The following model is used to calculate the shear strength of strengthened beams,

$$V_n = V_c + V_s + V_{frp} \tag{2.6.1}$$

The concrete shear capacity (V_c) and the contribution of the steel stirrups (V_s) can be calculated using national codes described in section 2.2.1 and 2.2.2. The contribution of the FRP (V_{frp}) can be calculated using a number of models [Triantafillou (1998),Khalifa A, et al. (1999),Teng, et al. (2002),Taljsten (2003)]. However, the accuracy of V_s calculated must be properly investigated because not all of the steel shear reinforcement will reach its yield strength in shear strengthened RC beams with externally bonded FRPs. Hence, the steel shear reinforcement may contribute less than that predicted by existing codes of practice for RC structures. Therefore, this analysis using Eq. 2.6.1 will try to identify the contribution of the internal stirrup to the total shear capacity of strengthened beams with transverse plates.

V_c calculated using existing codes gives a lower bound. Meanwhile, Zhang's iterative approach (Critical Diagonal Crack analysis) was calibrated only for concrete strength up to 60MPa, beam depth up to 700mm and reinforcement ratio of 4.5%.

Although codes give lower bound values for concrete shear capacity, the prediction agree well with experiments results when no safety factor are used. Although more than 200 tested beams from previous researchers are available for the V_c only 100 beams are suitable for this

analysis (because of the restriction on concrete strength, beam depth and reinforcement ratio for the CDC analysis). The reason of using the CDC analysis is that this method could provide the load to cause failure, load to cause cracking and the crack angle as explained earlier in section 2.1.1.1. In the next section, the analysis done to know the concrete shear capacity will be discussed.

2.6.1 Concrete Shear Capacity (V_c)

The concrete shear capacity (V_c) can be predicted using existing design codes. In this analysis V_c is calculated using the EC2, AS 3600 and Zhang's iterative approach, or the Critical Diagonal Crack (CDC) approach, which has been explained in detail in section 2.1.1.1. Using the experimental data from concrete beams without internal stirrups, the ratio between the experimental and theoretical shear failure loads 'k_c' can be determined. The ratio k_c is defined by the following equation and will be used to predict the actual shear failure load of beams based on code equations when the experimental value is not given.

$$k_c = \frac{Vc_{exp}}{Vc_{cal}} \tag{2.6.2}$$

where Vc_{exp} is the experiment shear capacity of the beam without shear reinforcement and Vc_{cal} is the predicted shear capacity calculated according to AS3600, EC2 and the CDC approach.

Table 2.6.1: Comparison for V_{exp}/V_{cal} for the unstrengthen beams without internal stirrups

Approach	Mean	Standard Deviation	Coefficient of Variance
Eurocode2	1.02	0.15	14.70
AS3600	1.03	0.16	15.77
CDC Analysis	0.96	0.22	22.41

The coefficient of variance is a measure of the relative to the mean; this parameter was preferred to the standard deviation as a basis for comparison of the models rather than the absolute error, this is measured by the standard deviation. Thus, in comparing models the mean and coefficient of variance of k_c was considered.

Codes give a lower bound to the 'true' failure of beams without steel shear reinforcement. The partial safety factors [γ_c, γ_s] were set to unity for the purpose of this comparison when calculating. Table 2.6.1 shows that the codes are predicting the shear capacity close to the experiment results, meanwhile the CDC analysis is predicting the shear capacity slightly higher (k_c<1) than the experiment results.

It worth noting that with EC2 and AS3600 gave similar results, both approaches were conservative to approximately the same degree. However, the scatter of these three approaches can be clearly seen from the Coefficient of Variance especially the CDC analysis. A graphical comparison of these three approaches is shown in Figures 2.6.1 – 2.6.3 where k_c is plotted against a/d (a = shear span, d = effective beam depth). Details of this analysis can be view in Appendix B.

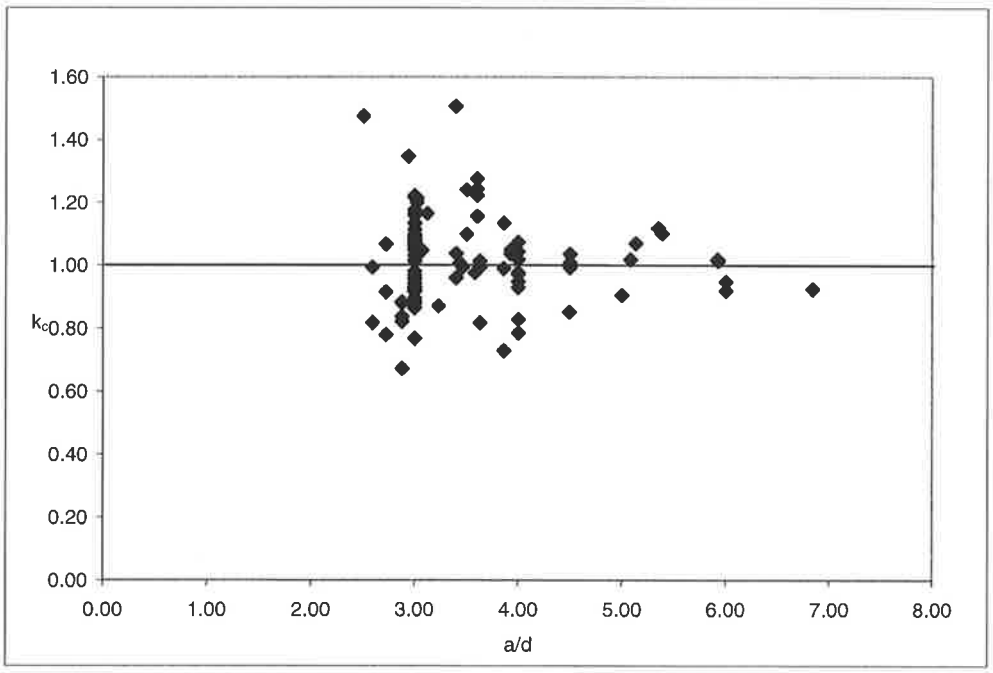

Figure 2.6.1: Comparison of k_c using Eurocode2.

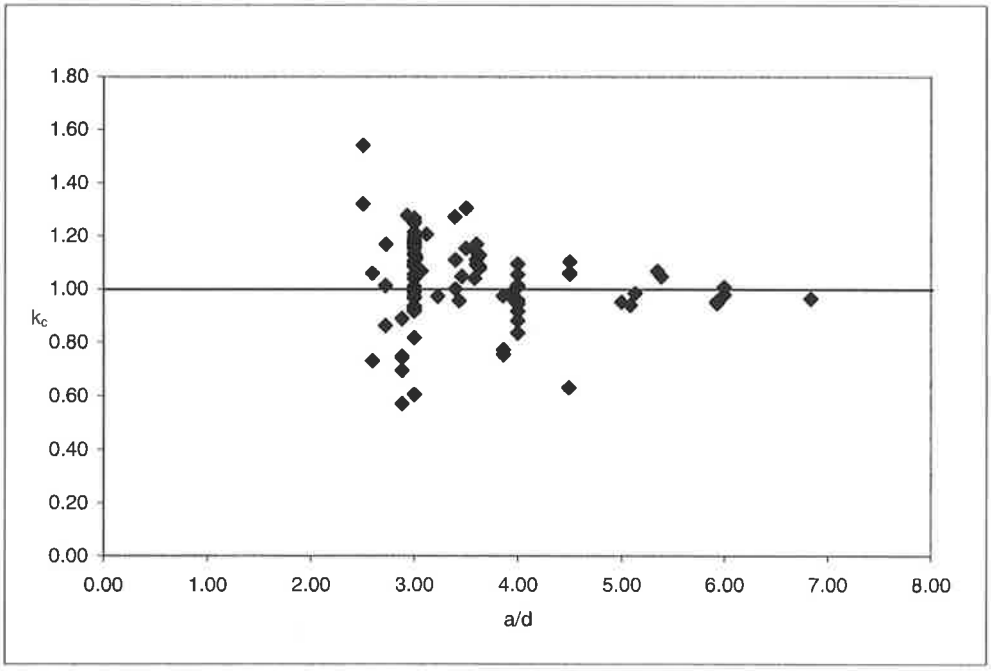

Figure 2.6.2: Comparison k_c using AS3600.

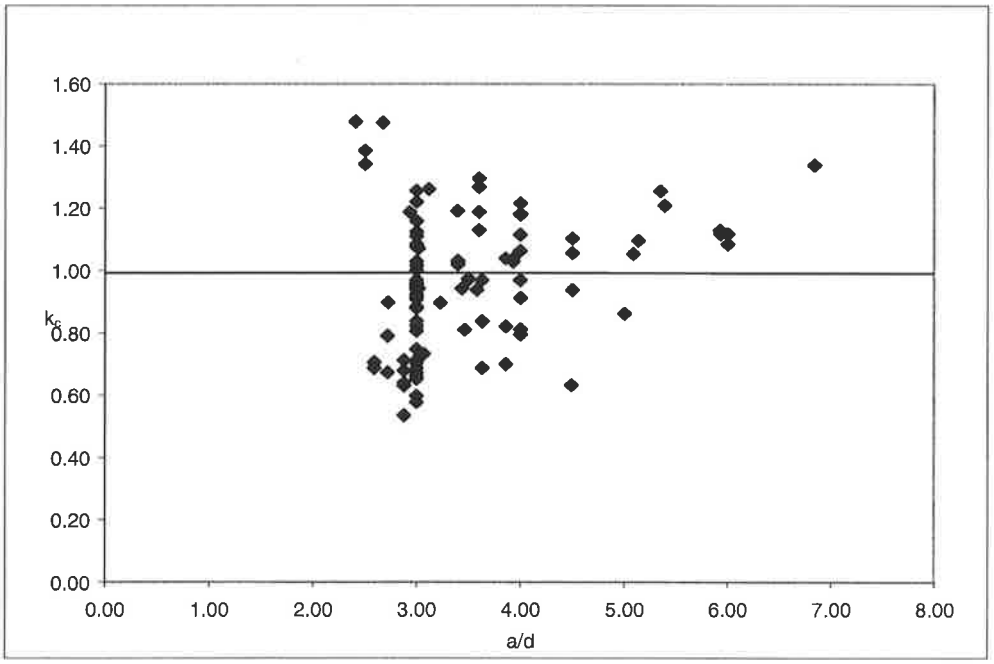

Figure 2.6.3: Comparison of k_c using CDC analysis.

Comparisons between the code predictions and the experimental results (Figures 2.6.1 – 2.6.2) show that the codes give a good correlation with the mean k_c close to unity and not much scatter. Meanwhile, the CDC analysis compared with the experiment results also gives a good correlation (Figure 2.6.3) with slightly higher scatter.

Considering the brittle behaviour of shear failure, the scatter of results is considered reasonable as most point are within ± 20 % of the mean. The value k_c determined in this section is later used to find the concrete contribution towards the shear capacity of a shear strengthened beam with FRP plates.

2.6.2 Transverse FRP plates shear capacity (V_{frp})

Similar to k_c developed for V_c in section 2.6.1, the ratio k_{frp} is introduced to relate the predicted V_{frp} from Cheng and Teng's model to experimental data. The ratio k_{frp} is defined as,

$$k_{frp} = \frac{V_{frp(\exp)}}{V_{frp(cal)}} \tag{2.6.3}$$

where $V_{frp(\exp)}$ is the experiment shear contribution of the FRP for beams without internal steel stirrups or widely spaced stirrups define as

$$V_{\exp} - k_c V_c = V_{frp(\exp)} \tag{2.6.4}$$

and $V_{frp(cal)}$ is the predicted shear capacity calculated according to the Chen and Teng approach. V_{exp} is the shear capacity of strengthened beams taken from experimental data.
Although two different types of FRP failure, that is debonding and rupture, are possible only debonding failures were used to find k_{frp}. Chen and Teng's debonding failure calculations were used for the analysis and 6 strengthened beams with transverse FRP plates were used in this analysis. Only 6 beams were considered because not many tests were done on strengthened beams with FRP without the internal stirrups and with 90° fiber orientation. The outcome of this analysis is that the mean for k_{frp} is 1.06 (Appendix C), which means that Chen and Teng's approach for calculating V_{frp} is a good model of the experimental tests as shown in Figure 2.6.4. This is similar to Chen and Teng's test-to-predicted strength ratio for debonding in Teng, et al. (2002) where a value of 1.07 is given. Therefore, at this stage of research, Chen and Teng's approach will be use to predict the contribution of the FRP to shear strengthened beams.

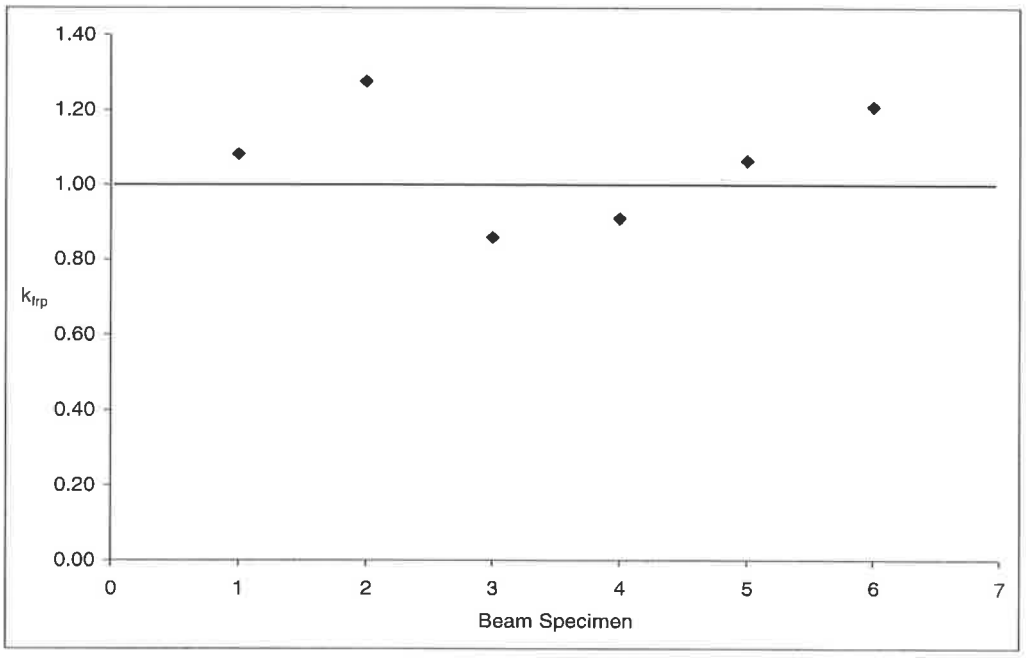

Figure 2.6.4: Comparison of k_{frp} using Chen and Teng's approach.

2.6.3 Internal Stirrups Shear Capacity (V_s)

It is worth noting that it is possible for a shear crack of 45° to cross the web without intersecting shear reinforcement if the spacing exceeds *d*. Therefore in this analysis only beams with steel shear reinforcement spacing less 2*d*/3 are taken into account.

Similar to k_c and k_{frp} developed for V_c and V_{frp} in section 2.6.1 and 2.6.2, the ratio k_s is introduced to relate the predicted V_s from codes model to experimental data. The ratio k_s is defined as,

$$k_s = \frac{V_{s(\exp)}}{V_{s(cal)}} \tag{2.6.5}$$

The contribution of internal stirrups to the shear capacity of strengthened RC beams, is considered in this section. For beams with internal stirrups and transverse FRP reinforcement, the experimental contribution of the internal stirrups is given by:

$$V_{s\,exp} = V_{(exp)} - k_c V_c - k_{frp} V_{frp} \tag{2.6.6}$$

When the concrete shear strength was tested directly, the experimental value was used in place of $k_c V_c$. Calibration with 13 beams (Appendix D) tested with internal shear

reinforcement and 90° transverse FRP reinforcement proved that the internal steel shear reinforcement does contribute fully to the total shear capacity of strengthened beams.

Figures 2.6.5 – 2.6.6 plotted ($V_{s(exp)}/V_{s(cal)}$) against s/d, where s = spacing of the internal shear reinforcement and d = effective beam depth, shows that internal stirrups contribute to the total shear capacity of FRP strengthened beams. Figures 2.6.6 and 2.6.7 also shows the comparison for k_s for beams tested with and without the reference beam (V_c measured directly) included in the test series.

Prior to this analysis, the basic assumption was that internal stirrups do not contribute to the total shear capacity of strengthened beams. However, with these analysis results, it is proven that the assumption were invalid [Deniaud and Cheng (2001),Pellegrino and Modena (2002),Diagana, et al. (2003)].

The conclusion of this analysis is that the internal stirrups do contributed to the total shear capacity of strengthened beams. The reason only 90° fibre orientation was considered in this analysis is because tests with 60° and 45° fibre orientations were found to give $V_{s\,exp}$ higher than those predicted from EC2 and AS3600.

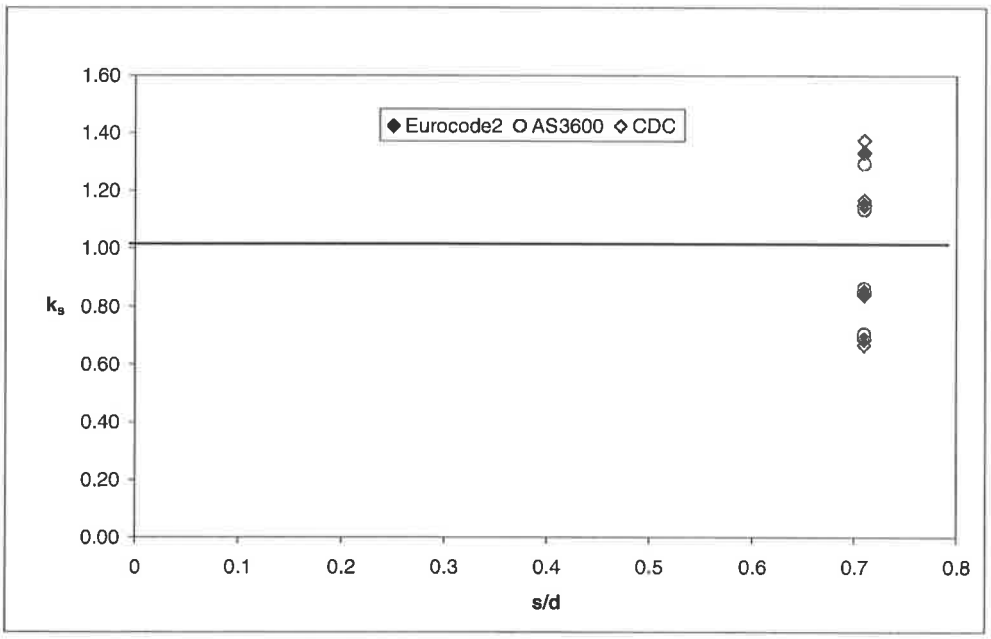

Figure 2.6.5: Comparison $V_{s(exp)}/V_{s(cal)}$ for Eurocode2, AS3600 and CDC analysis without reference beams.

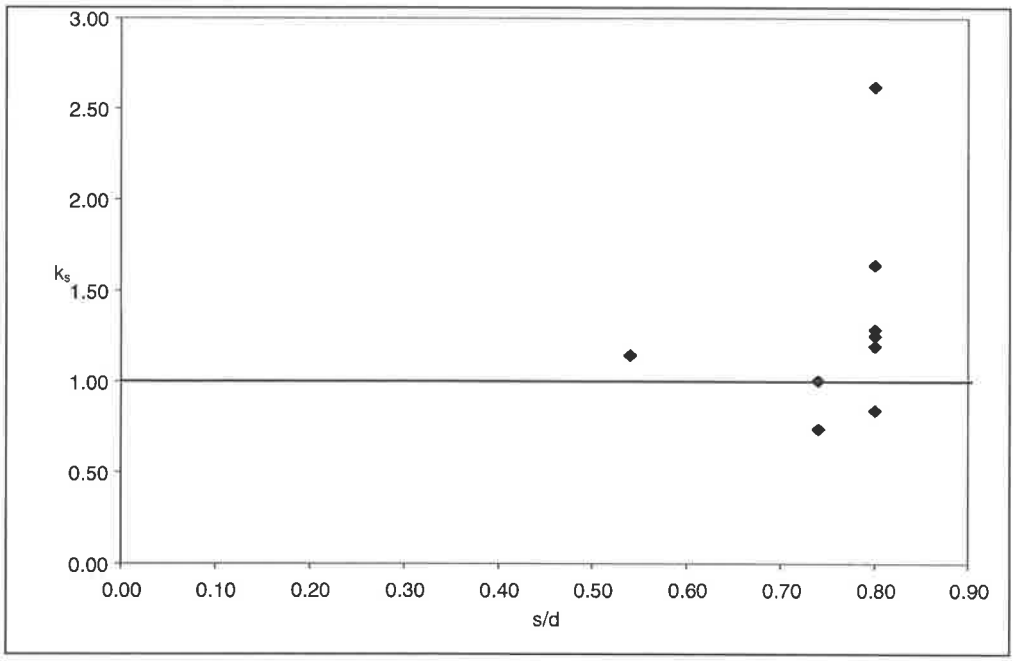

Figure 2.6.6: Results of comparison $V_{s(exp)}/V_{s(cal)}$ for beams with reference beams.

Hence, it is proposed that inclined fibres not only contribute to the vertical component of shear resistance as internal stirrups, but also to the horizontal component of force increasing the concrete shear capacity (V_c) as longitudinal plates do (ie ΔV_c in section 2.1.1.1). Hence, the total shear resistance is given in the following form.

$$V_n = k_c V_c + (\Delta V_c + k_{frp} V_{frp}) + k_s V_s \qquad (2.6.7)$$

where

V_c is the concrete shear capacity (from code or experiment)

$(\Delta V_c + k_{frp} V_{frp})$ is the contributions of FRP in the Horizontal and Vertical orientation respectively.

V_s is the contributions of the internal stirrups towards the shear capacity.

Next, analysis using passive prestress approach to quantify $0.15\sigma_{ps} b_c d \approx 0.15 F_{ps}$ from Eq. 2.2.19 that is the increase in the shear capacity due to prestress is described.

2.7 Analysis using Passive prestress approach

2.7.1 Passive Prestress Approach with Eurocode2

There are 30 beams available in the early stage of this analysis with EC2. Only steel plated beam were used in this analysis. The aim analysis is to find the contribution of longitudinal plating to the increased shear capacity of the concrete. In Eq. 2.2.19, the contribution of plating due to the passive prestress, this is 15% of the total P_{plate}.

In this analysis the angle crack was fixed to 45° and from this assumption the location where the crack intercepts the plate is known and this defines the bonded length of the plate. This bond length is required to give the force acting in the plate using Chen and Teng's equation for IC debonding:

$$\sigma_{IC} = \alpha\beta_p\beta_L\sqrt{\frac{E_p\sqrt{f_c}}{t_p}} \qquad \text{[N and mm]} \qquad (2.7.1)$$

where (β_p allows for the width of the plate relative to the width of the concrete element)

$$\beta_p = \sqrt{\frac{2-(b_p/b_c)}{1+(b_p/b_c)}} \qquad b_p/b_c \geq 0.33 \qquad (2.7.2)$$

The full anchorage length or effective length is given by

$$L_e = \sqrt{\frac{E_p t_p}{\sqrt{f_c}}} \qquad \text{[N and mm]} \qquad (2.7.3)$$

and

$$\beta_L = \begin{cases} 1 & \text{if } L \geq L_e \\ \sin[\pi L/2L_e] & \text{if } L < L_e \end{cases} \qquad (2.7.4)$$

It is worth noting that this P_{plate} (Eq. 2.2.19) are limited by the yield capacity of the steel plate. Only 24 beams were available for further analysis, which is a combination of fully plated (L_{end} = 0, terminated at the support) and partially plated (terminated short of the support) beams [Oehlers, et al. (2004)]. Six beams were rejected because the plate was terminated beyond the support clamping the plate in place after debonding.

Table 2.7.1: Mean and 95% characteristic for the Eurocode2 approach.

Eurocode2	mean	Standard Deviation	Coefficient of Variance
	0.15	0.0524	34.11
	95% characteristic	Standard Deviation	Coefficient of Variance
	0.07	0.0524	73.51

With P_{plate} known and $V_{c\ theory}$ from Eq. 2.2.12, the analysis for the contribution of the longitudinal plate to the total shear resistance was found by using this simple equation

$$(V_{exp} - V_{c\ theory})/ P_{plate.} \qquad (2.7.5)$$

Table 2.7.1 shows that the mean value of Eq. 2.7.5 for the 24 beams is 0.15. This is the value assumed in the beginning of this analysis, which was derived from Eq. 2.2.19 and proves that the increase in shear capacity of the concrete due to longitudinal plating is $0.15P_{plate.}$ The analysis continues by fixing the 'k_{pres}' factor (P_{plate} factor) ranging from 0.12 to 0.20. Figure 2.7.1 clearly shows that the value 0.155 is the value of the contribution of the longitudinal plating to the total shear capacity.

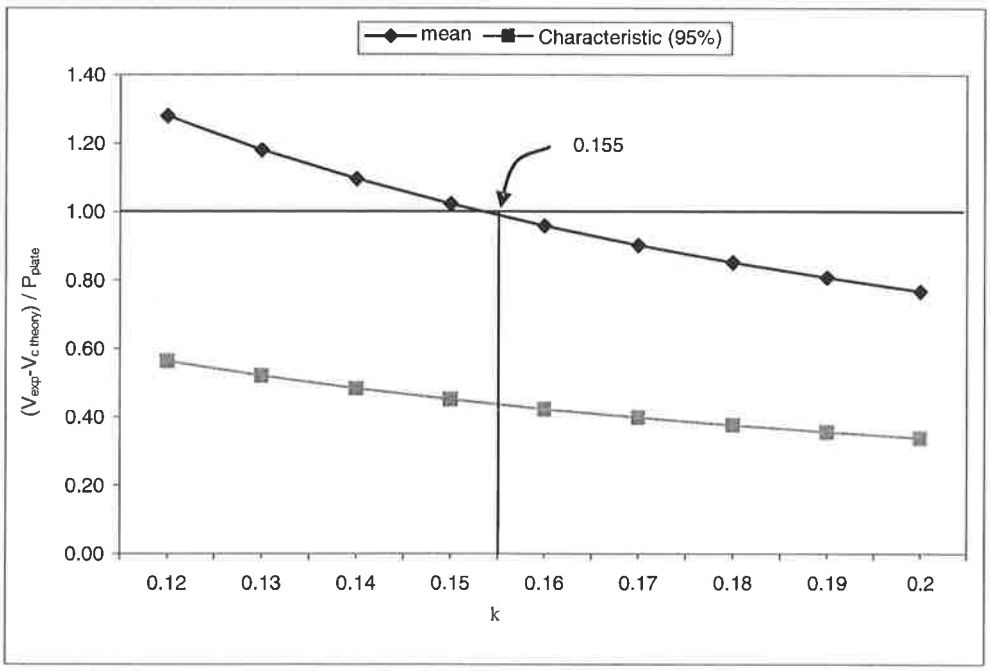

Figure 2.7.1: Increase due to longitudinal plating with mean and 95% characteristic value (Eurocode2).

2.7.2 Passive Prestressed Approach with CDC Analysis

The same twenty four beams were analysed to determine whether the coefficient 4 in Eq. 2.2.9, is an appropriate value for the contribution of the plate towards the increase in the concrete shear capacity the CDC analysis.

In this analysis the position of the critical diagonal crack is known from the focal point and with this, the location of the crack intercepting the plate is known and defines the bonded length of the plate, similar to the analysis using EC2. Chen and Teng's equation for the IC debonding stress (or strain) in the longitudinal plate was again used. However, for compression longitudinal type of plating, there are three stages involved for the shear to crack ($V_{cr\ plated}$) in the CDC analysis. Although the beam was plated, the first stage is to calculate the V_{cr} unplated. Then second stage is to calculate the $V_{cr\ plated}$ using what was explained in section 2.1.1.1 and consider it to be on the hogging section of a continuous beam. Finally using the free body diagram, calculate the V_{cr} unplated from the support to the point of loading. This show that there are three values for $V_{cr\ plated}$ compression, only the second stage of analysis to be consider as the $V_{cr\ plated}$ compression and the reason is out of all three stages involve, only this stage consider the contribution of plate to the shear to cause crack.

Figure 2.7.2, drawn from the data available in Table 2.7.2, shows that for the CDC approach, the value of 4 previously assumed is conservative and a more appropriate value is 6.5. However, this is the mean value of the 24 beams that were analysed. This value may not be suitable for very deep beams and thicker plates.

Table 2.7.2: Mean and 95% Characteristic value for the CDC approach.

'k_{press}'	3.5	4.0	4.5	5.5	6.0	6.5	7.0
Mean	1.12	1.09	1.08	1.05	1.03	1.01	0.98
Standard Deviation	0.139	0.143	0.135	0.131	0.137	0.137	0.134
Coefficient of Variance	12.38	13.03	12.50	12.50	13.31	13.49	13.64
95% Characteristic	0.89	0.86	0.86	0.83	0.80	0.79	0.76

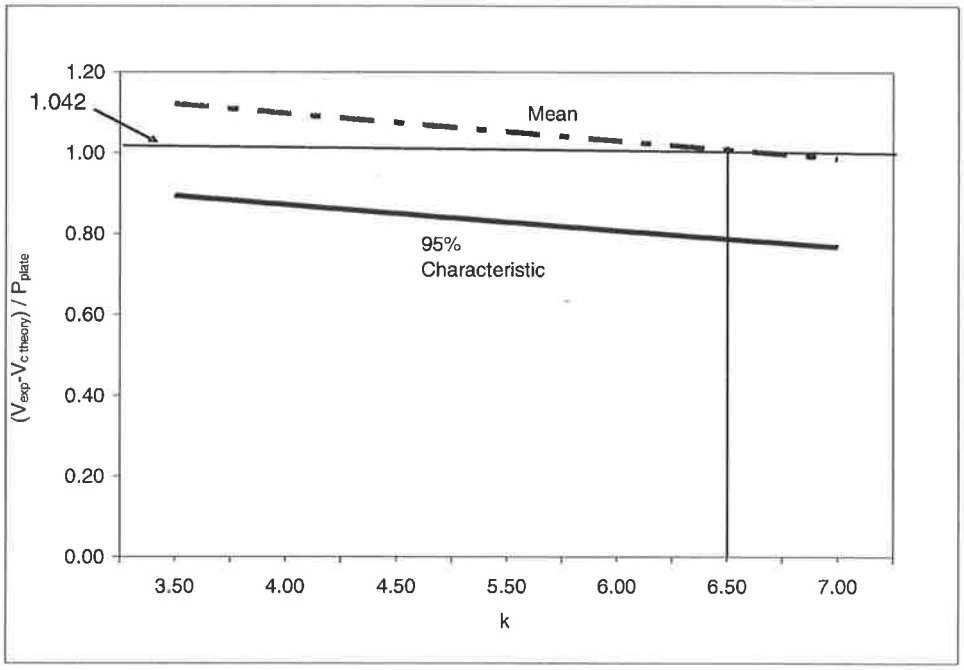

Figure 2.7.2: Increase in Concrete Shear Capacity due to Longitudinal Plating: Passive Prestressed Approach.

All the data for this analysis can be view in the appendix E and F. Comparison between Table 2.7.1 and Table 2.7.2 shows that the coefficient of variance for the passive prestress approach with CDC is less than that for EC2. The reason is, EC2 is a simple passive prestress approach for calculating the increase in shear capacity on concrete due to longitudinal plating. Meanwhile the CDC analysis is the rigorous method.

2.8 Conclusion

The conclusion on shear capacity analysis is that contribution of concrete shear capacity, steel shear reinforcement and FRP; proves that there is an interaction between the three of these components and as for the passive prestress approach; CDC analysis is the accurate approach for calculating increase in concrete shear capacity due to plating.

From the previous section, it stated the work that had been done from previous researcher. With this known, the overall aim of this research is to know the interaction between the FRP (EB and NSM) plating with the steel shear reinforcement. Understanding the main failure mechanisms are the key in achieving this aim.

The specific aims to achieve this are:

1) To conduct a series of pull test (NSM plating) which represent the IC debonding failure with various type of plate materials such as steel, FRP and aluminium and thickness.
2) To develop the shear and slip relationship of NSM plating from the pull test database available which will also provide the bond strength and bond characteristic between the FRP and the concrete.
3) To come out with equation for predicting the bond strength contributes by the NSM. For the time being not many model available for NSM plating.

To understand more of these three component interaction (concrete, FRP plates and internal steel stirrups), first tests will be a series of pull test with NSM plates with various type of plate materials and dimension. The planned pull test set-up will as shown in Figure 2.8.1.

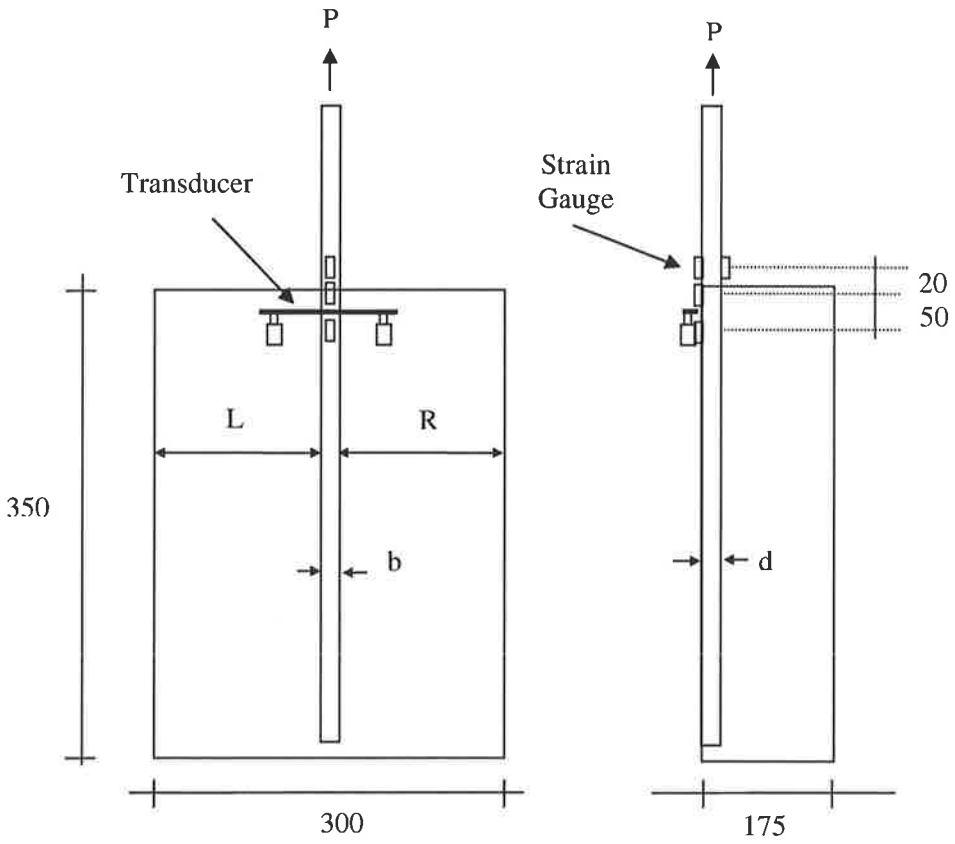

Figure 2.8.1: NSM pull test details.

Results from this pull test series will complete the existing database as stated in the research aims earlier and develop the shear slip relations of the bond strength for both type of plating (EB and NSM). Only NSM plating was planned because this is one of the latest approaches of FRP plating and it is assumed to have a very good interaction with the internal shear reinforcement. Detail discussion on the pull test is described in chapter 3 - 6.

The next series of experiments is to conduct 6 beam tests for the NSM plates including 2 reference beam test. This will be described in chapter 7.

Figure 2.20 – 2.22 shows the beams setup for each test for different type of NSM plating and FRP plates will be the plate material for the experiment. All the beams must be designed to fail in shear well before the flexure capacity is reached.

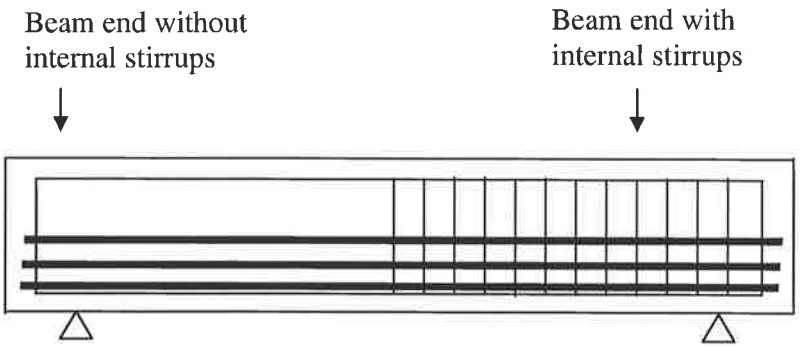

Figure 2.8.2: Beam test setup for longitudinal NSM plating.

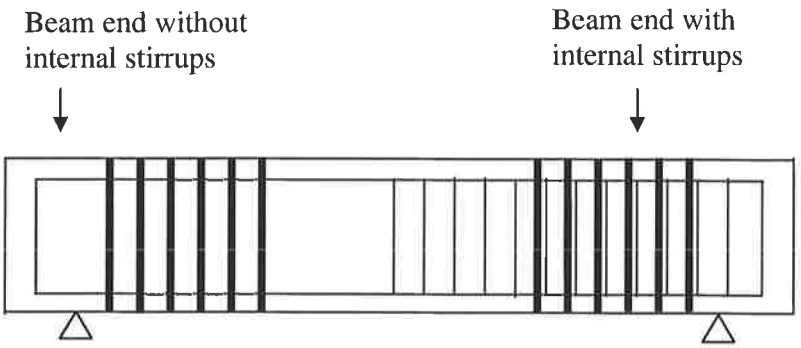

Figure 2.8.3:Beam test setup for transverse NSM plating.

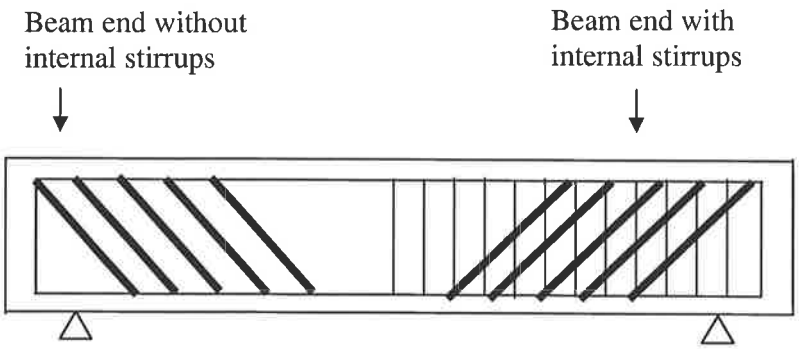

Figure 2.8.4: Beam test setup for incline NSM plating.

All beam test planned is to demonstrate an increase in shear strength that would induce IC and CDC failure. Reason for each beam side had with and without steel shear reinforcement is to look into the increase in shear due to NSM plating. This will indicate the increase in concrete shear capacity and also the increase in shear capacity with the existence of shear steel reinforcement. In the next chapter, the single NSM pull test which is the first series of pull test is described.

2.9 References

1. ACI440R-96 (1996). State-of-the Art Report on Fiber Reinforced Plastic (FRP) Reinforcement fo Concrete Structures. Farmington Hills, Michigan, USA, American Concrete Institute (ACI).

2. Adebar, Collins Perry and P., M. (1996). "Shear strength of members without transverse reinforcement." Canadian Journal of Civil Engineering **23**(1): 30-41.

3. Australian Standard : Concrete Structures (AS3600-2001) (2001). Australia**:** 176.

4. Bousselham, A. and Chaallal, O. (2004). "Shear strengthening reinforced concrete beams with fiber-reinforced polymer: Assessment of Influencing parameter and required research." ACI Structural Journal **101**(2): 210-227.

5. Chen, J. F. and Teng, J. G. (2003). "Shear Capacity of Fiber-Reinforced Polymer-Strengthened Reinforced Concrete Beams: Fiber Reinforced Polymer Rupture." Journal of Structural Engineering **129**(5): 615-625.

6. Deniaud, C. and Cheng, J. J. R. (2001). "Review of Shear Design Methods for Reinforced Concrete Beams Strengthened with Fibre Reinforced Polymer Sheets." Canadian Journal of Civil Engineering **28**: 271-281.

7. Diagana, C., Li, A., Gedalia, B. and Delmas, Y. (2003). "Shear strengthening effectiveness with CFF strips." Engineering Structures **25**(4): 507-516.

8. Eurocode 2: Design of Concrete Structures : Part 1: General rules and rules for buildings. (2002). 226.

9. Hassan, T. and Rizkalla, S. (2003). "Investigation of bond in concrete structures strengthened with near surface mounted carbon fiber reinforced polymer strips." Journal of Composites for Construction **7**(3): 248-257.

10. Ing, L. K., Jones, N., Page, M. and Ward, S. (2004). Intermediate Crack Debonding of Near Surface Mounted Strips. Adelaide, University of Adelaide**:** 91.

11. Khalifa A, Gold W.J., NanniA and M.I., A. A. (1998). "Contribution of Externally Bonded FRP to Shear Capcity of Flexural Members." Composites for Construction **2**(4): 195-203.

12. Khalifa A and Nanni A (2000). "Improving shear capacity of existing RC T-section beams using CFRP composites." Cement and Concrete Composite **22**: 165-74.

13. Khalifa A, Tumialan G, Nanni A and A, B. (1999). Shear strengthening of continuous RC beams using externally bonded CFRP sheets. Fiber-reinforced plastics for reinforced concrete structures, Baltimore, MD.

14. Li, A., Diagana C. and Y., D. (2003). Shear performance with externally bonded Carbon Fibre Fabrics. Fiber-reinforced plastics for reinforced concrete structures, Singapore, World Scientific Publishing Company.

15. Liu, I. (2005). Intermediate Crack Debonding of Plated Reinforced Concrete Beams. School of Civil and Environmental Engineering. Adelaide, University of Adelaide**:** 610.

16. Meier, U. (1995). "Strengthening of structures using carbon fibre/epoxy composites." Construction and Building Material **9**(6): pp 341-351.

17. Mohamed Ali, M. S. (2000). Peeling of Plates Adhesively Bonded to Reinforced Concrete Beams. Department of Civil and Environmental Engineering. Adelaide, University of Adelaide**:** 593.

18. Oehlers, D. J., I.Liu, Seracino, R. and Mohamed Ali, M. S. S. (2004). "Prestress model for shear deformation debonding of FRP and steel plated RC beams." Magazine of Concrete Research.

19. Oehlers, D. J. and Seracino, R. (2004). "Design of FRP and Steel Plated RC Structures." 222.

20. Pellegrino, C. and Modena, C. (2002). "Fiber Reinforced Polymer Shear Strengthening of Reinforced Concrete Beams with Transverse Steel Reinforcement." Journal of Composites for Construction **6**(2): 104-111.

21. "Recent approaches to shear design of structural concrete." (1998). ASCE-ACI Committee 445,Journal of Structural Engineering **124**(12): 1375-1417.

22. Sato, Y., Ueda, T., Kakuta, Y. and Ono, S. (1997). Ultimate shear capacity of reinforced concrete beams with carbon fiber sheet. Non-Metallic (FRP) Reinforcement for Concrete Structures, Sapporo, Japan, Japan Concrete Institude.

23. The shear strength of reinforced concrete members. (1973). ASCE-ACI Committee 426,Journal of Structural Engineering. **99:** 1091-1187.

24. Taljsten, B. (2003). "Strengthening concrete beams for shear with CFRP sheets." Construction and Building Materials **17**: 15-26.

25. Taljsten, B. and Elfgren, L. (2000). "Strenthening Concrete Beams for Shear using CFRP-materials: Evaluation of difference application methods." Composite **31**: 87-96.

26. Teng, J. G. and Chen, J. F. (2003). "Shear Capacity of FRP-strengthened RC beams : FRP debonding." Construction and Building Material **17**: 27-41.

27. Teng, J. G., Chen, J. F. and Smith, S. T. (2002). FRP Strengthened RC Structures. England, John Wiley & Sons, Ltd.

28. Triantafillou, T. C. (1998). "Shear Strengthening of Reinforced Concrete Beams Using Epoxy-Bonded FRP Composites." ACI Structural Journal **95**(2): 107-115.

29. Triantafillou, T. C. and Antonopoulos, C. P. (2000). "Design of Concrete Flexural Members Strengthened in Shear with FRP." Journal of Composites for Construction **4**(4): 198-204.

30. Triantafillou, T. C. and Plevris, N. (1992). "Strengthening of RC beams with epoxy bonded fibre-composite materials." Materials and Structures. **25**: 201-211.

31. Zhang, J.-P. (1994). "Strength of Cracked Concrete. Part 1." Department of Structural Engineering, Technical University of Denmark **311**.

32. Zhang, J.-P. (1997). "Diagonal cracking and shear strength of reinforced concrete." Magazine of Concrete Research **49**(178): 55-65.

2.10 Notation

A_c	area of concrete cross section (mm^2)
A_{rect}	cross-sectional area of rectangular section of the plate,
A_{st}	cross-sectional area of longitudinal reinforcement provided in the tension zone and fully anchored at the cross-section under consideration
A_{sv}	cross-sectional area of shear reinforcement,
b_c	width of the slab or the width of the web of a beam,
b_p	Plate width
CFRP	Carbon Fiber Reinforced Polymer
d_{frp}	distance from the compression face to the lower edge of the FRP
$d_{frp,t}$	distance from the compression face to the top edge of the FRP
d_p	Plate depth
d_{ps}	lever arm of the prestressing force from the compression face,
EB	Externally Bonded
E_c	Concrete Young's Modulus
E_{frp}	FRP Plate Young's Modulus
E_p	Plate Young's Modulus
f_c	Concrete compressive strength
F_{ps}	prestressing force,
$f_{sy,f}$	yield strength of shear reinforcement,
f_t	tensile strength of concrete, $0.4\sqrt{f_c}$,
f_{tef}	effective tensile strength of the concrete,
h	total depth of the beam or slab,
K_M	moment factor, and
K_W	the load factor.
L_o	length of the free body,
L_{rect}	lever arm from the centroid of the rectangular section to the compression face,
m_p	modular ratio of the plate and concrete, $\frac{E_p}{E_c}$,
NSM	Near Surface Mounted
s	centre-to-centre spacing of shear reinforcement, measured parallel to the longitudinal axis of the member,
s_{frp}	spacing of the FRP,
V_c	shear capacity of unplated beam or slab without stirrups, concrete component of shear capacity
V_{cr}	shear load to cause cracking
V_{dat}	shear load at any convenient datum point
V_{frp}	contributions of the FRP plates towards the shear capacity
V_s	contributions of the internal stirrups towards the shear capacity
V_u	shear capacity across a diagonal crack; equal to V_c for the CDC in a unplated beam
$(M_{dat})_{cr}$	moment at datum point when a diagonal crack forms and when $(V_{dat})_{cr}$ is acting
$(V_{dat})_{u(plated)}$	shear load at datum point to cause crack sliding in a plated beam
$(V_{dat})_{cr\ (plated)}$	shear load at the datum point to cause cracking in the plated

$(V_{dat})_{cr}$	vertical shear load at datum point when diagonal crack forms; shear at datum point to cause cracking in unplated beam
$(V_{dat})_u$	shear load at datum point to cause shear failure across a diagonal crack; shear load at the datum point to cause crack sliding across a diagonal crack; shear load at datum point to cause crack sliding in unplated beam
$(W_{dat})_{cr}$	resultant of applied loads acting on free body when $(V_{dat})_{cr}$ is acting in deriving the load to cause cracking
x	inclination θ of the diagonal crack
θ_v	angle between the axis of the concrete compression strut and the longitudinal axis of the member, taken conservatively as 45°

Chapter

3 EXPERIMENTS ON SINGLE NSM PLATES

3.1 Introduction

This chapter explains the push-pull experiments (herein referred to simply as pull-test) of Near-Surface Mounted strips adhesively bonded to a concrete block. The results obtain from these experiments are required in Chapter 4 to fill the gaps between Near-Surface Mounted (NSM) and Externally Bonded (EB) plates to validate the generic equation for Intermediate Crack (IC) debonding resistance (Eq. 4.2.7). Another objective of the tests is to prove that the generic equation is applicable for both, NSM and EB plating by looking into the prediction on the ultimate load (P_{ult}) of each individual test with different plate aspect ratios. The next section of this chapter will cover the description of the specimens, the test set-up and the material properties. Then, the observations from each individual test are described. Finally, the conclusions made from all the test results are discussed.

3.2 Specimen

The plate specimens used consisted of 16 NSM plates for this series of pull tests with varied plate thickness and materials. The plates were glued to the centre of the concrete prism located 150mm from the edge of concrete block using MBrace Laminate Adhesive as shown in Figure 3.2.2. The plate was located at the centre of the concrete block to avoid any edge effects that might affect the ultimate load (P_{ult}) of pull tests. The parameters and materials of the 16 plates in this test series are summarise in Table 3.2.1 and in Appendix G.

The nominal thickness of the FRP plates used was 1.2mm thickness commercially known as MBrace S&P CFK Laminate. When fabricating plates thicker than 1.2mm, the plates were glue together using MBrace Laminate Adhesive to reach the target thickness shown in Table 3.2.1. The plate depth (d_p) and width (b_p) were measured for each test which was with 350mm plate length. The selection of plate dimensions were based on the need to fill the gap between NSM plates and EB plates that will be explained in Chapter 4. Another important reason for all of this test done is to understand seamless transition of EB to NSM plating shown in Figure 3.2.1. The test setup will be presented next.

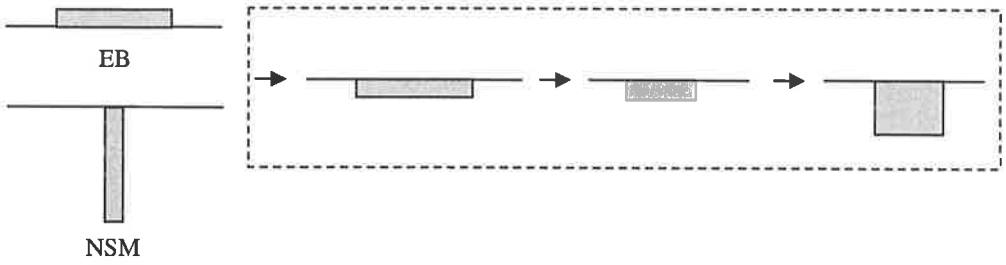

Figure 3.2.1: Transition of EB to NSM plating.

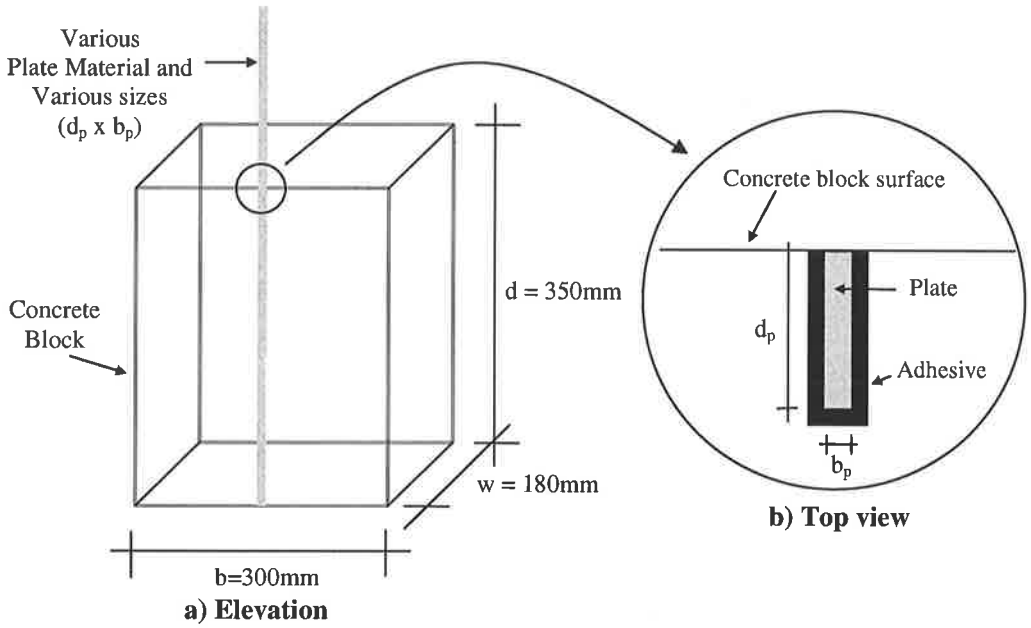

Figure 3.2.2: Near-Surface Mounted pull test specimen details.

Table 3.2.1: Summary of plate geometric and material properties.

Specimen	d_p (mm)	b_p (mm)	Materials
12x12	11.91	11.92	Steel
12x12	12.42	12.40	Aluminium
12x12	12.76	11.88	CFRP
12x3	12.37	2.76	CFRP
12x4	12.73	4.28	CFRP
12x6	12.51	5.78	CFRP
24x4	24.14	4.37	CFRP
30x7	30.55	7.39	CFRP
12x5	12.00	5.00	Steel
26x20	25.26	20.6	CFRP
12x30	12.02	30.92	CFRP
12x50	12.20	50.33	CFRP
12x60	11.74	61.03	CFRP
12x70	11.93	71.25	CFRP
12x80	12.28	81.00	CFRP
12x100	12.30	101.08	CFRP

3.3 Test Setup

When a specimen consisting of the concrete block and plate is ready to be tested, it is placed in the rig as shown in Figure 3.3.1. The specimens were rotated 90°, so that the concrete block faced the side of rig, compared to EB pull test specimens due to the clamping mechanism and orientation of the plate. However for last 6 pull tests (12mm x 30mm to 12mm x 100mm), the specimen were placed in the rig with the same orientation of EB. The plates were strengthened to avoid plate crushing or splitting due to the clamping force that may cause premature failure of the plate. Aluminium plates of 1.5 mm thickness were used as the grips. The dimensions of the aluminium plates were 100mm high and 5mm wider than the plates; that is, 100mm x 25mm for a 20mm strip. The aluminium was roughened using course emery cloth and cleaned thoroughly with acetone before gluing to the plates. The plates were also cleaned thoroughly with acetone.

The adhesive used to glue the aluminium grips to the plates was CIBA Adaldite K340 High Performance Adhesive Paste. This adhesive has a stronger bond compared to the MBrace Laminate Adhesive that is used to glue the plates to the concrete, ensuring that the grips do not debond before specimen failure occurs. The instrumentation of the each pull test is described next.

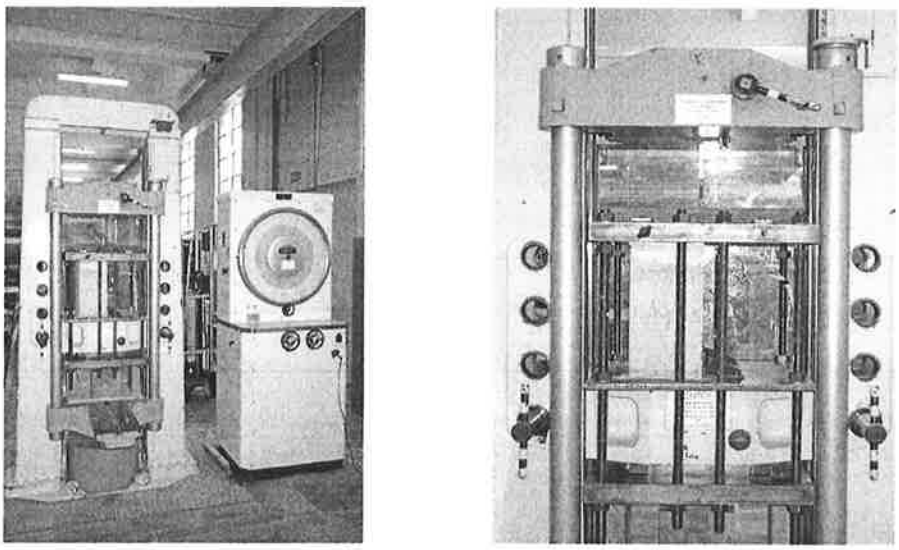

Figure 3.3.1: The Avery Universal Testing Machine.

3.4 Instrumentation

Strain gauges 1 and 2 (Figure 3.4.1), for the first two tests (mild steel and Aluminium) were located 25mm above the concrete block attached to the plates. These strain gauges provide information relating to the plates young's modulus. Meanwhile, strain gauges 3 and 4, were located 50mm and 100mm, respectively, from top of concrete block. These locations were chosen based on previous experiments Ing, et. al.(2004). Suitable strain readings were recorded approximately 50 mm from the top of the concrete prism to provide the peak shear stress of a NSM pull test. The strain gauges also provide an indication of plate debonding along the bonded length. The plate slip was monitored using transducers T1 and T2 between strain gauges 3 and 4, as shown in Figure 3.4.1.

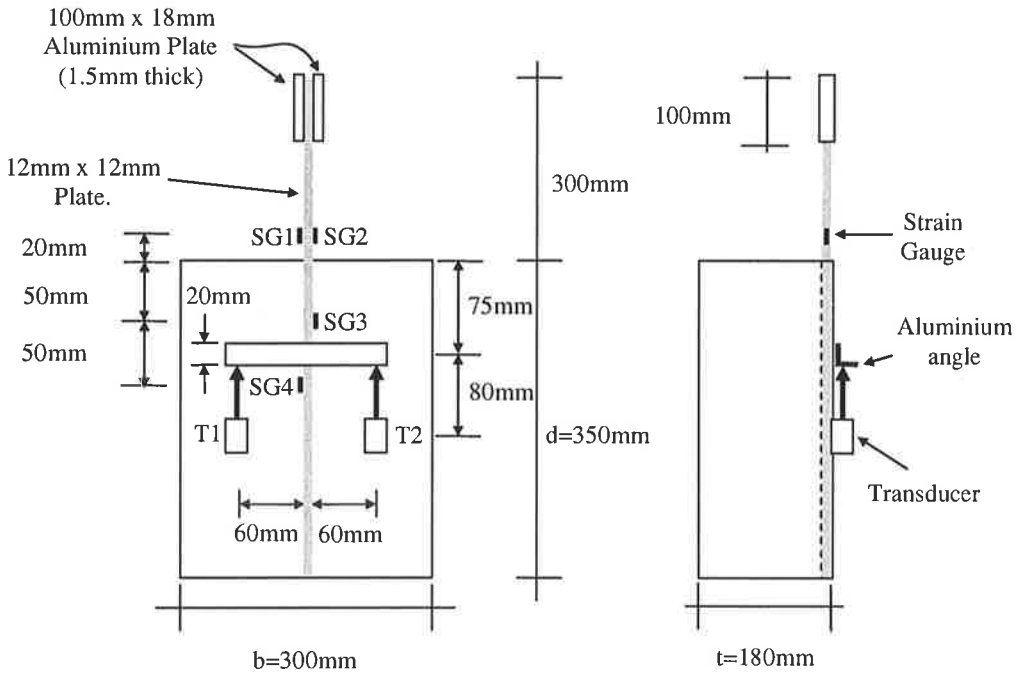

Figure 3.4.1: Pull test of 12mm x 12 mm Mild Steel and Aluminium plate details.

Strain gauge location and quantity differed for each pull test specimen depending on the plate material and size. For the 12mm x 12mm CFRP specimen, 7 strain gauges as shown in Figure 3.4.2. The 12mm x 12mm CFRP plate was fabricated using 8 CFRP plates with nominal thickness of 1.2mm glued together creating two surfaces available, one is only CFRP and the other is with CFRP and adhesive. The additional strain gauges, SG5, SG6 and

SG7 were located on the CFRP and adhesive surface to compare the strain reading located on the CFRP surface. In this test and 26mm x 20mm CFRP pull test, aluminium tube shown in Figures 3.4.2 and 3.4.9 was used to strengthen the plate to avoid premature failure due to clamping force.

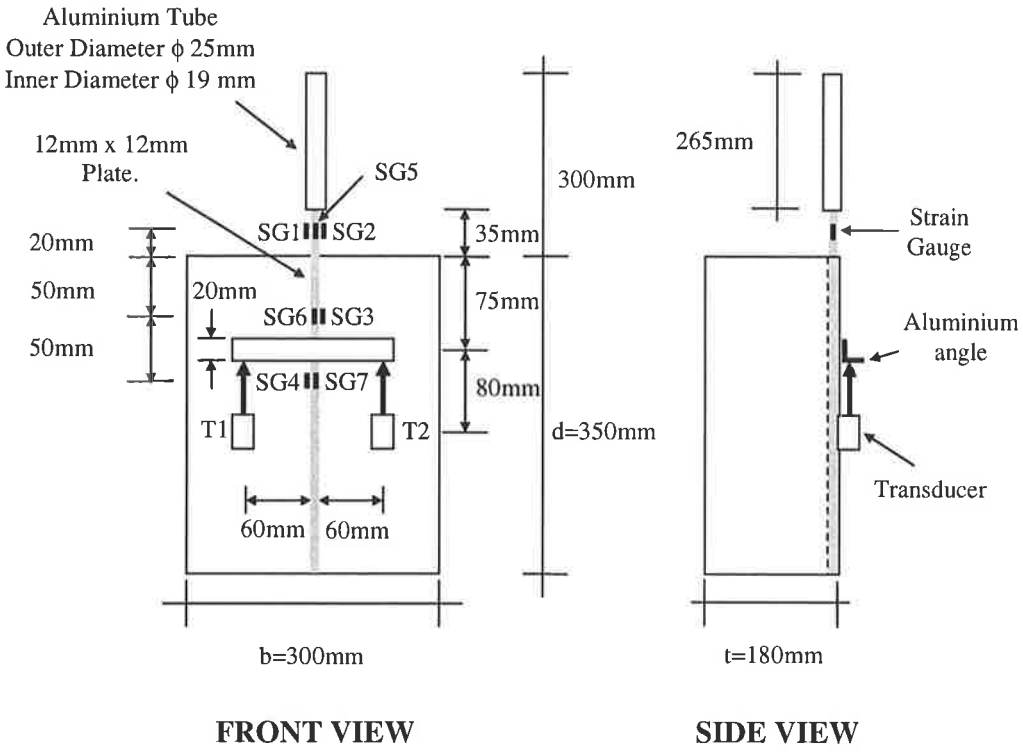

Figure 3.4.2: Pull test of 12mm x 12 mm CFRP plate details.

The next 6 tests shown in Figures 3.4.3 to 3.4.8 had similar instrumentation to the first two tests. However, for 26mm x 20mm CFRP plate pull test, another 4 strain gauges were added to monitor the strain profiles of the specimen (Figure 3.4.9). The number of strain gauges and positions were the same as 26mm x 20mm for specimen 12mm x 30mm (Figure 3.4.10), 12mm x 70mm (Figure 3.4.13), 12mm x 80mm (Figure 3.4.14) and 12mm x 100mm (Figure 3.4.15). For specimen 12mm x 50mm and 12mm x 60mm (Figures 3.4.11 and 3.4.12) only 4 strain gauges were used with SG3 and SG4 located 25mm and 50mm apart between each other to know whether reducing the distance between these two strain gauges will provide better shear stress reading (τ_{max}) between plate and concrete. Next, the material properties of the pull test specimen are described.

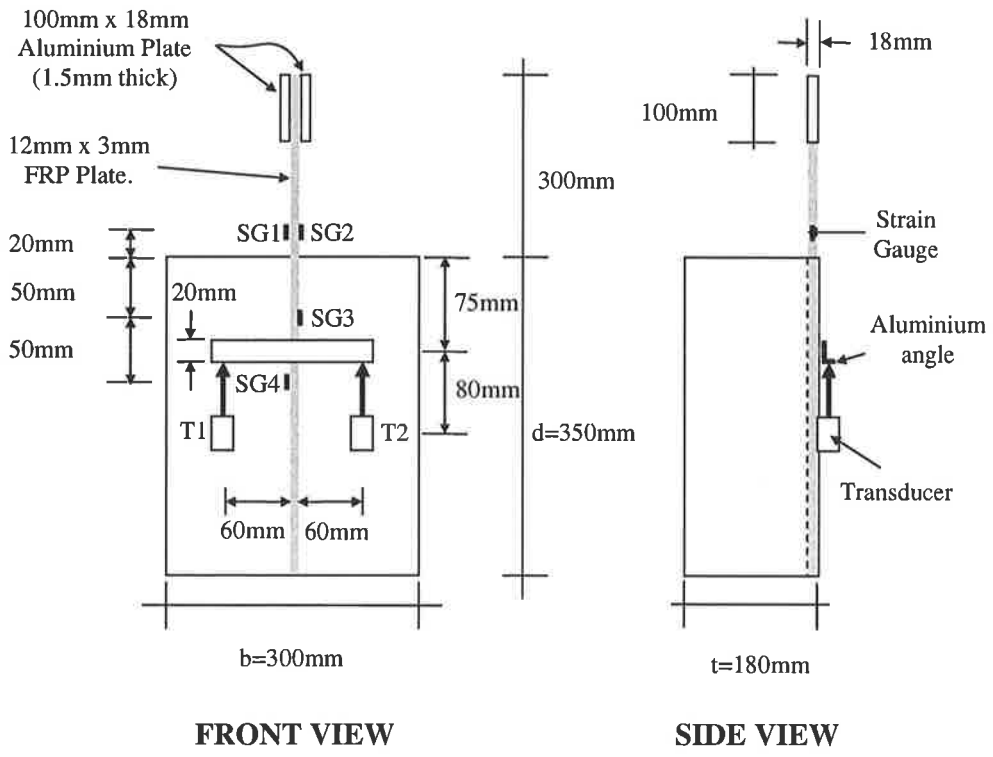

Figure 3.4.3: Pull test of 12mm x 3mm FRP plate details.

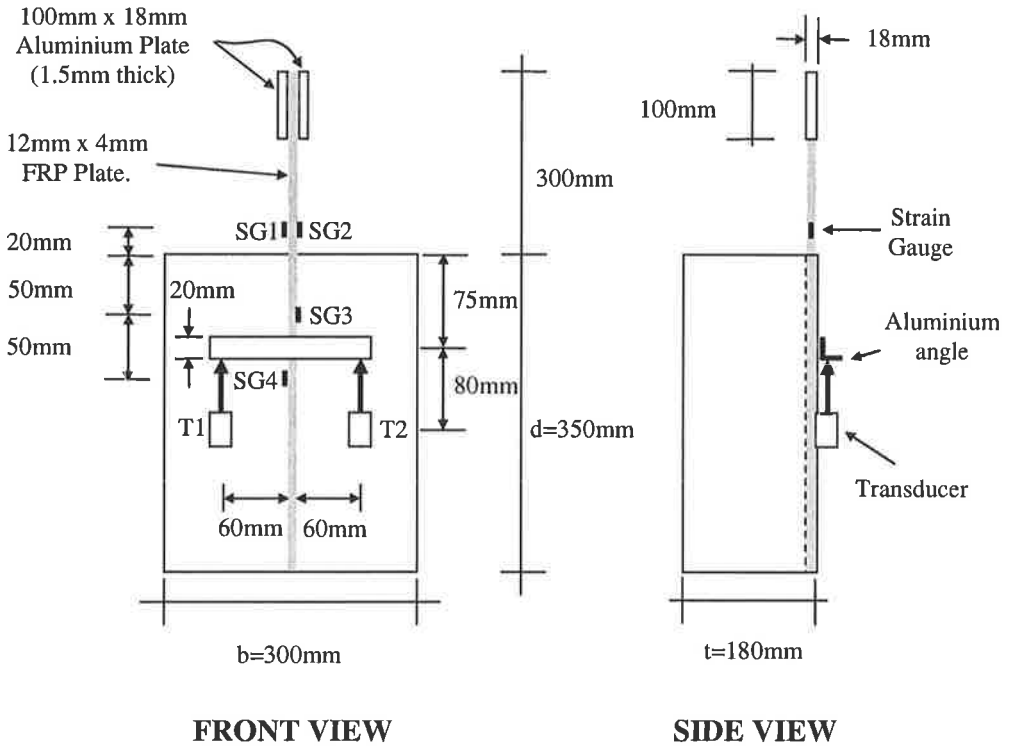

Figure 3.4.4: Pull test of 12mm x 4mm FRP plate details.

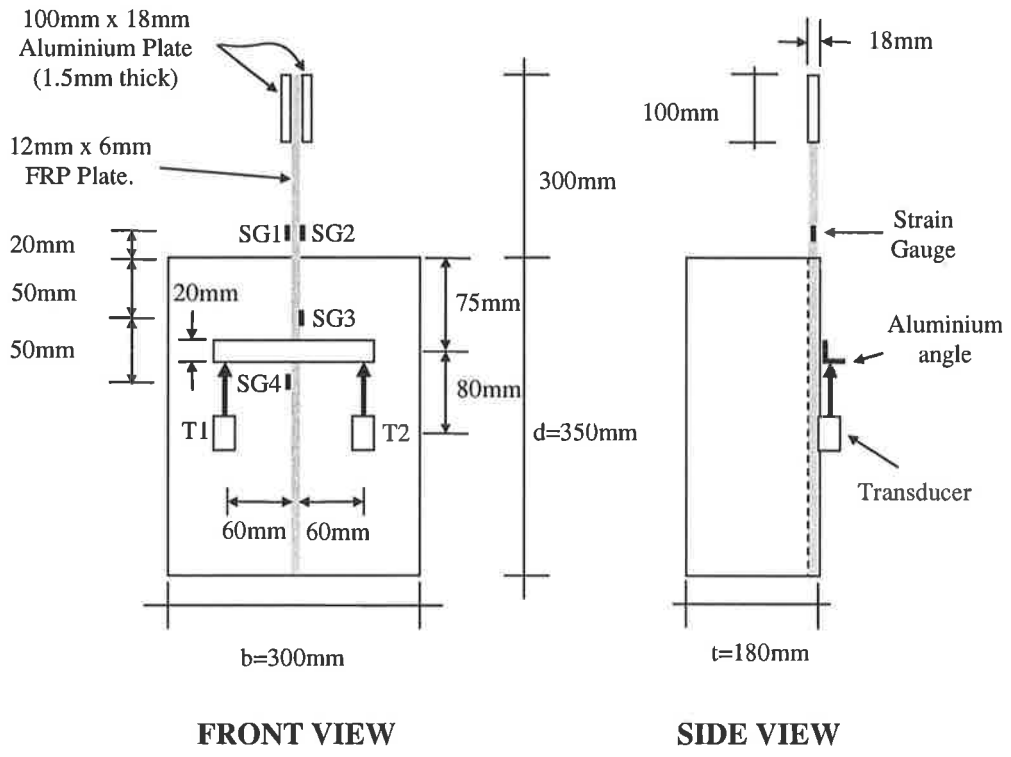

Figure 3.4.5: Pull test of 12mm x 6mm FRP plate details.

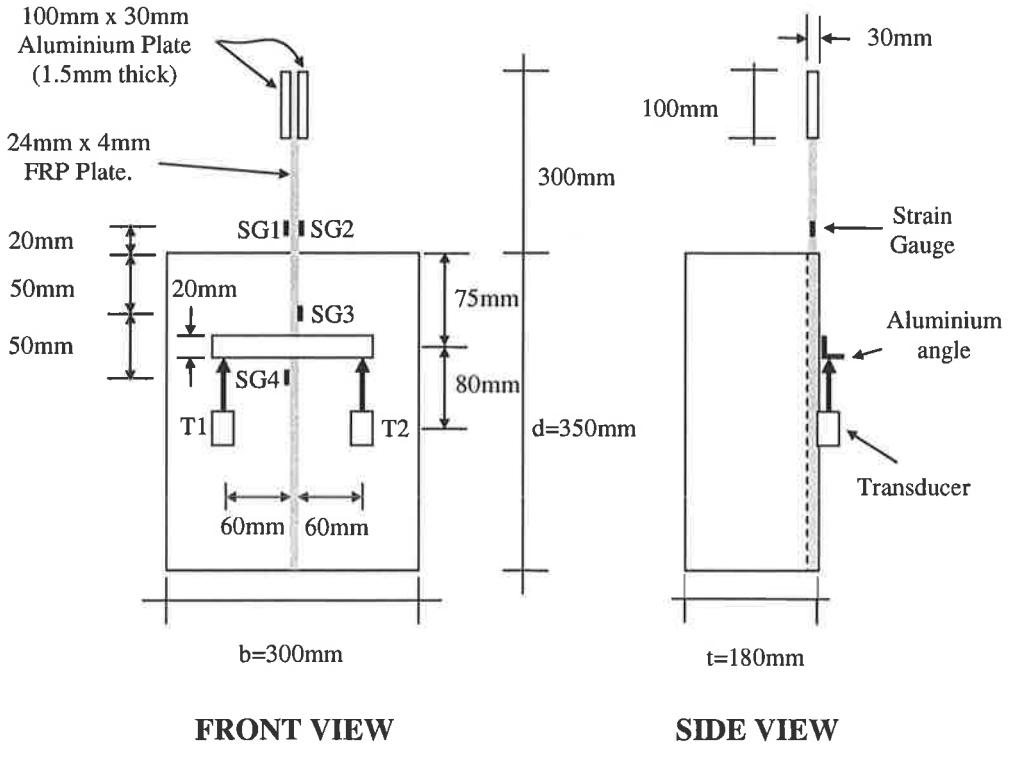

Figure 3.4.6: Pull test of 24mm x 4mm FRP plate details.

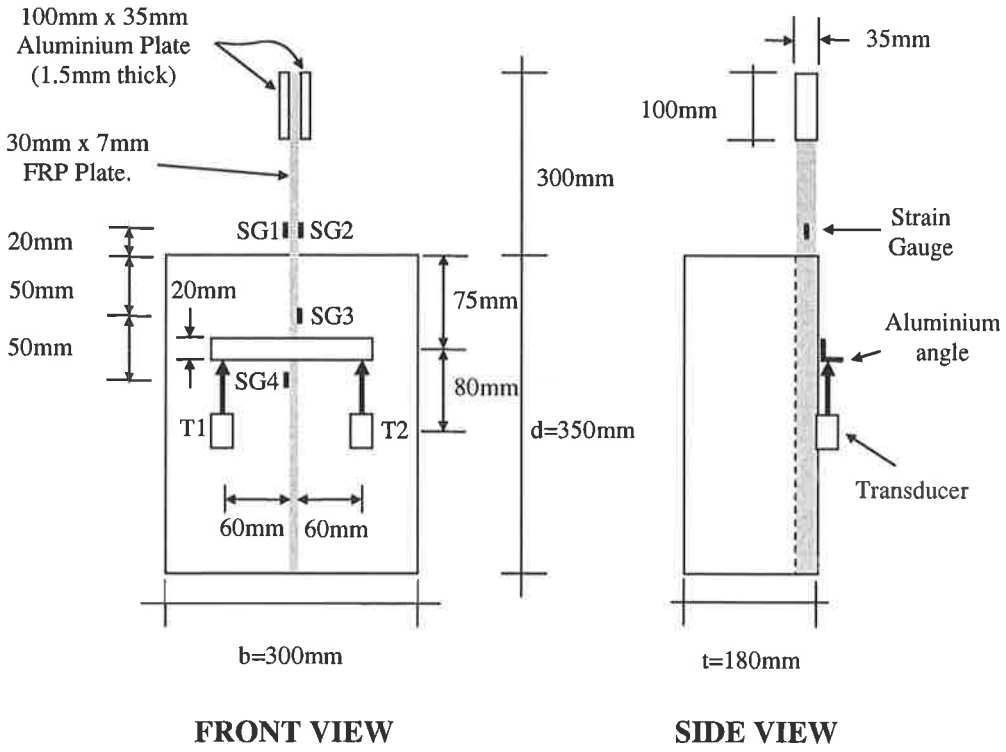

Figure 3.4.7: Pull test of 30mm x 7mm FRP plate details.

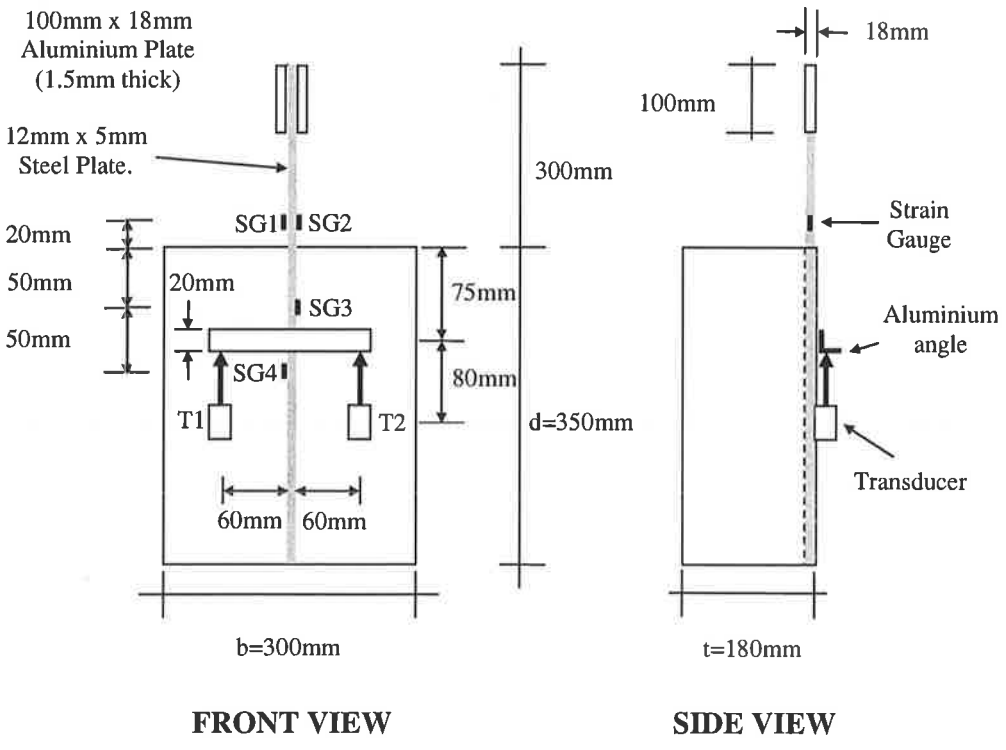

Figure 3.4.8: Pull test of 12mm x 5mm Steel plate details.

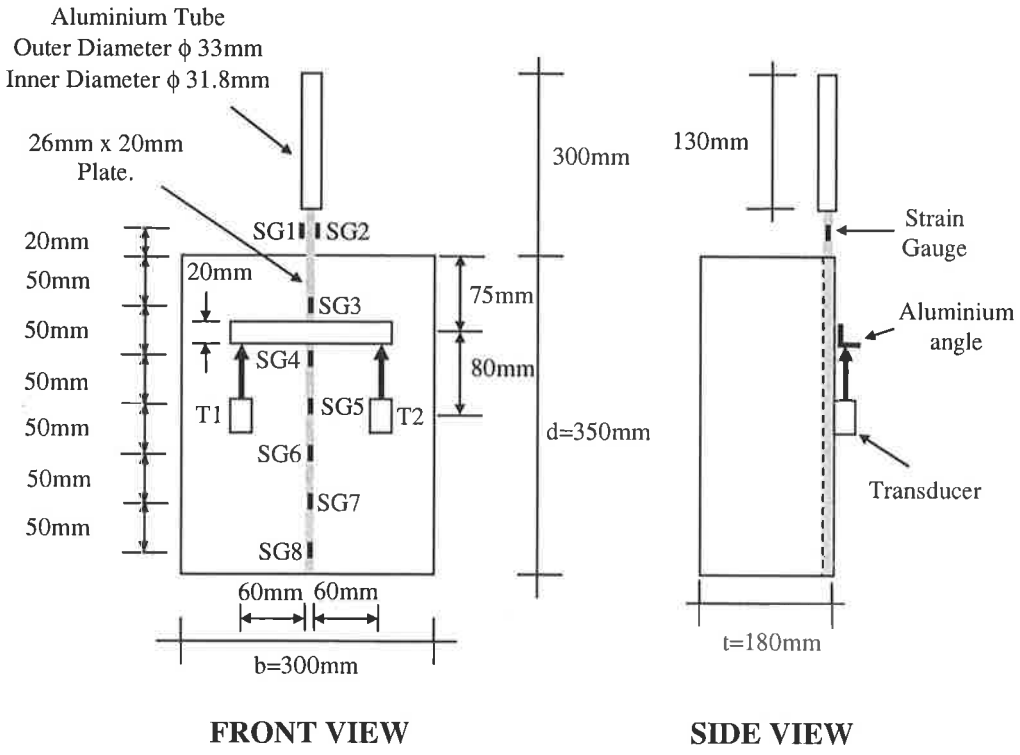

Figure 3.4.9: Pull test of 26mm x 20mm FRP plate details.

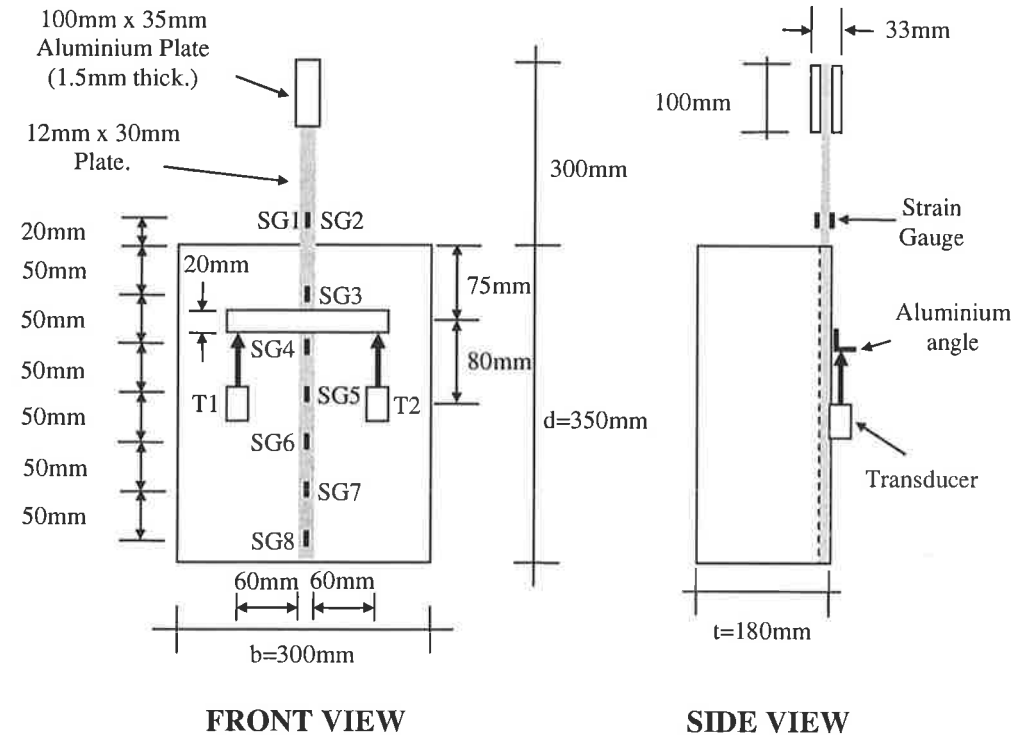

Figure 3.4.10: Pull test of 12mm x 30mm FRP plate details.

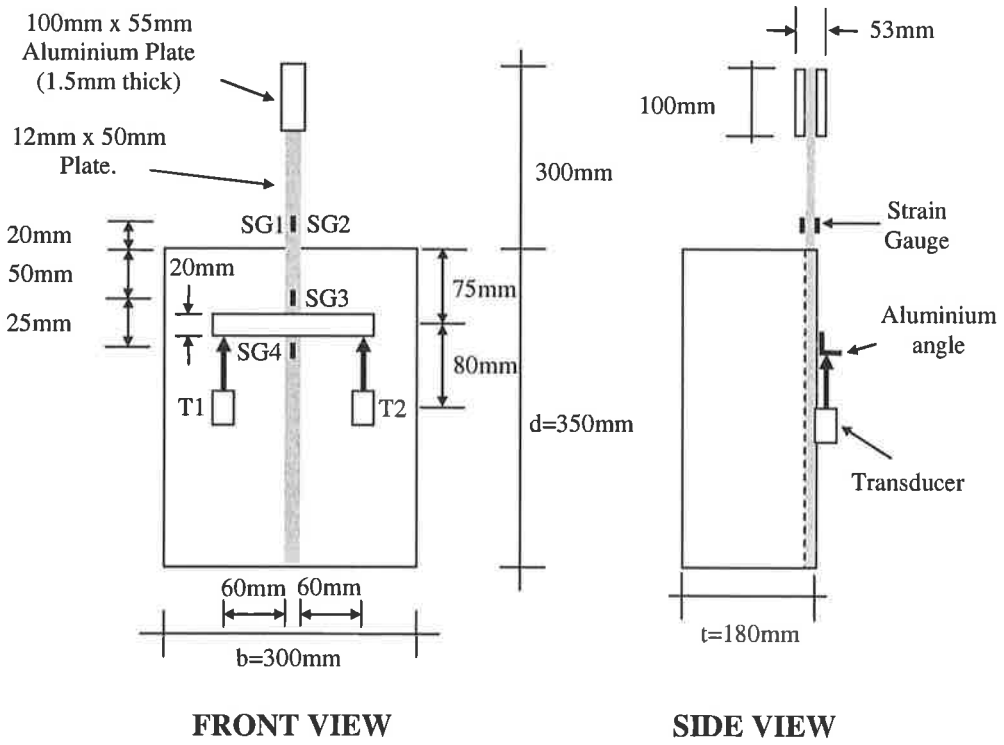

Figure 3.4.11: Pull test of 12mm x 50mm FRP plate details.

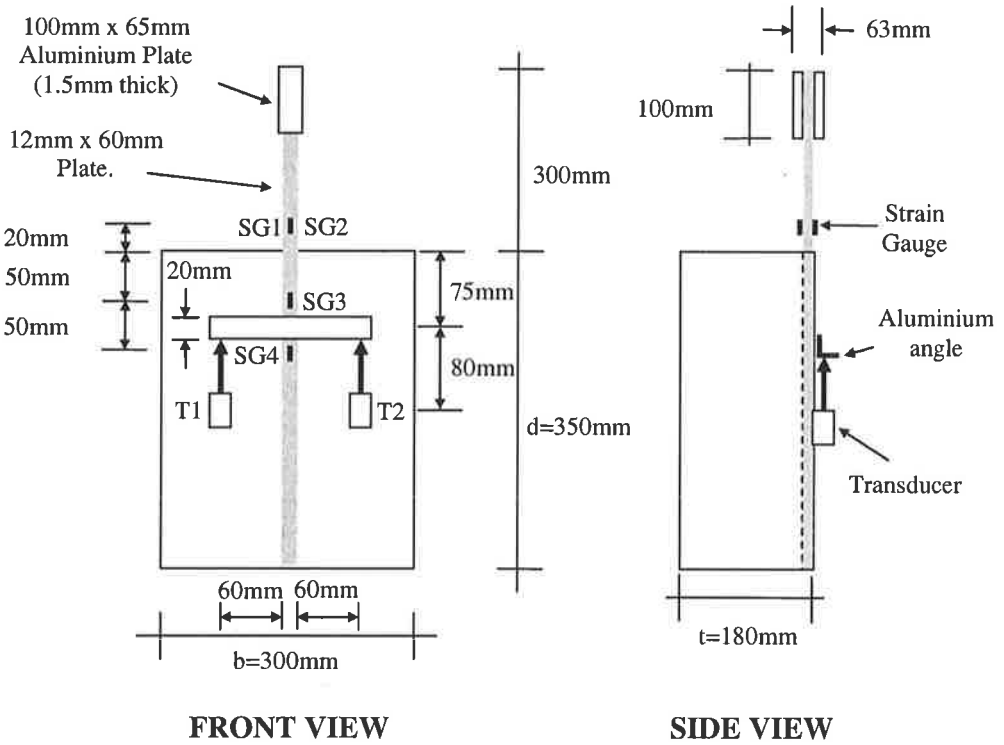

Figure 3.4.12: Pull test of 12mm x 60mm FRP plate details.

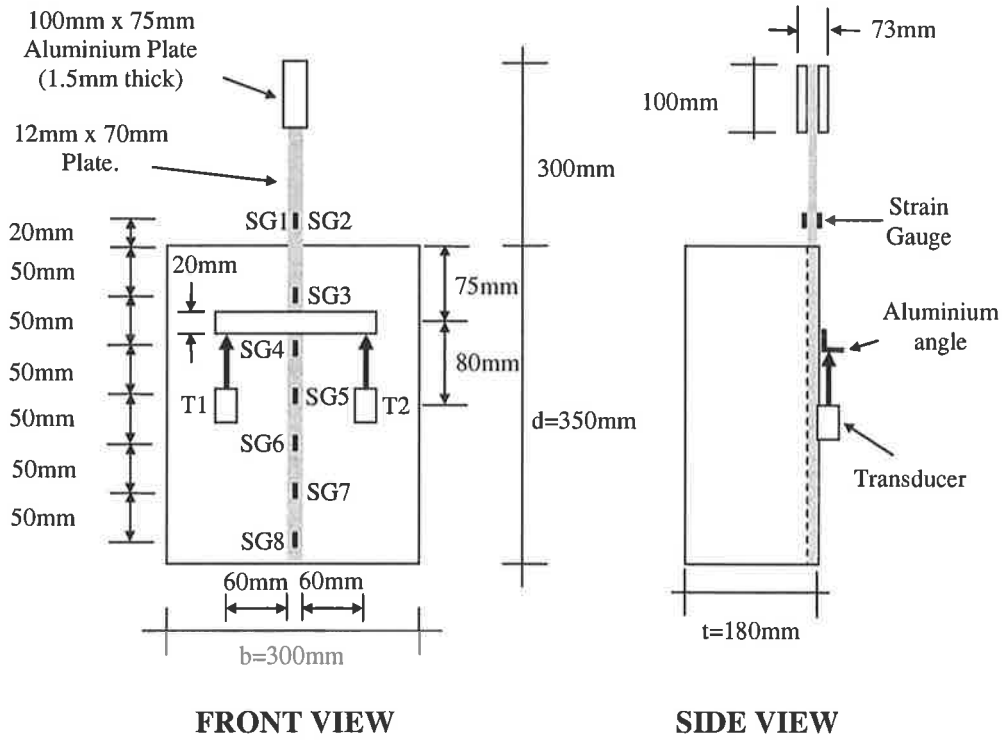

Figure 3.4.13: Pull test of 12mm x 70mm FRP plate details.

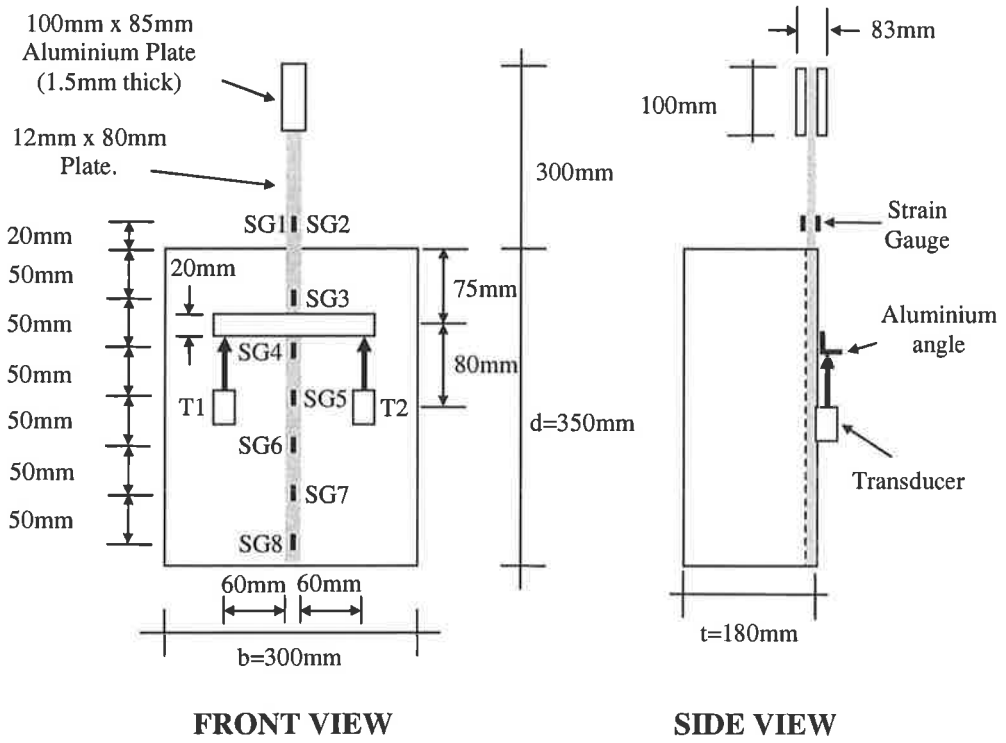

Figure 3.4.14: Pull test of 12mm x 80mm FRP plate details.

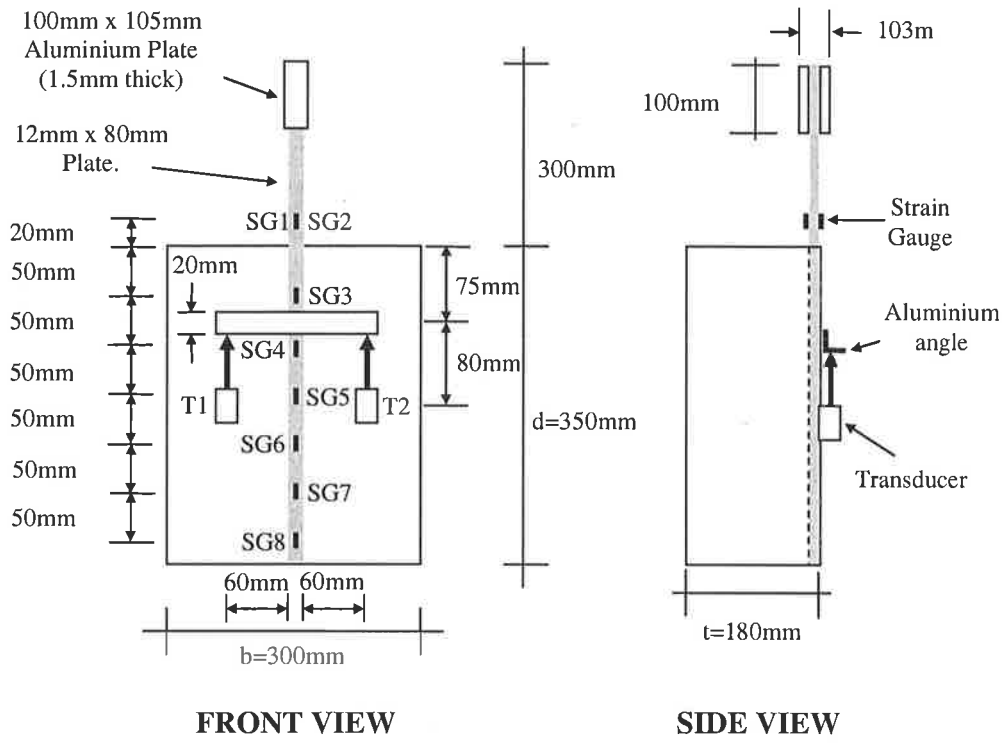

Figure 3.4.15: Pull test of 12mm x 100mm FRP plate details.

3.5 Material Properties

The concrete blocks were cast as part of another project [Liu (2005)] using concrete supplied by a local ready mixed concrete supplier. Table 3.5.1 summarises the concrete compressive cylinder strength (f_c) including Young's Modulus (E_c).

Table 3.5.1: Concrete material properties.

Concrete Cylinder Age (days)	E_c (MPa)		f_c (MPa)	
489	Tests	Average	Tests	Average
	1. 36708	37354	1. 36.1	36.7
	2. 37830		2. 37.02	
	3. 37525		3. 37.08	
656	Test	Average	Tests	Average
	1. 28603	30151	1. 33.64	35.3
	2. 32635		2. 38.32	
	3. 29216		3. 33.9	

Table 3.5.2 gives the plate geometric and material properties where d_p is the plate depth, b_p is the plate width and E_p is the plate Young's Modulus measured from SG1 and SG2 in each pull test. The adhesive properties are presented in Table 3.5.3 using information provided by the manufactures with the exception of the adhesive Young's Modulus E_g which was determine experimentally.

Table 3.5.2: Material properties of the plate.

Specimen	d_p (mm)	b_p (mm)	Materials	E_p (MPa)
12x12	11.91	11.92	Steel	183044
12x12	12.42	12.40	Aluminium	63819
12x12	12.76	11.88	CFRP	131566
12x3	12.37	2.76	CFRP	146348
12x4	12.73	4.28	CFRP	134467
12x6	12.51	5.78	CFRP	130489
24x4	24.14	4.37	CFRP	141434
30x7	30.55	7.39	CFRP	134562
12x5	12.00	5.00	Steel	195494
26x20	25.26	20.6	CFRP	129837
12x30	12.02	30.92	CFRP	135113
12x50	12.20	50.33	CFRP	132761
12x60	11.74	61.03	CFRP	126511
12x70	11.93	71.25	CFRP	135810
12x80	12.28	81.00	CFRP	137139
12x100	12.30	101.08	CFRP	135000

Table 3.5.3: Materials properties of the adhesive.

Adhesive	Experimentally tested		Manufacturer specification	
	E_g (MPa)		Compression Strength (MPa)	Flexural Strength (MPa)
	Tests	Average		
MBrace Laminate Adhesive	1. 5669 2. 6091 3. 6102	5954	> 60	> 30
CIBA Adaldite K340 High Performance Adehesive	1. 4434 2. 4677 3. 3895	4335	100 – 120	20 - 30

3.6 Test Results

This section, describes the experimental results of all 16 pull tests.

3.6.1 Shear Stress-Slip Graph

In the discussion of all 16 pull tests, shear stress-slip graph at a point will be provided using the difference in the SG3 and SG4 readings. This indicates the shear stress that has been transferred to the concrete over the length between these two strain gauges. This is shown in Eq. 3.6.1 and 3.6.2

$$Change\ in\ Shear\ Stress = \frac{Change\ in\ Force\ in\ Strip}{Change\ in\ Surface\ Area\ of\ Strip} \tag{3.6.1}$$

$$\Delta\tau_p = \frac{(\Delta\varepsilon)E_p d_p b_p}{(\Delta L)(2d_p + b_p)} \tag{3.6.2}$$

where $\Delta\varepsilon$ = change in strain over the length ΔL, ΔL = distance between strain gauges, $\Delta\tau_p$ = change in shear stress. An example of a shear stress-slip graph is shown in Figure 3.6.3.

3.6.2 Mild Steel 12mm x 12mm Pull Test

The 12mm x 12mm dimension of the mild steel was chosen because of its availability, without the need of cutting. Another reason is that this dimension was used to avoid failure cause by plate yielding. In this experiment, the mild steel plate debonded at a load of 74.1kN. The maximum slip recorded prior to debonding was 0.53mm and the maximum shear stress calculated from the strain profile was 6.5 MPa (Figure 3.6.3).From the strain profile in Figure 3.6.2, the steel plate did not yield reaching a maximum strain at 2911 $\mu\varepsilon$. Observations from the experiment (Figure 3.6.1) and referring to the strain profile (Figure 3.6.2), failure of this test was catastrophic as the major cracks only started to appear at 70kN.

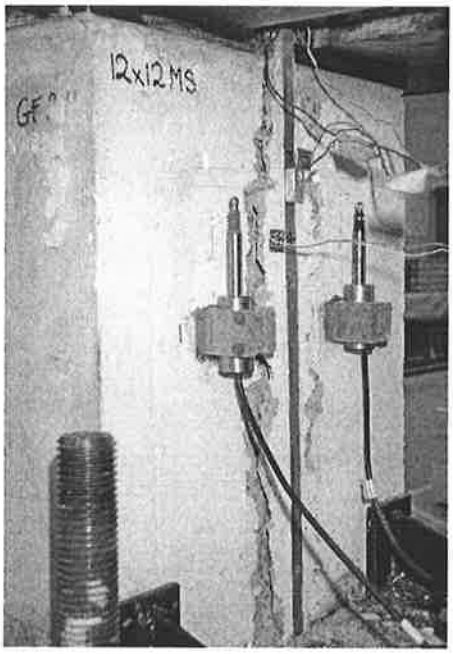

Figure 3.6.1: 12mm x 12mm Mild Steel failure pattern.

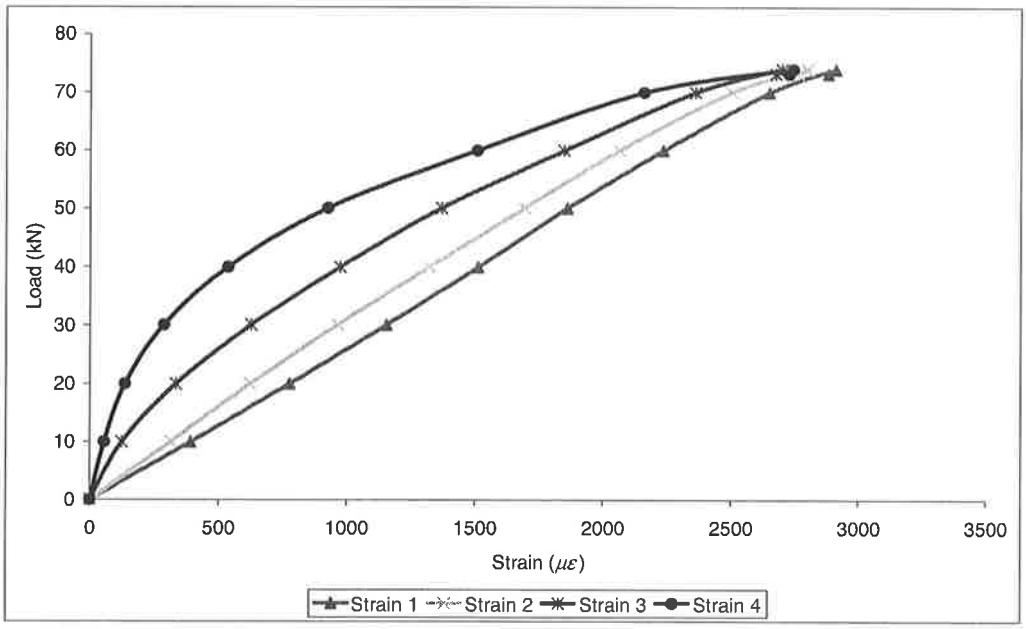

Figure 3.6.2: Load – Strain Graph for NSM 12mm x 12mm Mild Steel.

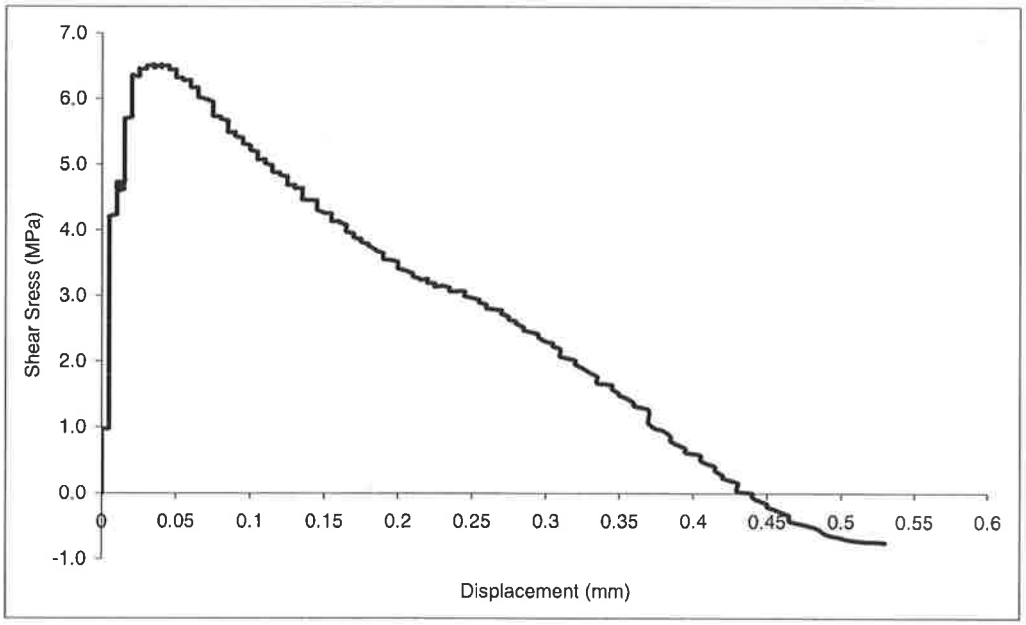

Figure 3.6.3: Shear Stress – Slip Graph for NSM 12mm x 12mm Mild Steel.

3.6.3 Aluminium 12mm x 12mm Pull Test

In this pull test the yield strain based on Young's Modulus of 63819 MPa and yield stress of 180 MPa was calculated to be 2820 $\mu\varepsilon$. The strain in the plate reached 2800 $\mu\varepsilon$ at a load of 23kN and as the load increased, the plate yielded as shown by the plateau in Figure 3.6.4, reaching a maximum load of 30.4kN at a strain of 27581 $\mu\varepsilon$ and fails by yielding. Figure 3.6.4 also shows deformability of the aluminium plate with low loads provides high level of strain. This pull test demonstrates that aluminium is not a practical material for plating as it cannot sustain high loads. This result is not considered as in the developing of the generic equation for Intermediate Crack (IC) debonding resistance (Eq. 4.2.7) because it did not fail by debonding.

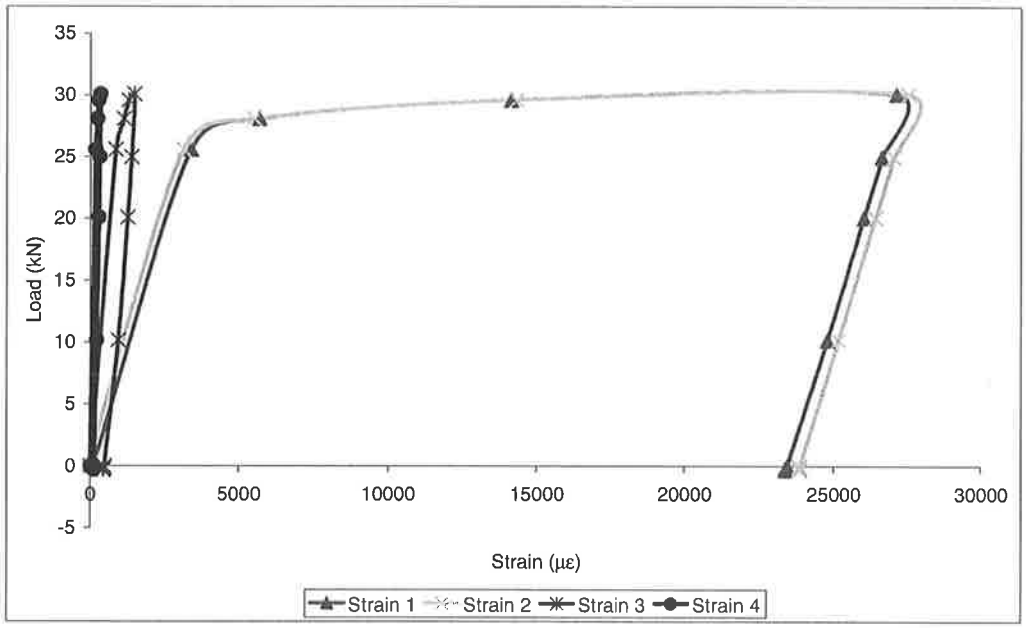

Figure 3.6.4: Load – Strain Graph for NSM 12mm x 12mm Aluminium.

3.6.4 CFRP 12mm x 12mm Pull Test

As describe earlier, this CFRP plate was fabricated by gluing 8 CFRP plates together and as a result there are two surface types as shown in Figure 3.6.5; one contains the glue interface perpendicular to the concrete surface, and the other surface consists only the CFRP plate. To determine if any differential slip occurs between the plates, an additional 3 strain gauges were added (Figure 3.4.2), to monitor strain on the surface that is perpendicular to the concrete surface.

From the strain profile in Figure 3.6.7, the additional strain gauges show that there was no slip between plates and also that the occurrence of major cracks were observed at 60kN, 50 mm from the loaded end propagating towards the unloaded end.

The maximum load that the plate could sustain before debonding was 85.9kN making it the strongest among the 12mm x 12mm plates. Meanwhile the maximum slip for this test was 0.72mm and from the strain profile, the peak shear stress calculated is 9.16 MPa (Figure 3.6.8). The failure pattern for this pull test is shown in Figure 3.6.6 where it is showing the crack pattern is along the plate length.

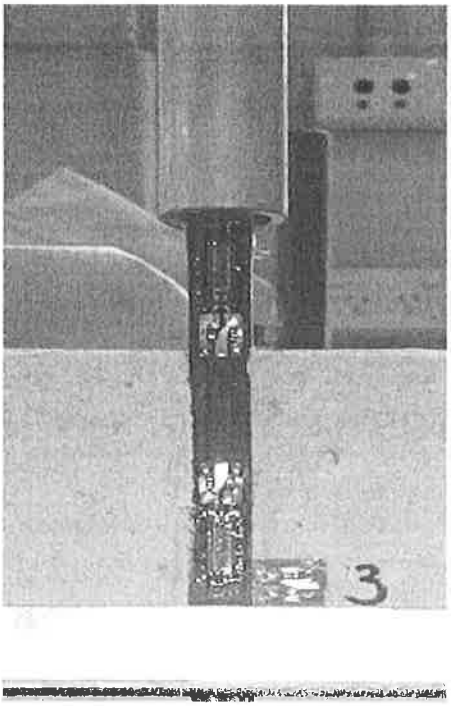

Figure 3.6.5: CFRP surface with the adhesive interface.

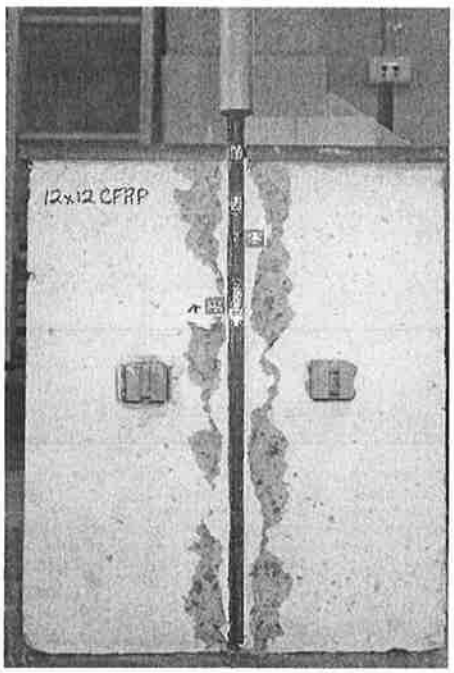

Figure 3.6.6: 12mm x 12mm CFRP failure pattern.

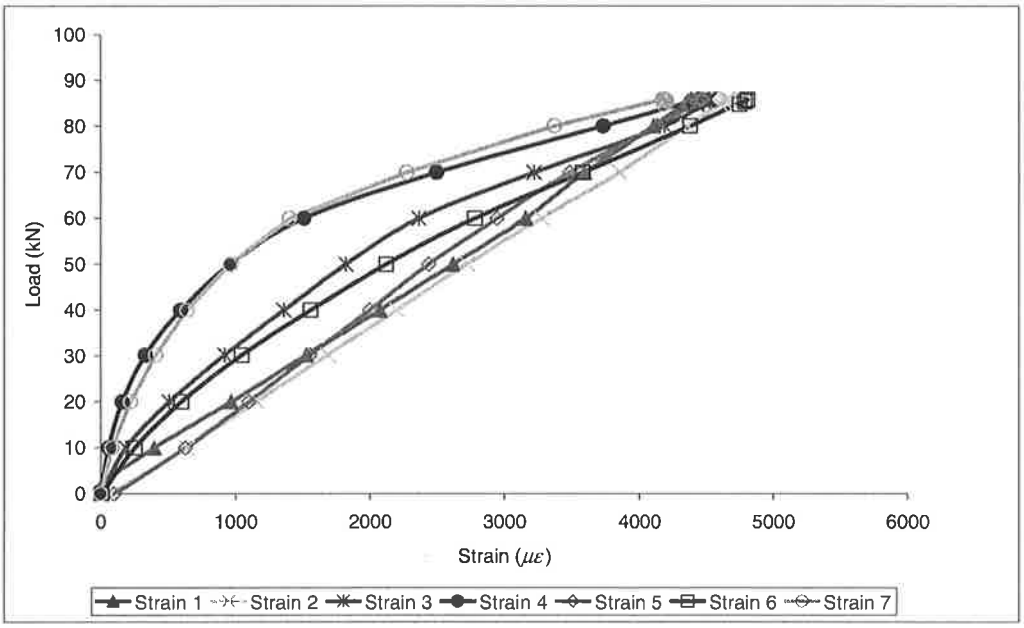

Figure 3.6.7: Load – Strain Graph for NSM 12mm x 12mm FRP.

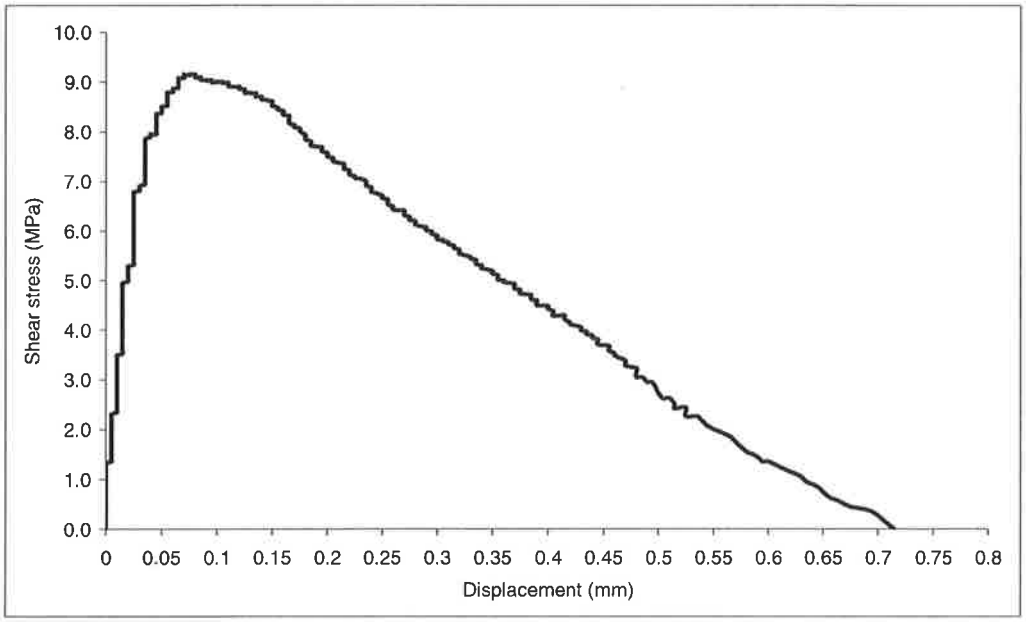

Figure 3.6.8: Shear Stress – Slip Graph for NSM 12mm x 12mm FRP.

3.6.5 CFRP 12mm x 3mm Pull Test

In this test strain gauge number 4 (SG4) was faulty and did not give correct readings. In Figure 3.6.9 the typical crack pattern can be seen at debonding at a load of 59.2kN and maximum slip of 0.97mm (Figure 3.6.10). Figures 3.6.10 and 3.6.11 shows the erratic

behaviour of the strain profile and shear-slip relationship due to the faulty strain gauge. However, the maximum shear stress can still be extracted from the data which is 15.00 MPa and from the strain profile, debonding occurs at approximately 20kN located 50mm from the loaded end.

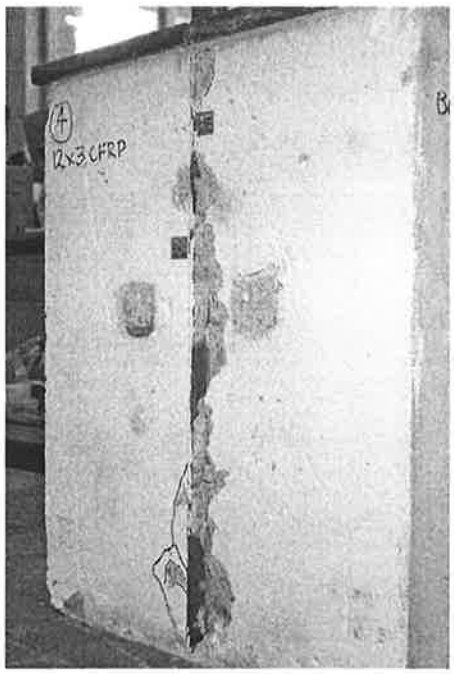

Figure 3.6.9: 12mm x 3mm CFRP failure pattern.

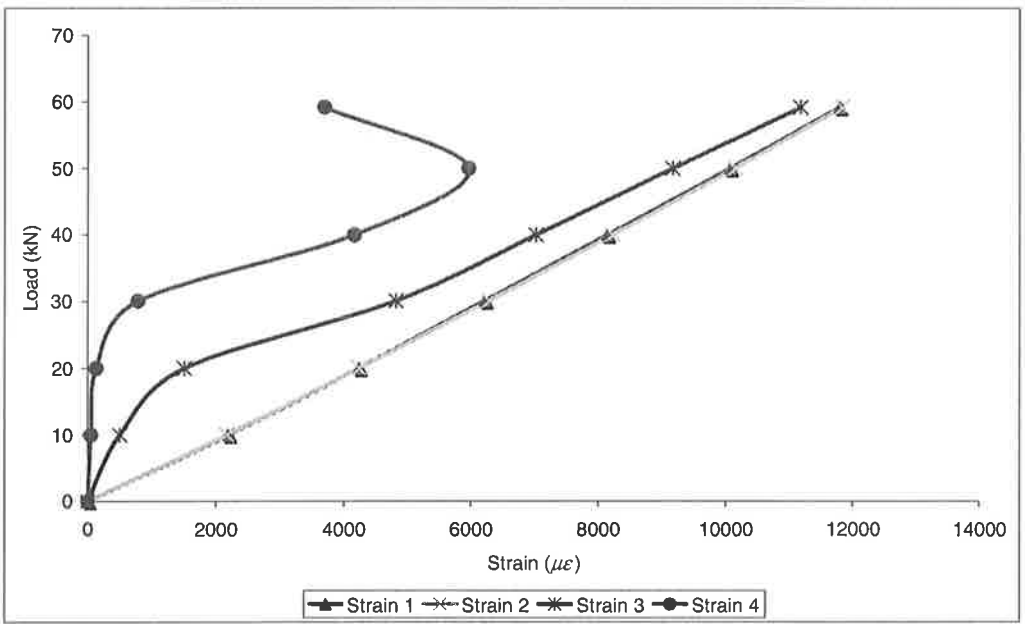

Figure 3.6.10: Load – Strain Graph for 12mm x 3mm FRP.

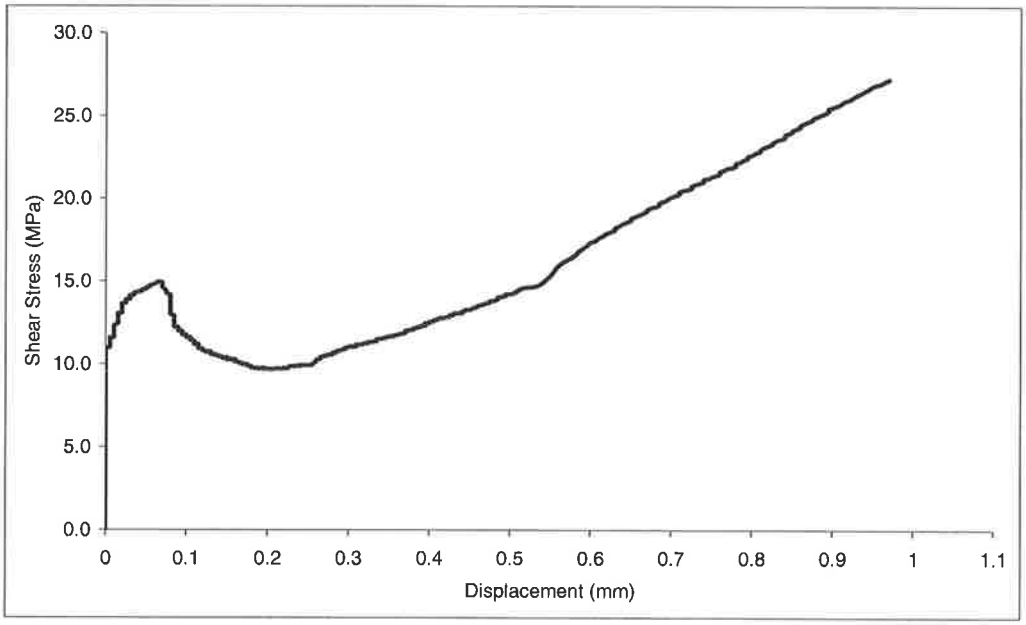

Figure 3.6.11: Shear Stress – Slip Graph for NSM 12mm x 3 mm FRP.

3.6.6 CFRP 12mm x 4mm Pull Test

The pull tests continued with CFRP plate dimensions of 12mm x 4mm. Figure 3.6.12 shows the typical crack pattern for this test at a failure load of 54.1 kN. Meanwhile, Figures 3.6.13 and 3.6.14 show the typical strain profile and shear-slip relationship with maximum shear stress of 12.50 MPa and maximum slip of 1.15mm.

Comparison with the previous, 12mm x 3mm test shows that by increasing the plate thickness and maintaining the plate depth; the ultimate load, maximum shear stress and slip is reduced. This is as a result of the young's modulus reducing due to more adhesive in the composite fabricated plate.

From the strain profile shown in Figure 3.6.13, strain gauge 3 (SG3) shows that the plate starts to debond 50mm from the loaded end at loading approximately 42.00kN.

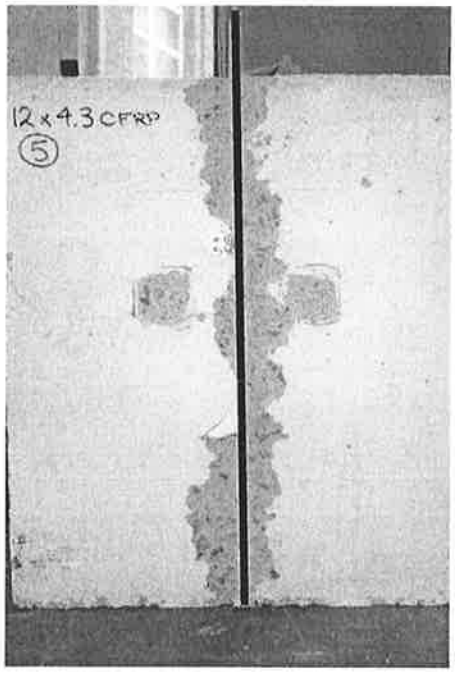

Figure 3.6.12: 12mm x 4mm CFRP failure pattern.

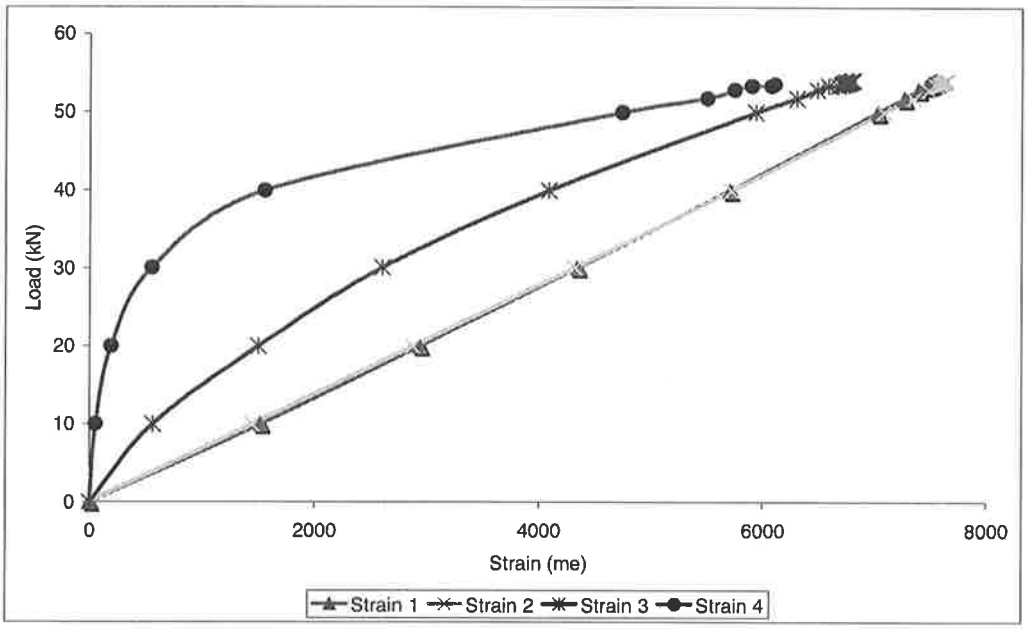

Figure 3.6.13: Load – Strain Graph for 12mm x 4mm FRP.

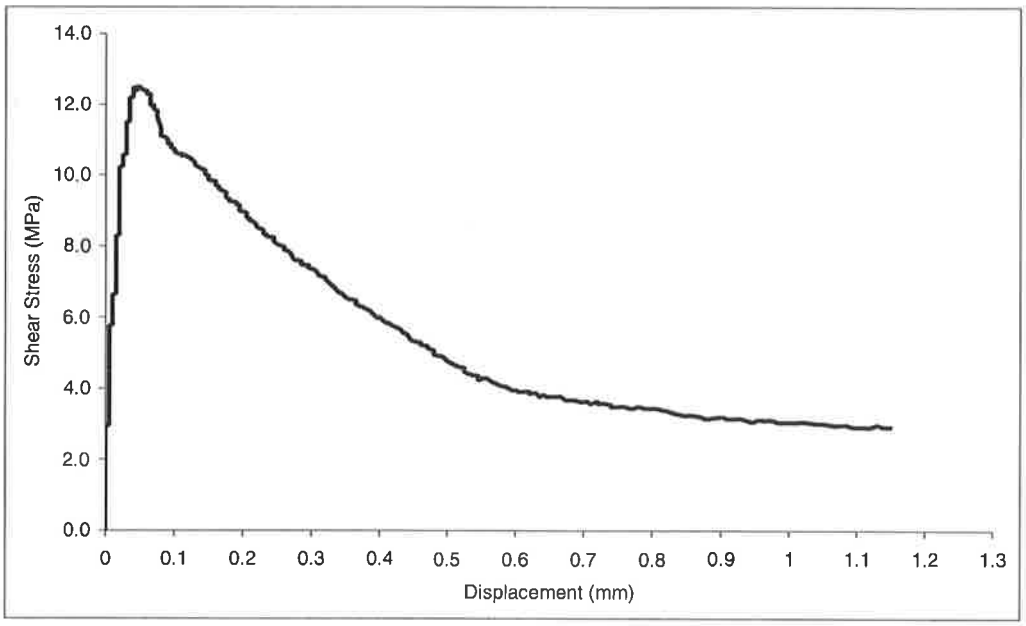

Figure 3.6.14: Shear Stress – Slip Graph for NSM 12mm x 4 mm FRP.

3.6.7 CFRP 12mm x 6mm Pull Test

A plate thickness of 6mm with the same depth as previous experiment was used in this test. Again, the typical failure pattern, strain profile and shear slip relationship is shown in Figures 3.6.15 to 3.6.17. The ultimate load for this test was 47.6kN with maximum shear stress of 9.93 MPa and maximum slip of 1.00 mm (Figure 3.6.17). Readings from SG3 show that first debonding occurs at a load of approximately 33kN. The maximum strain recorded from SG1 was 5136 microstrain. The final crack patterns after debonding occur along the plate length with a small amount of concrete attached to the plate.

Comparison with specimens 12mm x 3mm and 12mm x 4mm shows that as the plate thickness increases the ultimate load, maximum shear stress and maximum slip reduces.

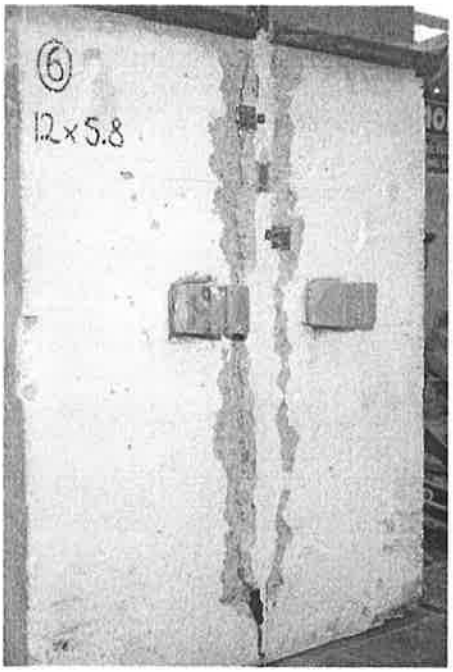

Figure 3.6.15: 12mm x 6mm CFRP failure pattern.

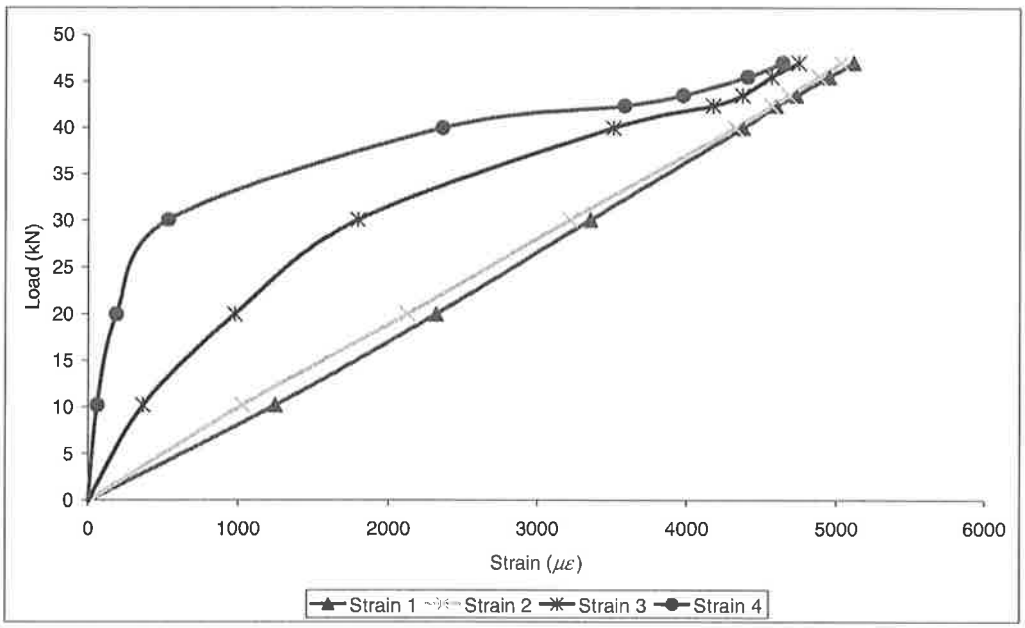

Figure 3.6.16: Load – Strain Graph for 12mm x 6mm FRP.

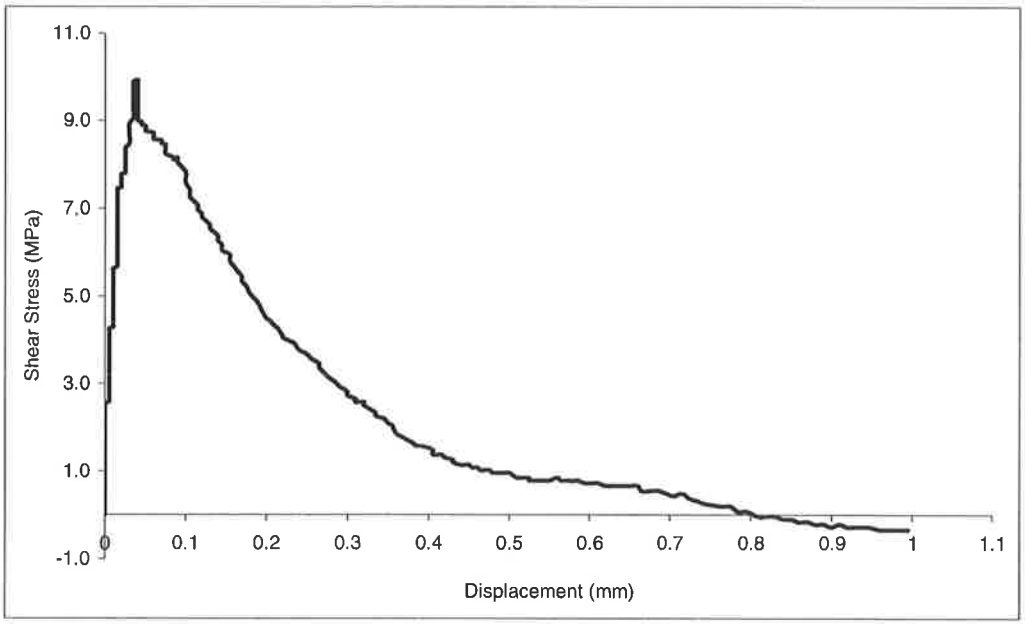

Figure 3.6.17: Shear Stress – Slip Graph for NSM 12mm x 6 mm FRP.

3.6.8 CFRP 24mm x 4mm Pull Test

Different plate dimensions were used in this test by doubling the plate depth with respect to the previous tests. In this test the failure load was 136.5kN showing an increase of 82.4kN (152%) compare to the 12mm x 4mm pull test. A different failure pattern was also found as shown in Figure 3.6.18 where 'herring bone' cracks can be seen including a large amount of concrete peeling from the concrete surface. The strain profile shown in Figure 3.6.19 shows a gradually increasing of strain due to the stiffness of the plate until it reaches approximately 95kN where debonding start to occur at 50mm from the loaded end.

The maximum strain recorded was from SG2 at 8846 $\mu\varepsilon$, meanwhile the maximum shear stress was 16.94 MPa (Figure 3.6.20) and from the transducers readings the maximum slip was 1.55 mm.

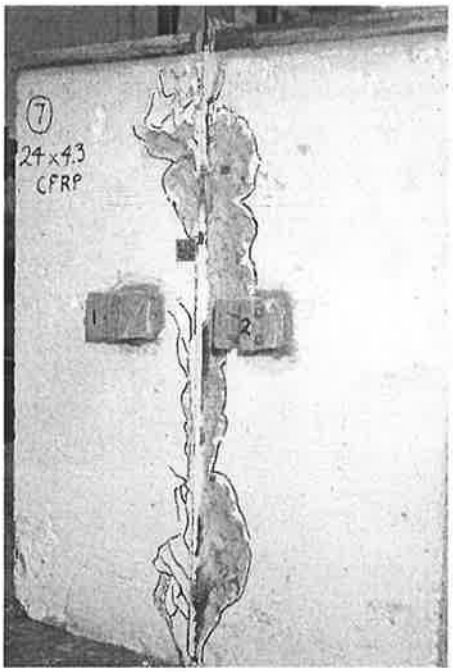

Figure 3.6.18: 24mm x 4mm CFRP failure pattern.

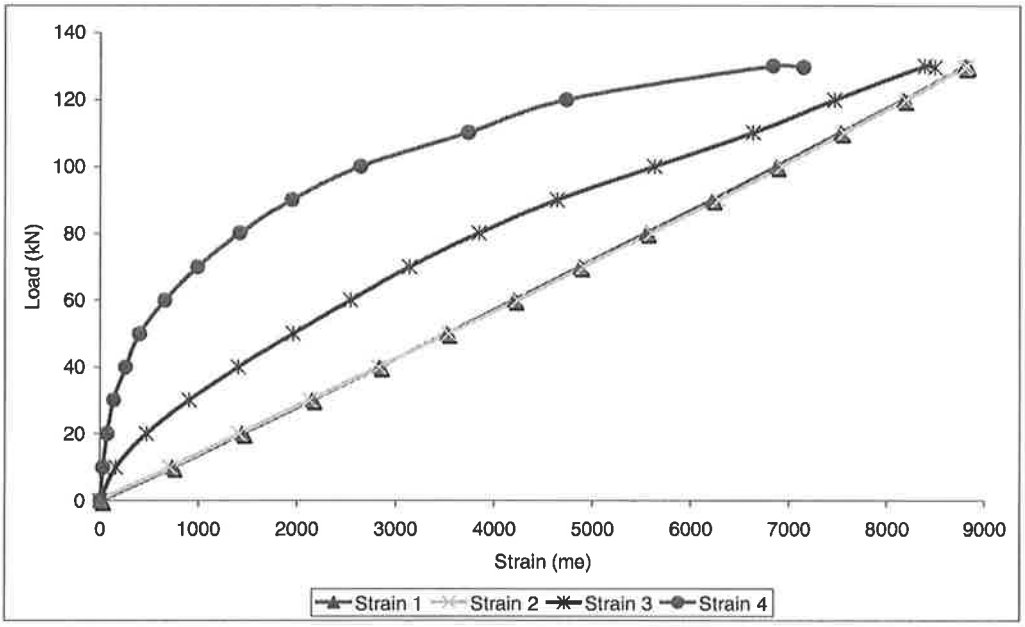

Figure 3.6.19: Load – Strain Graph for 24mm x 4mm FRP.

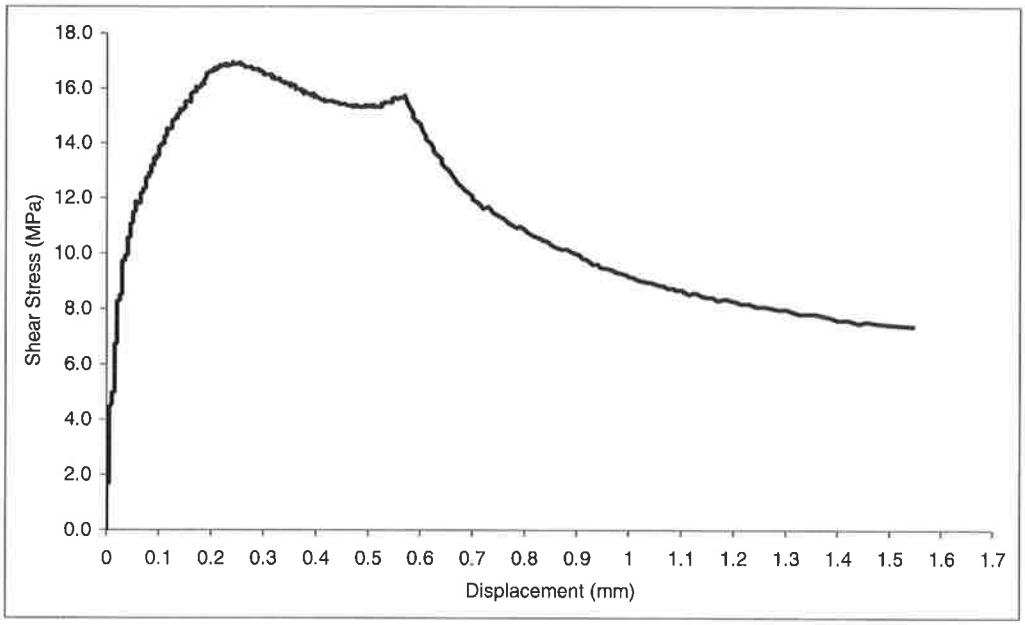

Figure 3.6.20: Shear Stress – Slip Graph for NSM 24mm x 4mm FRP.

3.6.9 CFRP 30mm x 7mm Pull Test

Thicker and deeper plate dimensions were used in this pull test with nominal dimensions of 30mm x 7mm. The failure pattern shown in Figure 3.6.21 is similar to that of 24mm x 4mm with the appearance of 'herring bone' cracks and peeling from the concrete surface with a failure load of 165.3kN. Looking at the strain profile (Figure 3.6.22) SG1, SG2 and SG3 is showing gradually increasing of strain meanwhile SG4 shows that debonding starts to occur at a load of 115kN, 100mm from the loaded end.

From the strain readings, the maximum strain recorded was from SG1 at 5522 $\mu\varepsilon$, meanwhile the maximum shear stress was 15.4 MPa (Figure 3.6.23) and from the transducers readings maximum slip was 0.7 mm.

Results from this pull test and 24mm x 4mm shows that as the plate depth increases the ultimate load, maximum shear stress and maximum slip increase which demonstrate more effective confinement of the plates.

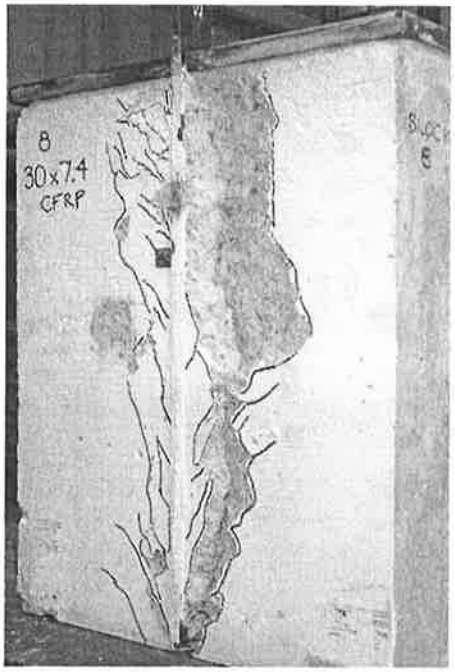

Figure 3.6.21: 30mm x 7mm CFRP failure pattern.

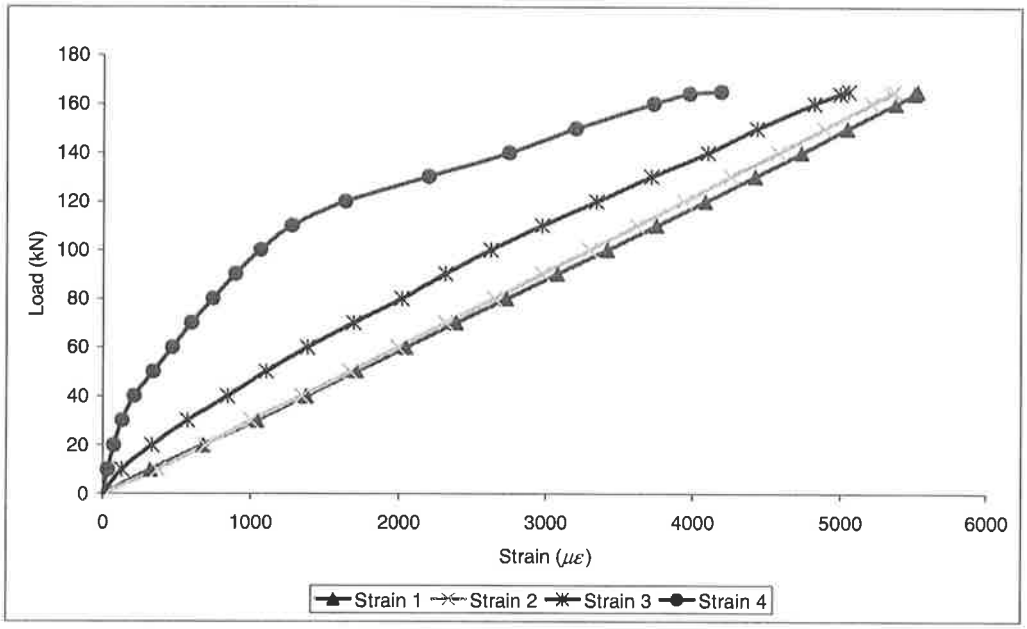

Figure 3.6.22: Load – Strain Graph for 30mm x 7mm FRP.

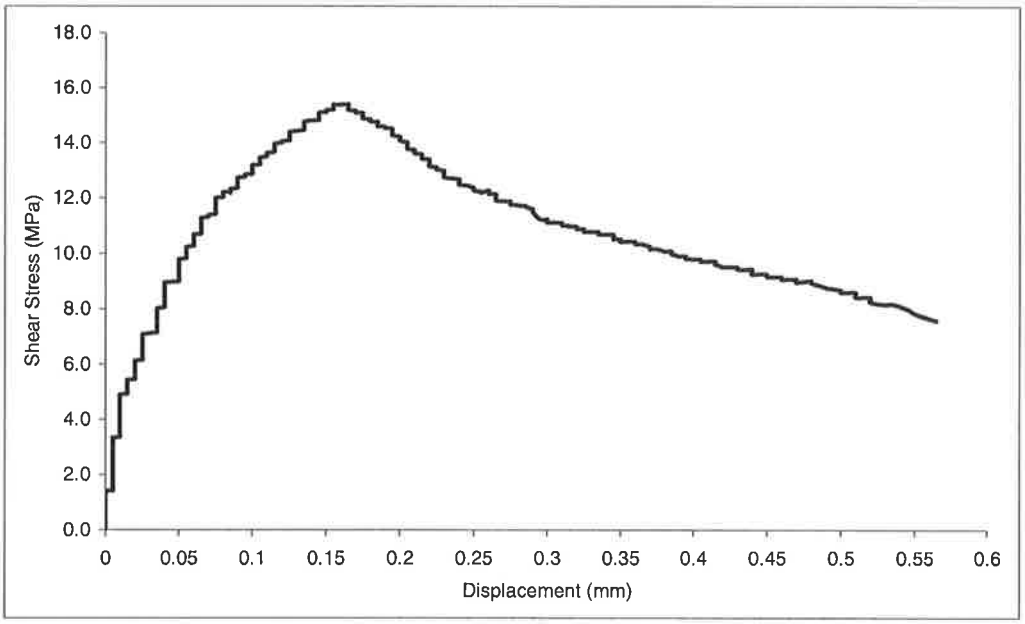

Figure 3.6.23: Shear Stress – Slip Graph for NSM 30mm x 7mm FRP.

3.6.10 Mild Steel 12mm x 5mm Pull Test

In this test a thinner steel plate was used with thickness of 5mm compared the earlier test of 12mm x 12mm. The yield strain based on Young's Modulus of 195494 MPa and yield stress of 400 MPa was calculated to be 2046 $\mu\varepsilon$.

The strain in the plate reached 2075 $\mu\varepsilon$ at a load of 20kN and as the load increased, the plate started to yield as shown in the strain profile in Figure 3.6.24 giving a plateau until reaching a maximum load of 24.3kN at a strain of 7200 $\mu\varepsilon$ and fails by yielding. This pull test illustrate that thinner steel plates are not a practical material as they cannot sustain high load. Due to the yielding this result also will not to be considered in the development of the generic equation, along with the aluminium plate.

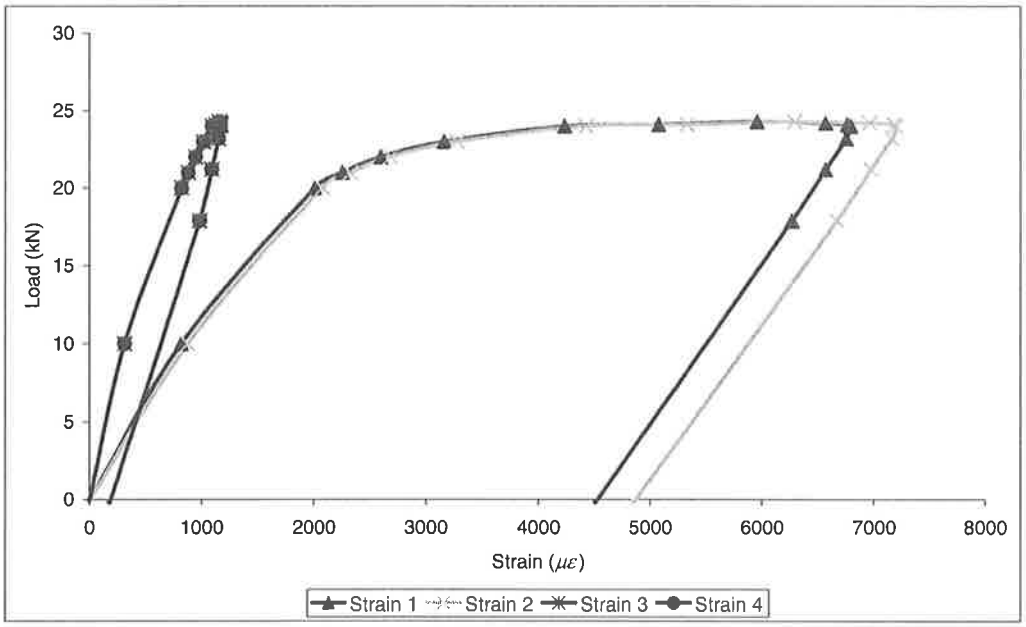

Figure 3.6.24: Load – Strain Graph for 12mm x 5mm Mild Steel.

3.6.11 CFRP 26mm x 20mm Pull Test

This pull test has the stiffest plate (in terms of $(EA)_p$) in this series of tests with width of 26mm and depth of 20mm. This plate was fabricated by gluing 17 plates together. The specimens failed at a maximum load of 199.4kN, also with the occurrence of 'herring bone' cracks as shown in Figure 3.6.25. Due to the plate being so stiff, looking at the strain profile (Figure 3.6.26) it does not show any significant change in strain until it reach loading of 190kN and fail immediately after that. The maximum strain recorded by SG2 was 3800 $\mu\varepsilon$. Analysis using the strain profile (Figure 3.6.26) giving the maximum shear stress of 10.0 MPa (Figure 3.6.27) and reading from the transducer giving a maximum slip of 0.4 mm.

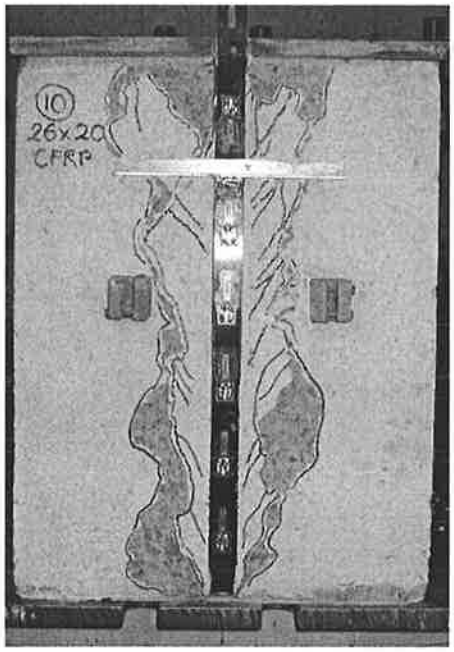

Figure 3.6.25: 26mm x 20mm CFRP failure pattern.

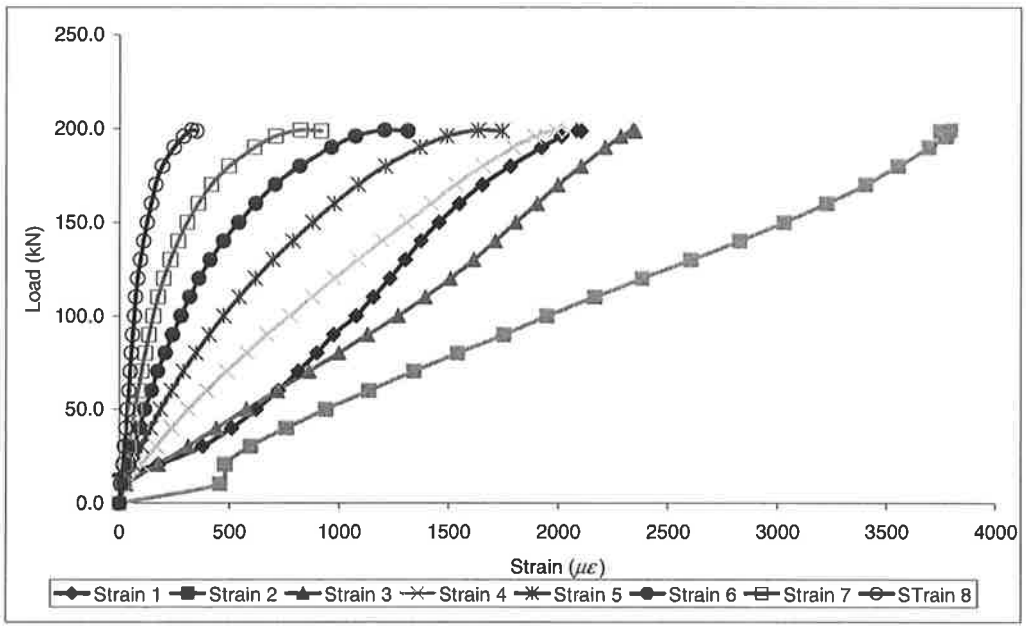

Figure 3.6.26: Load – Strain Graph for 26mm x 20mm FRP.

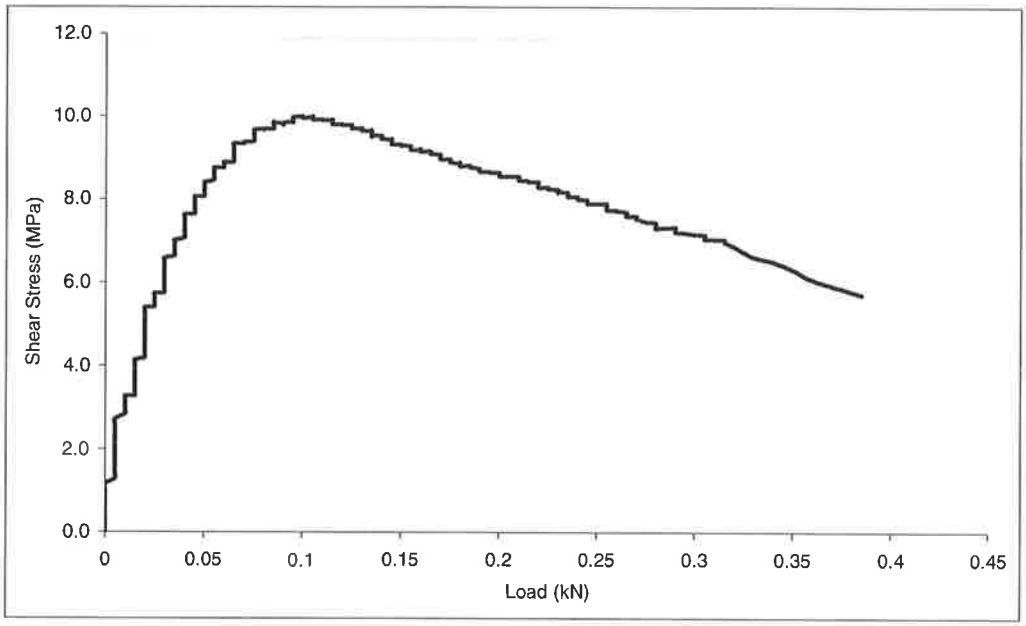

Figure 3.6.27: Shear Stress – Slip Graph for NSM 26mm x 20mm FRP.

3.6.12 CFRP 12mm x 30mm Pull Test

In the next 6 tests, including this test, the plates had the same thickness but with different width. Also in the next 6 tests, the orientation of the concrete block in the test rig was different, that is; facing forward due to the geometry of the plate. Another interesting factor about these tests is that the plate orientation is similar to an EB plate, but glued to the concrete prism using the NSM method.

Again an additional 4 strain gauge were added to monitor the strain profile. The failure for this pull test was also found with the occurrence of 'herring bone' cracks as shown in Figure 3.6.28 and the strain readings (Figure 3.6.29) show a gradual increase until 100kN. The maximum strain was recorded by SG2 was 2557 $\mu\varepsilon$. The plate failed at an ultimate load of 115.8kN. Analysis from the strain profile gives a maximum shear stress of 11.78 MPa (Figure 3.6.27) and from the transducer a maximum slip of 0.32 mm.

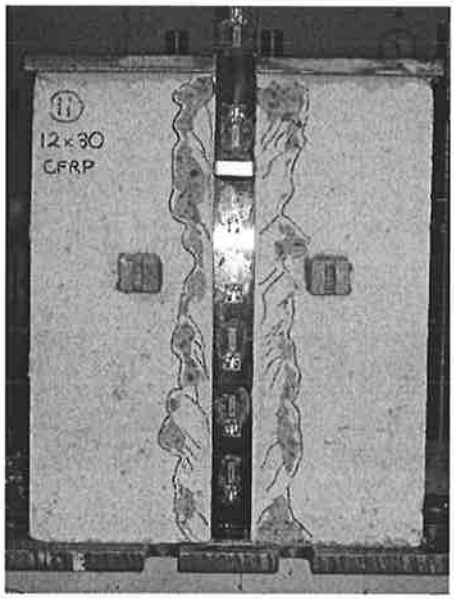

Figure 3.6.28: 12mm x 30mm CFRP failure pattern.

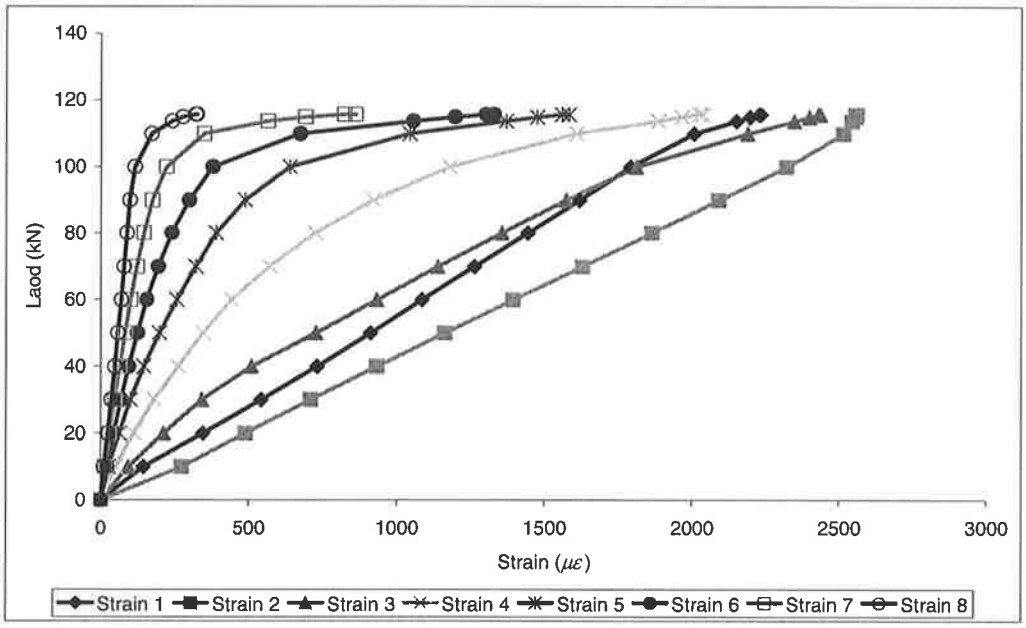

Figure 3.6.29: Load – Strain Graph for 12mm x 30mm FRP.

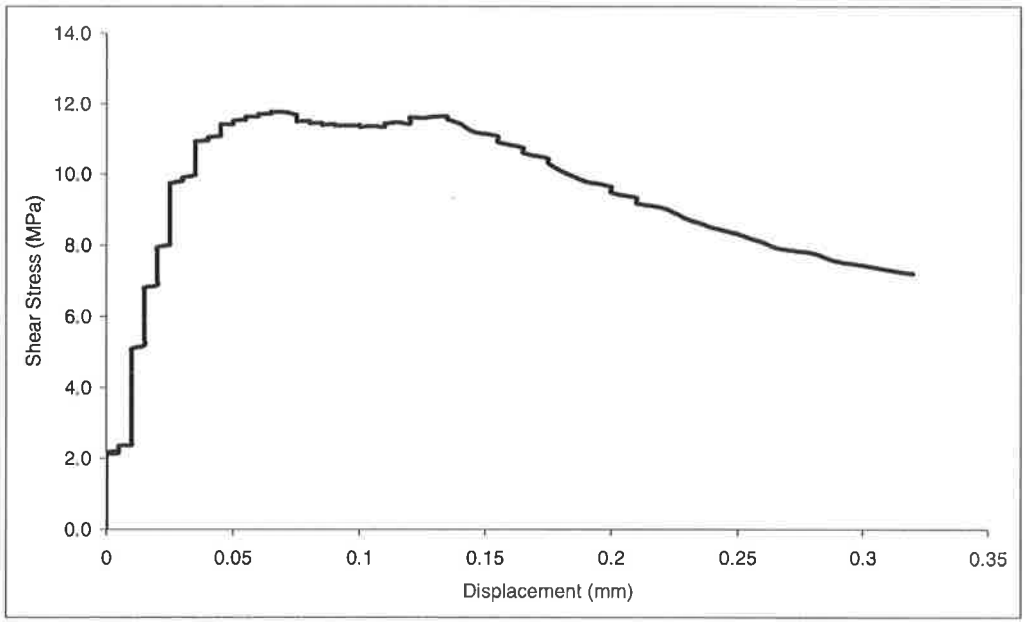

Figure 3.6.30: Shear Stress – Slip Graph for NSM 12mm x 30mm FRP.

3.6.13 CFRP 12mm x 50mm Pull Test

In this pull test, the plate width was increased to 50mm and the number of strain gauges was reduced to only 4 with 25mm distance between SG3 and SG4. The reason for reducing the number of strain gauges was that the additional strain gauges in 12mm x 30mm strain profile (Figure 3.6.29) did not provide any additional useful information. The reduced spacing between SG3 and SG4 (Figure 3.4.11) is to improve the shear stress readings.

The failure load for this test was 110.5kN without showing any clear occurrence of 'herring bone' cracks (Figure 3.6.31). The strain profile (Figure 3.6.32) for SG1 and SG2 is interesting; showing that SG1 located parallel with the concrete surface, is under compression while SG2 on the opposite side of the plate is in tension. This due to the plate is stiff and wide, any bending occurs on plate will give significant strain reading. Meanwhile for SG3 and SG4, the strain readings are similar due to the close spacing between strain gauge. Again from the analysis of strain profile, the maximum shear stress was found to be 2.93 MPa (Figure 3.6.33) and maximum slip of 0.21 mm. It was found that reducing the distance between SG3 and SG4 did not improve the shear stress readings. Meanwhile the maximum strain in SG2 is of 2650 $\mu\varepsilon$.

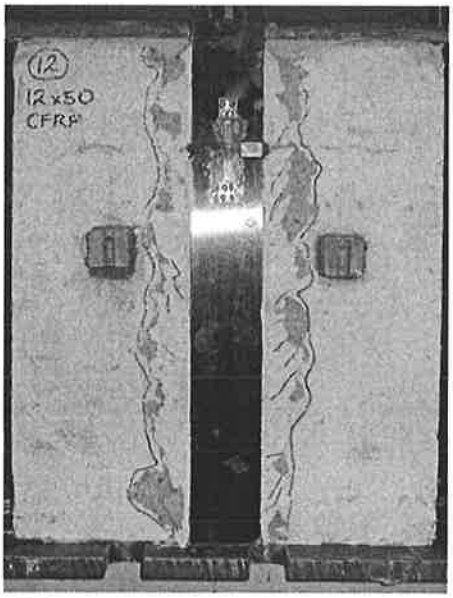

Figure 3.6.31: 12mm x 50mm CFRP failure pattern.

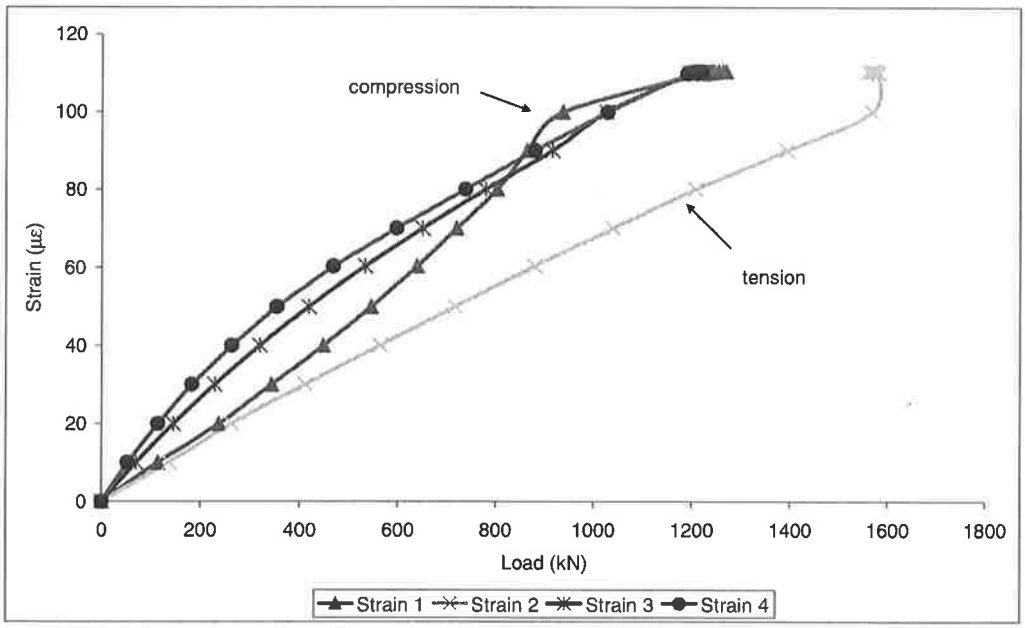

Figure 3.6.32: Strain – Load Graph for 12mm x 50mm FRP.

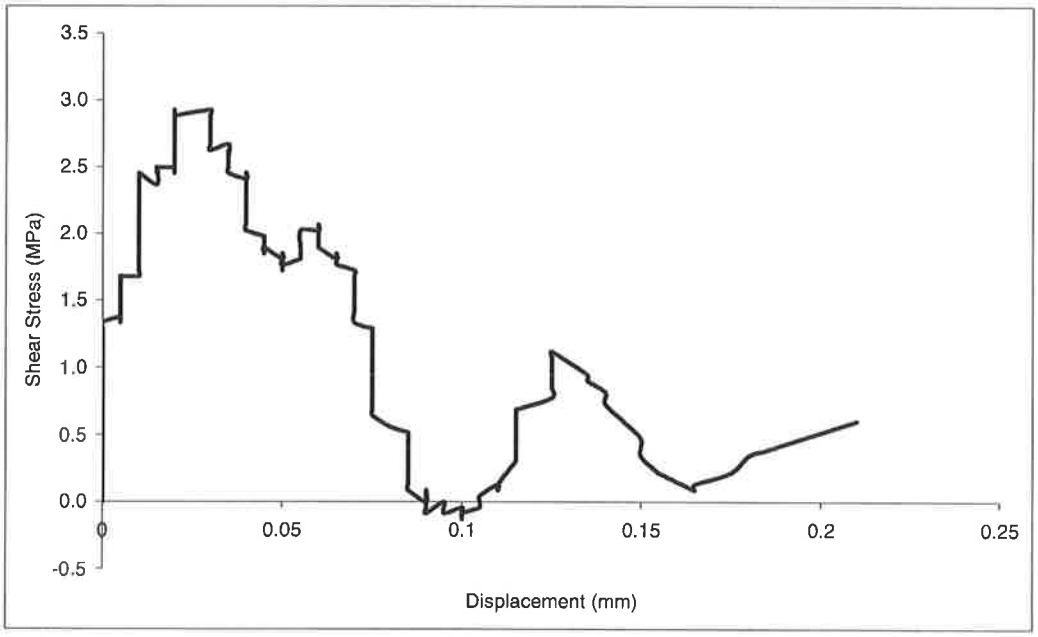

Figure 3.6.33: Shear Stress – Slip Graph for NSM 12mm x 50mm FRP.

3.6.14 CFRP 12mm x 60mm Pull Test

In this test the plate width was increased to 60mm and the number of strain gauges was kept the same as for the previous test (12mm x 50mm) but with a spacing of 50mm distance between SG3 and SG4. The failure load for this test was 133.6kN without the occurrence of the 'herring bone' cracks (Figure 3.6.34). Again it is interesting to look at the strain profile (Figure 3.6.35); readings from SG1 and SG2 are similar to the previous test. SG1 which is the plate surface parallel to the concrete surface is showing it is under compression meanwhile SG2 located opposite SG1 is showing that the plate is on tension.

Analysis from the strain profile is gives a maximum shear stress of 5.92 MPa (Figure 3.6.36) and maximum slip of 0.20 mm. Meanwhile, again the maximum strain in SG2 is1892 $\mu\varepsilon$.

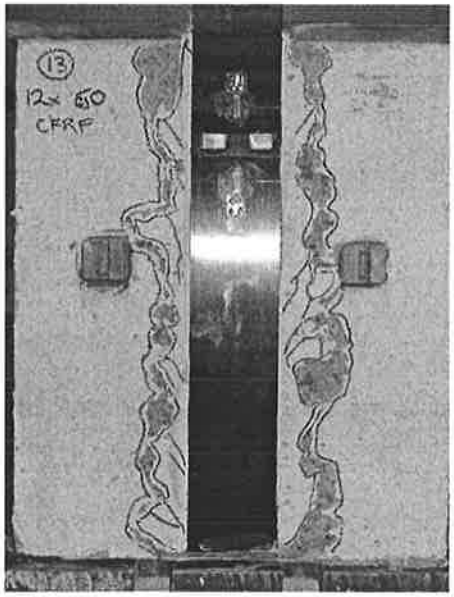

Figure 3.6.34: 12mm x 60mm CFRP failure pattern.

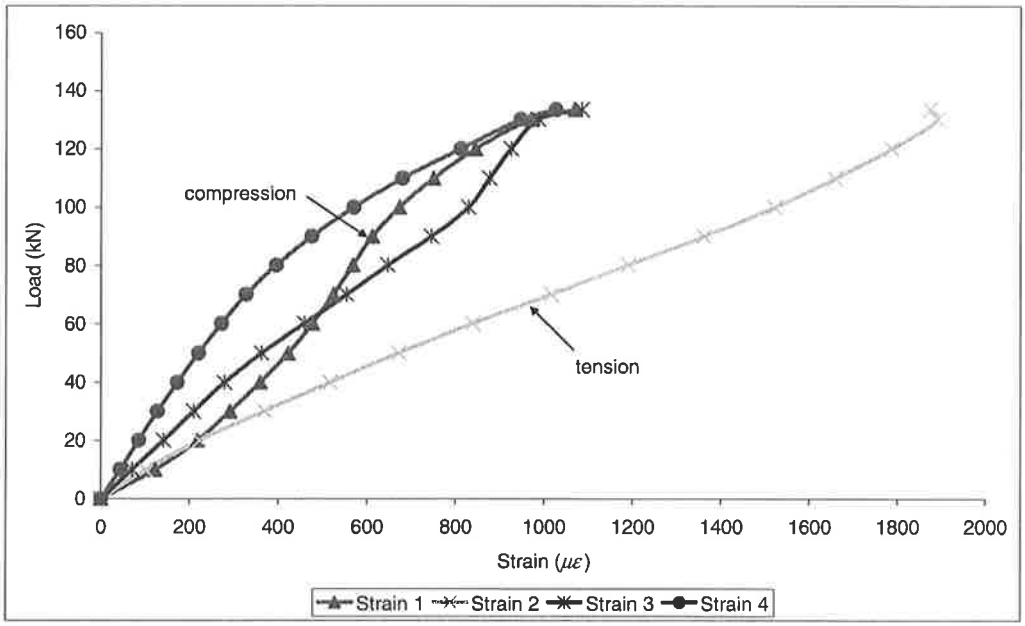

Figure 3.6.35: Load – Strain Graph for 12mm x 60mm FRP.

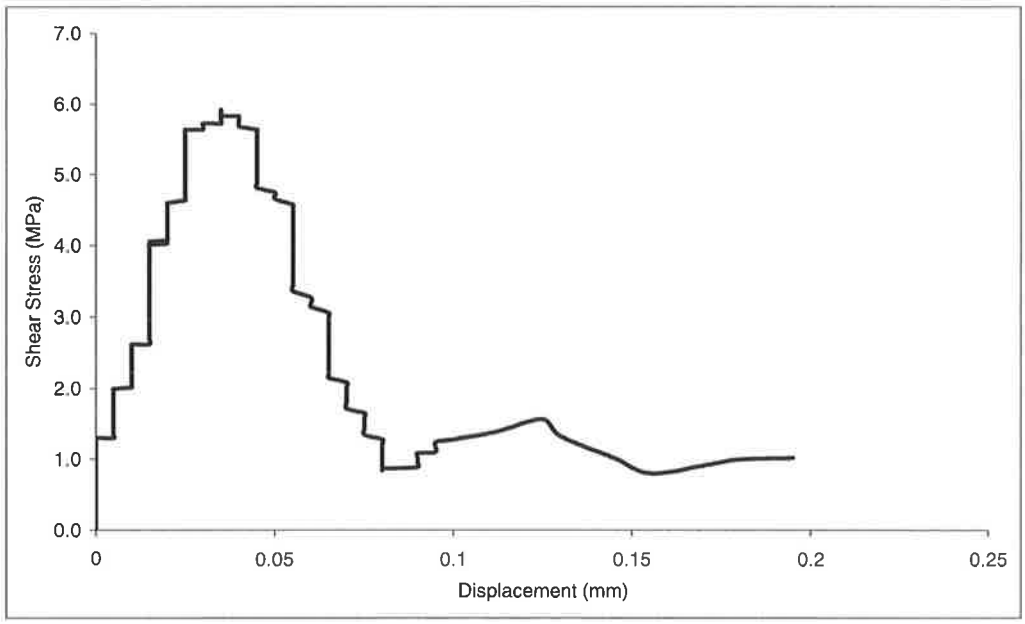

Figure 3.6.36: Shear Stress – Slip Graph for NSM 12mm x 60mm FRP.

3.6.15 CFRP 12mm x 70mm Pull Test

Width of the plate again was increased to 70mm and the number of strain gauges on plate was again using 8 strain gauges to monitor the strain profile along the plate and debonding. For clarification purpose, reason for the number of strain gauges was kept at 8 from this test onwards was to monitor strain along the plates which this plate dimension were never been done by other researchers. The failure load for this test was 144.8kN; also was without the occurrence of the 'herring bone' cracks (Figure 3.6.37). Looking at the strain profile (Figure 3.6.38), reading from SG1 and SG2 is similar to both of the earlier test (12mm x 50mm and 12mm x 60mm). SG1 which is the plate surface parallel to the concrete surface is also showing it is under compression meanwhile SG2 located opposite SG1 is also showing that the plate is on tension.

Analysing strain reading from the strain profile gives a maximum shear stress of 6.46 MPa (Figure 3.6.39) and maximum slip of 0.15 mm. Figure 3.6.39 also shows the difference in the SG3 and SG4 readings gives shear stress values reducing dramatically reaching a negative value for wider plates. Meanwhile the maximum strain is now in SG1 with reading of 1552 $\mu\varepsilon$.

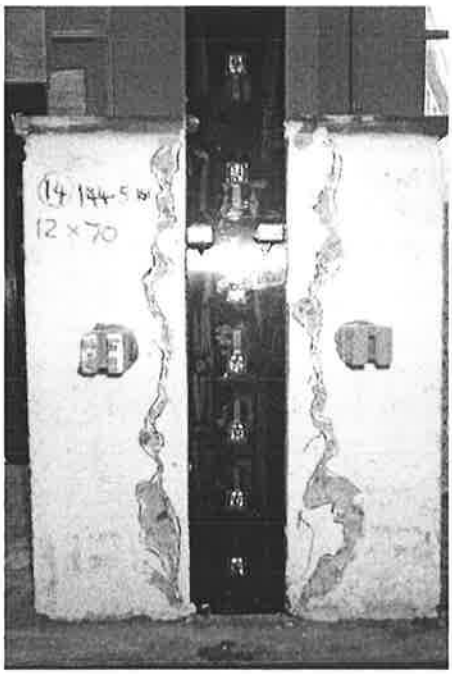

Figure 3.6.37: 12mm x 70mm CFRP failure pattern.

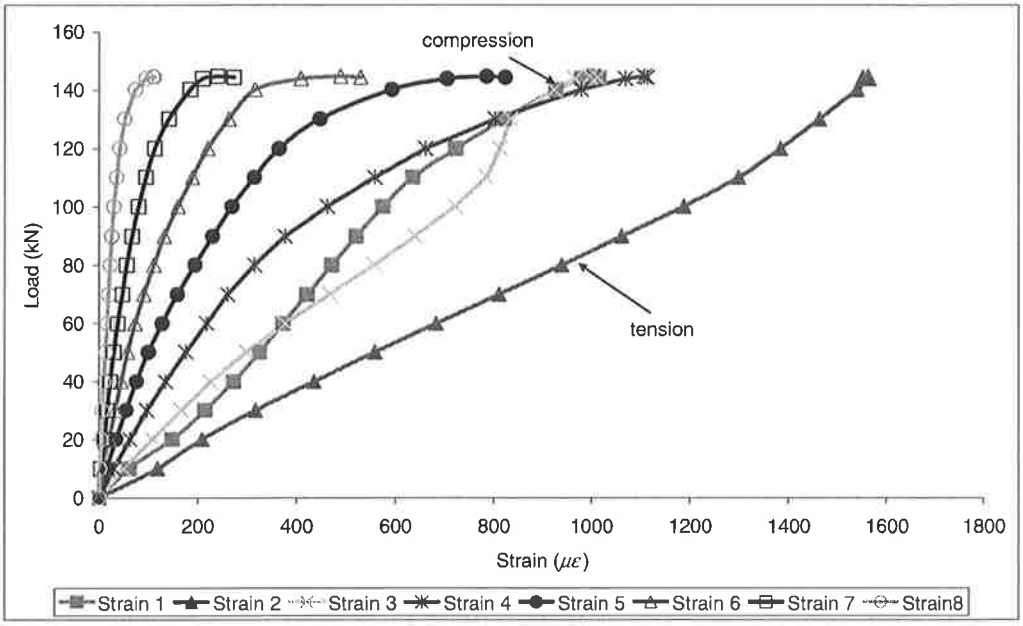

Figure 3.6.38: Load – Strain Graph for 12mm x 70mm FRP.

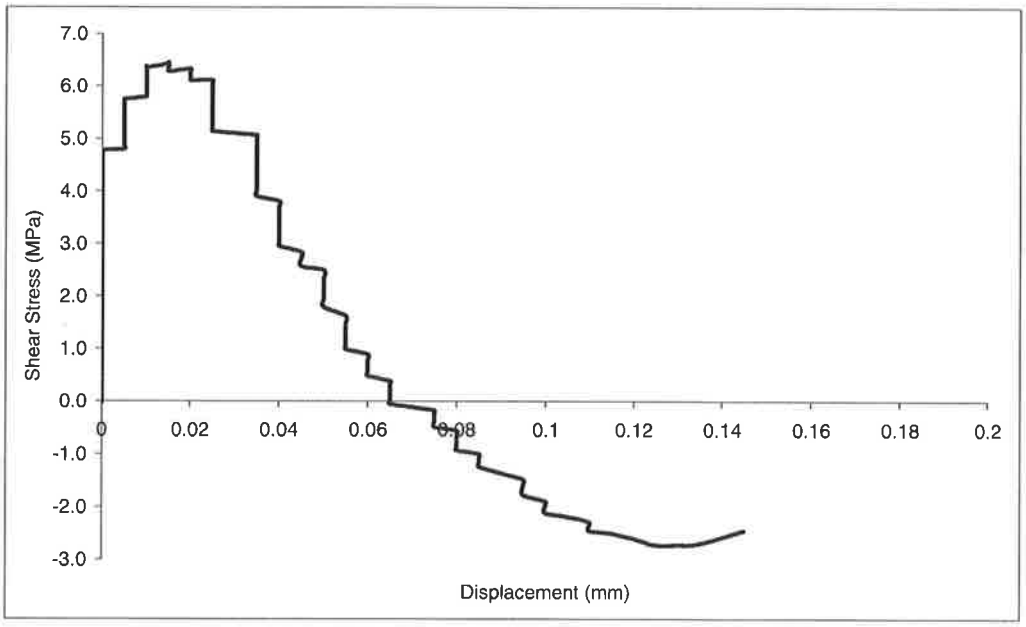

Figure 3.6.39: Shear Stress – Slip Graph for NSM 12mm x 70mm FRP.

3.6.16 CFRP 12mm x 80mm Pull Test

The failure load for this test was 134.6kN also without the occurrence of the 'herring bone' cracks (Figure 3.6.40). From the strain profile (Figure 3.6.41), reading from SG1 and SG2 is similar to previous tests. SG1 which is located on the plate surface parallel to the concrete surface is showing it is under compression meanwhile SG2 located opposite SG1 is showing that the plate is on tension.

Analysing strain reading from the strain profile gives a maximum shear stress of 3.90 MPa (Figure 3.6.42) and maximum slip of 0.17 mm. Again in Figure 3.6.42 shows the difference in the SG3 and SG4 readings gives shear stress values reducing reaching a negative value for wider plates. The maximum strain in SG2 is 1253 $\mu\varepsilon$.

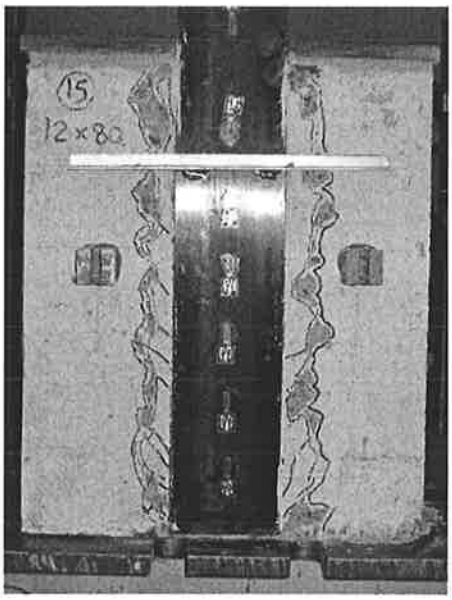

Figure 3.6.40: 12mm x 80mm CFRP failure pattern.

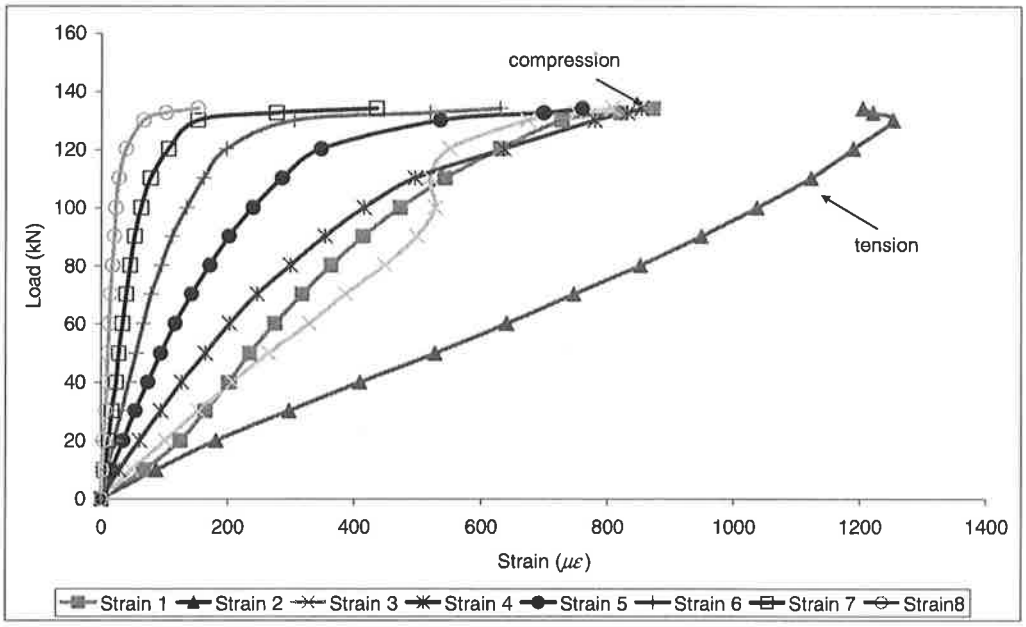

Figure 3.6.41: Strain – Load Graph for 12mm x 80mm FRP.

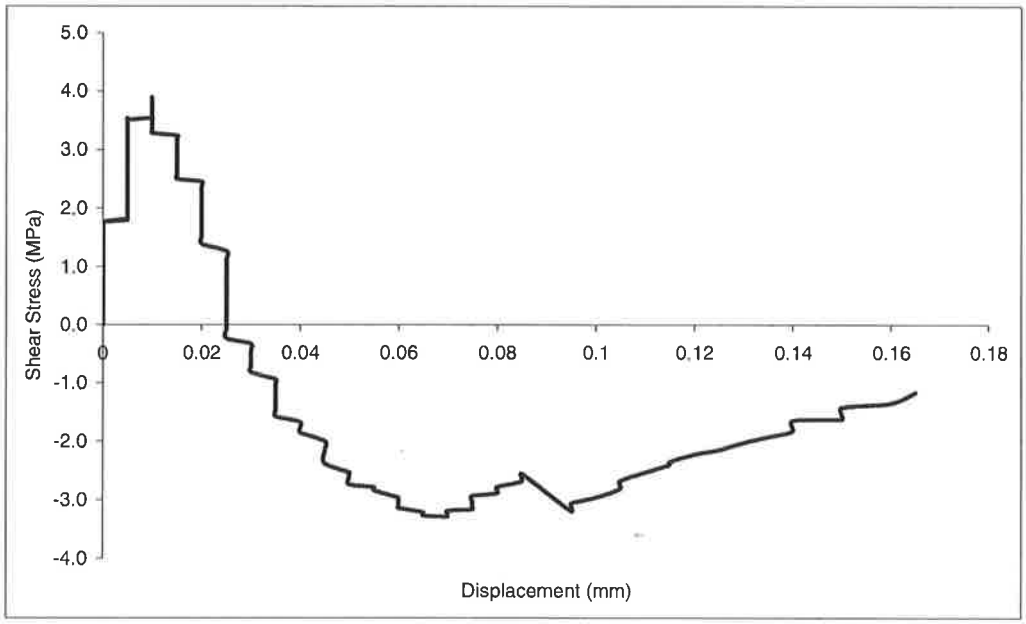

Figure 3.6.42: Shear Stress – Slip Graph for NSM 12mm x 80mm FRP.

3.6.17 CFRP 12mm x 100mm Pull Test

Finally, the last test of this series had the widest NSM plate of 100mm. The failure load for this test was 155.6kN without the occurrence of the 'herring bone' cracks (Figure 3.6.43) similar to the previous 4 wide NSM plate tests (12mm x 50mm, 12mm x 60mm, 12mm x 70mm and 12mm x 80mm). Looking at the strain profile (Figure 3.6.44), again typical reading from SG1 and SG2 is shown. SG1 which is located on the plate surface parallel to the concrete surface, is showing it is under compressive meanwhile SG2 located opposite SG1 is showing that the plate is on tension.

Analysing strain reading from the strain profile gives a maximum shear stress of 4.08 MPa (Figure 3.6.45) and maximum slip of 0.1 mm. Again in Figure 3.6.45 shows the difference in the SG3 and SG4 readings gives shear stress values reducing reaching a negative value for wider plates. The maximum strain in SG2 is 1326 $\mu\varepsilon$. Next the materials axial stiffness of the fabricated plates will be elaborate.

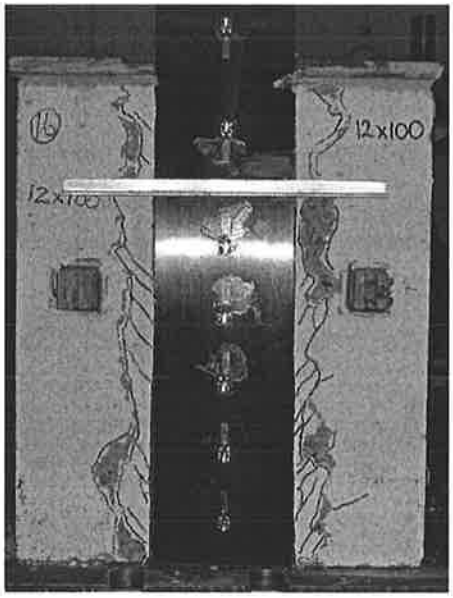

Figure 3.6.43: 12mm x 100mm CFRP failure pattern.

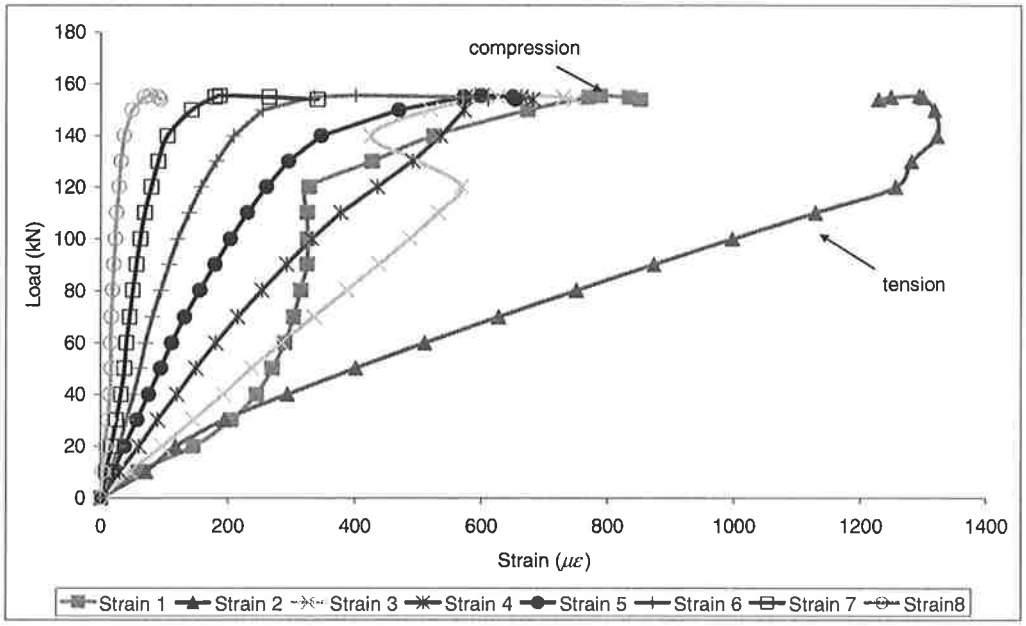

Figure 3.6.44: Load - Strain Graph for 12mm x 100mm FRP.

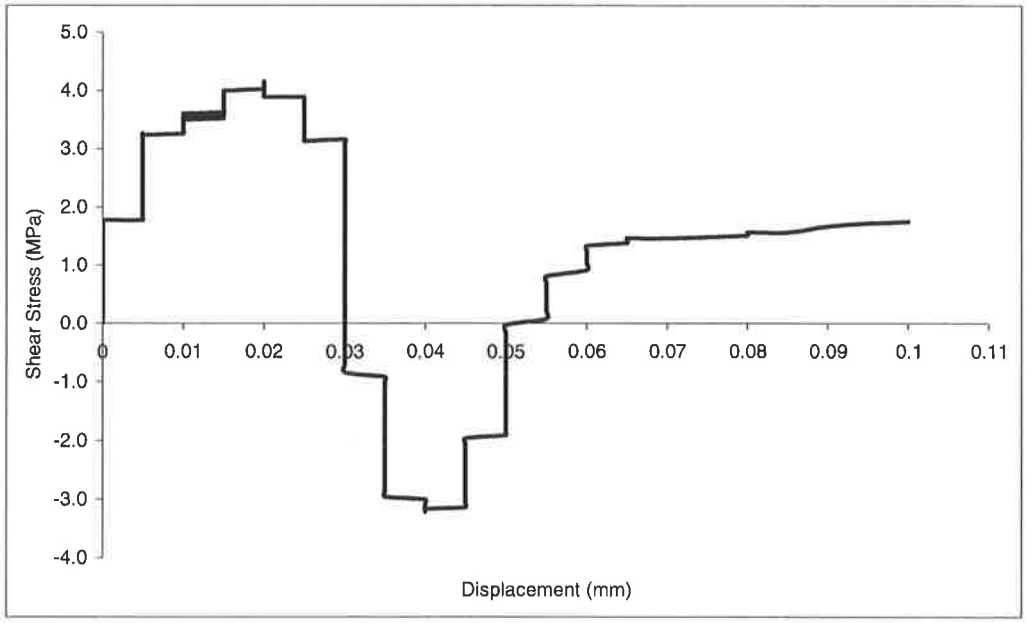

Figure 3.6.45: Shear Stress – Slip Graph for NSM 12mm x 100mm FRP.

3.7 Young's Modulus (E_p)

Discussion on whether the axial stiffness in the plate or Young's Modulus equivalent $(E_p)_{eq}$ will give the same value obtain from the experiments is presented here. Experimentally, the value of E_p is determined from the strain reading and the corresponding axial force acting on the plate. Meanwhile, the $(E_p)_{eq}$ is calculated using Eq. 3.7.1 or 3.7.2 based on the material stiffness equation.

$$(E_p)_{eq}\,(A_{frp} + A_{glue}) = A_{frp}\,E_{frp} + A_{glue}\,E_{glue} \tag{3.7.1}$$

or

$$E_{eq} = \frac{(t_{frp}\,E_{frp} + t_{glue}\,E_{glue})b}{(t_{frp} + t_{glue})\,b} \tag{3.7.2}$$

In the experiments explained earlier, 13 CFRP plate dimension were made with initial E_p and E_g to be 160000MPa and 5954 MPa respectively. For example, for plate size 12.37mm x 2.76mm, E_p was determined experimentally to be 146348 MPa. Meanwhile using the Eq. 3.7.1 or 3.7.2, $(E_p)_{eq}$ is 139907 MPa using E_{glue} of 5954 MPa from the MBrace Laminate Adhesive. This shows that using the $(E_p)_{eq}$ (Eq. 3.7.1 or 3.7.2) gives the similar values to that

obtain from experimentally and in Table 3.7.1 it is giving a mean value of 1.01. The summary of this analysis is presented in the Table 3.7.1. Finally, the conclusion of all the pull tests is covered.

Table 3.7.1: Comparison between calculation and experiment for E_p.

Plate Dimension	Plate Thickness (mm)	FRP Thickness (mm)	Glue Thickness (mm)	Experiment E_p (Mpa)	Calculated E_p (Mpa)	E (exp/cal)
12x3	2.76	2.4	0.36	146348	139907	1.05
12x4	4.24	3.6	0.64	134447	136748	0.98
24x4	4.33	3.6	0.73	141434	134029	1.06
12x6	5.73	4.8	0.93	130489	134998	0.97
12x12	12	9.6	2.4	131566	129191	1.02
30x7	7.3	6	1.3	134562	132567	1.02
26x20	20.6	20.4	0.2	129837	158504	0.82
12x30	12.02	9.6	2.42	135113	128986	1.05
12x50	12.2	9.6	2.6	132761	127171	1.04
12x60	11.74	9.6	2.14	126511	131920	0.96
12x70	11.93	9.6	2.33	135810	129914	1.05
12x80	12.28	9.6	2.68	137139	126381	1.09
12x100	12.3	9.6	2.7	135000	126185	1.07
					Mean	1.01

3.8 Discussion of Test Results

Appendix H summaries all the 16 pull tests of all the tests, 13 had plate depths of 12mm and 2 were neglected due to failure by yielding. From all the 12mm deep plates, the lowest debonding load was from the pull test of 12mm x 6mm CFRP plate (47.60kN), meanwhile the highest is from 12mm x 100mm CFRP pull test (155.6kN) with an increase of 226.9% due to larger area of bond between plate and the concrete and material stiffness (refer Appendix H)

Overall, 14 pull tests are useful in future analysis that is covered in Chapter 4. Among these 14 tests, the highest debonding load was from the 20mm x 26mm CFRP plate pull test with a loading of 199.40kN. However, the highest shear stress was from the 24mm x 4mm CFRP pull test with 16.94 MPa and also with the highest slip of 1.5mm. The material stiffness of 24mm x 4mm (E_p = 141434 MPa) was the reason of its having the highest shear stress and slip compared to 30mm x 7mm CFRP (E_p = 134562 MPa) and 20mm x 26mm CFRP plates (E_p = 129837 MPa) if the large area of bond between plate and concrete is to be considered.

3.9 Conclusion

These 16 pull tests make the understanding of a single plate NSM plating clearer due to the use of different materials and dimensions (with various aspect ratios) which leads in knowing the maximum failure load, shear stress, slip, strain, material stiffness and crack pattern.

Conclusions from these test is; large area of bond between plates does not mean it will give the highest debonding load if lower material stiffness is used. Based on material type, CFRP plates are preferred compared to aluminium and steel which does not depend on dimension of the plate. Looking at the 12mm x 12mm steel plate, it debonds thus giving a failure mode required. Meanwhile, the for 12mm x 5mm steel plate yielded making this size invalid for the used of validating the generic equation for Intermediate Crack (IC) debonding resistance (Eq. 4.2.7).

A simple analysis was conducted using these tests to compare material stiffness (Young's Modulus) obtained experimentally with calculated (Eq. 3.6.1 or 3.6.2). Using Eq. 3.6.1 and 3.6.2 proved to give close approximation of the experimental material stiffness. This equation is based on the understanding of equivalent axial stiffness.

Finally, observations of each pull test show a typical amount of concrete attached to the plate. This was not only found on the NSM plating technique but also in previous tests done by other researchers on EB plates. This leads to an introduction of confinement area ratio consisting of total depth of the plate with concrete layer divided with total thickness of plate also with the concrete layer attached. This confinement area ratio term in the generic equation for predicting the debonding failure load will be covered in detail in chapter 4.

3.10 Reference

1. Ing, L. K., Jones, N., Page, M. and Ward, S. (2004). Intermediate Crack Debonding of Near Surface Mounted Strips. Adelaide, University of Adelaide: 91.

2. Liu, I. (2005). Intermediate Crack Debonding of Plated Reinforced Concrete Beams. School of Civil and Environmental Engineering. Adelaide, University of Adelaide: 610.

3.11 Notation

EB	Externally Bonded
NSM	Near Surface Mounted
CFRP	Carbon Fiber Reinforced Polymer
SG	Strain Gauge
τ_f	Maximum shear capacity
δ_f	Maximum slip
b_p	Plate width
d_p	Plate depth
f_c	Concrete compressive strength
P_{ult}	Experiment intermediate crack debonding resistance
P_{cal}	Calculated intermediate crack debonding resistance
E_c	Concrete Young's Modulus
E_p	Plate Young's Modulus
E_g	Adhesive Young's Modulus
$(E_p)_{eq}$	Equivalent Young's Modulus
$\mu\varepsilon$	Microstrain

Chapter

4 EXPERIMENTS ANALYSIS ON SHEAR SLIP RELATIONSHIP

4.1 Introduction

In this chapter a generic design procedure is developed for a lower bound Intermediate Crack (IC) debonding resistance and behaviour for any given plate dimension and type of plates, with any degree of embedment for the plate which can be used in design to suit the requirement of retrofitting for strength or ductility and serviceability. The model has been calibrated with existing research data as well as a new series of pull.

Numerous pull-tests for example [Chajes, et al. (1996),Taljsten (1997),Teng and Chen (2001),Hassan and Rizkalla (2003),Ing, et al. (2004),Page, et al. (2005),Yao, et al. (2005)] have been done to understand the bond behaviour between FRP and concrete which is an important factor in the behaviour of concrete structures strengthened with FRP. As known, there are two plating techniques currently available, Externally Bonded (EB) and Near Surface Mounted (NSM), and up to now each technique has been treated separately. It is also been found [Mohamed Ali, et al. (2006)] that the shear-slip relationships (τ/δ), which controls the bond characteristics, have different equations for each technique. In this chapter, both EB and NSM pull-test results are analysed together and optimised in order to get a generic equation for the shear-slip relationship and IC debonding resistance.

The structure of this chapter is; in the following section, the derivation of the generic equation for IC debonding resistance is presented. In section three, calibration of the generic equation is explained in detail the parameters considered. Section four deals with the derivation of a model for the peak shear stress followed with the derivation of a model for the slip capacity. Section six is looking into compares the generic equation with the published models. Finally, conclusions of this chapter and an outline for future directions of this research are given.

4.2 Partial Interaction Debonding Model

The generic equation was derived by considering equilibrium and compatibility of a joint as shown in Figure 4.2.1. The governing differential given by Yuan, et al. (2004) is

$$\frac{d^2\delta}{dx^2} - Jf(\delta) = 0 \qquad (4.2.1)$$

where δ is displacement between the plate and concrete, and this slip is located at a distance x from the unloaded end of the plate, $f(\delta)$ is the function defining the interface shear stress-

slip relationship, which is referred to as bond-slip, and J is a term defining the axial rigidity and geometric properties of the components including the joint.

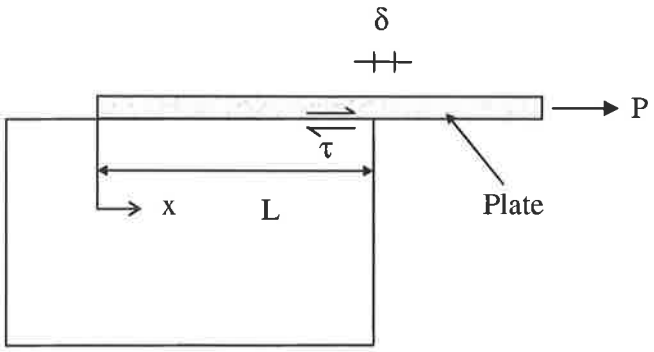

Figure 4.2.1: Push-pull test specimen.

The bond-slip relationship of such joints is typical bi-linear model shown in Figure 4.2.2, with a linear-elastic region to the maximum shear stress τ at slip of δ_1, followed by a softening region where micro-cracking develops to a slip of δ_f, which beyond macro-cracking occurs and the debonding interface can no longer transfer the shear force. However, for design purposes, it has been found [Ing, et al. (2004)] that the bond slip-slip model may be simplified to linear softening model as shown Figure 4.2.2. The model was found to have a reasonable approximation due to experimental data as the slip at maximum shear stress (τ_f) is small, about 0.2mm, compared to the maximum slip (δ_f) in the order of millimetre. A detail justification for this approach can be found in Mohamed Ali, et al. (2006).

The model is much simpler as only two coordinates are required to define the relationship and much more importantly, it allows a closed form equation; furthermore both models have the same fracture energy (area under $\tau_f\delta_f$) which has no effect on predicted IC debonding resistance.

Considering only bond lengths, L (Figure 4.2.1), that exceed the effective bond length so that the maximum strength can be achieve, the function defining the idealised linear softening bond-slip curve in Figure 4.2.2 is given by

$$f(\delta) = \frac{\tau_{max}}{\delta_f}(\delta_f - \delta) \qquad (4.2.2)$$

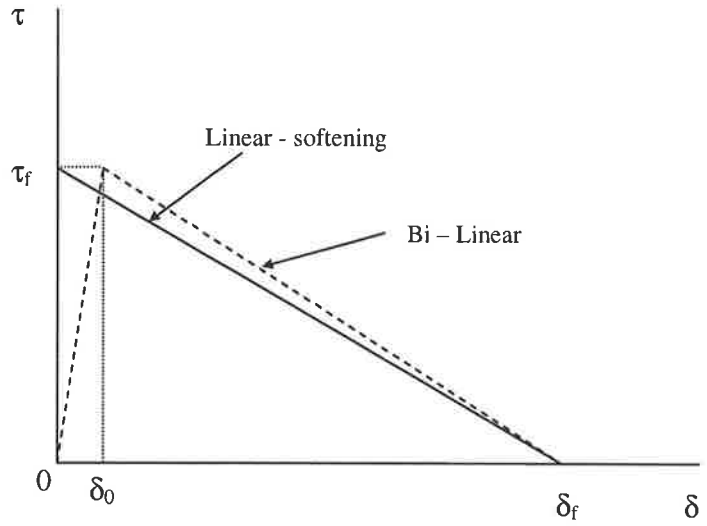

Figure 4.2.2: Common bond-slip models.

However, the fundamental difference between the current analytical model and earlier ones is that the term J in Eq. 4.2.1 incorporates the geometry of the interface debonding failure plane and not the geometry of the plate. Therefore, J is given by [Seracino, et al. (2005)].

$$J = L_{per}\left(\frac{1}{(EA)_p}+\frac{1}{(EA)_c}\right) \tag{4.2.3}$$

by substituting Eq. 4.2.2 and Eq. 4.2.3 into the Eq. 4.2.1 and solving the differential gives

$$P_{IC} = \frac{\tau_f\ L_{per}}{\lambda} \tag{4.2.4}$$

where P_{IC} is the maximum IC debonding resistance of a joint provided that the anchored length L is greater than L_{crit} which is given by

$$L_{crit} = \frac{\pi}{2\lambda} \tag{4.2.5}$$

where

$$\lambda^2 = \frac{\tau_f L_{per}}{\delta_f (EA)_p} \tag{4.2.6}$$

as the term $(EA)_c >> (EA)_p$ in Eq. 4.2.3, $(EA)_c$ tend to zero and can be ignored. Finally, by substituting Eq. 4.2.6 into Eq. 4.2.4 gives the following generic equation

$$P_{IC} = \sqrt{\tau_f \delta_f}\sqrt{L_{per}(EA)_P} \tag{4.2.7}$$

It is worth noting that this equation also includes the fracture energy term $\tau_f\delta_f$. Furthermore, the thickness of the plate is not the important input as the cross sectional area and in particular the axial stiffness $(EA)_p$ of the adhesively bonded plate now governs debonding. This makes the equation a generic form for any type of plating.

At this time, the only known parameters in Eq. 4.2.7 are Young's Modulus and the area of the plate. In deriving the unknowns which are L_{per} and $\tau_f\delta_f$, a series of 35 experimental results were used. L_{per}, which is the failure plane, was defined for both plating techniques (Figure 4.2.3 and Figure 4.2.4).

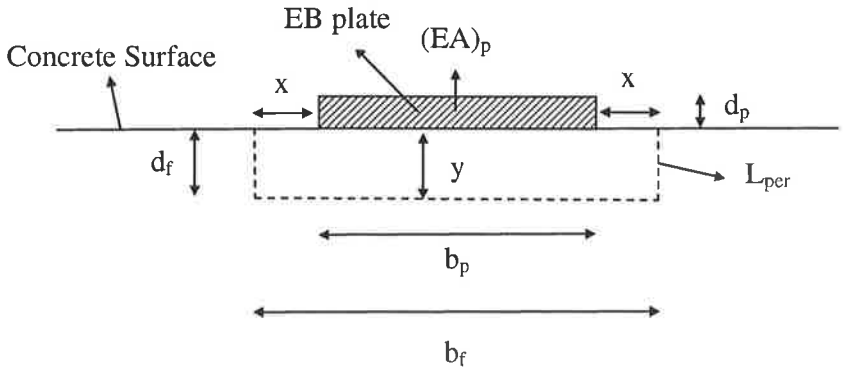

Figure 4.2.3: Debonding failure plane for Externally Bonded plates.

The Failure plane of an EB plate, which is on the concrete surface, is taken to be

$$\begin{aligned} L_{per} &= b_p + 2x + 2y \\ &= 2d_f + b_f \end{aligned} \tag{4.2.8}$$

as shown in Figure 4.2.3

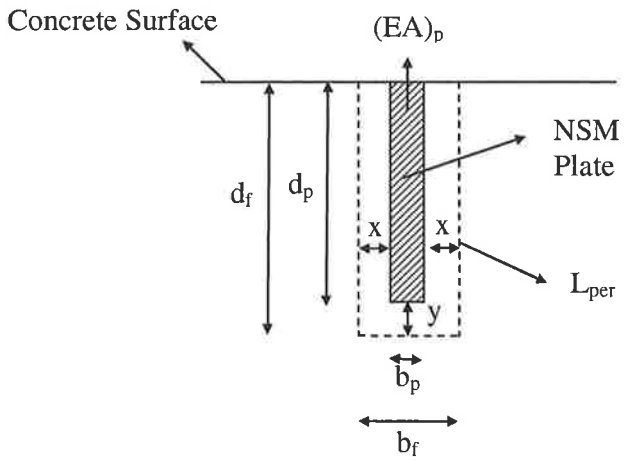

Figure 4.2.4: Debonding failure plane for Near Surface Mounted plates.

Meanwhile for NSM plating the failure plane making L_{per} is

$$L_{per} = 2d_p + b_p + 2x + y \qquad (4.2.9)$$
$$= 2d_f + b_f$$

as shown in Figure 4.2.4

In the next section, both of the unknown parameter (L_{per} and $\tau_f\delta_f$) calibration will be presented.

4.3 Calibration of Fracture Energy ($\tau_f\delta_f$) and Failure Plane (L_{per})

The first series of analyses were all based on the data tabulated in Table A1 in Appendix I which consists of 35 pull test experiments of NSM and EB pultruded plates. In order to calibrate L_{per} shown in Figure 4.2.3 and Figure 4.2.4, there are 2 unknown parameters that need to be quantified that is x and y. The effect of the concrete strength (f_c) also has to be determined, as well as the depth of the concrete failure zone (d_f) and width (b_f). The analysis for these variables is described below.

4.3.1 Development of Mathematical Debonding Model

4.3.1.1 Mathematical Model

The generic equation (Eq. 4.2.7) was optimised using various values of x and y which represents the failure plane (L_{per}) and the plate confinement ratio (d_f/b_f). It was found that a logarithmic variation in the following form gave the least scatter.

$$\log \tau_f \delta_f = \mathrm{m} \log \frac{\mathrm{d_f}}{\mathrm{b_f}} + \mathrm{C} \tag{4.3.1}$$

that is

$$\tau_f \delta_f = C \left(\frac{d_f}{b_f} \right)^m \tag{4.3.2}$$

It was also assumed that the concrete compressive strength has a significant influence on the fracture energy term $\tau_f \delta_f$ such that Eq. 4.3.2 was modified as follows

$$\frac{\tau_f \delta_f}{f_c^{\alpha}} = C \left(\frac{d_f}{b_f} \right)^m \tag{4.3.3}$$

where

$$\tau_f \delta_f = \frac{P_{exp}^{\ 2}}{L_{per}(E_p A_p)} \tag{4.3.4}$$

The confinement term d_f/b_f in Figure 4.2.3 for EB plates is given by

$$\frac{d_f}{b_f} = \frac{y}{b_p + 2x} \tag{4.3.5}$$

and for NSM plates in Figure 4.2.4 by

$$\frac{d_f}{b_f} = \frac{d_p + y}{b_p + 2x} \tag{4.3.6}$$

4.3.1.2 Initial Estimation of Concrete Component (α)

For the pull test given in Table A1 in Appendix I the concrete strengths ranged from 27.7 MPa to 69.1 MPa. The initially estimate of the concrete contribution (α) in Eq. 4.3.3 it was assumed at first to be $f_c^{0.25}$. It is known that the concrete tensile strength is proportional to the

concrete compressive strength. Clause 6.1.1.3 in the Australian Standard (AS3600) gives the concrete tensile strength at 28 days to be

$$f_{ct} = 0.4\sqrt{f_c} \tag{4.3.7}$$

The reason behind selecting $\alpha = 0.25$ is that this is relationship used in the model found by Teng, et al. (2002)

$$P_{IC} \propto \sqrt{\sqrt{fc}} \tag{4.3.8}$$

that is, the debonding resistance is proportional to the concrete tensile strength which is $f_t \, \alpha \sqrt{f_c}$.

4.3.1.3 Optimising the Mathematical Model

Various approaches were used to optimise Eq. 4.3.3. It was necessary to find the best values of x, y, α, m and C that gives the least scatter of P_{exp}/P_{cal}. For example α was initially assumed to be 0.25 for the reason discussed in the previous section and x or y was then varied. For each new value of x and y, $\tau_f\delta_f$ in Eq. 4.2.7 was obtained from test results and the exponent m in Eq. 4.3.3 determined from linear regression analysis. Equation 4.3.3 was then used to determine P_{cal} for each test results and the mean and scatter of P_{exp}/P_{cal} determined. The lowest coefficient of variance (COV) of P_{exp}/P_{cal} was assumed to give the optimum solution or by definition the mean of $P_{exp}/P_{cal} \approx 1$.

4.3.1.4 Fracture Energy and Failure Plane Analysis ($\tau_f\delta_f$ and L_{per})

In this section, the analysis focuses on the confinement ratio (d_f/b_f) and failure plane parameter (L_{per}) to quantify the optimum value for x and y > 0. It is imperative that the value of y in Figure 4.2.3 and Figure 4.2.4 must not be equal to zero as y = 0 will only giving values for the NSM plates and cannot be applied to EB plates as d_f would also equal zero.
The analysis begins by considering both techniques separately to identify suitable values of x and y for each type of plating technique. At this stage of analysis based on experimental observations as shown in Figure 4.3.1, the value for x and y is expected to be in the order of

2mm to determine the fracture energy from Eq. 4.2.7 and the confinement term from Eq. 4.3.5 and Eq. 4.3.6. Referring to Figure 4.3.2, it can be seen that C.O.V. of P_{exp}/P_{cal} for EB plating, increases with increasing values of x and y (x = y) for EB plates which the opposite is observed for NSM plates in Figure 4.3.3. Each individual result in Figures 4.3.2 and 4.3.3 are tabulated in Table 4.3.1 and Table 4.3.2. It can be seen that the COV is small for all results. Next, the axial rigidity analysis is presented.

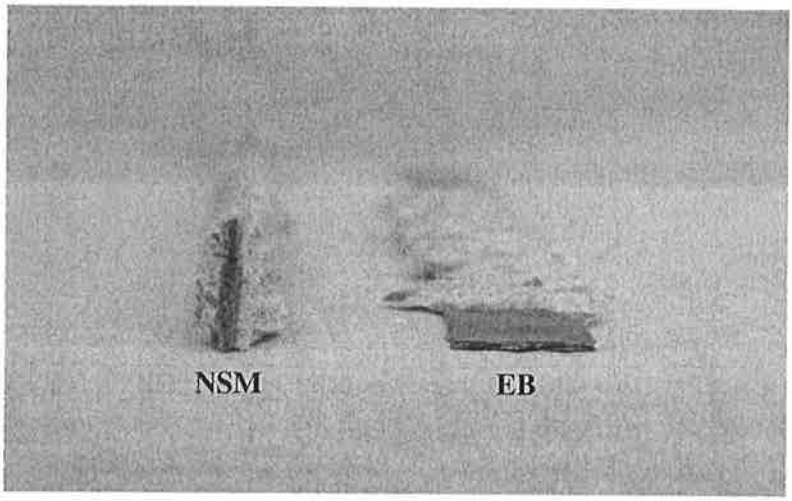

Figure 4.3.1: Typical pull test failure planes.

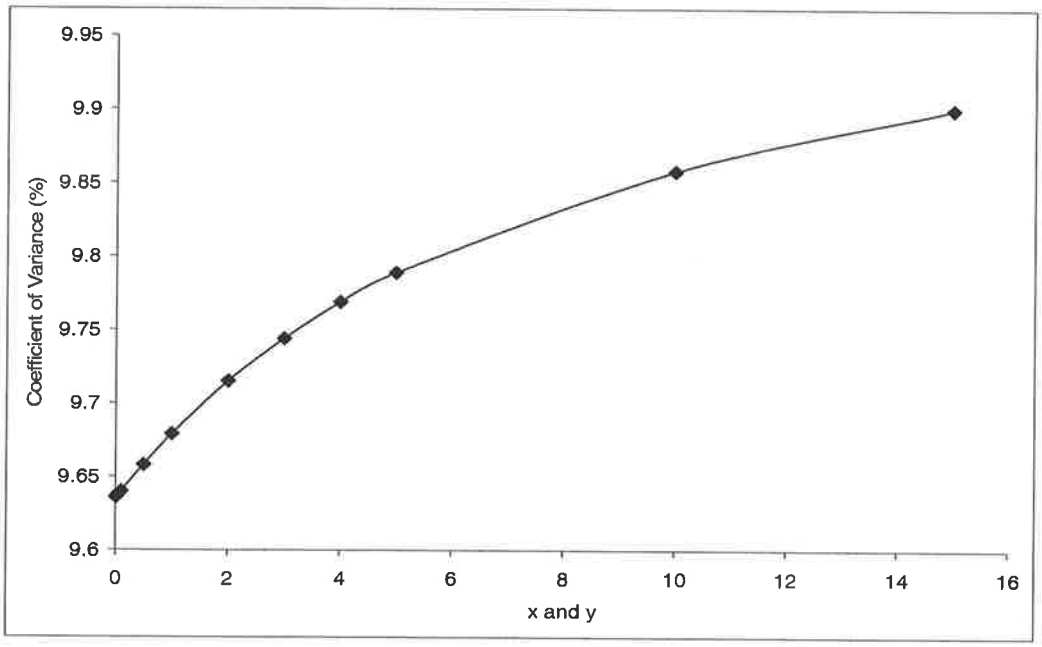

Figure 4.3.2: Coefficient of Variance of Pexp/Pcal Externally Bonded plates.

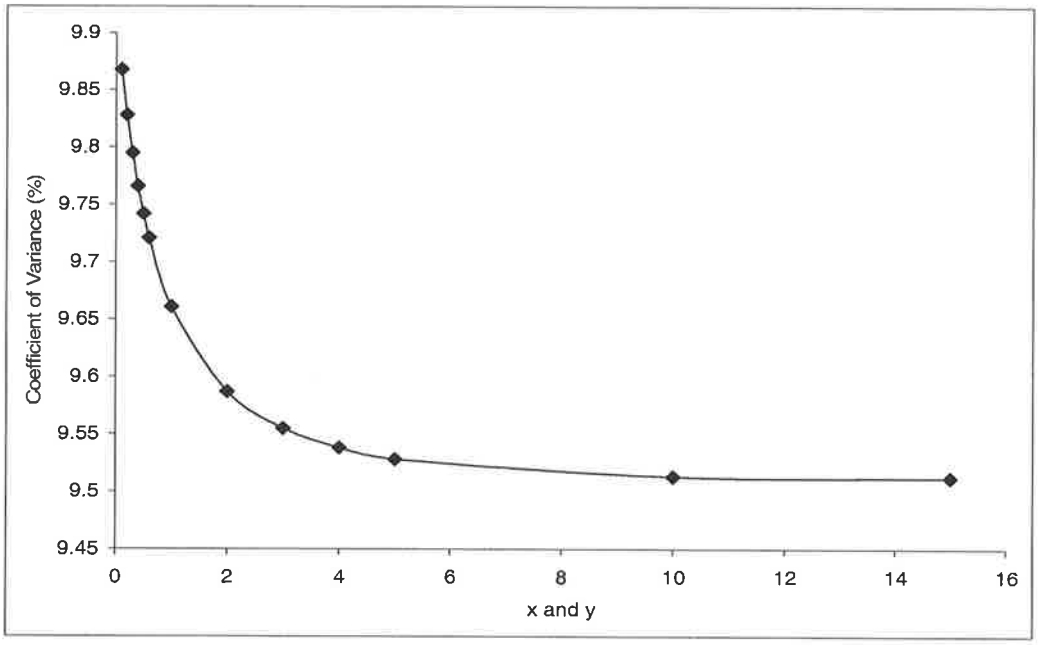

Figure 4.3.3: Coefficient of Variance of Pexp/Pcal Near Surface Mounted plates.

Table 4.3.1: Summary of the analysis for Externally Bonded Plates.

x and y (mm)	Linear regression	Pexp/Pcal		
		Mean	Standard Deviation	Coefficient Of Variance (%)
0.01	$\tau_f \delta_f = 22.23 \left(\frac{d_f}{b_f}\right)^{0.44} f_c^{0.25}$	1.004	0.097	9.636
0.05	$\tau_f \delta_f = 10.71 \left(\frac{d_f}{b_f}\right)^{0.44} f_c^{0.25}$	1.004	0.097	9.638
0.1	$\tau_f \delta_f = 7.72 \left(\frac{d_f}{b_f}\right)^{0.43} f_c^{0.25}$	1.004	0.097	9.640
0.5	$\tau_f \delta_f = 3.29 \left(\frac{d_f}{b_f}\right)^{0.4} f_c^{0.25}$	1.004	0.097	9.658
1	$\tau_f \delta_f = 2.11 \left(\frac{d_f}{b_f}\right)^{0.37} f_c^{0.25}$	1.004	0.097	9.679
2	$\tau_f \delta_f = 1.26 \left(\frac{d_f}{b_f}\right)^{0.31} f_c^{0.25}$	1.004	0.098	9.715
3	$\tau_f \delta_f = 0.89 \left(\frac{d_f}{b_f}\right)^{0.26} f_c^{0.25}$	1.004	0.098	9.744

x and y (mm)	Linear regression	Pexp/Pcal		
		Mean	Standard Deviation	Coefficient Of Variance (%)
4	$\tau_f \delta_f = 0.69 \left(\frac{d_f}{b_f}\right)^{0.21} f_c^{0.25}$	1.004	0.098	9.769
5	$\tau_f \delta_f = 0.55 \left(\frac{d_f}{b_f}\right)^{0.16} f_c^{0.25}$	1.004	0.098	9.789
10	$\tau_f \delta_f = 0.27 \left(\frac{d_f}{b_f}\right)^{-0.04} f_c^{0.25}$	1.004	0.099	9.858
15	$\tau_f \delta_f = 0.17 \left(\frac{d_f}{b_f}\right)^{-0.21} f_c^{0.25}$	1.004	0.099	9.900

Table 4.3.2: Summary of the analysis for Near Surface Mounted Plates.

x and y (mm)	Linear regression	Pexp/Pcal		
		Mean	Standard Deviation	Coefficient Of Variance (%)
0.1	$\tau_f \delta_f = 4.02 \left(\frac{d_f}{b_f}\right)^{0.36} f_c^{0.25}$	1.005	0.099	9.868
0.2	$\tau_f \delta_f = 3.93 \left(\frac{d_f}{b_f}\right)^{0.38} f_c^{0.25}$	1.005	0.099	9.828
0.3	$\tau_f \delta_f = 3.84 \left(\frac{d_f}{b_f}\right)^{0.41} f_c^{0.25}$	1.005	0.098	9.795
0.4	$\tau_f \delta_f = 3.77 \left(\frac{d_f}{b_f}\right)^{0.43} f_c^{0.25}$	1.005	0.098	9.766
0.5	$\tau_f \delta_f = 3.71 \left(\frac{d_f}{b_f}\right)^{0.45} f_c^{0.25}$	1.005	0.098	9.742
0.6	$\tau_f \delta_f = 3.66 \left(\frac{d_f}{b_f}\right)^{0.47} f_c^{0.25}$	1.005	0.098	9.721
1	$\tau_f \delta_f = 3.5 \left(\frac{d_f}{b_f}\right)^{0.55} f_c^{0.25}$	1.005	0.097	9.661
2	$\tau_f \delta_f = 3.25 \left(\frac{d_f}{b_f}\right)^{0.71} f_c^{0.25}$	1.005	0.096	9.587

x and y (mm)	Linear regression	Pexp/Pcal		
		Mean	Standard Deviation	Coefficient Of Variance (%)
3	$\tau_f \delta_f = 3.12 \left(\frac{d_f}{b_f}\right)^{0.85} f_c^{0.25}$	1.005	0.096	9.555
4	$\tau_f \delta_f = 3.04 \left(\frac{d_f}{b_f}\right)^{0.98} f_c^{0.25}$	1.005	0.096	9.538
5	$\tau_f \delta_f = 3.0 \left(\frac{d_f}{b_f}\right)^{1.11} f_c^{0.25}$	1.005	0.096	9.528
10	$\tau_f \delta_f = 3.07 \left(\frac{d_f}{b_f}\right)^{1.68} f_c^{0.25}$	1.005	0.096	9.513
15	$\tau_f \delta_f = 3.43 \left(\frac{d_f}{b_f}\right)^{2.22} f_c^{0.25}$	1.005	0.096	9.512

4.3.1.5 Axial Rigidity

The analysis continues by analysing the Axial Rigidity term $(EA)_p$ in Eq. 4.2.7 which can be considered to consist of the axial stiffness of the plate E_pA_p plus the axial rigidity of the concrete included with the failure plane of L_{per} in Figures 4.2.3 and 4.2.4, that is (E_pA_p+ E_cA_c). The following analysis takes x and y equal to 2 and that the concrete contribution as $f_c^{0.25}$. This was done to look specifically at the effect of both the concrete and FRP axial stiffness on the failure load as shown in Eq. 4.3.9 and Figure 4.3.4.

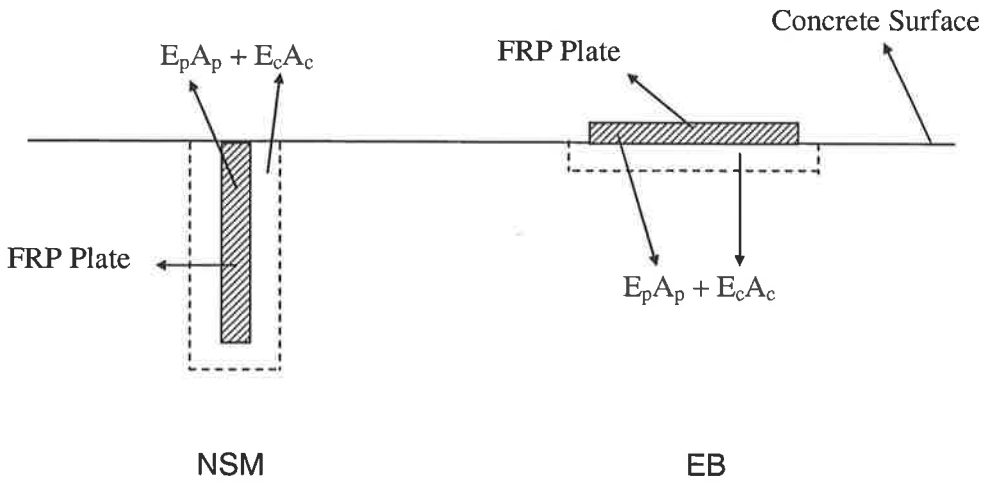

Figure 4.3.4: Axial Rigidity for NSM plate and EB plate.

$$\tau_f \delta_f = \frac{P_{ult}^{\ 2}}{L_{per}(E_p A_p + E_c A_c)} \tag{4.3.9}$$

From this analysis, shown in Figures 4.3.5 and 4.3.6, by including the concrete axial stiffness, does not improve the results based on the R^2 values, which clearly shows there is no need to consider concrete in debonding failure plane. The following section will be looking into the optimum value for α in Eq. 4.3.3 which will improves the fracture energy equation.

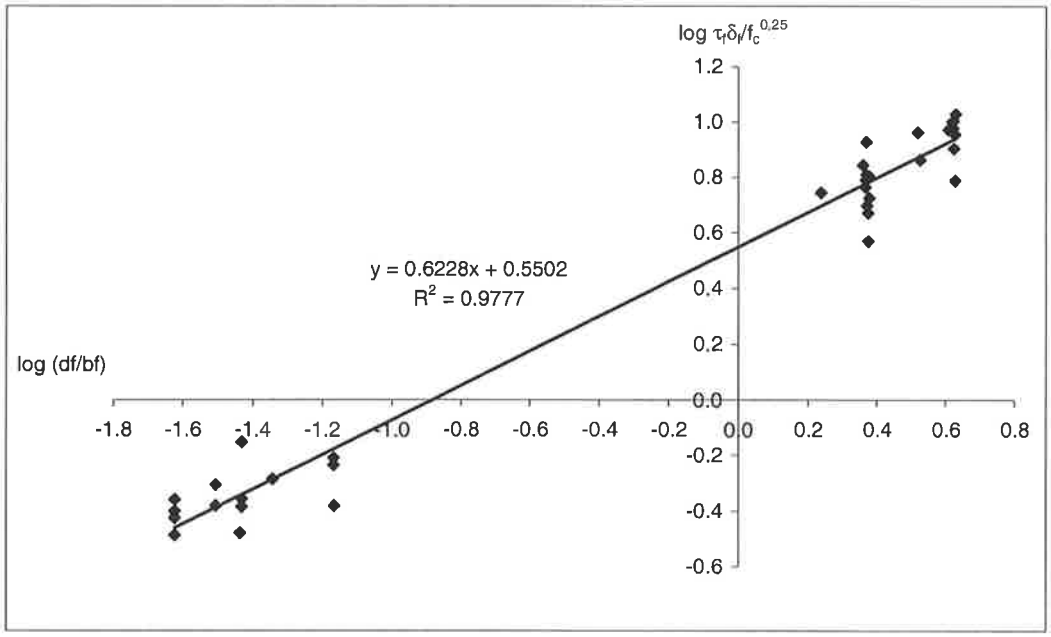

Figure 4.3.5: Linear Regression Analysis for EA_p and x = 2.

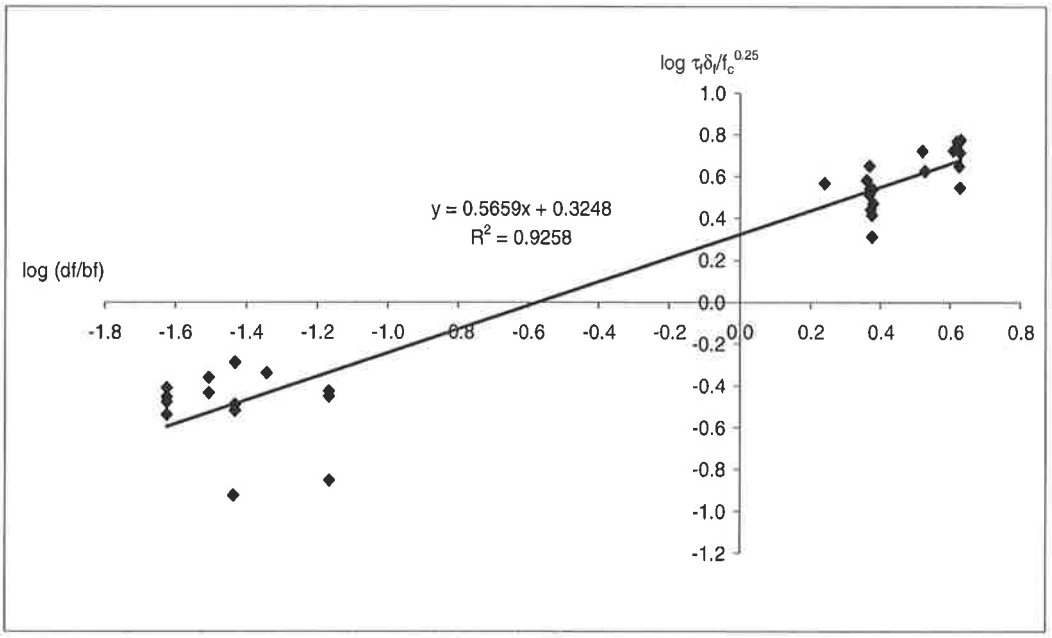

Figure 4.3.6: Linear Regression Analysis for (EA_c + EA_p) and x = 2.

4.3.1.6 Concrete Strength (f_c) Contribution

In section 4.3.1.2, an initial assumption was made that $\alpha = 0.25$ in Eq. 4.3.3. The optimum value of α is now determined using the test data given in Table 1A in Appendix I. Each

individual analysis of α was analyse as shown in Figures 4.3.7 and 4.3.8. The results summaries are tabulated in Table 4.3.3. In can be seen in Figure 4.3.9 and Table 4.3.3, the lowest COV is with α equal to 0.7 is giving the optimum solution for this analysis.

However for the reason of simplification, looking at Table 4.3.3, the difference between the COV for $f_c^{0.65}$ and $f_c^{0.7}$ is not much with a difference of 0.043%, making the equation for $\tau_f \delta_f$ is

$$\tau_f \delta_f = 0.78 \left(\frac{d_f}{b_f} \right)^{0.64} f_c^{0.65} \tag{4.3.10}$$

or in much simpler form in Eq. 4.2.7

$$\sqrt{\tau_f \delta_f} = 0.88 \sqrt[3]{\frac{d_f}{b_f} f_c} \tag{4.3.11}$$

It is also worth mentioning here that in Table 4.3.3, the exponent for (d_f / b_f) is varying from 0.61 to 0.66. This exponent represents the mean line slope coefficient as shown in Figure 4.3.7.

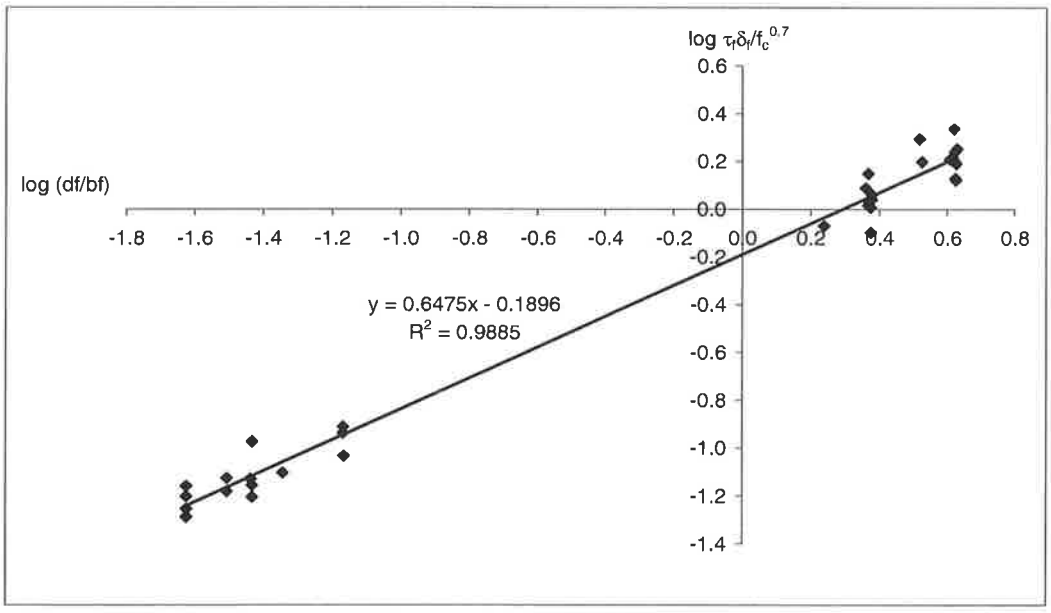

Figure 4.3.7: Linear Regression Analysis for $f_c^{0.7}$ with x=2 and y=2.

The linear regression for $f_c^{0.7}$

$$\tau_f \delta_f = 0.65 \left(\frac{d_f}{b_f} \right)^{0.65} f_c^{0.7} \tag{4.3.12}$$

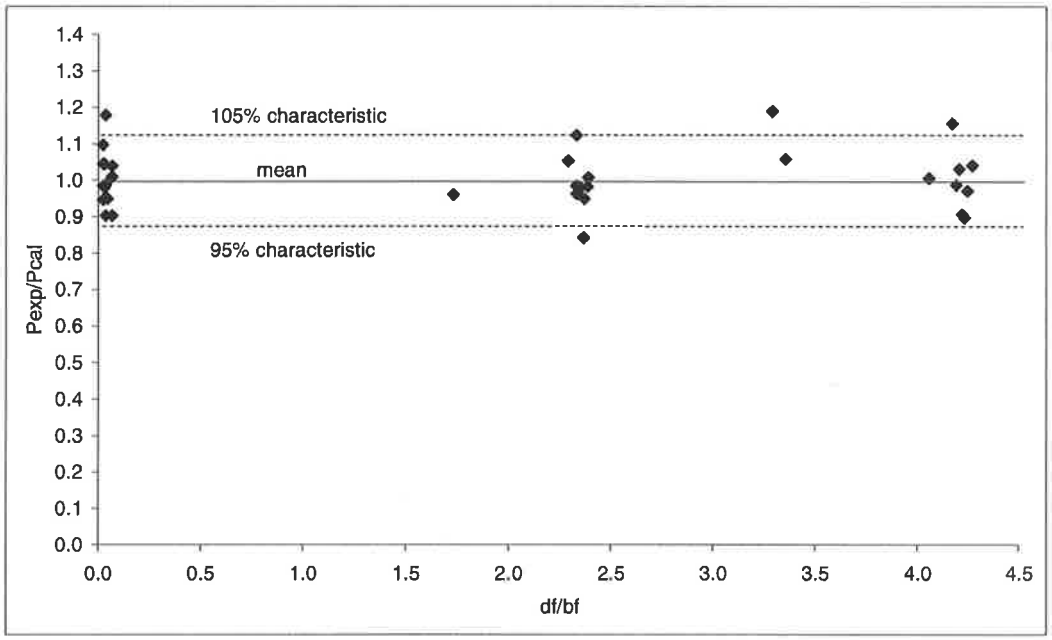

Figure 4.3.8: Comparison between experiment and the calculated value for $f_c^{0.7}$.

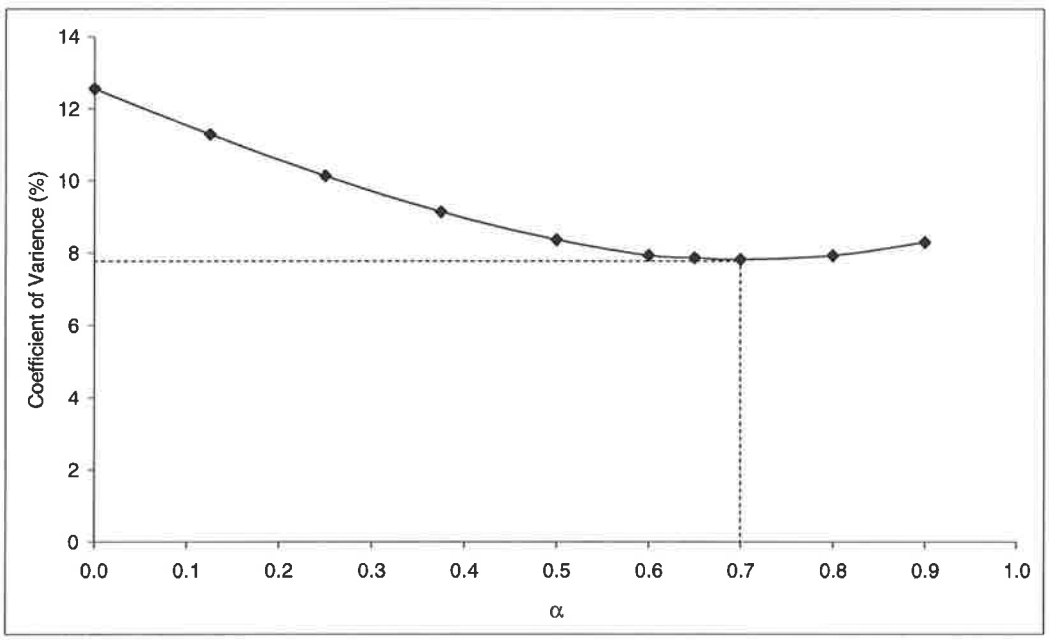

Figure 4.3.9: α by comparison of Coefficient of Variance Pexp/Pcal.

Table 4.3.3: Summary of the analysis for varying α.

		Pexp/Pcal		
f_c^{α}	Linear regression	Mean	Standard Deviation	Coefficient Of Variance (%)
f_c^{0}	$\tau_f \delta_f = 9.15\left(\frac{d_f}{b_f}\right)^{0.61} f_c^{0}$	1.008	0.127	12.560
$f_c^{0.125}$	$\tau_f \delta_f = 5.7\left(\frac{d_f}{b_f}\right)^{0.62} f_c^{0.125}$	1.007	0.114	11.296
$f_c^{0.25}$	$\tau_f \delta_f = 3.55\left(\frac{d_f}{b_f}\right)^{0.62} f_c^{0.25}$	1.005	0.102	10.138
$f_c^{0.375}$	$\tau_f \delta_f = 2.21\left(\frac{d_f}{b_f}\right)^{0.63} f_c^{0.375}$	1.005	0.092	9.140
$f_c^{0.5}$	$\tau_f \delta_f = 1.38\left(\frac{d_f}{b_f}\right)^{0.64} f_c^{0.5}$	1.004	0.084	8.373
$f_c^{0.6}$	$\tau_f \delta_f = 0.94\left(\frac{d_f}{b_f}\right)^{0.64} f_c^{0.6}$	1.003	0.080	7.982
$f_c^{0.65}$	$\tau_f \delta_f = 0.78\left(\frac{d_f}{b_f}\right)^{0.64} f_c^{0.65}$	1.004	0.079	7.874
$f_c^{0.7}$	$\tau_f \delta_f = 0.65\left(\frac{d_f}{b_f}\right)^{0.65} f_c^{0.7}$	1.003	0.079	7.831
$f_c^{0.8}$	$\tau_f \delta_f = 0.44\left(\frac{d_f}{b_f}\right)^{0.65} f_c^{0.8}$	1.004	0.080	7.938
$f_c^{0.9}$	$\tau_f \delta_f = 0.30\left(\frac{d_f}{b_f}\right)^{0.66} f_c^{0.9}$	1.003	0.083	8.305

4.3.1.7 Wet lay up plates

In the early stage of this analysis data was collected from other researches and mainly focused on pultruded plate of CFRP,GFRP and Steel plates. As the analysis continued, it was decided that the wet lay up plates should also be included in the database to include any EB plate type. However it was found that pull test using wet lay up plates by Yao, et al. (2005), provided E_{fiber} and also the thickness of the fiber, making such data can also be included in the existing analysis. The data for the wet lay up is presented in Table A2 in Appendix I.

In Figure 4.3.10, using Eq. 4.2.7 the wet lay up results are generally located slightly higher than the existing experimental data. This indicates that the wet lay up results can be added to the existing analysis. Next, the additional experiments test is described.

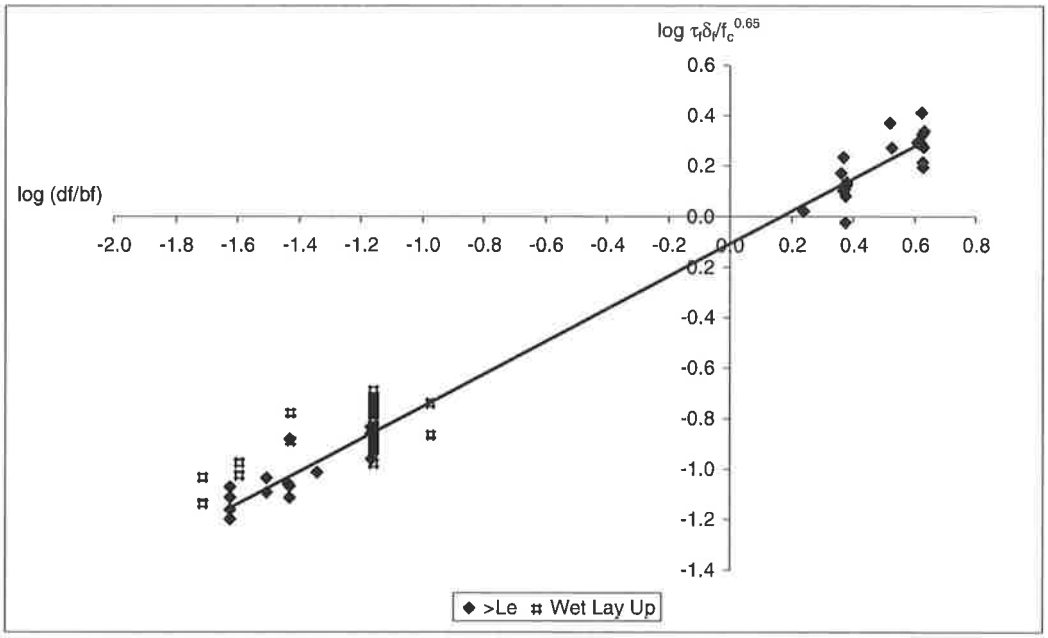

Figure 4.3.10: Linear Regression Analysis for wet lay up without any resin thickness.

4.3.1.8 Additional Experiment

In order to prove that Eq. 4.2.7 is suitable for any plate dimension, a series of tests were undertaken as summarised in Table 4.3.4. Details of the test were discussed in Chapter 3. Looking at the $\tau_f\delta_f$ graph earlier (Figure 4.3.10), it is showing that there is a gap exist between the NSM data (located in the 1st quadrant) and EB data (located in the 3rd quadrant). Designing test with appropriate aspect ratio to fill this gap will prove that the proposed model is suitable, 16 tests were undertaken, 13 were fabricated with CFRP strips. The details of the plates tested are as shown in Table 4.3.4 and in Table A3 in Appendix I.

Unfortunately, only 5 tests bond lengths exceeding the critical bond length (* in Table 4.3.4) and only 4 tests were considered as the 12mm x 12mm Aluminium plate failed by yielding. Meanwhile, for the remaining tests, 10 had bond lengths less than the critical bond length so that the maximum debonding resistance was not achieved and 1 test failed by yielding (12mmx5mm Steel). However for comparison purposes, all the results are used. Note that

the bonded length was limited by the dimensions of concrete prism available for the test which was design to suit the test rig.

Table 4.3.4: Summary of additional test.

Specimen	d_p (mm)	b_p (mm)	Material	E_p (MPa)	*fc* (MPa)	df/bf
12x12	12.00	12.00	Steel	183044	36.7	0.93
12x12	12.00	12.00	CFRP	131566	36.7	0.93
*12x12	12.00	12.00	Aluminium	63819	36.7	0.93
*12x3	12.37	2.76	CFRP	146348	36.7	2.81
*12x4	12.47	4.24	CFRP	134467	36.7	2.16
*12x6	12.35	5.73	CFRP	130489	36.7	1.73
*24x4	24.06	4.33	CFRP	141434	36.7	3.96
30x7	30.60	7.3	CFRP	134562	36.7	3.40
12x5	12.00	5.00	Steel	195494	36.7	1.86
26x20	25.26	20.6	CFRP	129837	36.7	1.16
12x30	12.01	30.75	CFRP	135113	36.7	0.40
12x50	12.19	50.33	CFRP	132761	36.7	0.25
12x60	11.74	61.03	CFRP	126511	36.7	0.20
12x70	11.93	71.25	CFRP	135810	36.7	0.18
12x80	12.28	81.02	CFRP	137139	36.7	0.16
12x100	12.30	101.08	CFRP	135000	36.7	0.13

It was also found that the higher rigidity of the plates in the current test made the specimens more sensitive to misalignment. Although only slight bending occurred when the pull tests were done, this had a significant effect on the ultimate load (P_{IC}). For example, from the pull test of CFRP plate 26mm x 20mm, the deflection (ϕ) was 3.85 x 10^{-5} mm which is much less than the 12mm x 30mm test which was 5.83 x 10^{-5} mm. This explains why in experiment 12mm x 30mm specimen fail earlier than the predicted value, although both were not considered in generating $\tau_f \delta_f$ equation due to lack of bond length. In the next section, with all the available additional data, the generic equation was reanalysing again.

4.3.1.9 Reanalyse data

Adding the wet lay up plates to the database and the additional tests data, the generic equation is now reanalysed with a total of 87 data point (Appendix I Table A1, A2 and A3) covering the range of values summarised in Table 4.3.5. The analysis begins by using an optimisation method and by fixing y = 1mm on the first iteration it was found that y = 0.9 mm gives the lowest coefficient of variance. This was determined when using $fc^{0.65}$ (Eq.

4.3.10). After completing four iteration, the final value of x and y from this analysis was x = 1mm and y = 0.9mm (Figure 4.3.11). For convenience, the final value for x and y at this stage was selected to be 1, which it not much different than the earlier assumption that x and y was equal to 2, the difference is now that it is proven by optimization method. Another parameter that needs to be quantified again is the contribution of the concrete compressive strength and each individual analysis was done shown in Figures 4.3.12 and 4.3.13.

Table 4.3.5: Range of parameters considered.

	Max	Min
Plate Depth (d_p)	30.6 mm	0.2 mm
Plate Width (b_p)	100 mm	1.2 mm
Bond Length (L)	800 mm	85 mm
Plate Young's Modulus (E)	256000 MPa	22500 MPa
Concrete Strength (*fc'*)	69.1 MPa	18.9 MPa
df/bf	6.59	0.0098

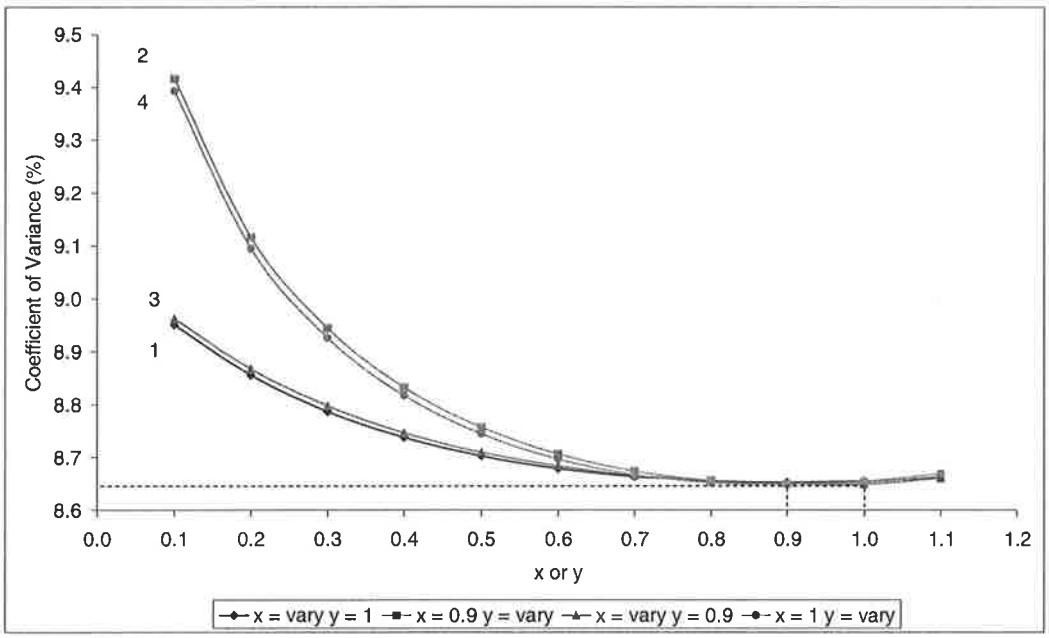

Figure 4.3.11: Coefficient of Variance of Pexp/Pcal from optimisation to obtaining x and y value.

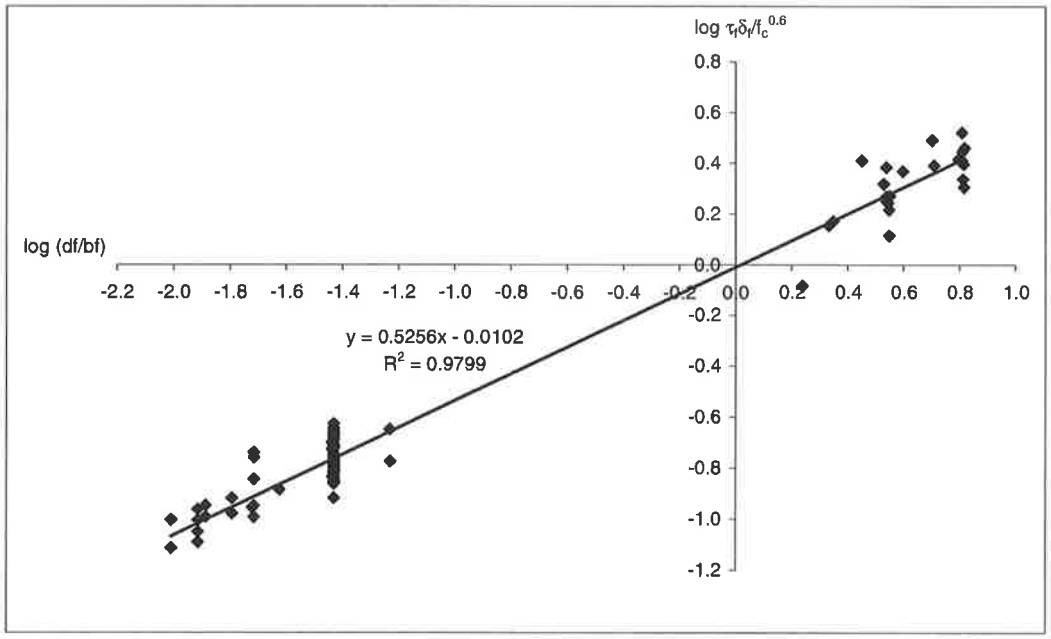

Figure 4.3.12: Linear Regression Analysis for $f_c^{0.6}$ with x=1 and y=1.

The linear regression for $f_c^{0.6}$

$$\tau_f \delta_f = 0.98 \left(\frac{d_f}{b_f} \right)^{0.525} f_c^{0.6} \tag{4.3.13}$$

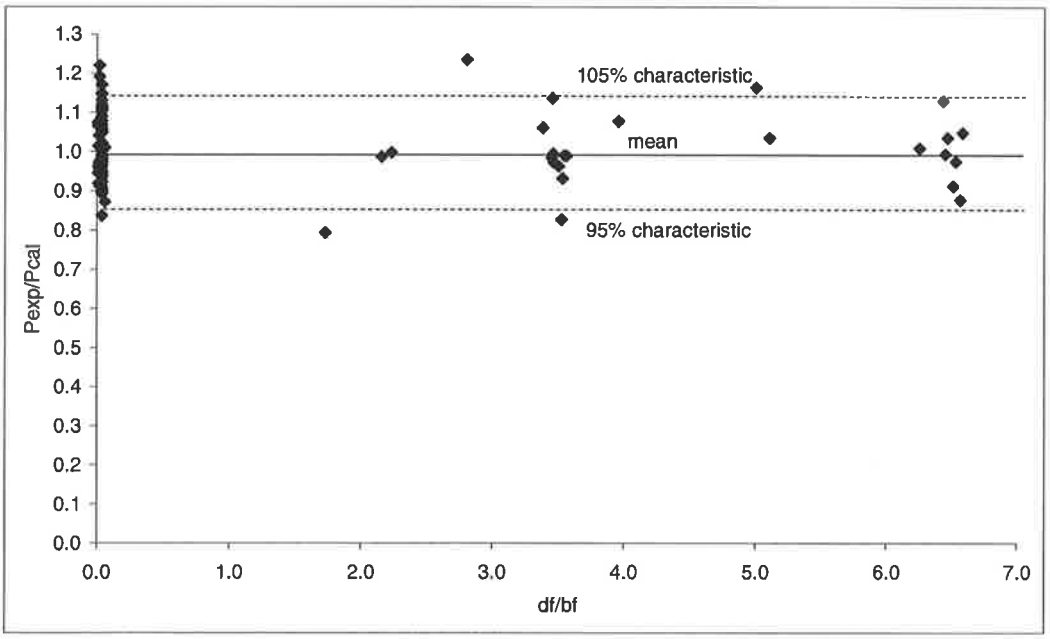

Figure 4.3.13: Comparison between experiment and the calculated value for $f_c^{0.6}$.

Repeating the analysis by comparing the Coefficient of Variance from the analysis done in section 4.3.1.6, it is clear that from the summary of analysis in Table 4.3.6 and Figure 4.3.14, $f_c^{0.6}$ is the appropriate value for the contribution of concrete strength giving the equation,

$$\tau_f \delta_f = 0.98 \left(\frac{d_f}{b_f} \right)^{0.525} f_c^{0.6} \tag{4.3.14}$$

with 95 percentile lower and upper bounds given by,

$$\tau_f \delta_f = 0.859 \left(0.98 \left(\frac{d_f}{b_f} \right)^{0.525} f_c^{0.6} \right) \quad \text{lower bound} \tag{4.3.15}$$

$$\tau_f \delta_f = 1.141 \left(0.98 \left(\frac{d_f}{b_f} \right)^{0.525} f_c^{0.6} \right) \quad \text{upper bound} \tag{4.3.16}$$

This final equation (Eq. 4.3.14) gives good correlation with the experiment shown in Figures 4.3.15 and 4.3.16 with the additional test data included. Although the results with insufficient bond length were not included in deriving Eq. 4.3.14, it still demonstrates that this model works for any type of plate, orientation and dimension. It is worth noting that in Figures 4.3.15 and 4.3.16, as $L < L_e$, the results fall below the mean line as the maximum resistance was not achieved.

Table 4.3.6: Summary of the all the analysis with various exponent of f_c.

		Pexp/Pcal		
f_c^{α}	Linear regression	Mean	Standard Deviation	Coefficient Of Variance (%)
f_c^{0}	$\tau_f \delta_f = 8.25 \left(\frac{d_f}{b_f} \right)^{0.57} f_c^{0}$	1.011	0.155	15.364
$f_c^{0.125}$	$\tau_f \delta_f = 5.29 \left(\frac{d_f}{b_f} \right)^{0.558} f_c^{0.125}$	1.009	0.113	13.223
$f_c^{0.25}$	$\tau_f \delta_f = 3.39 \left(\frac{d_f}{b_f} \right)^{0.55} f_c^{0.25}$	1.007	0.114	11.371

		Pexp/Pcal		
f_c^{α}	Linear regression	Mean	Standard Deviation	Coefficient Of Variance (%)
$f_c^{0.375}$	$_f\delta_f = 2.17\left(\frac{d_f}{b_f}\right)^{0.54} f_c^{0.375}$	1.005	0.100	9.909
$f_c^{0.5}$	$\tau_f\delta_f = 1.39\left(\frac{d_f}{b_f}\right)^{0.53} f_c^{0.5}$	1.005	0.090	8.964
$f_c^{0.6}$	$\tau_f\delta_f = 0.98\left(\frac{d_f}{b_f}\right)^{0.525} f_c^{0.6}$	1.004	0.087	8.654
$f_c^{0.65}$	$\tau_f\delta_f = 0.817\left(\frac{d_f}{b_f}\right)^{0.522} f_c^{0.65}$	1.004	0.087	8.655
$f_c^{0.7}$	$\tau_f\delta_f = 0.68\left(\frac{d_f}{b_f}\right)^{0.519} f_c^{0.7}$	1.007	0.088	8.757
$f_c^{0.8}$	$\tau_f\delta_f = 0.48\left(\frac{d_f}{b_f}\right)^{0.512} f_c^{0.8}$	1.005	0.093	9.231
$f_c^{0.9}$	$\tau_f\delta_f = 0.335\left(\frac{d_f}{b_f}\right)^{0.505} f_c^{0.9}$	1.005	0.100	10.001

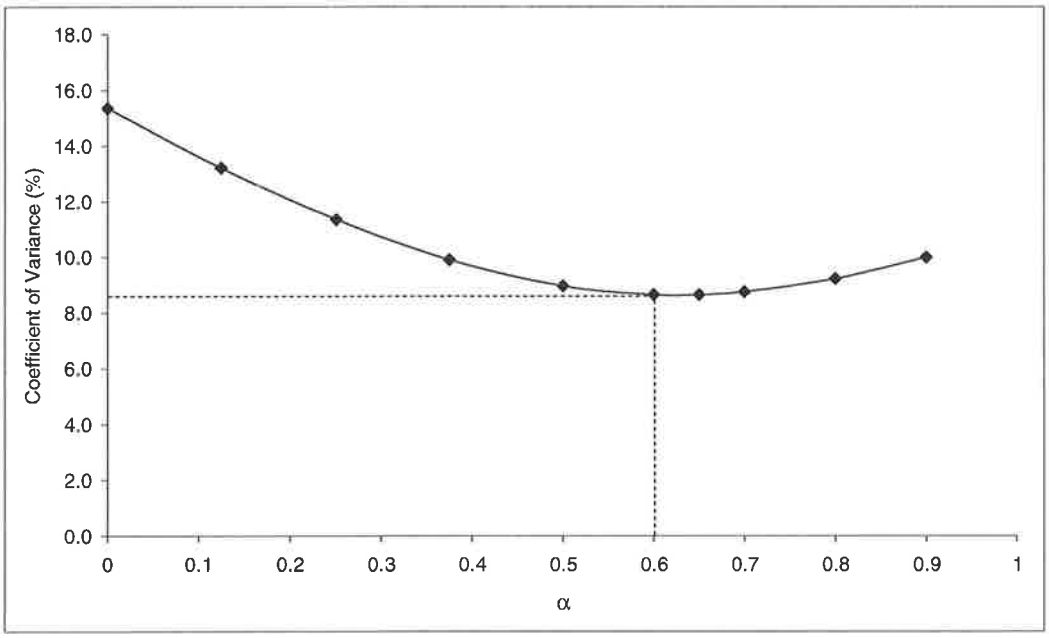

Figure 4.3.14: Exponent of f_c by comparison of Coefficient of Variance Pexp/Pcal.

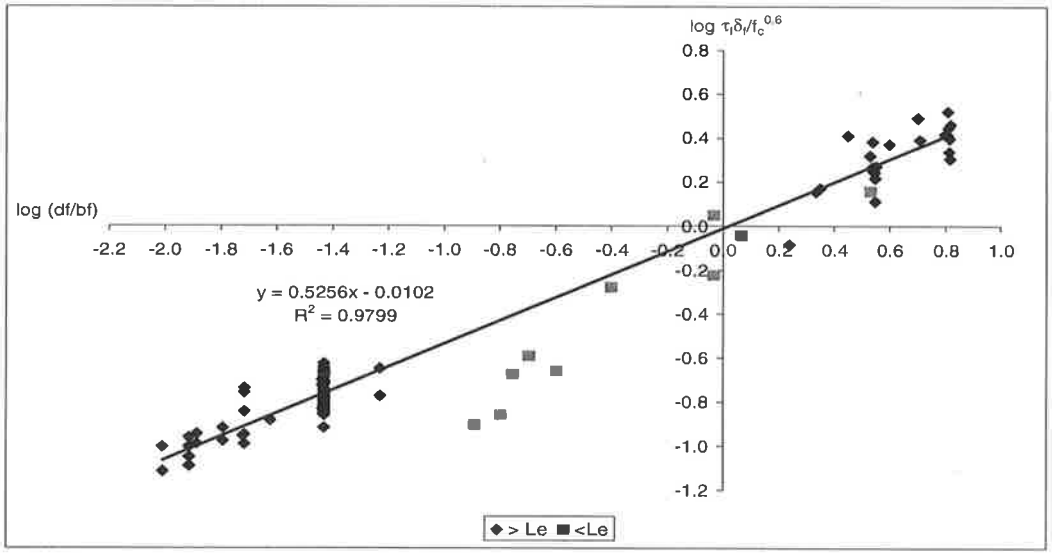

Figure 4.3.15: Linear Regression Analysis including the wet lay up and additional test.

Varying x and y in Figure 4.3.17 demonstrates that does not effect $\tau_f\delta_f$ significantly. The primary effect is to simply shift the data horizontally as the d_f/b_f ratio changes. Figure 4.3.17 also demonstrates that by varying y, it has more effect on EB and x on NSM. Similar R^2 values proving that the earlier assumption (x and y = 2, Figure 4.3.7) was acceptable in predicting the failure load. This ends this whole part of analysis for quantifying the failure plane and fracture energy equation which is Eq. 4.3.14. Next the peak shear stress (τ_f) equation, slip capacity (δ_f) equation and comparison Eq. 4.2.7 with published method is discussed.

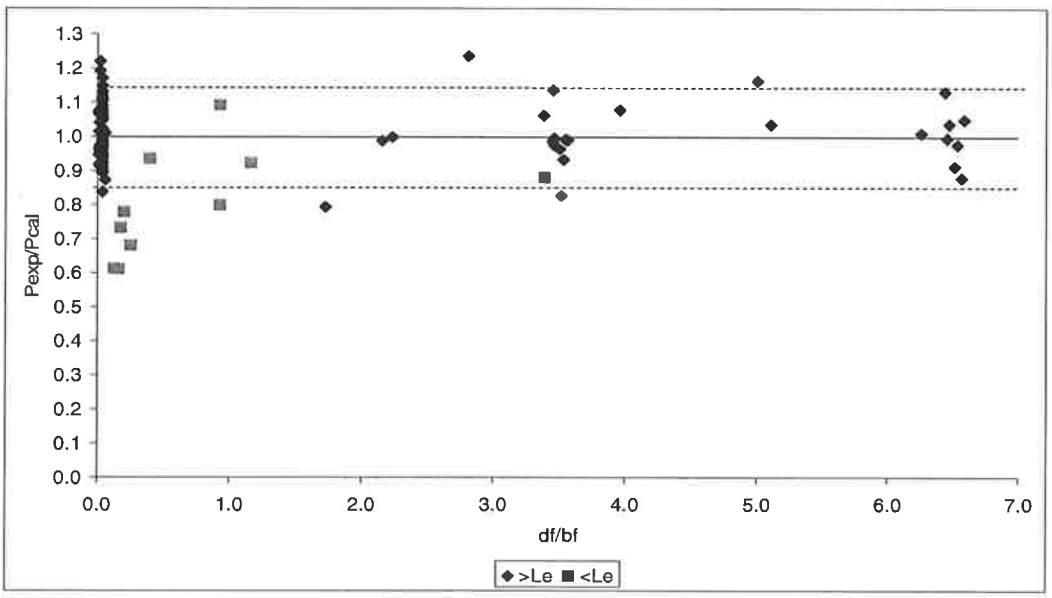

Figure 4.3.16: Comparison between experiment and the calculated value for all data.

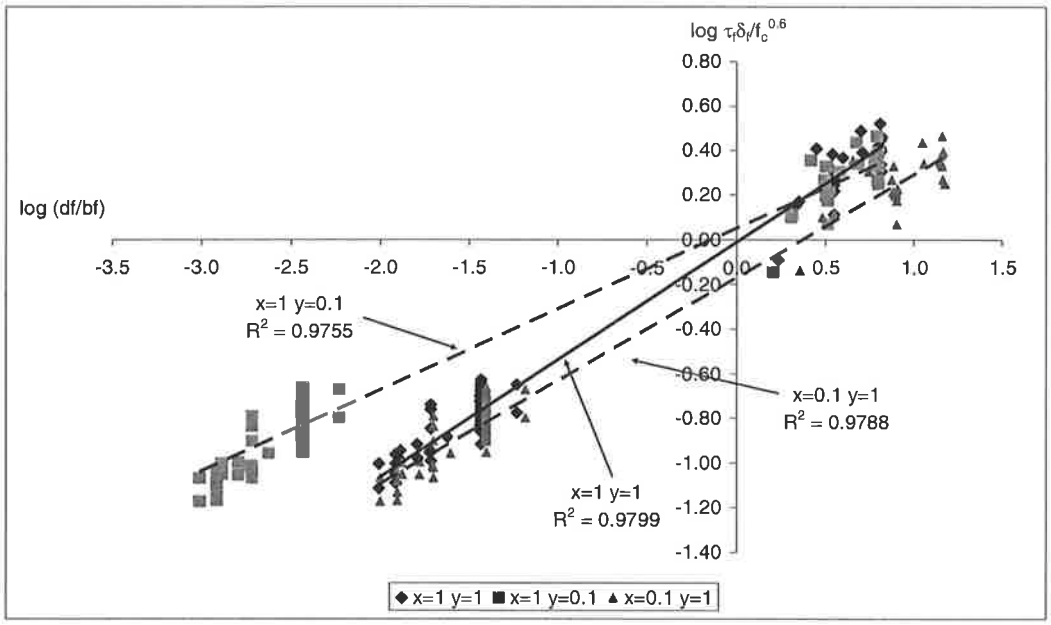

Figure 4.3.17: Effect of x and y values towards the fracture energy.

4.4 Peak Shear Stress Capacity (τ_f)

Another important factor is the shear stress acting on the plate and concrete interface. After all the analysis done on $\tau_f\delta_f$ in the previous section (section 4.3), τ_f is required in Eq. 4.2.6 to know the effective length Eq. 4.2.5. Knowing τ_f will also give the slip (δ_f) at failure load by dividing $\tau_f\delta_f$ with τ_f. Reason of selecting τ_f to instead of δ_f is due to δ_f is rarely recorded in the literature, only τ_f may be quantified with a reasonable degree of certainty. Again in this analysis the lowest Coefficient of Variance from τ_{exp}/τ_{cal} analysis will give the most appropriate or suitable equation.

The data available for this analysis is presented in Appendix J Table B1. The data were then analysed individually as Figures 4.4.1 and 4.4.2 which is consisting of 22 pull tests results. The majority of these results are from NSM published pull tests with only 1 from EB plate pull test. This is because not many published experiments measuring the peak shear stress (τ_f) directly.

The graph in Figure 4.4.3 was plotted using equation obtained from individual regression analysis by changing the f_c exponent and it is showing that f_c with exponent of 0.6 is with the lowest C.O.V and thus giving the suitable equation as Eq. 4.4.1.

$$\tau_f = \left(0.8 + 0.078\frac{d_f}{b_f}\right) fc^{0.6} \tag{4.4.1}$$

As for design purpose, lower bound and upper equation are needed and it is shown in Eq. 4.4.2 and Eq. 4.4.3.

$$\tau_f = \left(0.65 + 0.063\frac{d_f}{b_f}\right) fc^{0.6} \quad \text{Lower Bound} \tag{4.4.2}$$

$$\tau_f = \left(0.94 + 0.092\frac{d_f}{b_f}\right) fc^{0.6} \quad \text{Upper Bound} \tag{4.4.3}$$

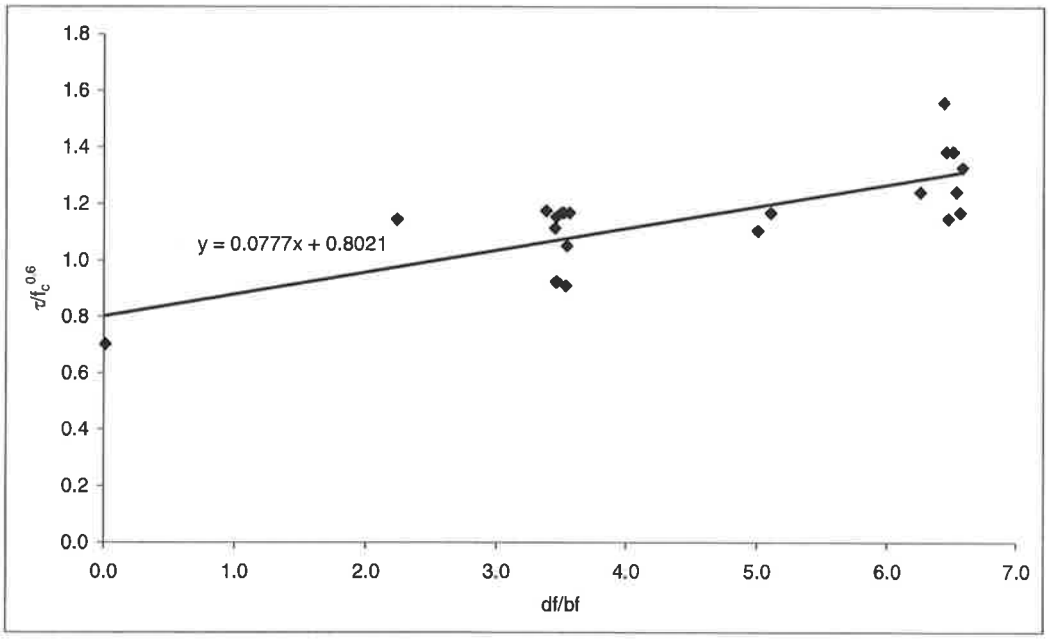

Figure 4.4.1: Linear Regression Analysis for $f_c^{0.6}$ with x=1 and y=1.

The linear regression for $f_c^{0.6}$

$$\tau_f = \left(0.8 + 0.078\left(\frac{d_f}{b_f}\right)\right) f_c^{0.6} \tag{4.4.4}$$

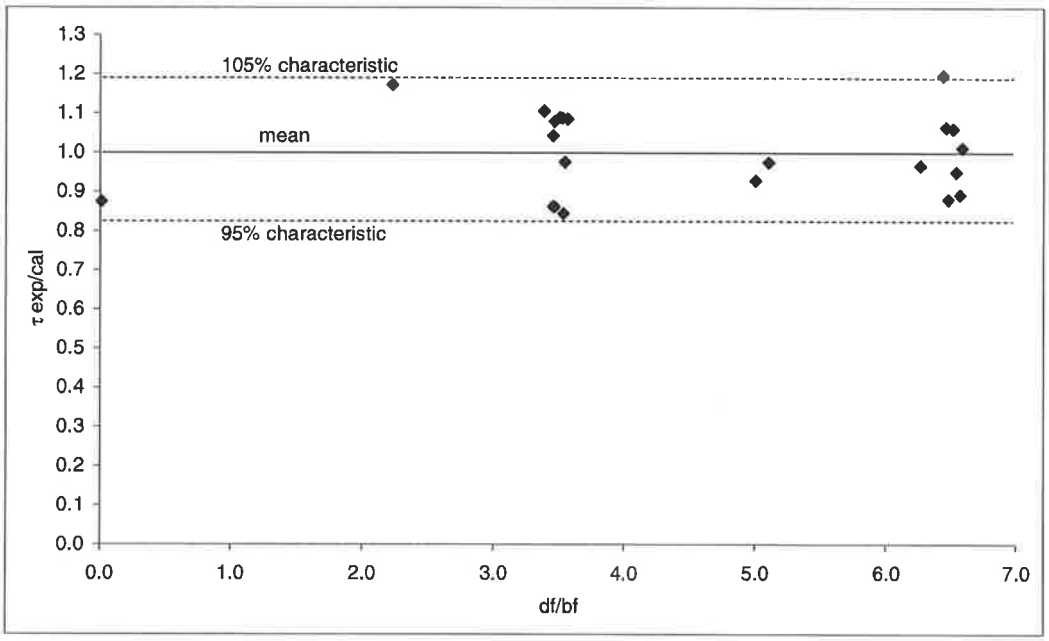

Figure 4.4.2: Comparison between experiment and the calculated value for $f_c^{0.6}$.

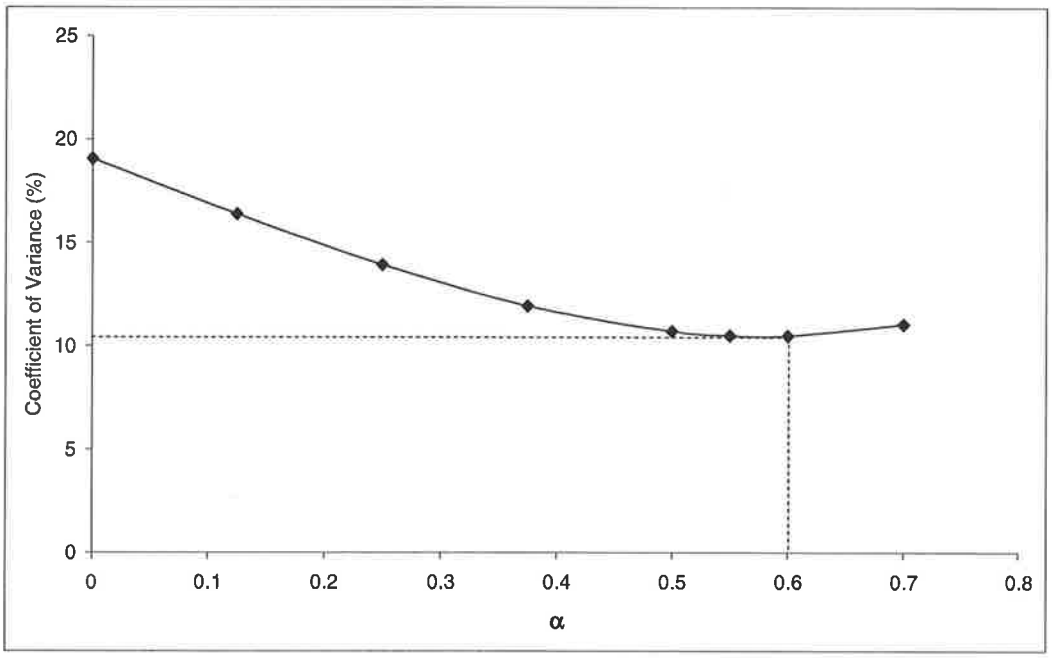

Figure 4.4.3: Exponent of f_c by comparison of C.O.V.

Table 4.4.1: Summary of the all the analysis with various exponent of f_c.

		Pexp/Pcal		
f_c^{α}	Linear regression	Mean	Standard Deviation	Coefficient Of Variance (%)
f_c^{0}	$\tau_f = \left(8.10 + 0.654\left(\frac{d_f}{b_f}\right)\right) f_c^{\,0}$	1.000	0.191	19.076
$f_c^{0.125}$	$\tau_f = \left(4.99 + 0.421\left(\frac{d_f}{b_f}\right)\right) f_c^{)0.125}$	1.000	0.164	16.382
$f_c^{0.25}$	$\tau_f = \left(3.08 + 0.27\left(\frac{d_f}{b_f}\right)\right) f_c^{\,0.25}$	1.000	0.139	13.935
$f_c^{0.375}$	$\tau_f = \left(1.9 + 0.17\left(\frac{d_f}{b_f}\right)\right) f_c^{\,0.375}$	1.000	0.119	11.941
$f_c^{0.5}$	$\tau_f = \left(1.18 + 0.11\left(\frac{d_f}{b_f}\right)\right) f_c^{\,0.5}$	1.000	0.107	10.712
$f_c^{0.55}$	$\tau_f = \left(0.97 + 0.09\left(\frac{d_f}{b_f}\right)\right) f_c^{\,0.55}$	1.000	0.105	10.511
$f_c^{0.6}$	$\tau_f = \left(0.8 + 0.078\left(\frac{d_f}{b_f}\right)\right) f_c^{\,0.6}$	1.000	0.105	10.500
$f_c^{0.7}$	$\tau_f = \left(0.55 + 0.05\left(\frac{d_f}{b_f}\right)\right) f_c^{\,0.7}$	1.000	0.110	11.049

Obtaining the peak shear stress equation; concluded this section of analysis for quantifying the peak shear stress and in the next section, the slip capacity is quantified

4.5 Slip Capacity τ_f

To obtain the slip capacity equation, simply use Eq. 4.23 and divided it with Eq. 4.26 giving the following

$$\delta_f = \frac{0.98\left(\frac{d_f}{b_f}\right)^{0.525}}{0.802 + 0.078\left(\frac{d_f}{b_f}\right)} \qquad (4.5.1)$$

and it is worth noting that Eq. 4.5.1 (mean equation) is in mm without the function of the concrete strength f_c as it cancels out making it more reasonable and acceptable as slip has no relation with concrete strength. With equation for τ_f and δ_f obtained, L_{crit} (Eq. 4.2.5) can be calculated. Next comparison of the generic equation (Eq. 4.2.7) with published method.

4.6 Comparison with publish method.

The generic equation presented is now compared with other methods. There is no other published model currently exists that can be use for both EB and NSM retrofitting techniques. The only other model currently published that gives the IC debonding resistance of NSM strips is that of Blaschko (2003). The data used to derive Balschko's model consisted predominately of adhesive failures, the model only considers adhesive properties and hence, is also not applicable.

Therefore, the current model can only be compared with those available for EB plates. Of these, the well-known bond strength model of Chen and Teng (2002), given by the following expression, is used in the comparison as it has recently been identified as the most accurate one by Lu *et al.* (2005). Using the values obtain in the analysis, the generic equation for debonding resistance is given by the following expression

$$P_{IC} = \eta 0.85 \frac{d_f}{b_f}^{0.25} f_c^{0.33} \sqrt{L_{per}(EA)_p} < \begin{cases} f_{rupt} A_p & \textit{for FRP plates} \\ f_y A_p & \textit{for metallic plates} \end{cases} \quad (4.6.1)$$

where units of Newtons and millimeters are used, f_{rupt} is the rupture stress of an FRP plate, f_y is the yield stress of a metallic plate and

$$\eta = \begin{cases} 1.0 & \textit{mean} \\ 0.85 & \textit{characteristic} \end{cases} \quad (4.6.2)$$

4.6.1 Chen and Teng's Approach

Chen and Teng's equation for IC debonding of a pull test as given:

$$\sigma_{IC} = \eta\beta_p\beta_L\sqrt{\frac{E_p\sqrt{f_c}}{t_p}} \tag{4.6.3}$$

where

$$\eta = \begin{cases} 0.427 & mean \\ 0.315 & characteristic \end{cases}$$

$$\beta_p = \sqrt{\frac{2-(b_p/b_c)}{1+(b_p/b_c)}} \tag{4.6.4}$$

$$\beta_L = \begin{cases} 1 & if\ L \geq L_e \\ \sin \pi L/2L_e & if\ L < L_e \end{cases} \tag{4.6.5}$$

where β_p allows for the width of the plate relative to the width of the concrete element and β_L allows for bond lengths less than L_e. The full anchorage length or effective length is given by

$$L_e = \sqrt{\frac{E_p t_p}{\sqrt{f_c}}} \qquad \text{[N and mm]} \tag{4.6.6}$$

where P_{IC} for Chen and Teng's method is as given below

$$P_{IC} = \eta\beta_p\beta_L\sqrt{f_c}b_p L_{crit} \tag{4.6.7}$$

Comparison P_{IC} with P_{exp} using the mean value of Eq. 4.6.1 and Eq. 4.6.7 for EB plates is shown in Figure 4.6.1. The mean using the generic equation (Eq. 4.31) has a mean of 1.004 and standard deviation of 0.091, and is slightly better than Chen and Teng's model (Eq. 4.6.7), which has a mean and standard deviation of 1.016 and 0.103. Meanwhile, comparison using characteristic value is shown in Figure 4.6.2 where the generic equation (Eq. 4.6.1) is also giving a better mean and standard deviation of 1.006 and 0.089 compared to Chen and

Teng's model (Eq. 4.6.7), 1.016 and 0.103. This shows that the generic equation is gives a better prediction compared to Chen and Teng's model.

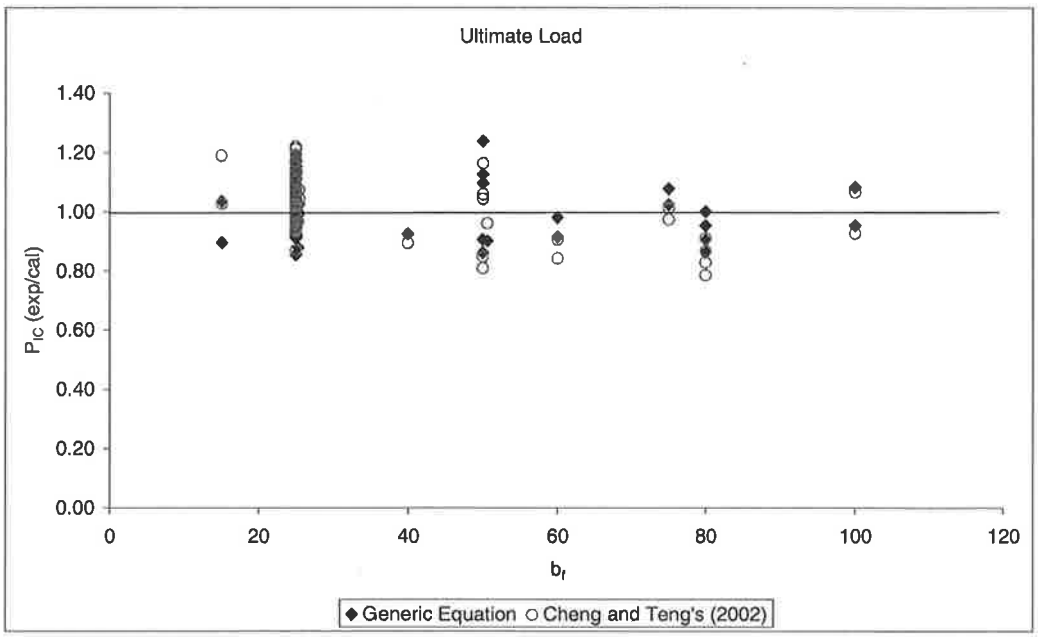

Figure 4.6.1: Comparison for calculating P_{IC} with mean value.

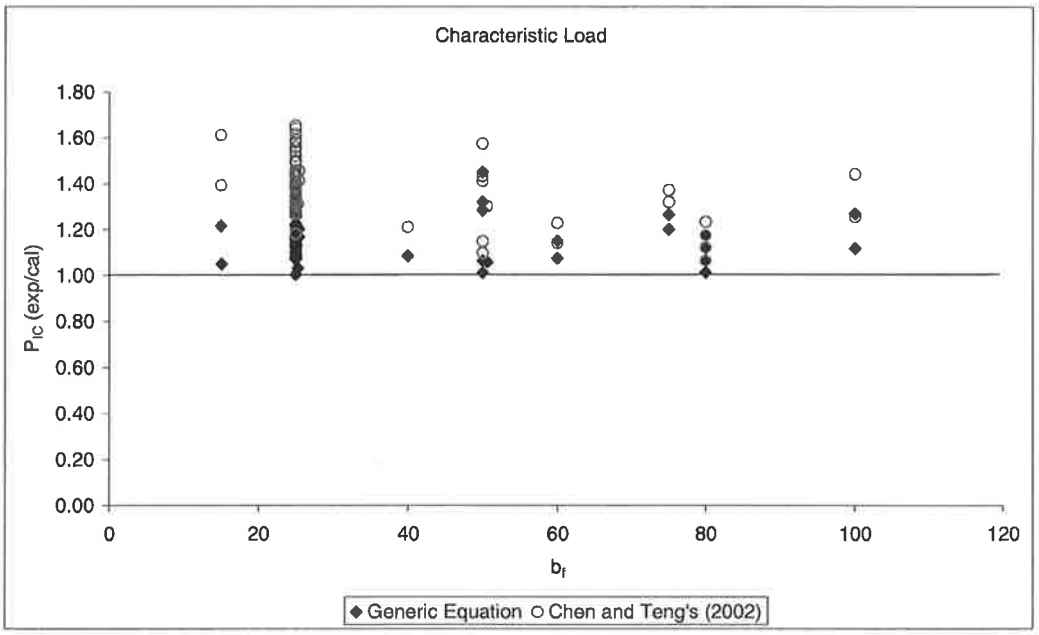

Figure 4.6.2: Comparison for calculating P_{IC} with mean value.

4.7 Conclusion

It is worth mentioning that this finding is the first of it kind, combining EB plates and NSM plates in one equation. The model is only a function of geometric and material properties and is applicable to any type of plate material. It is derived using an idealized linear softening bond-slip model and is a function of: the aspect ratio d_f/b_f of the interface debonding crack, which is a measure of the confinement effect of the cover concrete; the concrete compressive strength; and the axial rigidity of the plate alone.

Finally, the generic equation is validated by comparison with existing push-pull data, 14 new push-pull tests and a well-known existing model which is Chen and Teng's (2002). An empirical model for the fundamental bond-slip relationship, suitable for use in numerical simulations, is also presented.

4.8 Notation

EB	Externally Bonded
NSM	Near Surface Mounted
IC	Intermediate Crack
τ	Shear capacity
δ	Slip capacity
$\frac{d^2\delta}{dx}$	Double differential of slip capacity
J	Geometry of the debonding interface
$f(\delta)$	Slip function
τ_f	Maximum shear capacity
δ_0	Slip at maximum shear capacity
δ_f	Maximum slip
τ/δ	Shear slip relationships
$\tau_f \delta_f$	Fracture energy
$(EA)_p$	Plate axial rigidity
$(EA)_c$	Concrete axial rigidity
P_{IC}	Intermediate crack debonding resistance
L_{per}	Failure plane perimeter
L_{crit}	Critical Bond length
b_p	Plate width
x	Failure plane in x direction
y	Failure plane in y direction
d_p	Plate depth
f_c	Concrete compressive strength
m	Linear regression best fit line slope value
C	Linear regression best fit line interception on y axis value
P_{exp}	Experiment intermediate crack debonding resistance
d_f	Failure plane depth
b_f	Failure plane width
f_{ct}/f_t	Concrete tensile strength
P_{cal}	Calculated intermediate crack debonding resistance
$C.O.V$	Coefficient of variance
α	Exponent of concrete compressive strength
E_{fiber}	Fiber Young's Modulus
A_{resin}	Resin area
E_p	Plate Young's Modulus
ϕ	Deflection
R^2	Coefficient of determination
σ_{IC}	Intermediate crack debonding stress
ε_{IC}	Intermediate crack debonding strain
t_{frp}	Composite Fiber reinforced polymer thickness
t_{fiber}	Fiber reinforce polymer sheets thickness
$t_{adhesive}$	Adhesive thickness

4.9 References

1. Australian Standard : Concrete Structures (AS3600-2001) (2001). Australia: 176.

2. Blaschko, M. (2003). Bond behaviour of CFRP strips glued into slits. Proceeding 6th International Symposioum on FRPRCS., Singapore.

3. Chajes, M. J., Finch, W. W. J., Januszka, T. F. and Thomson, T. A. J. (1996). "Bond and Force Transfrer of Composite Material Plates Bonded to Concrete." ACI Structural Journal **93**(2): 295-303.

4. Hassan, T. and Rizkalla, S. (2003). "Investigation of bond in concrete structures strengthened with near surface mounted carbon fiber reinforced polymer strips." Journal of Composites for Construction **7**(3): 248-257.

5. Ing, L. K., Jones, N., Page, M. and Ward, S. (2004). Intermediate Crack Debonding of Near Surface Mounted Strips. Adelaide, University of Adelaide: 91.

6. Mohamed Ali, M. S., Oehlers, D. J. and Seracino, R. (2006). "Vertical shear interaction model between external FRP transverse plates and internal steel stirrups." Engineering Structures **28**(pp 381-389).

7. Page, M., Seracino, R., Jones, N., Ali and Oehlers, D. J. (2005). "Interfacial Stress Transfer of Near-Surface Mounted FRP-to-concrete Joints." In Preparation for Journal Publication.

8. Seracino, R., Page, M. W., Mohamed Ali, M. S., Jones, N. M. and Oehlers, D. J. (2005). "Interfacial stress transfer of near surface mounted FRP-to-concrete joints." Submitted to Advances in Structural Engineering.

9. Taljsten, B. (1997). "Defining anchor lengths of steel and CFRP plates bonded to concrete." Adhesion and Adhesive **17**(4): 319327.

10. Teng, J. G. and Chen, J. F. (2001). "Anchorage Strength Models for FRP and Steel Plates Bonded to Concrete." Journal of Structural Engineering **127**(7): 784-791.

11. Teng, J. G., Chen, J. F. and Smith, S. T. (2002). FRP Strengthened RC Structures. England, John Wiley & Sons, Ltd.

12. Yao, J., Teng, J. G. and Chen, J. F. (2005). "Experimental study on FRP-to-concrete bonded joints." Composite **B**(36): 99-113.

13. Yuan, H., Teng, J. G., Seracino, R., Wu, Z. S. and Yao, J. (2004). "Full-Range behavior of FRP-to-concrete bonded joints." Engineering Structures **26(5)**: 553-565.

Chapter

5 PULL TEST – UNDERSTANDING PLATE AND COVER INTERACTION

5.1 Introduction

Chapter 3 generally focused on pull test experiments on single NSM plates with various plate materials that were used to quantify the generic debonding resistance of an individual plate in Chapter 4. In this chapter, all the experiments are looking into adapting the generic equation in Chapter 4 to allow for the interaction between pairs of plates and the interaction of the plate with cover for NSM plates.

This chapter covers the description of the specimens, the test set-up and the material properties. Then, the observations from each individual test are described. Finally, the conclusions made from all the test results are discussed.

5.2 Specimen Geometries

All the pull tests done were divided into two series of pull tests. The first series of pull test is for the interaction between pairs of plates and the second series is on the interaction of plates with cover for NSM plates.

Referring to Figure 5.2.1 and Figure 5.2.2, the plates dimension depends on plate orientation. For the NSM orientation Figure 5.2.1, the plate dimension is 20 mm depth (d_p) x 1.4 mm width (b_p) meanwhile for the EB orientation it is with 1.4 mm depth (d_p) x 20 mm width (b_p). The plates were place symmetrically about the centre line.

The concrete block used in the first series is with dimensions of 350 mm x 300 mm x 180 mm (height x width x thickness) as shown in Figure 5.2.1 for NSM plates and in Figure 5.2.2 for EB plates. The gaps between plates were measured from the inner sides of the plates as shown. In this chapter, Plate A is referred to as the plate on the left meanwhile plate B is on the right. A summary of pull test series 1, consisting of 10 pull tests, is shown in Table 5.2.1.

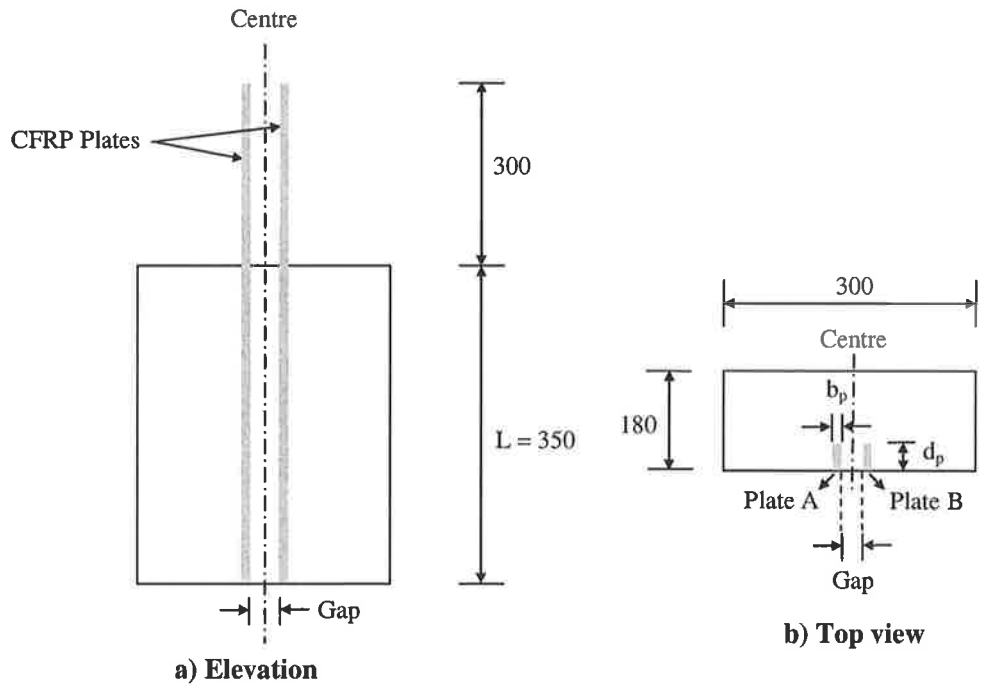

Figure 5.2.1: Series 1: Typical specimens dimension for NSM interaction pull tests.

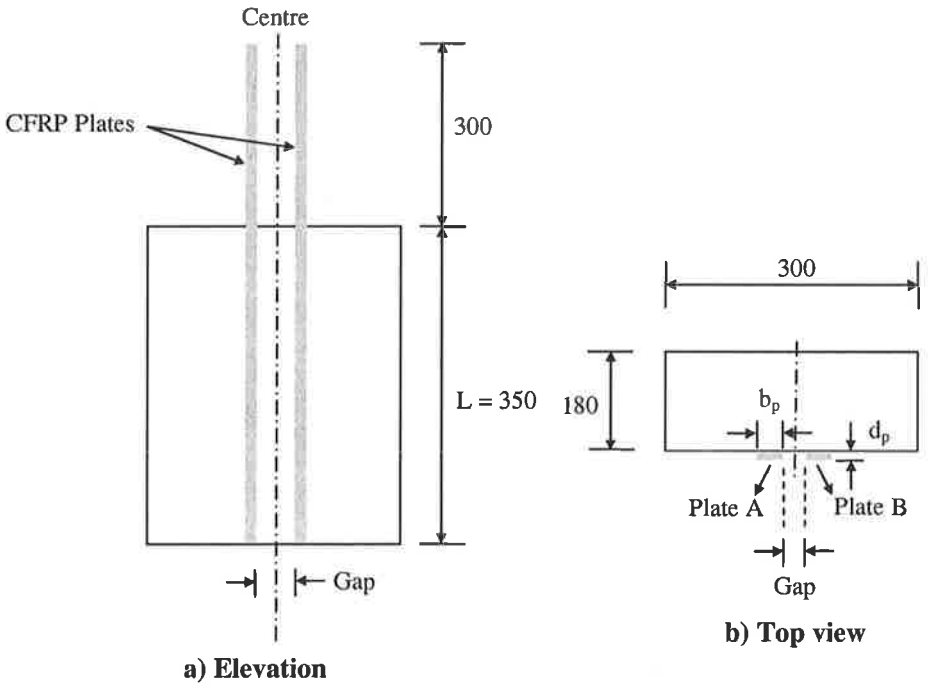

Figure 5.2.2: Series 1: Typical specimens dimension for EB interaction pull tests.

Table 5.2.1: Series 1 Pull test: Interaction between pairs of plates.

Test	Gap (mm)	Plate A		Plate B		Materials	Type of Plating	L (mm)
		d_p (mm)	b_p (mm)	d_p (mm)	b_p (mm)			
G0NSM	-	20	1.2	-	-	CFRP	NSM	350
G30NSM	30	20	1.2	20	1.2	CFRP	NSM	350
G40NSM	40	20	1.2	20	1.2	CFRP	NSM	350
G50NSM	50	20	1.2	20	1.2	CFRP	NSM	350
G70NSM	70	20	1.2	20	1.2	CFRP	NSM	350
G0EB	-	1.2	20	-	-	CFRP	EB	350
G30EB	30	1.2	20	1.2	20	CFRP	EB	350
G40EB	40	1.2	20	1.2	20	CFRP	EB	350
G50EB	50	1.2	20	1.2	20	CFRP	EB	350
G60EB	60	1.2	20	1.2	20	CFRP	EB	350

The same concrete block dimension was used in series 2 pull test (Figure 5.2.3). The plate distances for cover in series 2 were measured from the outer side of concrete block to the side of plates shown in Figure 5.2.3. In this series only NSM plate orientation were tested. A summary of the 11 pull tests in series 2, for the interaction with cover, are in Table 5.2.2. Next, the test setup for the entire pull test will be elaborated.

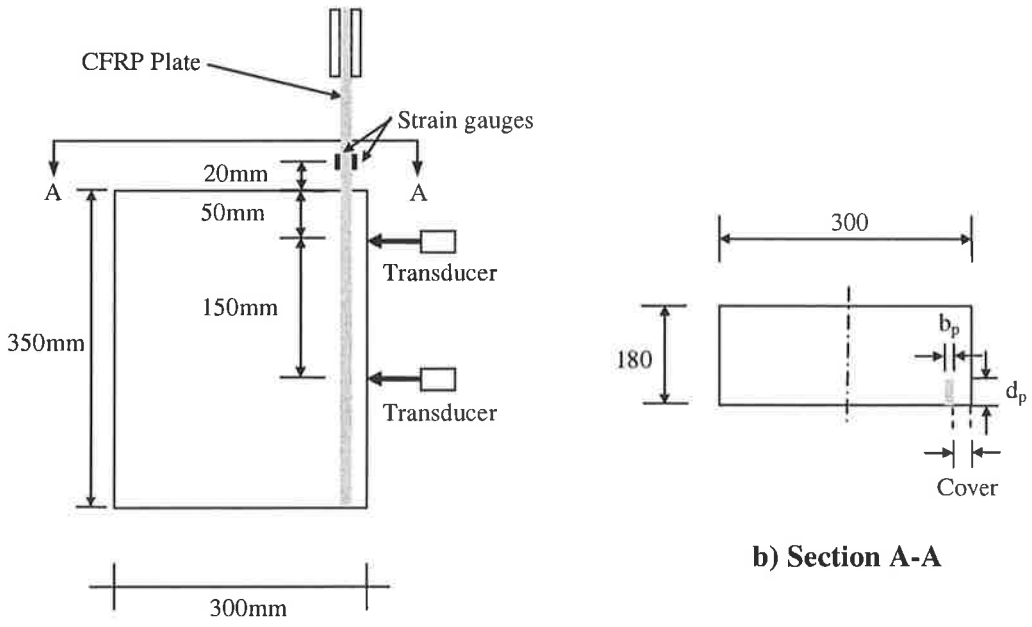

Figure 5.2.3: Series 2: Typical specimens dimension for cover interaction specimen.

Table 5.2.2: Series 2 Pull test: Interaction with covers.

		Plate				
Test	Cover	d_p (mm)	b_p (mm)	Materials	Type of Plating	L (mm)
C150NSMa	150mm	20	1.2	CFRP	NSM	350
C10NSMa	10 mm	20	1.2	CFRP	NSM	350
C20NSMa	20 mm	20	1.2	CFRP	NSM	350
C30NSMa	30 mm	20	1.2	CFRP	NSM	350
C40NSMa	40 mm	20	1.2	CFRP	NSM	350
C60NSMa	60 mm	20	1.2	CFRP	NSM	350
C85NSMa	85 mm	20	1.2	CFRP	NSM	350
C150NSMb	150 mm	40	2.4	CFRP	NSM	350
C50NSMb	50 mm	40	2.4	CFRP	NSM	350
C75NSMb	75 mm	40	2.4	CFRP	NSM	350
C100NSMb	100 mm	40	2.4	CFRP	NSM	350

5.3 Test Setup

The same test rig used in the earlier series of pull test (chapter 3) was again used for this series of pull test. All the specimens with two plates were placed in the rig as shown in Figure 5.3.1 and in Figure 5.3.2.

Three clamping methods were used in series 1 pull tests shown in Figure 5.2.1 and Figure 5.2.2. The first clamping method used for the NSM interaction test is shown in Figure 5.3.3(a) with details in Figure 5.3.4. However this method only worked for tests G30NSM and G40NSM but failed for test G50NSM due to insufficient bond at the grips. Additional plates were added on both outer sides to increase the bond at the grips (Figure 5.3.3(b)). The steel plate used for the grips was chosen to be 25 mm thick with 2.5mm clearance for the 20mm plate depths on each side to avoid the CFRP plates failing due to crushing cause by the testing rig clamping system. Details for second clamping method are shown in Figure 5.3.5.

In series 1, the third clamping method was for the EB interaction pull test (Figure 5.3.3(c)). Aluminum plates were used as the grips with the width vary according to the plates gap. Details for the third clamping method are shown in Figure 5.3.6.

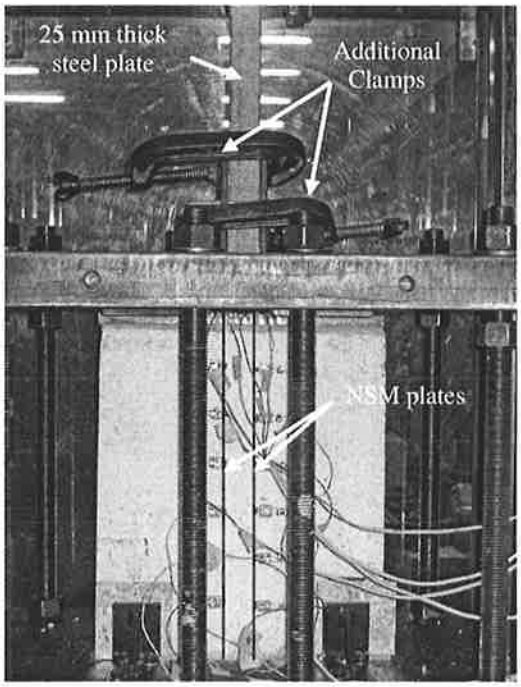

Figure 5.3.1: Test setup for series 1; interaction between NSM plates.

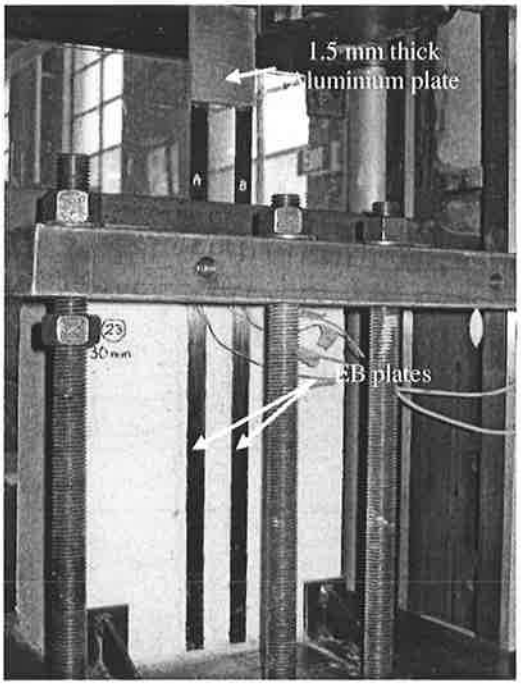

Figure 5.3.2: Test setup for series 1; interaction between EB plates.

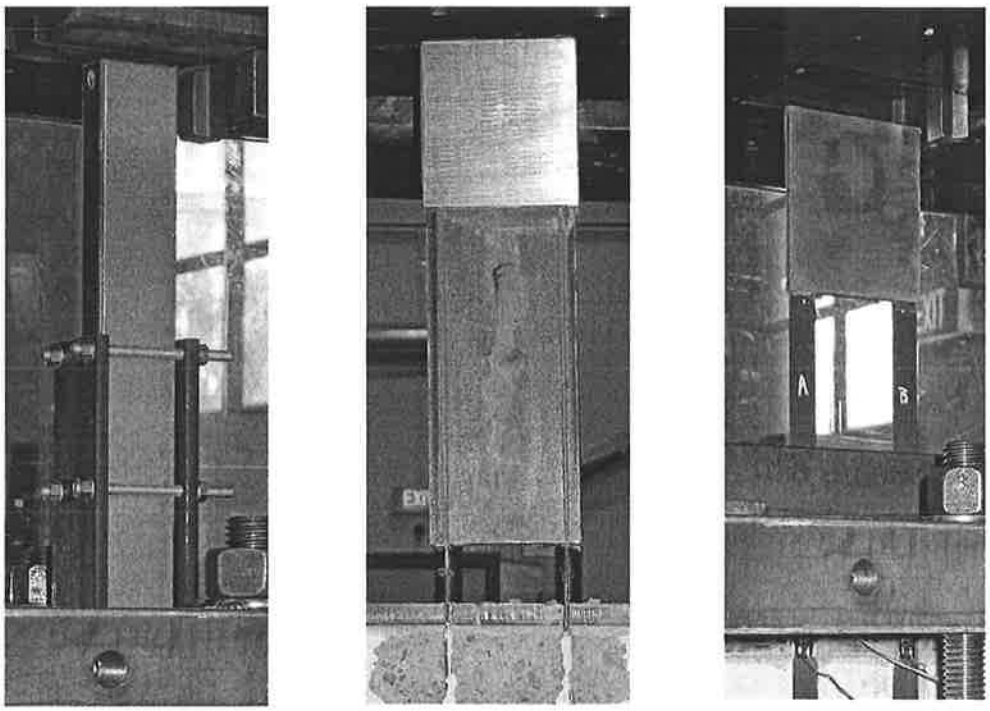

a) NSM clamping method for G30NSM and G40NSM plate gap.

b) Improved NSM clamping method for G50NSM and G70NSM plate gap.

c) Typical EB plate clamping method.

Figure 5.3.3: Clamping method for pull test series 1.

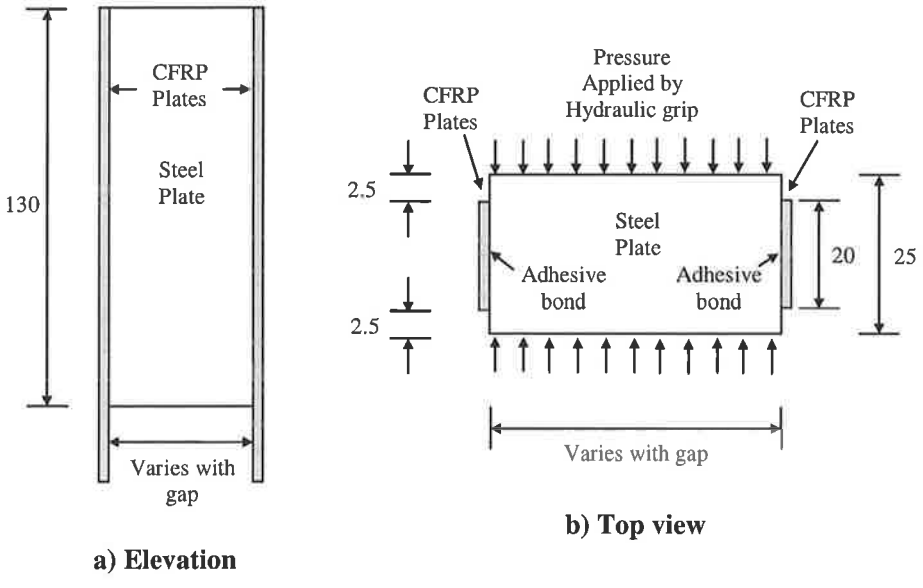

Note: All dimensions are in mm

Figure 5.3.4: Details for test G30NSM and G40NSM clamping method in series 1.

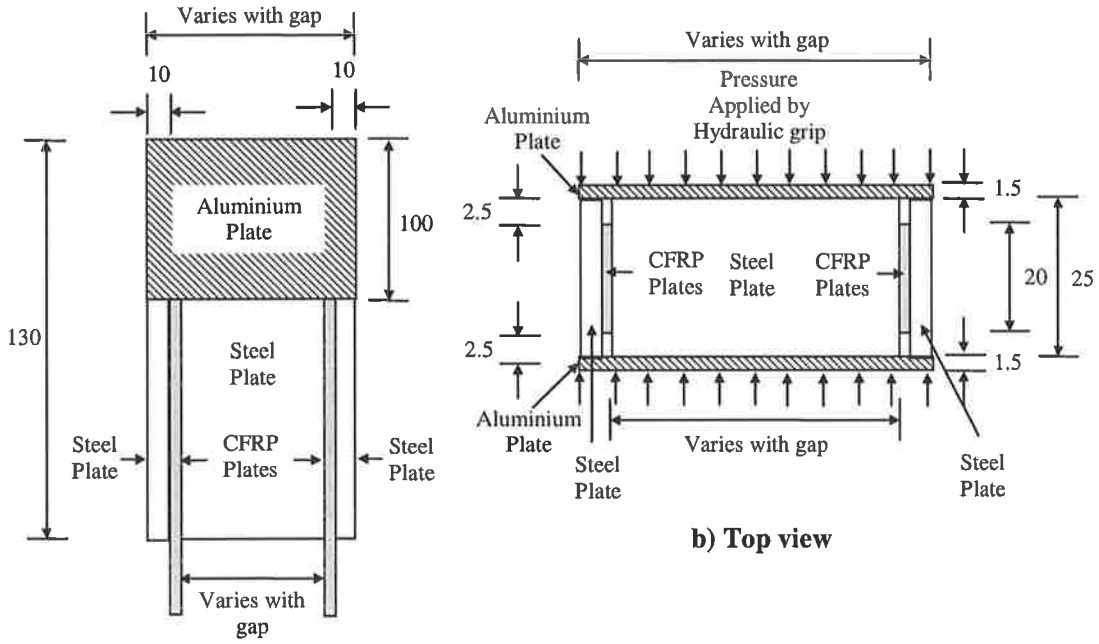

Note: All dimensions are in mm

Figure 5.3.5: Details for test G50NSM and G70NSM clamping method in series 1.

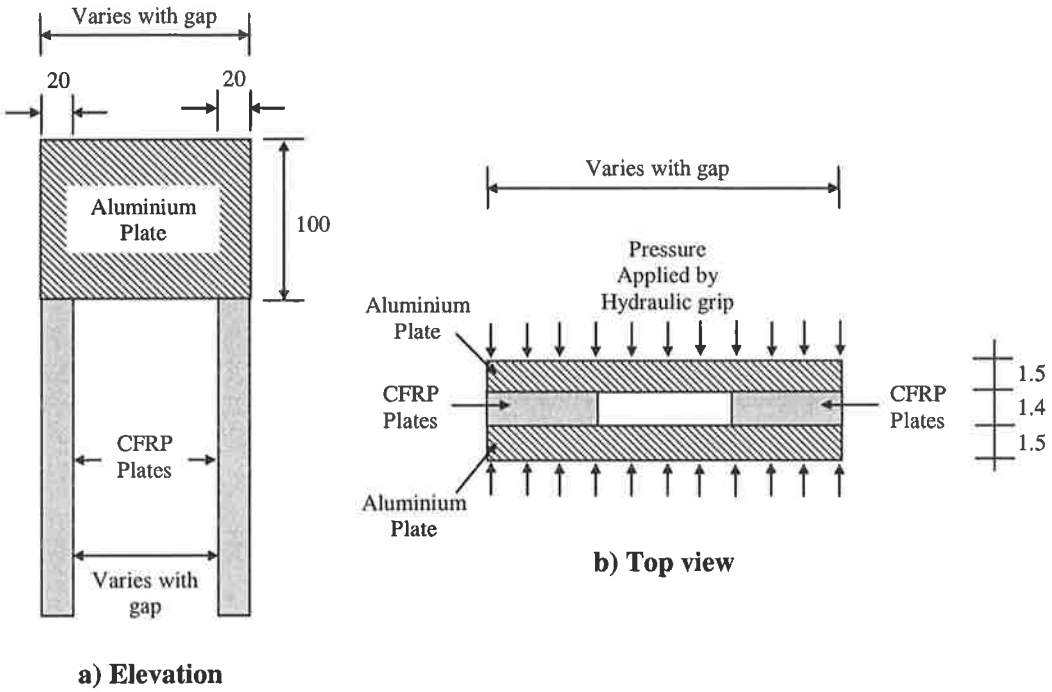

Note: All dimensions are in mm

Figure 5.3.6: Details for EB interaction clamping method in series 1.

All the specimens for pull tests series 2, which studied the interaction with cover shown in Figure 5.2.3, were placed in the rig facing sideways as shown in Figure 5.3.7. Aluminum plates were used as grips as shown in Figure 5.3.8 and Figure 5.3.9.

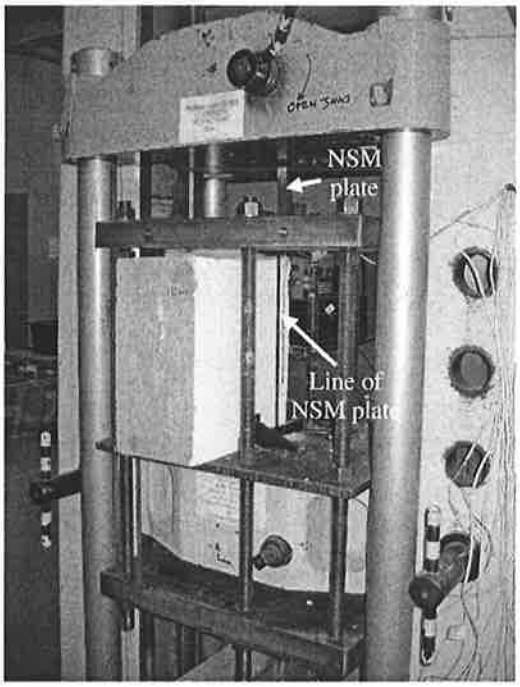

Figure 5.3.7 Test setup for series 2: interaction with covers.

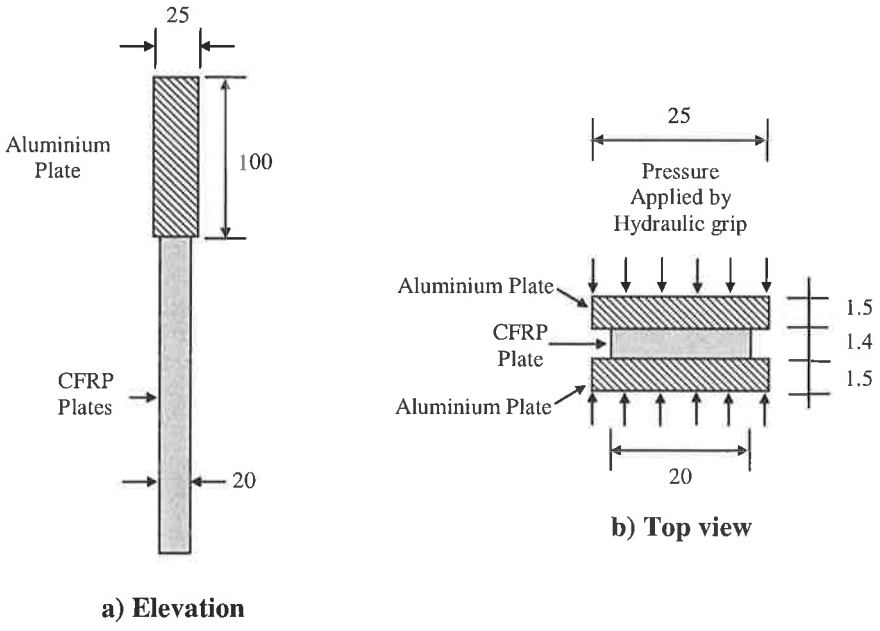

Note: All dimensions are in mm

Figure 5.3.8: Details for series 2 pull tests clamping method (20 mm x 1.4 mm plates).

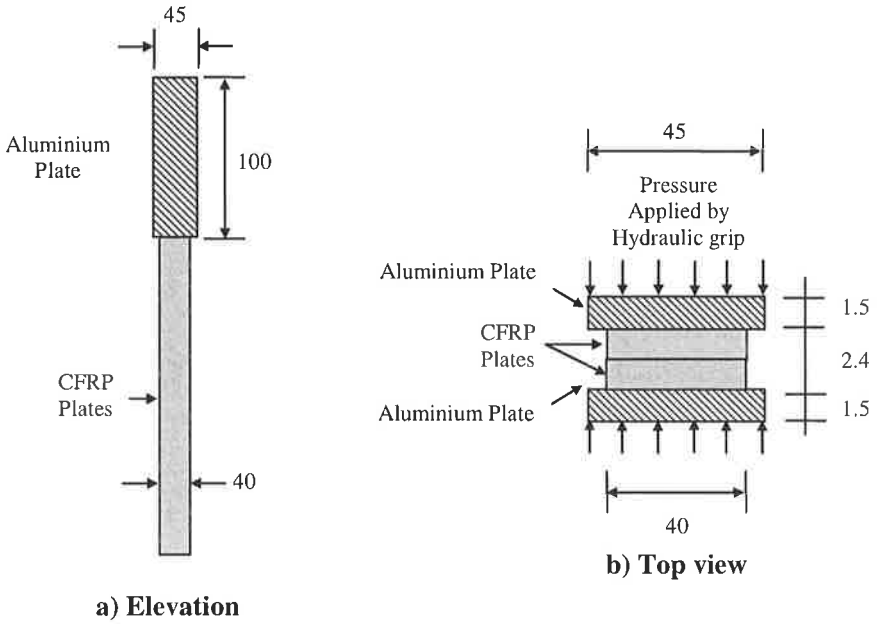

Note: All dimensions are in mm

Figure 5.3.9 : Details for series 2 pull tests clamping method (40 mm x 2.4 mm plates).

Finally in every pull test setup, a steel plate was placed on top of the concrete block as a restraint to accurately simulate IC debonding as shown in Figure 5.3.10. Next, the instrumentation and clamping method of each individual pull test will be described.

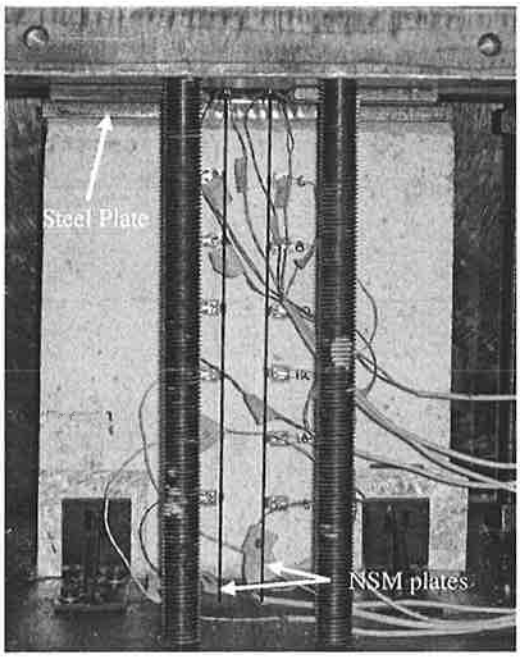

Figure 5.3.10: Steel plate restraining pull test specimens.

5.4 Instrumentation

In pull test series 1, there were 16 strain gauges (SG). The strain gauges for pull test G30NSM are shown in Figure 5.4.1 and for G40NSM in Figure 5.4.2. There were 8 strain gauges on each plate attached to the plate depth surface (d_p) as shown in Figure 5.4.3. In later tests only SG1 to SG8 were used. It is worth mentioning here that for interaction pull tests G30NSM and G40NSM the grips used and shown in Figure 5.4.1 and Figure 5.4.2 did not have the additional steel plate as shown in Figure 5.3.5.

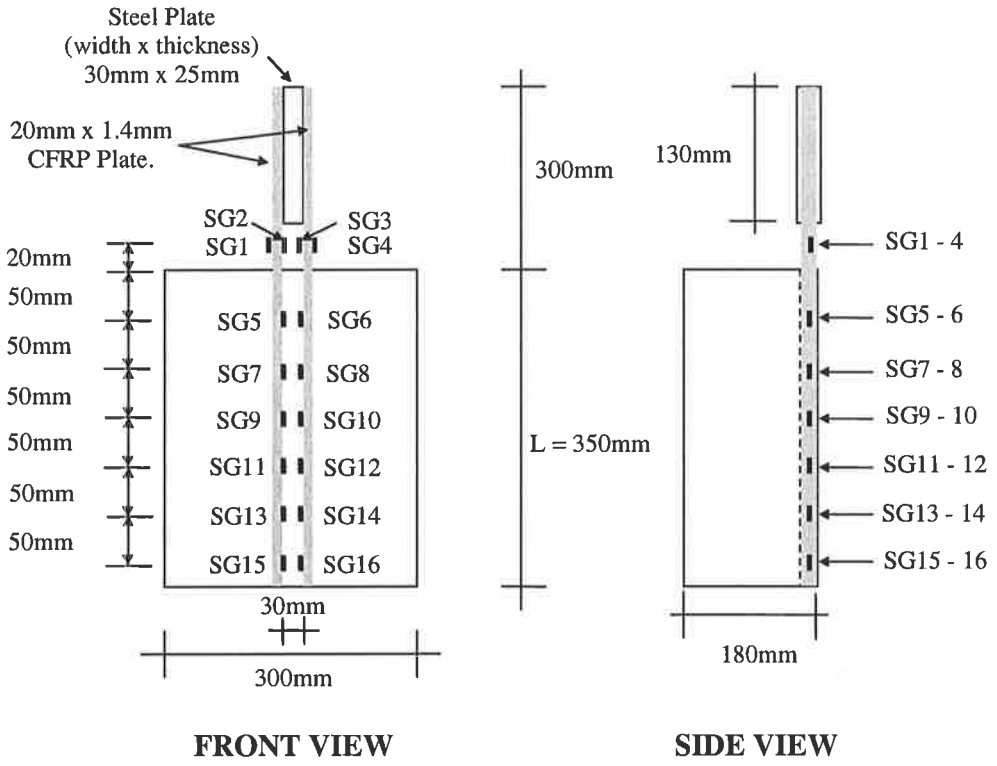

Figure 5.4.1: Instrumentation for test G30NSM.

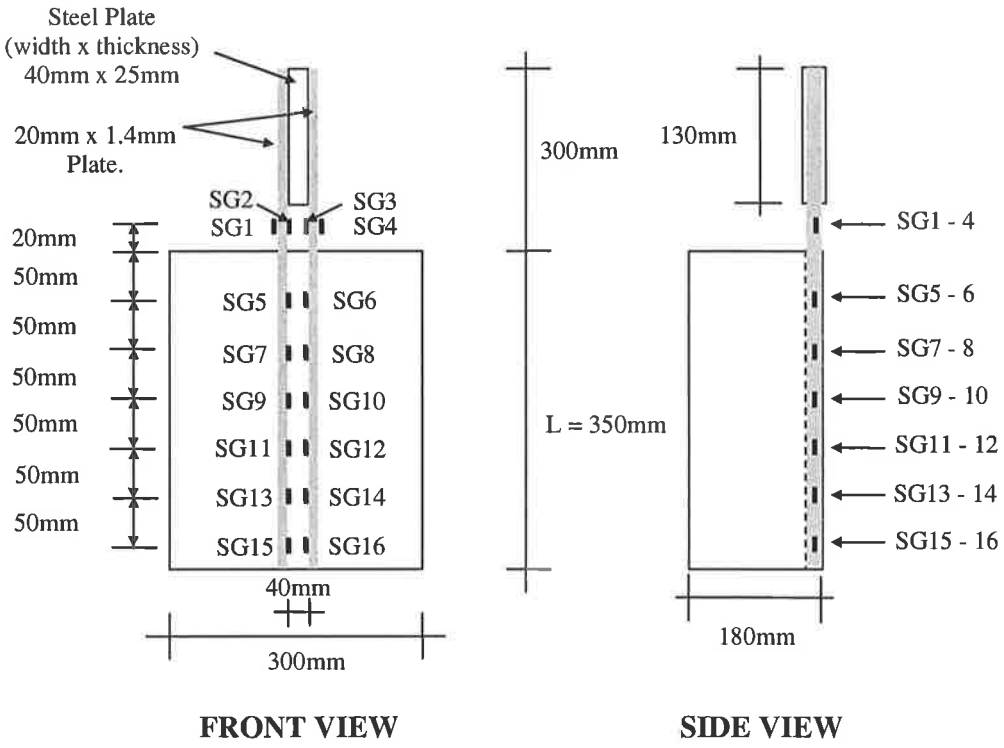

Figure 5.4.2: Instrumentation for test G40NSM.

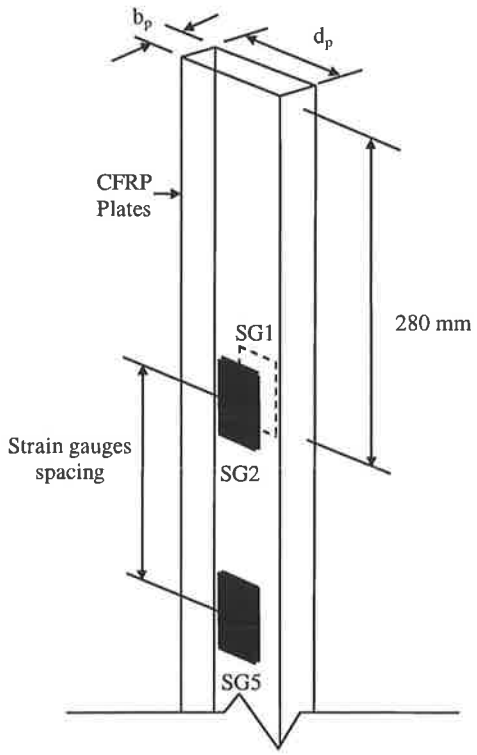

Figure 5.4.3: Detail of strain gauges position on NSM plates.

Pull test G50NSM was done three times as the first and second tests failed at the grip and Figure 5.4.4 shows the third pull test instrumentation with only 4 strain gauges located 20 mm above the concrete block. This instrumentation setup with only 4 strain gauges, was also used for test G70NSM shown in Figure 5.4.5.

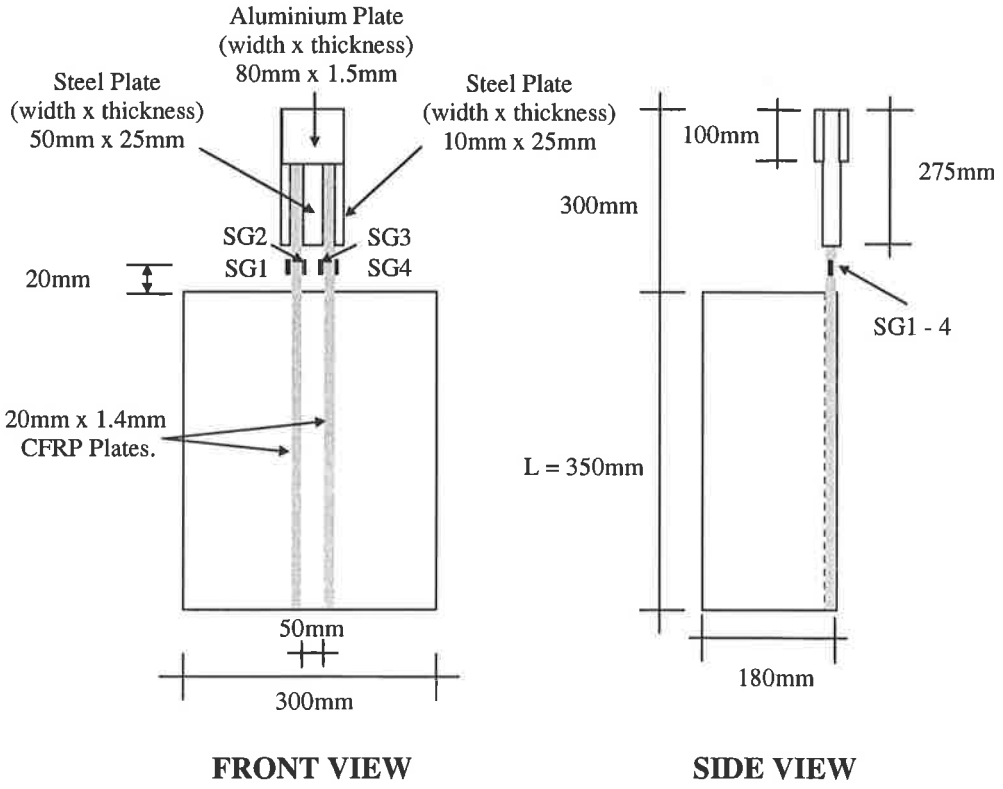

Figure 5.4.4: Instrumentation for test G50NSM.

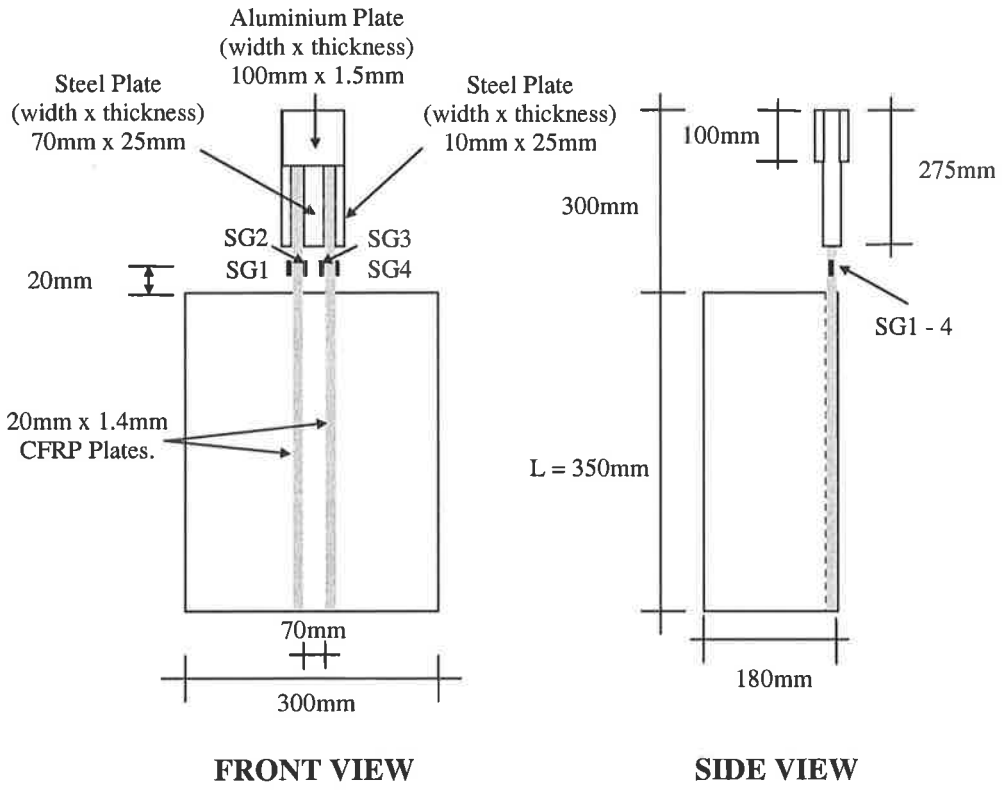

Figure 5.4.5: Instrumentation for test G70NSM.

Instrumentation for interaction pull tests G30EB with externally bonded plates is shown in Figure 5.4.6. The strain gauges for the EB plates was attached to the plate widths (b_p) as shown in Figure 5.4.7. However this pull test in Figure 5.4.6 did not have the steel plate of top on the concrete block as a restrain as in Figure 5.3.10. As a result, a large wedge of concrete detached reducing the ultimate failure load. Hence the test was repeated with 16 strain gauges in Figure 5.4.8 as well as the restrained in Figure 5.3.10. The EB interaction pull tests for G40EB, G50EB and G70EB are shown in Figure 5.4.9.

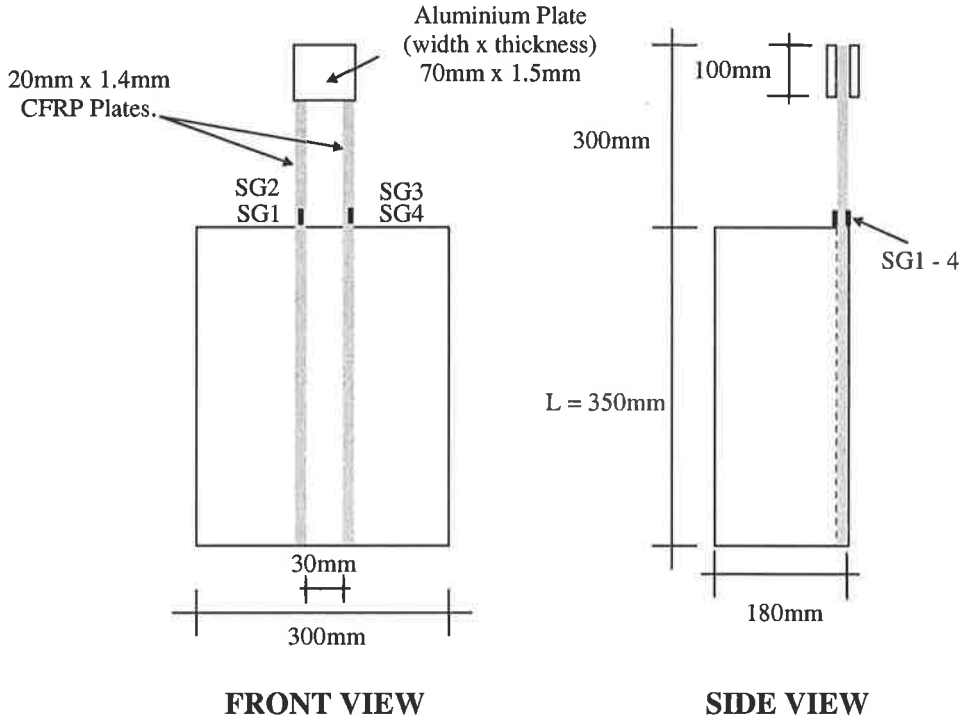

Figure 5.4.6: Instrumentation for test G30EBu (Unrestrained).

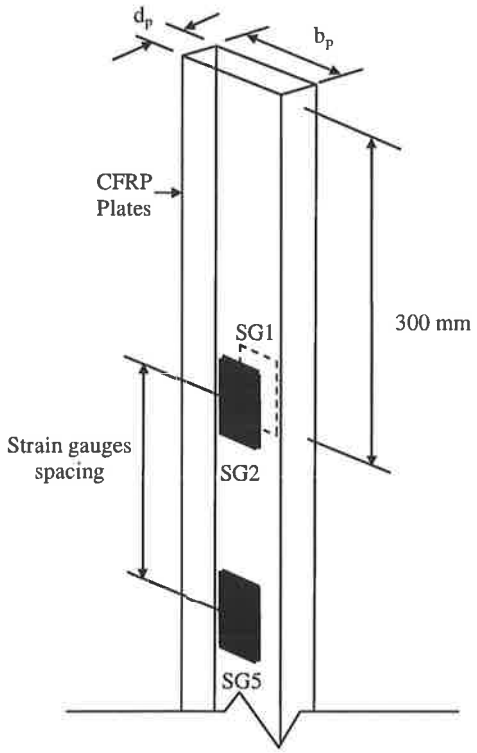

Figure 5.4.7: Detail of strain gauges position on EB plates.

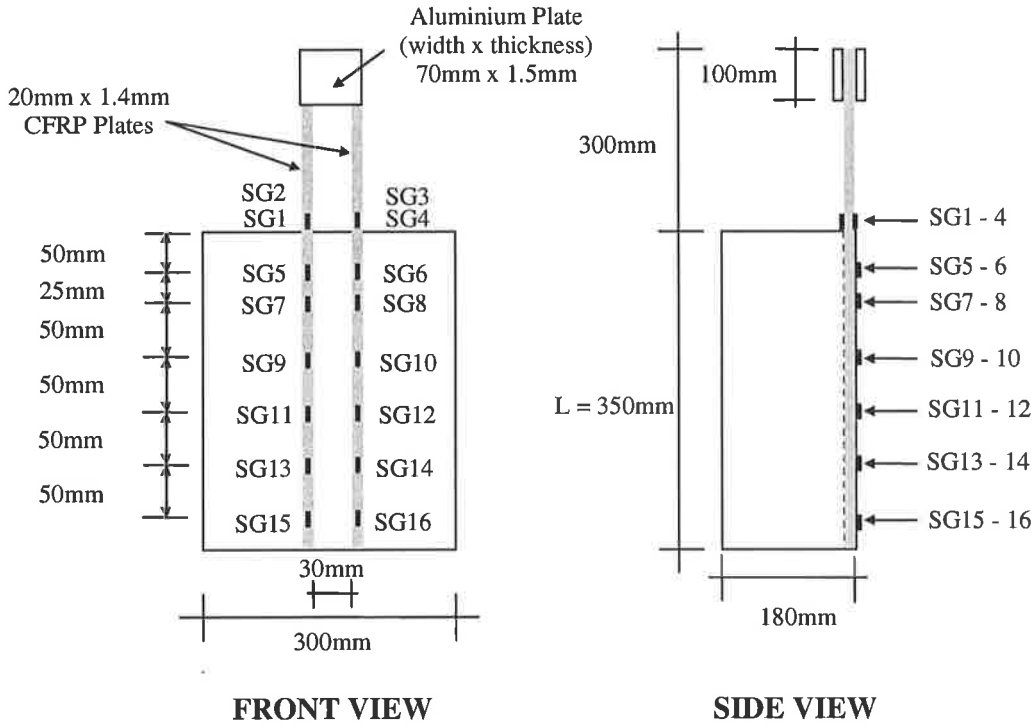

Figure 5.4.8: Instrumentation for test G30EBr (Restrained).

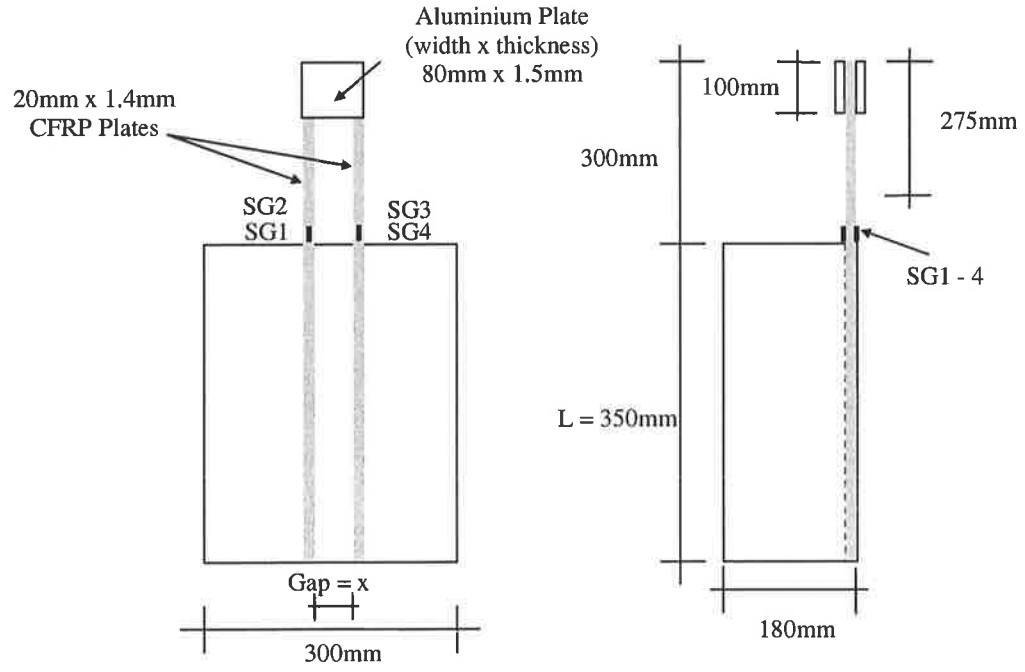

x = 40mm, 50mm and 60mm.

Figure 5.4.9: Instrumentation for test G40EB, G50EB and G60EB.

The instrumentation for series 2 pull tests consisted of only two strain gauges located 20 mm above the concrete block as in Figure 5.4.10. The edge pull test used two plate dimensions; 20 mm x 1.4mm and 40 mm x 2.4 mm. Two transducers, T1 and T2, were located 50 mm and 200 mm from the top of the concrete block and which pointed to the centre of plate depth (10 mm from concrete block surface) as shown in Figure 5.4.10 and Figure 5.4.11. The transducers measured the displacement of the concrete block cover whilst loading. The transducers were attached to the concrete block as in Figure 5.4.12 using clamps with 10 mm spacers.

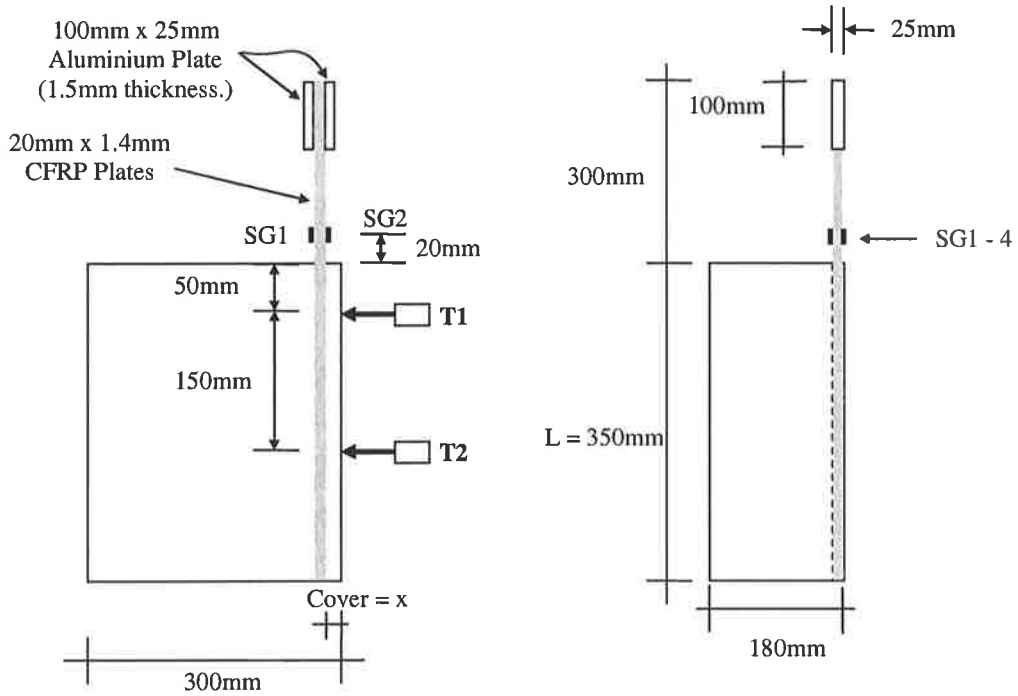

x = 10mm, 20mm, 30mm, 40mm, 60mm and 85mm.

Figure 5.4.10: Instrumentation for series 2 pull test (20 mm x 1.4mm plates).

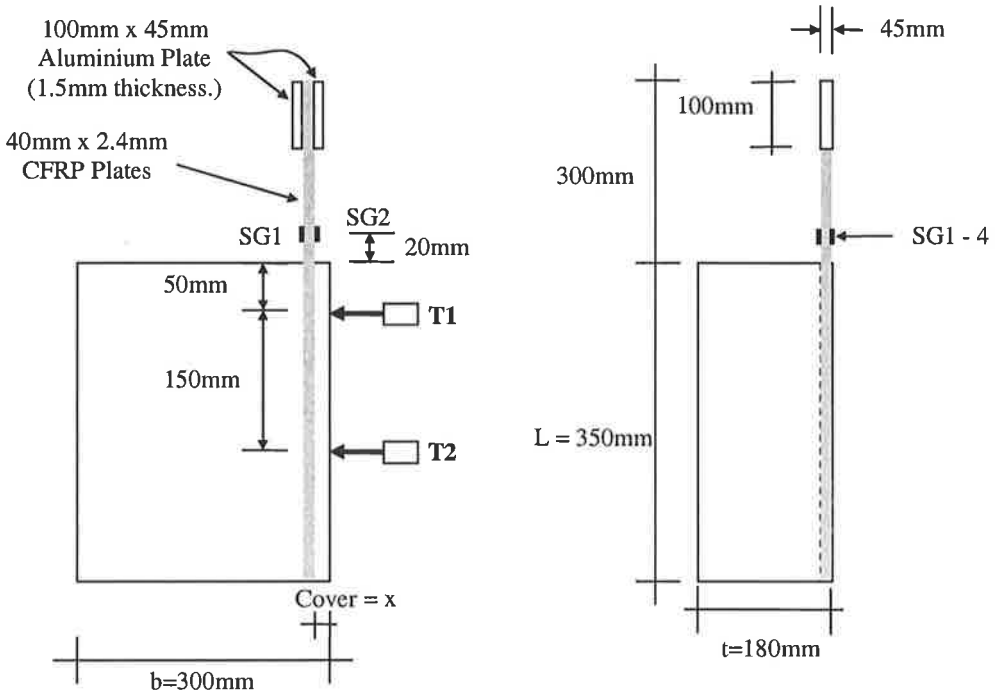

x = 50mm, 75mm, 100mm and 150mm.

Figure 5.4.11: Instrumentation for series 2 pull test (40 mm x 1.4mm plates).

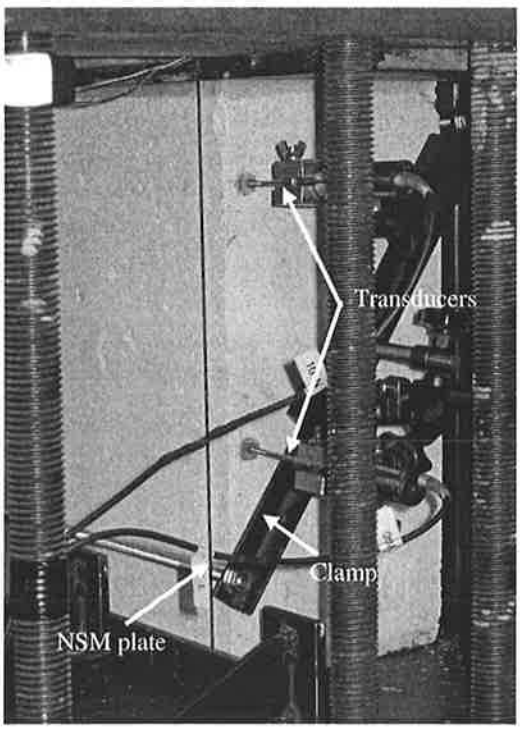

Figure 5.4.12: Transducers were placed next to the specimen using clamp.

5.5 Material Properties

The concrete blocks in this series of pull tests were from the same batch used in the previous pull tests in chapter 3. In Table 5.5.1 are summaries of concrete cylinder test showing Young's Modulus (E_c) and compressive strength (f_c) for the concrete blocks. It can be seen that the concrete was mature and hence the reduction could be during the duration of tests.

Table 5.5.1: Material properties of the concrete block.

Concrete Age (days)	E_c (MPa)		f_c (MPa)	
489	Tests	Average	Tests	Average
	1. 36708	37354	1. 36.1	36.7
	2. 37830		2. 37.02	
	3. 37525		3. 37.08	
656	Test	Average	Tests	Average
	1. 28603	30151	1. 33.64	35.28
	2. 32635		2. 38.32	
	3. 29216		3. 33.9	

Table 5.5.2 gave the Young's Modulus of the NSM and EB plates that was measured from strain gauges SG1 and SG2 in each pull test.

Table 5.5.2: Material properties of the plate specimens.

				E_p (MPa)	
Specimen	d_p (mm)	b_p (mm)	Materials	Test	Average
20x1.4	20	1.4	CFRP	1. 161663	161455
	20	1.4		2. 161041	
	20	1.4		3. 161663	
40x2.4	40	2.4	CFRP	1. 172548	172548

The adhesive properties are presented in Table 5.5.3 which also gives information provided by the manufacturer. The Young's Modulus (E_g) of the adhesives were obtain from tensile tests.

Table 5.5.3: Materials properties of the adhesives.

Adhesive	Tested in the Lab		Tested by the manufacturer	
	E_g (MPa)		Compression Strength (MPa)	Flexural Strength (MPa)
	Tests	Average		
MBrace Laminate Adhesive	1. 5669 2. 6091 3. 6102	5954	> 60	> 30
CIBA Adaldite K340 High Performance Adhesive	1. 4434 2. 4677 3. 3895	4335	100 – 120	20 - 30

5.6 Test Results

In this section, all the pull tests done for the interaction and edge distances will be described individually beginning with the single pull test as a reference pull test. The summaries of all 12 pull tests in series 1 is presented in Table 5.6.1 and the 10 pull tests in series 2 are in Table 5.6.2 were test C150NSMa is G0NSM (average) in Table 5.6.1.

Table 5.6.1: Summaries of series 1 pull tests.

Test	Gap (mm)	Load P_u (kN)	Failure Load P (kN)	Mean Max. Strain Plate A ε_u ($\mu\varepsilon$)	Mean Max. Strain Plate B ε_u ($\mu\varepsilon$)	Strain Prior Debonding Plate A ε_f ($\mu\varepsilon$)	Strain Prior Debonding Plate B ε_f ($\mu\varepsilon$)	Type of Plating	Notes
G0NSM1	0	61.2	44.6	13007	-	11579	-	NSM	reference test
G0NSM2	0	64.8	52.0	13767	-	12107	-	NSM	reference test
G0NSM (average)	0	63.0	48.3	13387	-	11843	-	NSM	reference test (Average)
G30NSM	30	102.3	94	11230	11056	10195	10324	NSM	single failure plane
G40NSM	40	124.3	97.9	13367	13523	10991	10668	NSM	single failure plane
G50NSM	50	118.5	99.1	12354	13019	10023	10267	NSM	single failure plane
G70NSM	70	135.5	119.4	15076	14171	12477	13336	NSM	individual failure plane
G0EB	0	11.9	10.8	2731	2750	2463	2488	EB	reference test
G30EBu	30	18.8	8.1	2072	1810	2224	2002	EB	plate A debonded first.
G30EBr	30	26	11.8	3034	2991	2775	2830	EB	plate B debonded first.
G40EB	40	21.1	12.8	2446	2459	2446	2929	EB	plate A debonded first.
G50EB	50	21.4	11.5	2696	2270	2270	2664	EB	plate A debonded first.
G60EB	60	24.0	12.5	3024	3216	3024	3216	EB	plate A debonded first.

Table 5.6.2: Summaries of series 2 pull test.

Test	Cover	Ult. Load P_u (kN)	Failure Load P (kN)	Ave. Max. Strain Plate A ε_{max} ($\mu\varepsilon$)	Max. Disp. (mm)	Plate Size in mm (d_p x b_p)	Type of Plating	Notes
C150NSMa	150	63	48.3	13364	N.A	20 x 1.4	NSM	no edge effect.
C10NSMa	10	22.2	19.9	4984	2.9	20 x 1.4	NSM	effected by edge.
C20NSMa	20	33.8	30.6	7578	24.9	20 x 1.4	NSM	effected by edge.
C30NSMa	30	40.6	37.9	8950	3.1	20 x 1.4	NSM	effected by edge.
C40NSMa	40	50.2	46.1	10883	N.A.	20 x 1.4	NSM	effected by edge.
C60NSMa	60	59.2	52.1	12712	1.4	20 x 1.4	NSM	effected by edge.
C85NSMa	85	75.7	72.1	16403	0.16	20 x 1.4	NSM	no edge effect.
C150NSMb	150	205.1	197.4	11881	1.1	40 x 2.4	NSM	concrete block split into two.
C50NSMb	50	119.9	114.8	7340	5.5	40 x 2.4	NSM	effected by edge.
C75NSMb	75	170.9	164.6	10174	2.6	40 x 2.4	NSM	effected by edge.
C100NSMb	100	194.9	190.5	11406	1.13	40 x 2.4	NSM	concrete block split into two and no edge effect

5.6.1 Pull Test G0NSM

Two single plate pull tests were done using NSM plating located in the centre of the concrete block. The first pull test debonded at a load of 61.2 kN whereas the second single plate pull test failed at 64.8 kN, giving an average of 63.0 kN. Observations from the experiments showed typical failure patterns with cracks appearing along the bonded length and concrete attached to the plate as shown in Figure 5.6.1 and in Figure 5.6.3. In the first pull test, plate splitting occured along the length between the grip and the concrete block (Figure 5.6.2). This was found not to affect the failure load as it was caused by plate crushing at the grips.

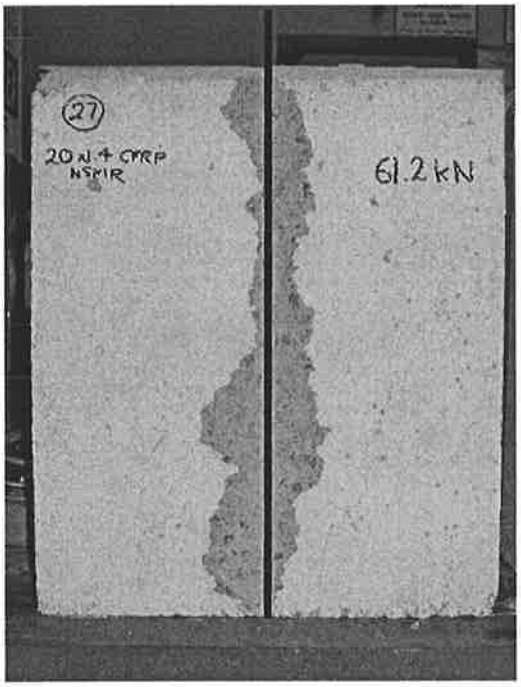

Figure 5.6.1: Failure for pull test G0NSM (First test).

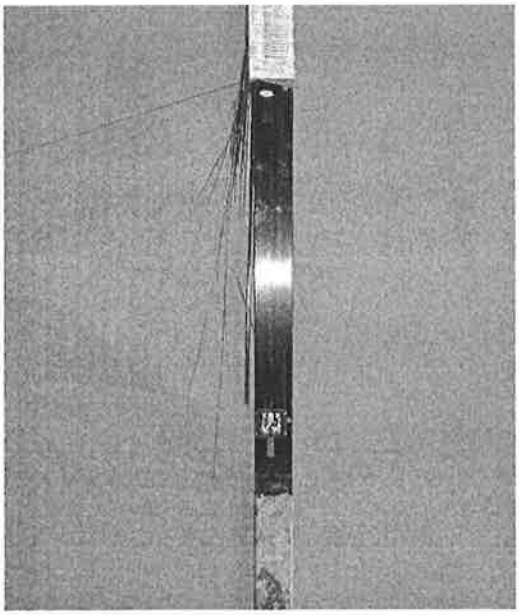

Figure 5.6.2: Occurrences of plate splitting at the grip for G0NSM (First test).

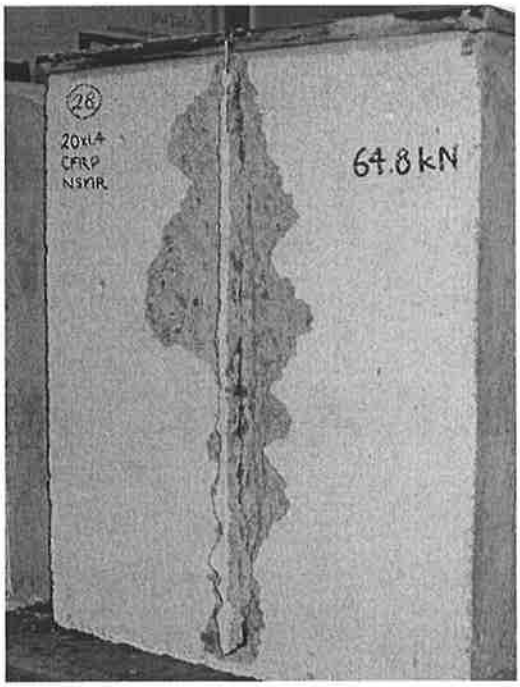

Figure 5.6.3: Failure for pull test G0NSM (Second test).

5.6.2 Pull Test G30NSM

This is the first double NSM plate pull test and has a gap of 30 mm. In this test, the failure pattern is shown in Figure 5.6.4 with the appearance of 'herring bones' along the length the outer sides of the plates. The failure load for this test was 102.3 kN. As this is less that twice the strength of G0NSM, this test fails with the occurrence of interaction between the two plates. Figure 5.6.5 shows the both of the plates fail as a single failure plane due to interaction between the plates.

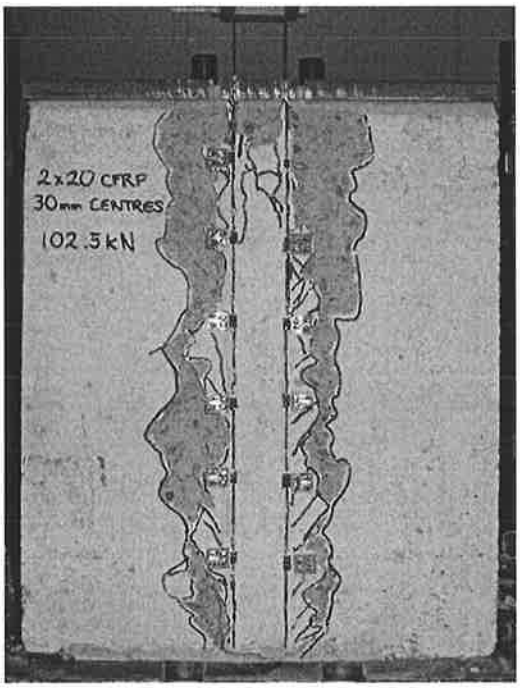

Figure 5.6.4: Failure for pull test G30NSM.

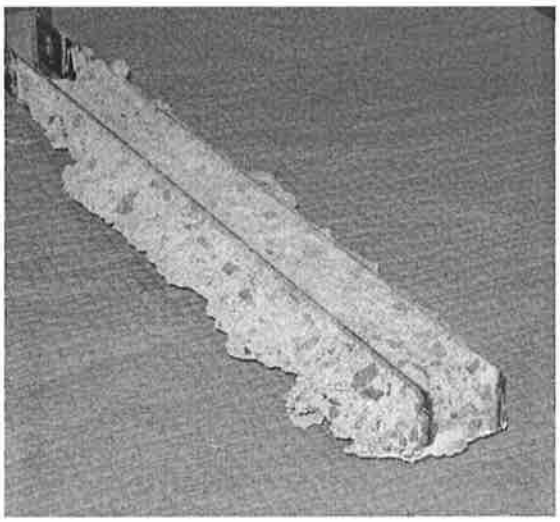

Figure 5.6.5: Single failure plane for pull test G30NSM.

The strain profiles from all the 16 strain gauges are plotted in Figure 5.6.6 which show the maximum strain reading recorded was 11361 microstrains by strain gauge 2. Figure 5.6.6 also shows by looking at strain reading for SG1, SG2, SG3 and SG4 that both of the plates failed together.

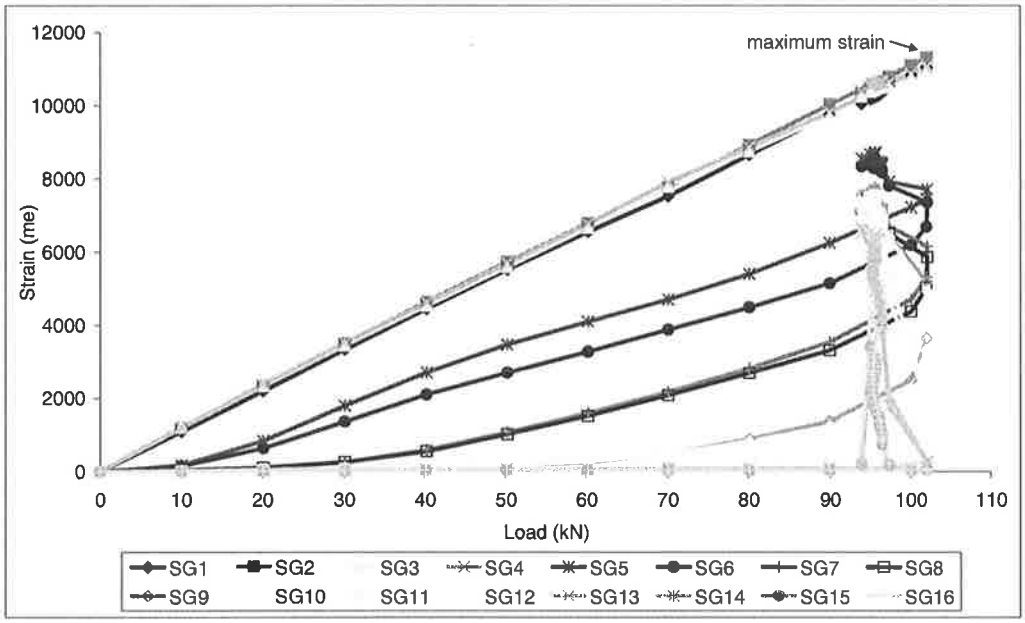

Figure 5.6.6: Strain profile for pull test G30NSM.

5.6.3 Pull Test G40NSM

This test has gap of 40 mm between the plates. The failure pattern (Figure 5.6.7) also has the appearance of 'herring bones' along the plate length. The failure load for this test was 124.3 kN, again showing this test failed with the existence of interaction between the two plates similar to G30NSM with a 30 mm gap spacing. Figure 5.6.8 shows both of the plates fail as a single failure plane due to interaction and similar to the specimen with a 30 mm gap.

The strain profiles from all the 16 strain gauges (Figure 5.6.9) show that the maximum strain reading recorded was 13576 microstrains provided by strain gauge 3. Figure 5.6.9 also shows that both of the plates failed together by looking at the strain reading for SG1, SG2, SG3 and SG4.

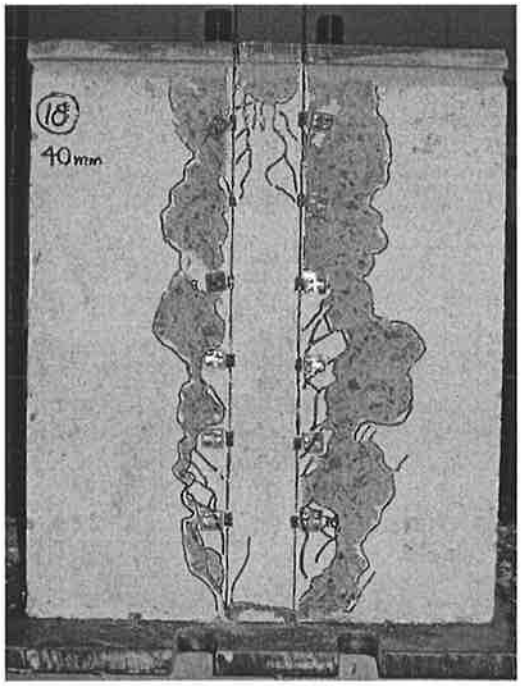

Figure 5.6.7: Failure for pull test G40NSM.

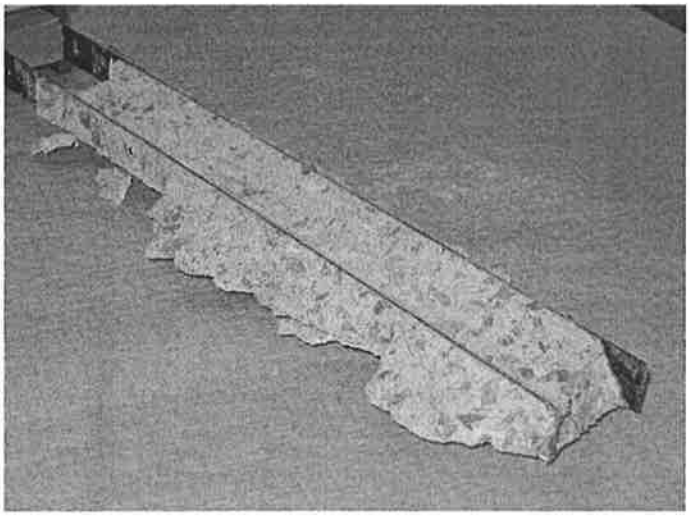

Figure 5.6.8: Single failure plane for pull test G40NSM.

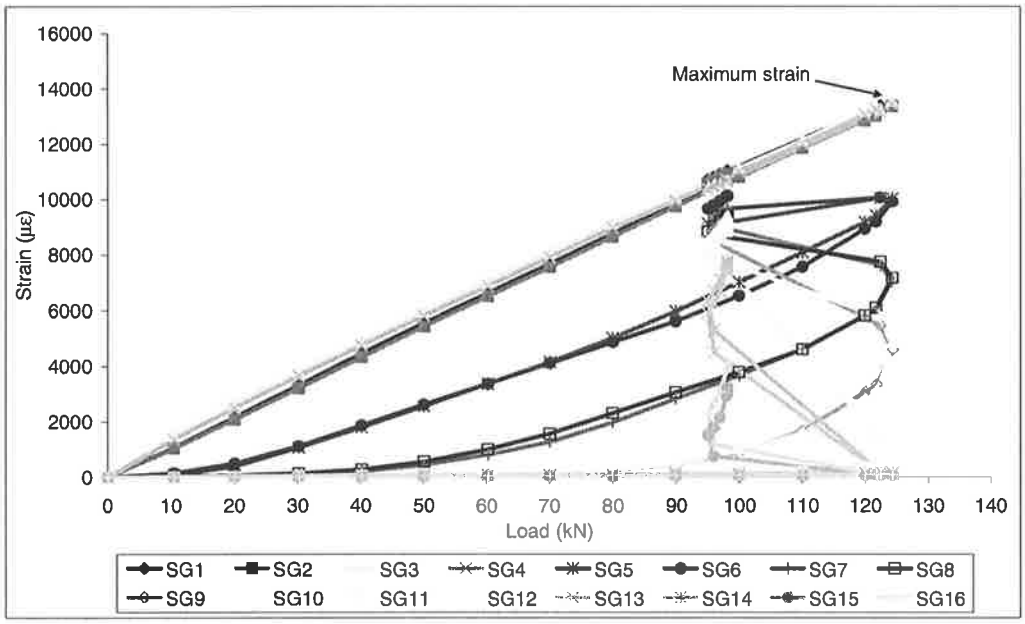

Figure 5.6.9: Strain profile for pull test G40NSM.

5.6.4 Pull Test G50NSM

As mentioned in section 5.4, the specimen with a 50mm gap was tested three times. The first test failed at the grips and has the same setup as for tests G30NSM and G40NSM, that is without the additional steel plating as shown in Figure 5.3.4. The second test was with the additional steel plate as shown in Figure 5.3.5 and Figure 5.6.10 but this also failed at the grips which may have been caused by faulty preparation.

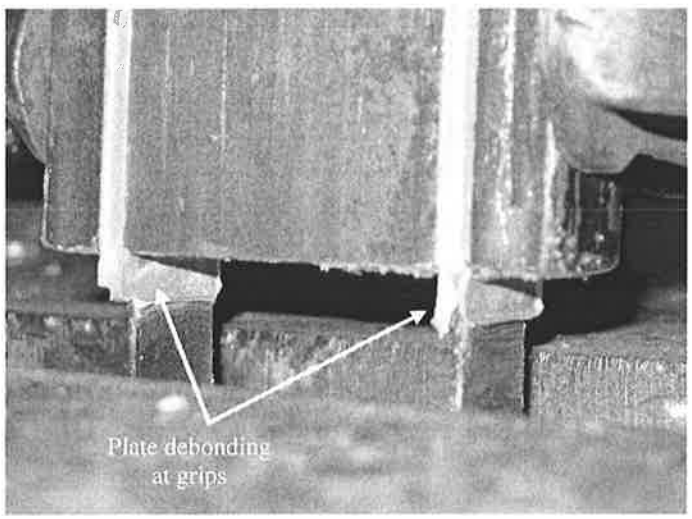

Figure 5.6.10: Premature failure at the steel grips (G50NSM second test).

During the third test, the shear stresses on the plates created the clear appearance of typical IC debonding on the outer sides of each plate and the interaction cracks between the two plates is shown in Figure 5.6.11. Many of theses cracks however were not apparent after failure (Figure 5.6.12). The failure load for this pull test was 118.5 kN.

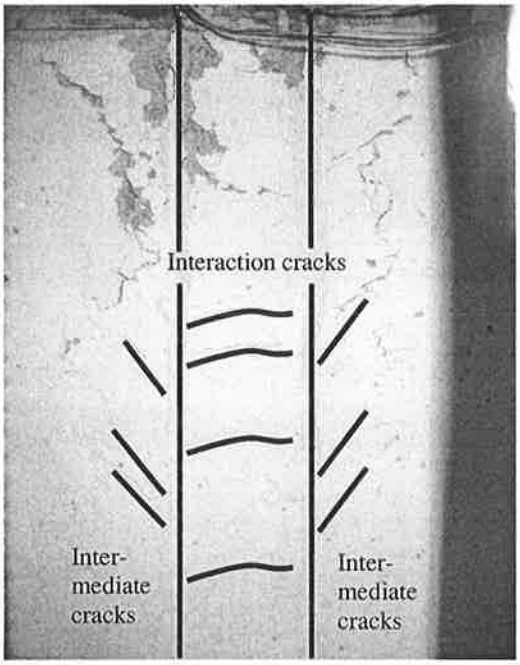

Figure 5.6.11: Appearance of IC and interaction cracks during testing.

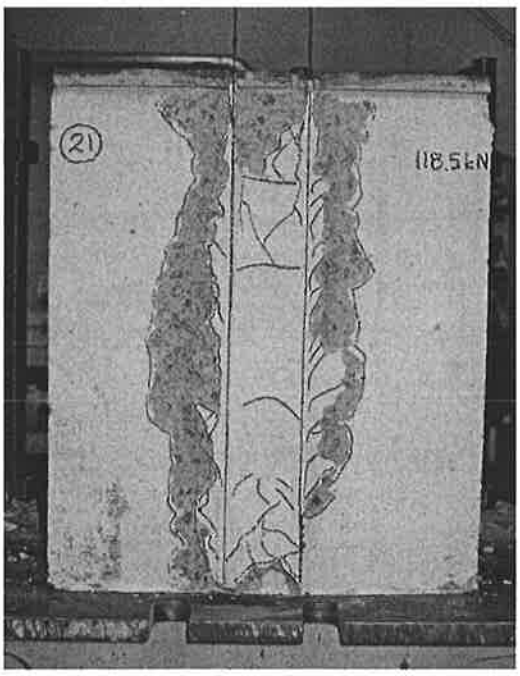

Figure 5.6.12: Failure pattern for pull test G50NSM after failure.

Figure 5.6.13 is the strain profile for this test which consists of straight line for all 4 strain gauge readings when plotted again load. The maximum strain reading is given by strain gauge 4 with 13046 microstrains. This is also shows that the plates with a 50 mm gap debonded simultaneously.

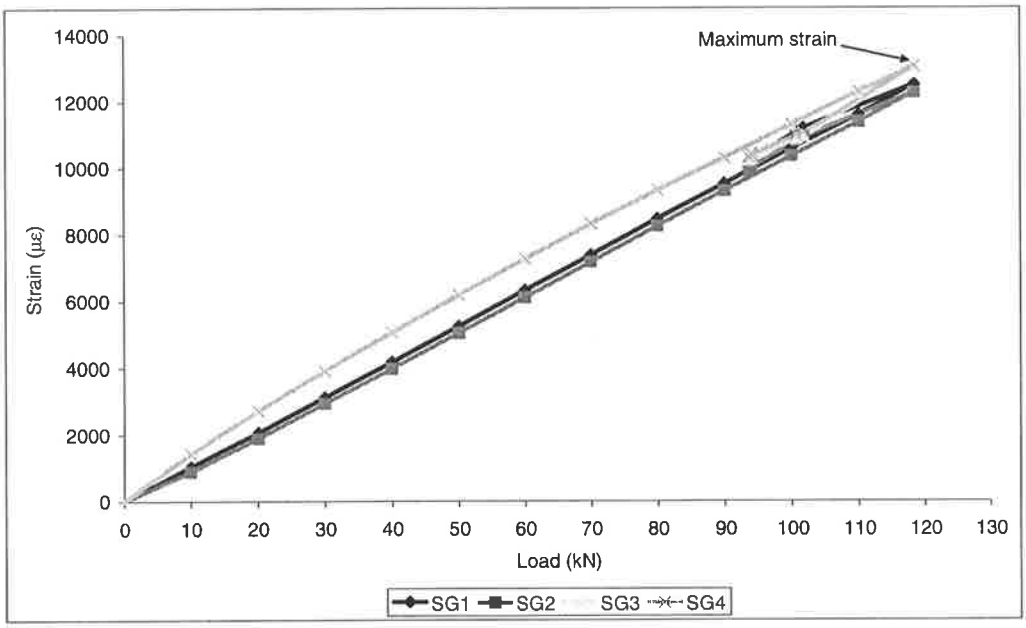

Figure 5.6.13: Strain profile for pull test G50NSM.

5.6.5 Pull Test G70NSM

This experiment failed at a load of 135.5 kN; this is more than double that of the single pull test, G0NSM (average), suggesting this test has individual plate failure. Observations from the experiment shown in Figure 5.6.14, show the appearance of individual IC debonding hearing bone cracks on each plate which also proves that the plates did not fail as a single failure plane. After the test ended, the plates were found to have split (Figure 5.6.16) which was also found in previous NSM [Jones (2004)] pull tests in which the plate exceeded 10 mm of plate depth.

Again in this test only 4 strain gauges were attached to the plates providing a straight line strain profile (Figure 5.6.17). The maximum strain was 15297 microstrain which was recorded by strain gauge 1. Looking at the strain profile, both of the plates were also failing simultaneously. This completes the NSM interaction pull test. The next section will be looking into interaction of EB plates.

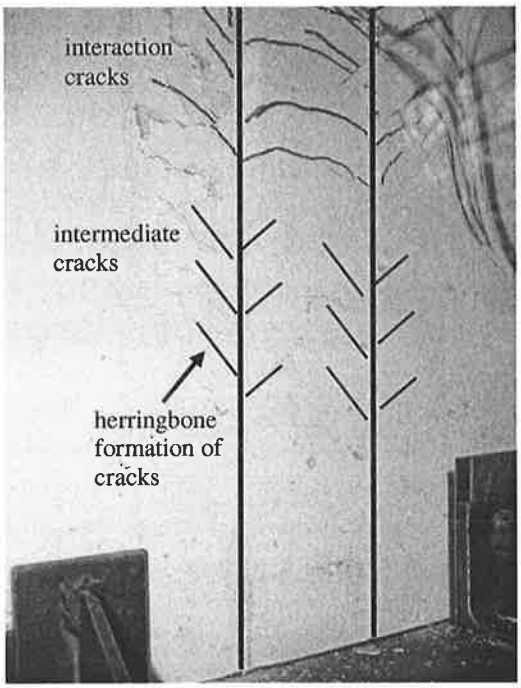

Figure 5.6.14: Appearance of IC and interaction cracks.

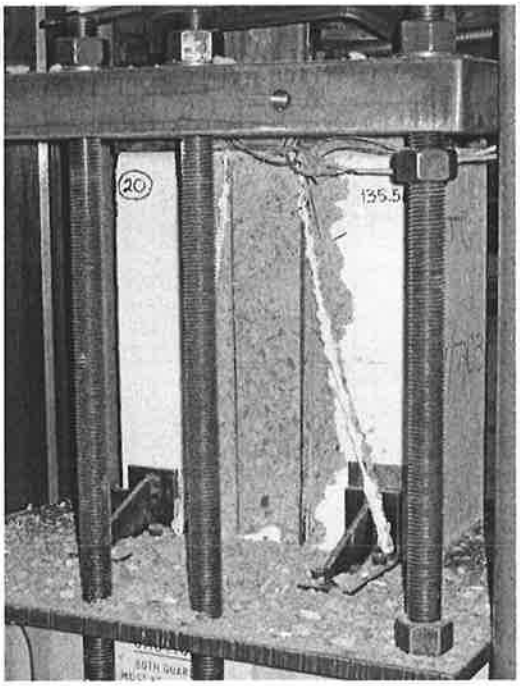

Figure 5.6.15: Failure for pull test G70NSM.

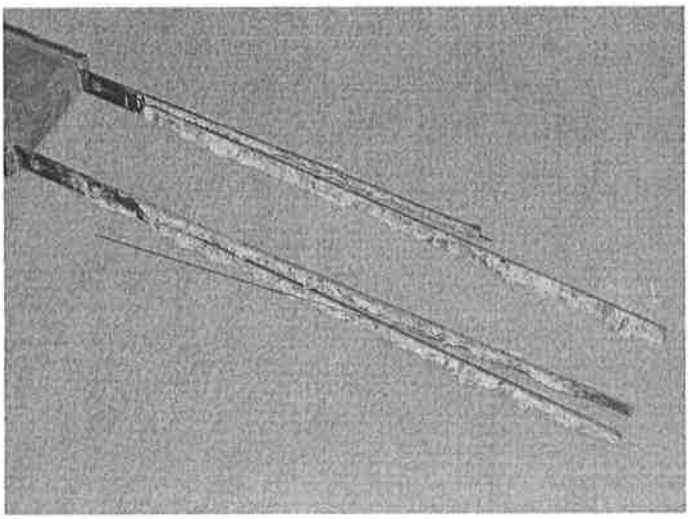

Figure 5.6.16: Plate splitting cause by individual failure.

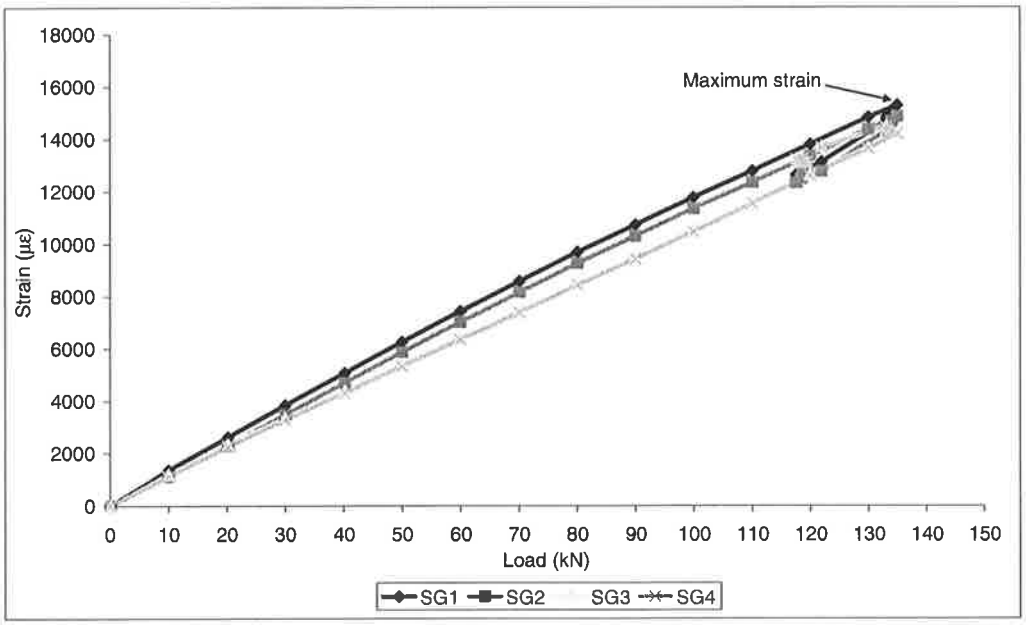

Figure 5.6.17: Strain profile for pull test G70NSM.

5.6.6 Pull Test G0EB

One test was done with a single EB plate. This test was a reference for the double EB plate pull tests, for the same reason as the single NSM plate pull test in order to know whether the double tests failed with interaction or as individual plates. Eight strain gauges were attached to the plate as in Figure 5.4.8 and in Figure 5.6.18 giving the strain profiles shown in Figure 5.6.19. Maximum load for this test was 11.9 kN with maximum strain of 2953 microstrain recorded by SG3.

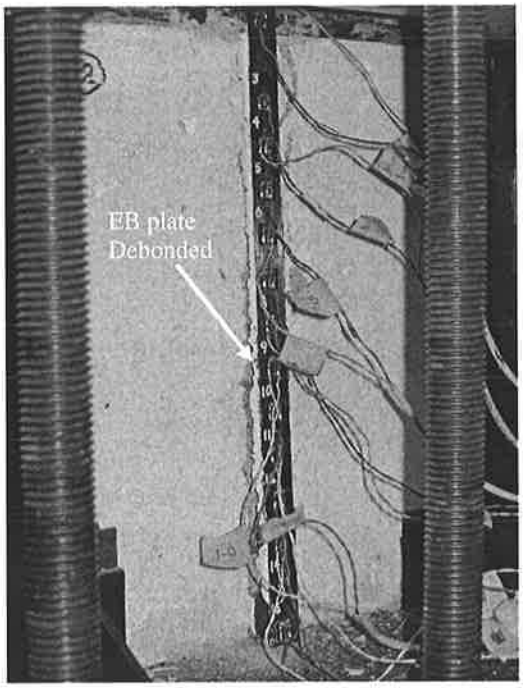

Figure 5.6.18: Failure for pull test G0EB.

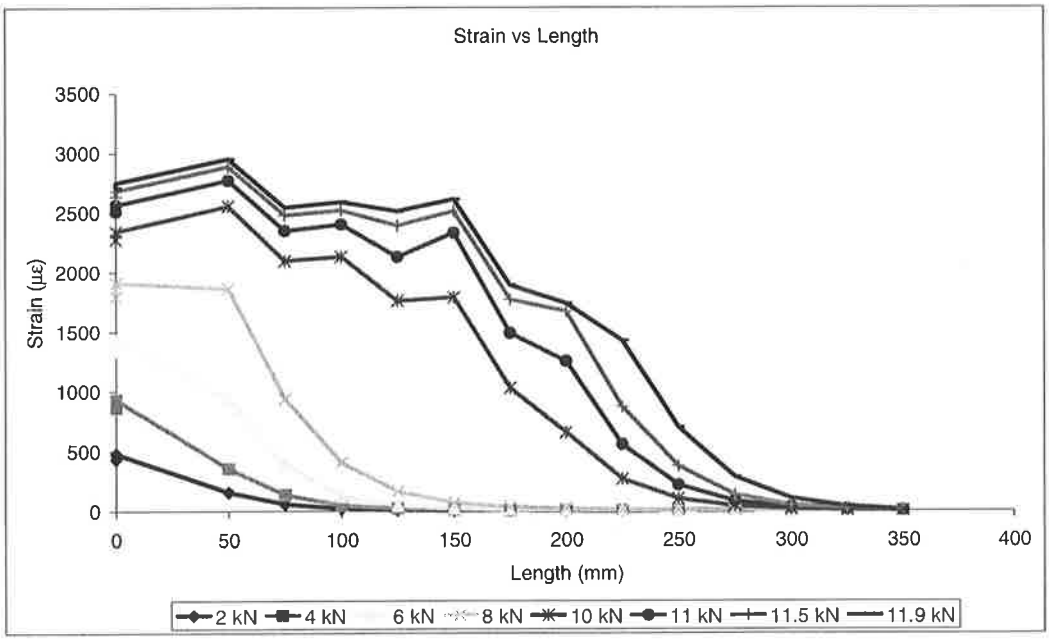

Figure 5.6.19: Strain profile for pull test G0EB.

5.6.7 Pull Test G30EBu (Unrestrained)

This test failed at a loading of 18.8 kN with debonding crack propagating from the top of the concrete block towards the unloaded end. The failure pattern for these two EB plates is shown in Figure 5.6.20; a thin layer of concrete is attached to the CFRP plates.

The behaviour at failure for this 30 mm gap EB plated specimen was different from the 30 mm spacing NSM plated in whilst one of the plates debond first and then followed immediately by debonding of the second plate. This difference can be explained by referring to Figure 5.6.21 which uses the average strain reading from strain gauges SG1 to SG4 in Figure 5.4.6. From Figure 5.6.21, both of the plate strains gradually increase until a loading of 18.8 kN and at this stage the load dropped to 18.1 kN with plate A (plate on the left) maintaining a high strain. The load then dropped to 16.9 kN with plate A still with the highest strain reading among the two plates. At this stage (16.9 kN), Plate A debonded and plate B now sustained the load.

Immediately as plate A debonded the load dropped to 8.6 kN and continued dropping to 8.1 kN. Plate B then sustained a small load increment off load to 8.5 kN which were followed by load dropping to 8.1 kN and failure immediately after that. All of this is shown in Figure 5.6.21 and it is represented with a circle.

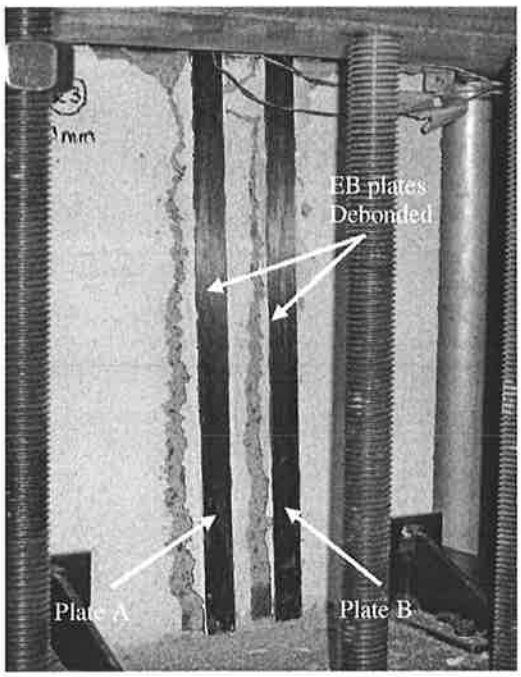

Figure 5.6.20: Failure for pull test G30EBu (Unrestrained).

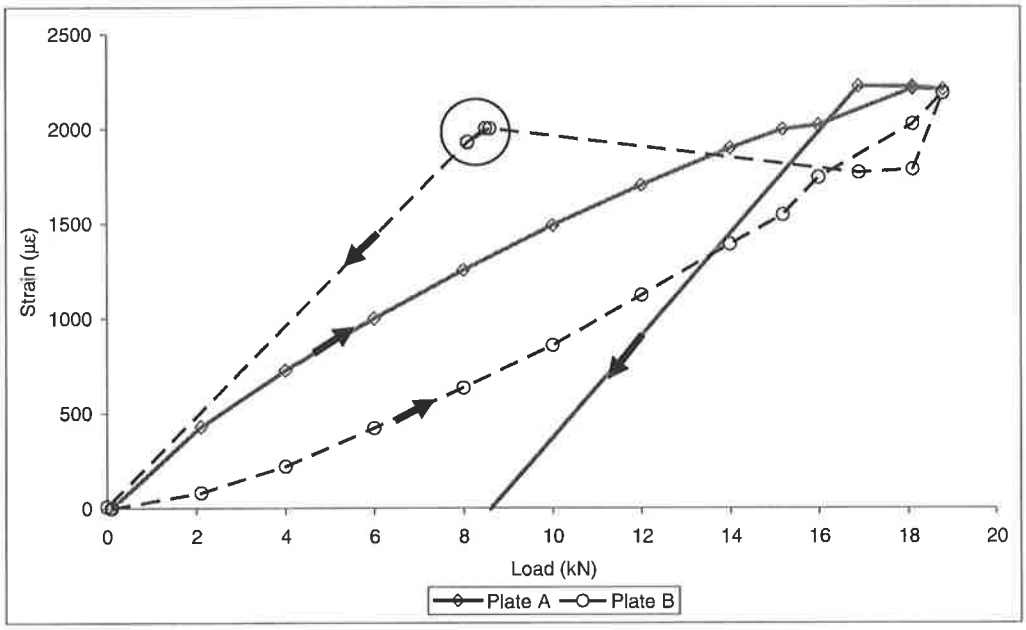

Figure 5.6.21: Strain profile for pull test G30EBu (Unrestrained).

This pull test was not restrained by the steel plate as shown Figure 5.3.10. Hence the results were not correct and not considered but the failure mechanism is interesting to understand.

5.6.8 Pull Test G30EBr (Restrained)

This experiment was a retest of G30EBr, for a 30 mm gap, and failed at a loading of 26.0 kN. Figure 5.6.22 shows that Plate B was the first plate to debond. The failure pattern for these two EB plates is shown in Figure 5.6.23 with cracks along the plate length and thin layers of concrete attached to the CFRP plates.

From Figure 5.6.24, the strain profile (average strain on each plate) also shows what was observed form the previous experiment in section 5.6.7. Plate B debonded first. After reaching 26.0 kN, the load dropped to 24.0 kN with Plate A having a higher strain which was then followed by another load drop to 23.0 kN but now with Plate B is now on high strain.

Immediately after this, Plate B debonded and the load dropped to 11.6 kN and Plate A now sustained all the load. Plate A managed to continued sustaining a small increments to 11.8 kN which was followed by Plate A debonding. All of this is shown in Figure 5.6.24.

Figure 5.6.22: Debonding of Plate B.

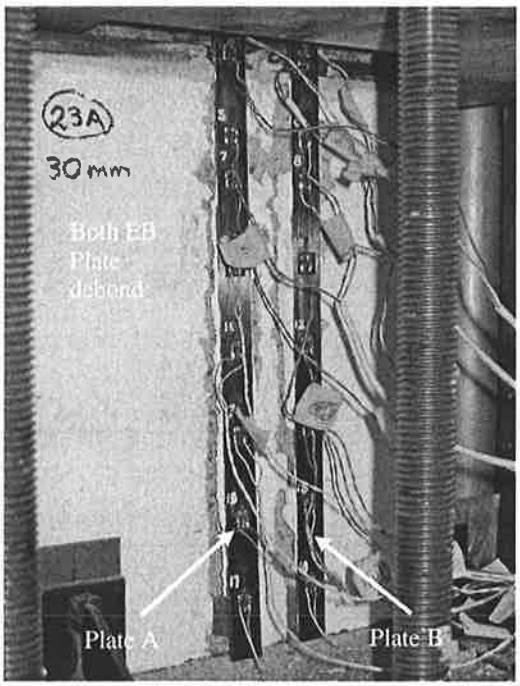

Figure 5.6.23: Failure for pull test G30EBr (Restrained).

This pull test was found to be double the failure load as compared to the single plate pull test. Next the 40 mm spacing that will be described.

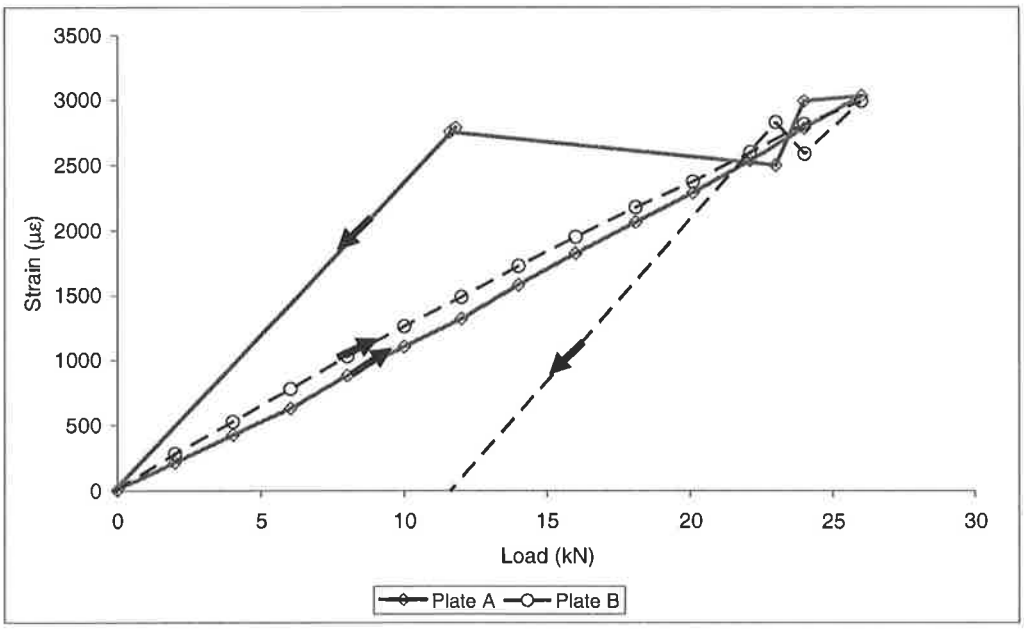

Figure 5.6.24: Strain profile for pull test G30EBr (Restrained).

5.6.9 Pull Test G40EB

This experiment failed at a loading of 21.1 kN, which was lower compare to the 30 mm gap test. Figure 5.6.25 shows debonding crack propagation of Plate A towards the unloaded end. Figure 5.6.25 also shows that the test had only 4 strain gauges. The failure pattern for this two EB plated specimen is shown in Figure 5.6.26 with cracks along the plate lengths and thin layers of concrete attached to the CFRP plates.

Figure 5.6.27 shows the typical strain profile (average strain on each plate) and it also shows Plate A debonds first. After reaching 21.1 kN, the load dropped to 20.9 kN which was followed by debonding of Plate A. Immediately after Plate A debonded, the load dropped to 11.4 kN and Plate B now sustained the load. Plate B managed to continue sustaining a small increment of loading to 12.8 kN which was followed by Plate B debonding. All of this is shown in Figure 5.6.27 in typically circular fashion.

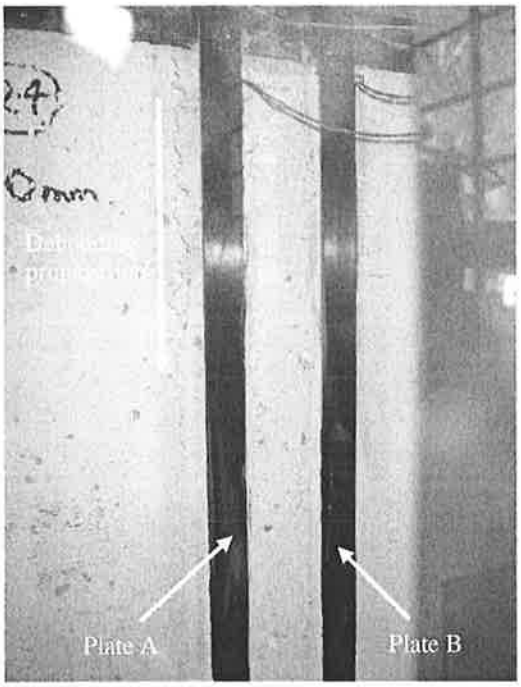

Figure 5.6.25: Propagation debonding for plate A.

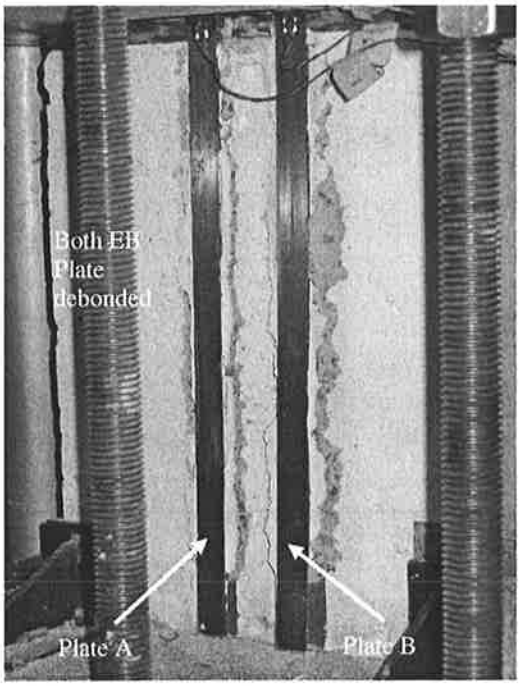

Figure 5.6.26: Failure for pull test G40EB.

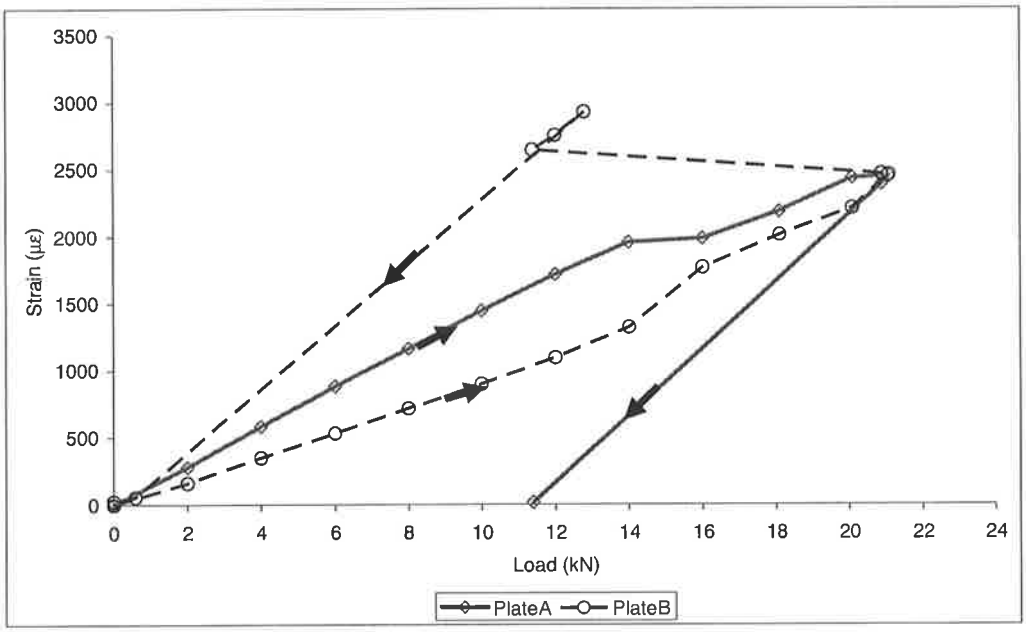

Figure 5.6.27: Strain profile for pull test G40EB.

5.6.10 Pull Test G50EB

This experiment failed at a load of 21.4 kN, which was similar to that for the 40 mm gap test. Figure 5.6.28 shows debonding of Plate A and also shows that the test had only 4 strain gauges. The failure pattern for this two EB plated specimen is shown in Figure 5.6.29 with cracks along the plate lengths and thin layers of concrete attached to both of the CFRP plates.

Figure 5.6.30 again shows the typical strain profile (average strain on each plate) and also shows what was observed form the experiment that Plate A debond first. At 21.4 kN, Plate B has the highest strain and this was followed by debonding of Plate A. Immediately after Plate A debonded, the load dropped to 12.1 kN and Plate B now sustained the load. Plate B managed to continue sustaining a small increment of load before dropping to 11.6 kN which was followed by Plate B debonding. All of this is shown in Figure 5.6.30 with the typical circle.

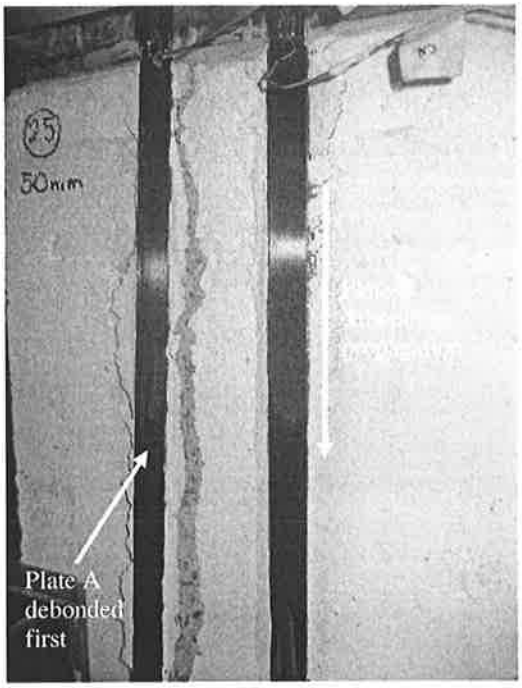

Figure 5.6.28: Debonding of Plate A.

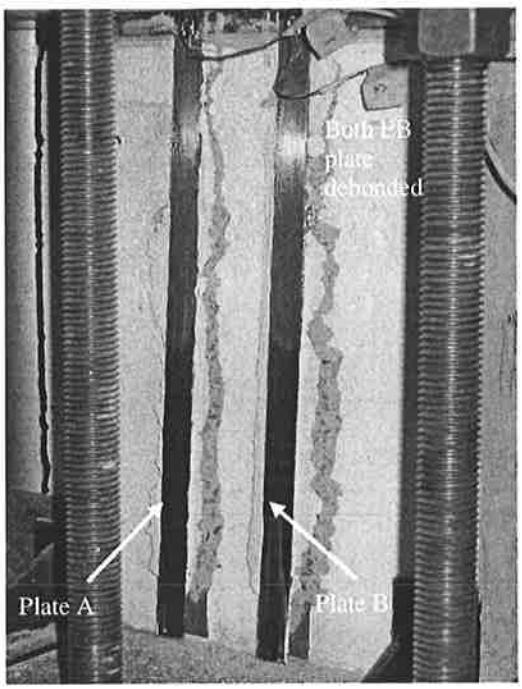

Figure 5.6.29: Failure for pull test G50EB.

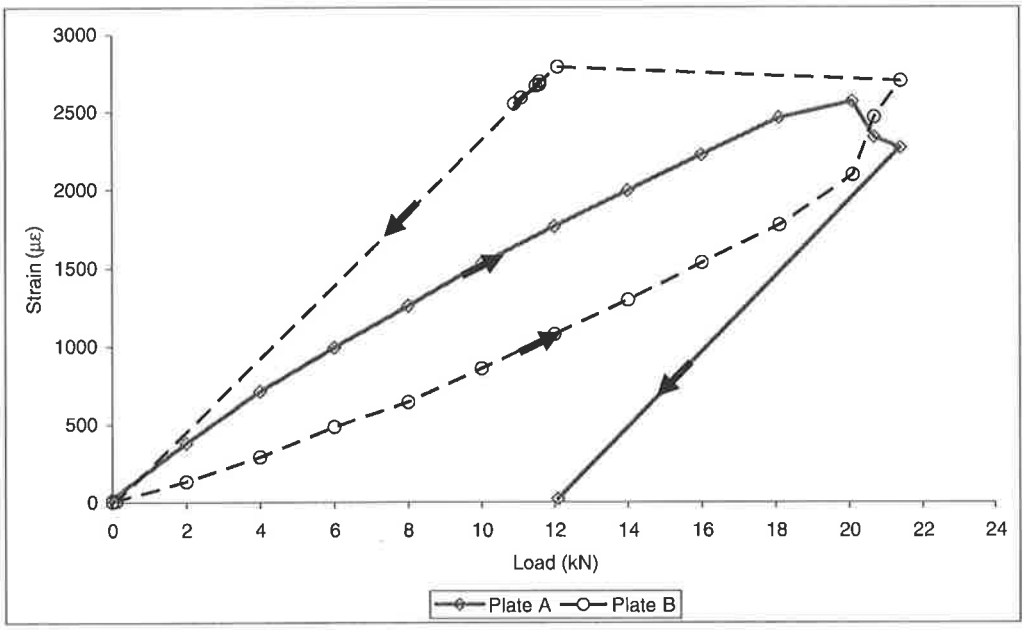

Figure 5.6.30: Strain profile for pull test G50EB.

5.6.11 Pull Test G60EB

This experiment failed at a loading of 24.0 kN, which was a slightly higher failure load compared to the 50 mm gap test and double the failure for a single plate. Figure 5.6.31 shows debonding of Plate A and also shows that the test has only 4 strain gauges. The failure pattern for this two EB plated specimen is in Figure 5.6.32 with cracks along the plate length and a thin layer of concrete attached to both of the CFRP plates.

Figure 5.6.33 again shows the typical strain profile and also shows what was observed form the experiment that Plate A debonded first. At 24.0 kN, Plate A has the highest strain between the plates which is followed by debonding of Plate A. Immediately after this the load dropped to 11.4 kN with Plate B now sustaining the load. Plate B managed to continue sustaining a small increment of loading to 13.4 kN before dropping to 11.9 kN and then Plate B debonded.

From all the EB tests, shows that any spacing distance between EB plates allows the plates fail individually. The crack patterns around the plates were the same as that for the reference beam G0EB which had an individual plate, suggesting individual plate debonding as opposed to group plate debonding. Next, the tests for the interaction with cover for NSM plates are described.

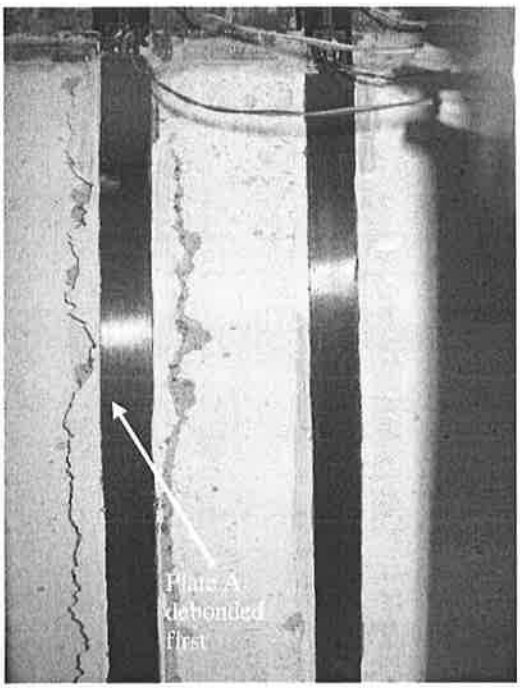

Figure 5.6.31: Debonding of Plate A.

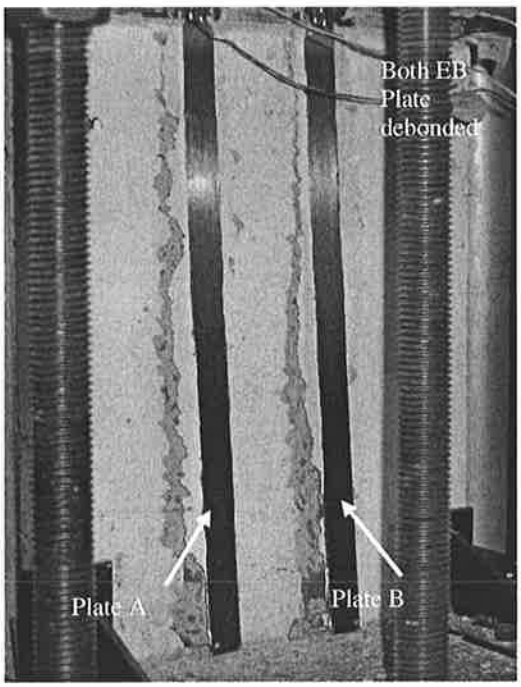

Figure 5.6.32: Failure for pull test G60EB.

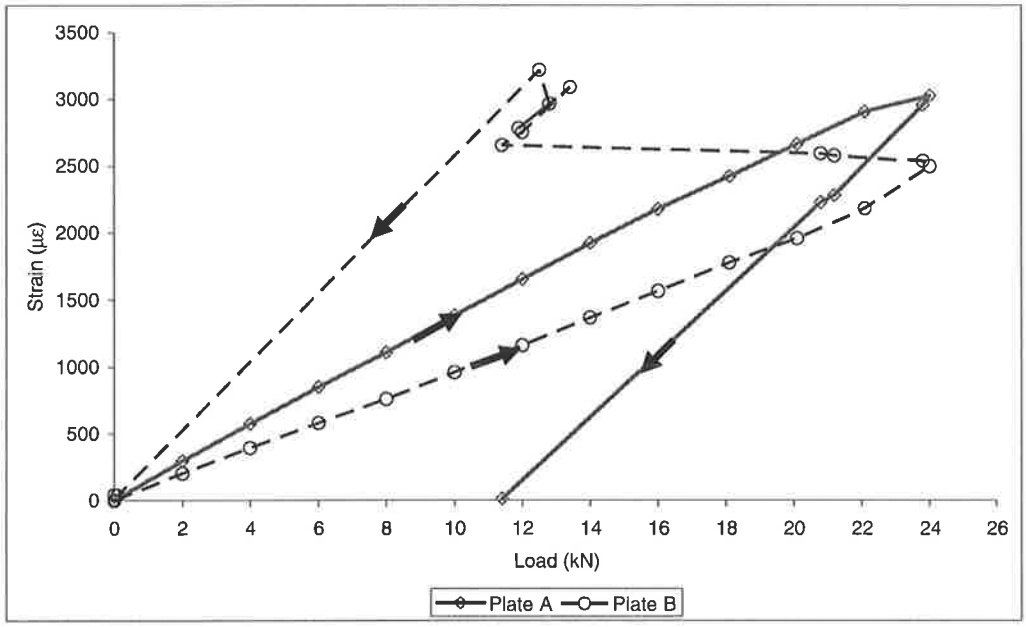

Figure 5.6.33: Strain profile for pull test G60EB.

5.6.12 Pull Test C150NSMa (G0NSM)

All the pull tests discussed earlier are for series 1 tests. For series 2 pull test, the tests look at the interaction of a 20 mm x 1.4 mm NSM plate with cover. The reference test is the NSM plate located 150 mm from the edge of concrete block which is test G0NSM in section 5.6.1, renamed here as C150NSMa.

5.6.13 Pull Test C10NSMa

Figure 5.6.34 shows the crack propagation for the 10 mm edge distance pull test. The transducer, as described earlier in the instrumentation section 5.4 and in Figure 5.4.10 was located 50 mm for T1 and 200 mm for T2 from the top of concrete block and at the centre of the plate depth (d_p). The failure load for this test was 22.4 kN with concrete peeling off on the outer side of the concrete block shown in Figure 5.6.35.

The transducer measuring the lateral concrete displacement as the plate is being pulled. In Figure 5.6.36 there is not much displacement when loading until just after the peak load T1 giving the maximum displacement of 2.9 mm. This failure load shows that 10 mm is not a suitable cover for plating when compared with the single and middle plate failure load of 63 kN.

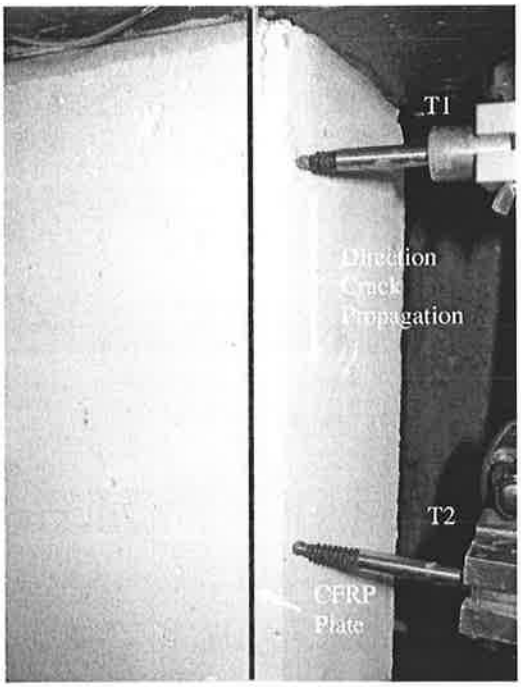

Figure 5.6.34: Crack propagation for C10NSMa pull test.

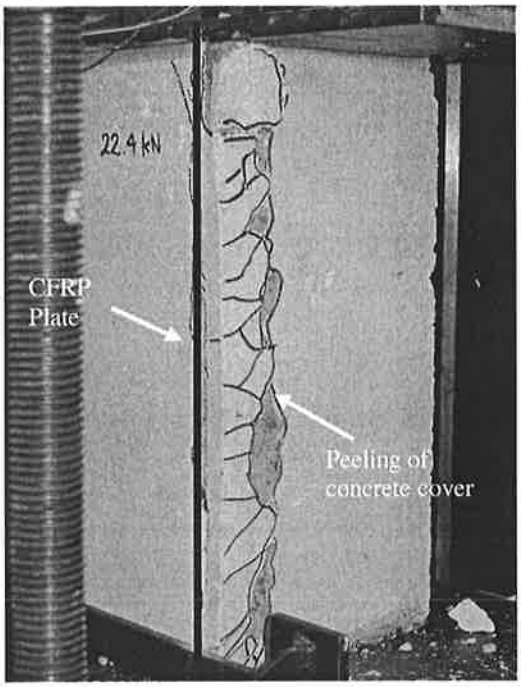

Figure 5.6.35: Failure for pull test C10NSMa.

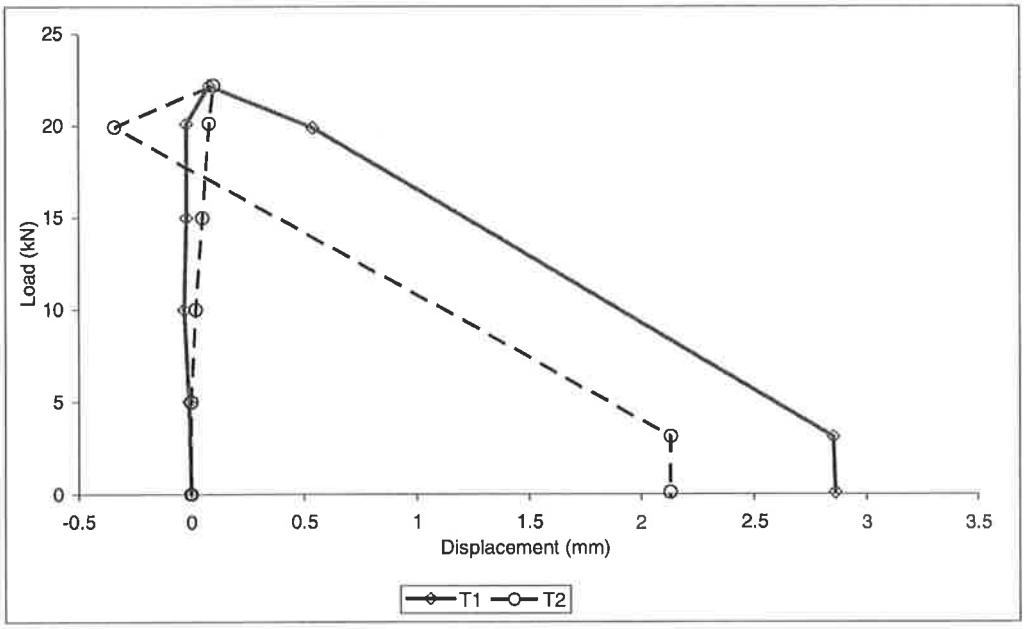

Figure 5.6.36: Load displacement graph for C10NSMa.

5.6.14 Pull Test C20NSMa

The failure load for this test was 34.2 kN with concrete peeling off on the outer side of the concrete block as shown in Figure 5.6.37. In Figure 5.6.38, not much lateral displacement occurred whilst loading until prior to failure with T1 giving a maximum displacement of 24.9 mm.

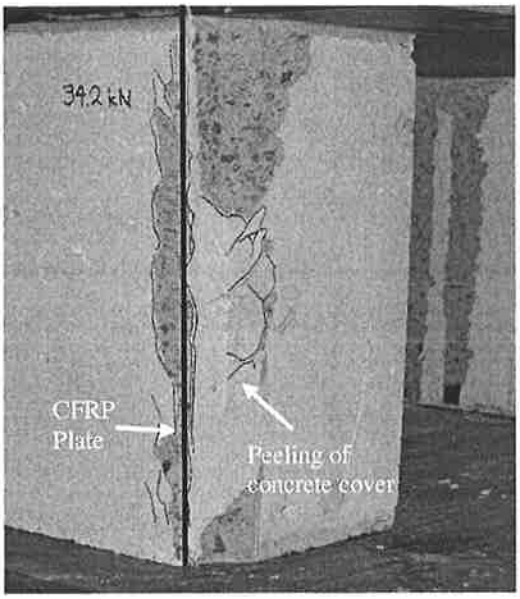

Figure 5.6.37: Failure for pull test C20NSMa.

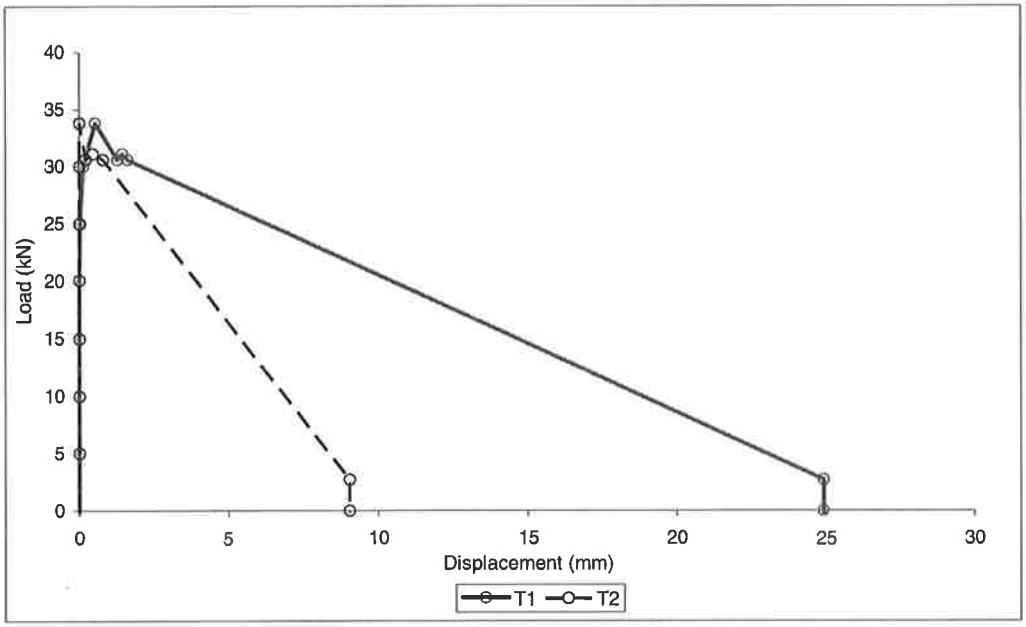

Figure 5.6.38: Load displacement graph for C20NSMa.

5.6.15 Pull Test C30NSMa

The failure load for this test was 40.6 kN with typical failure of concrete peeling off on the outer side of the concrete block shown in Figure 5.6.39. In Figure 5.6.40 as in the previous tests, not much lateral displacement occurred until the peak load was approached.

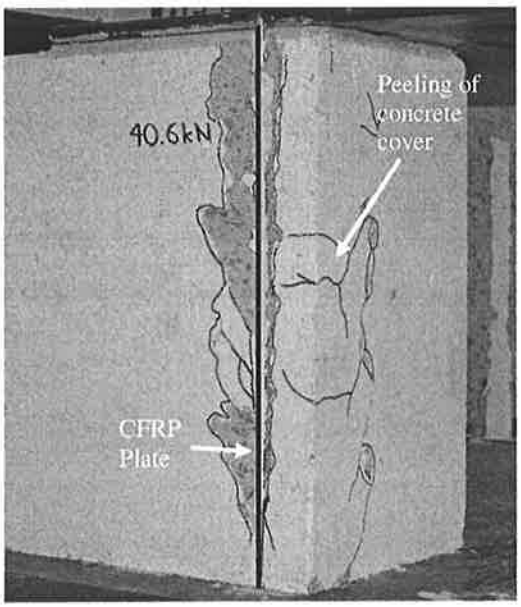

Figure 5.6.39: Failure for pull test C30NSMa.

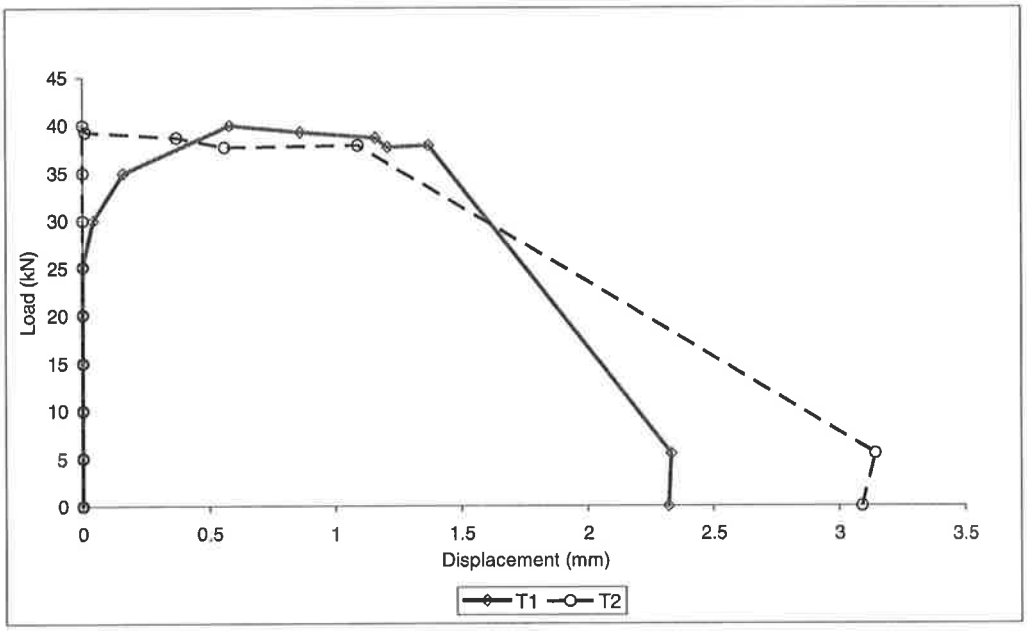

Figure 5.6.40: Load displacement graph for C30NSMa.

5.6.16 Pull Test C40NSMa

The failure load for this test was 50.2 kN with typical failure of concrete peeling off on the outer side of the concrete block as shown in Figure 5.6.41.

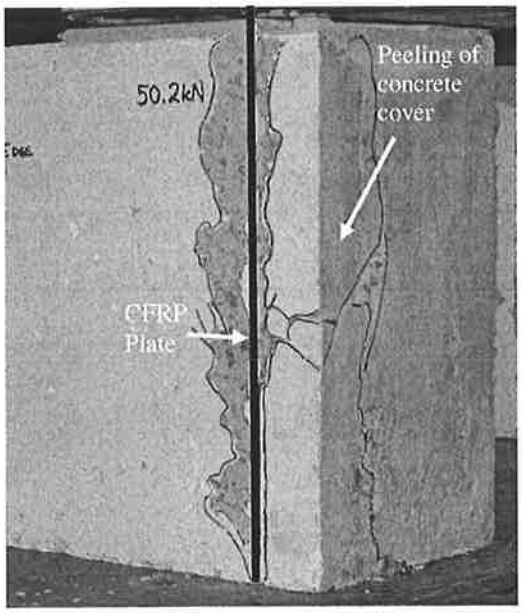

Figure 5.6.41: Failure for pull test C40NSMa.

5.6.17 Pull Test C60NSMa

The failure load for this test was 59.2 kN with typical failure of concrete peeling off on the outer side of the concrete block shown in Figure 5.6.42. The lateral displacement is shown in Figure 5.6.43.

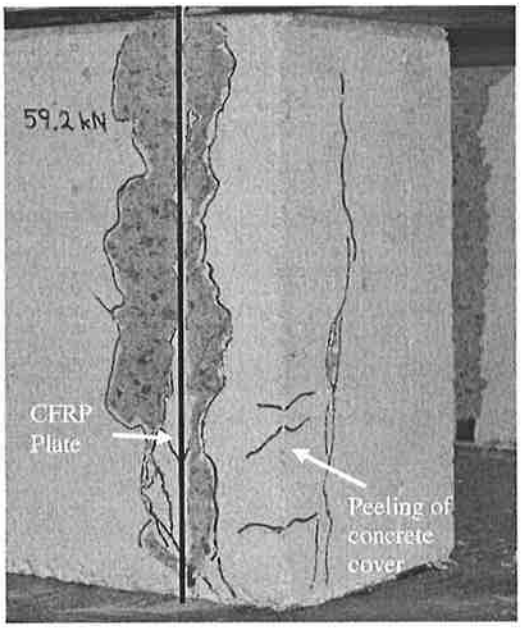

Figure 5.6.42: Failure for pull test C60NSMa.

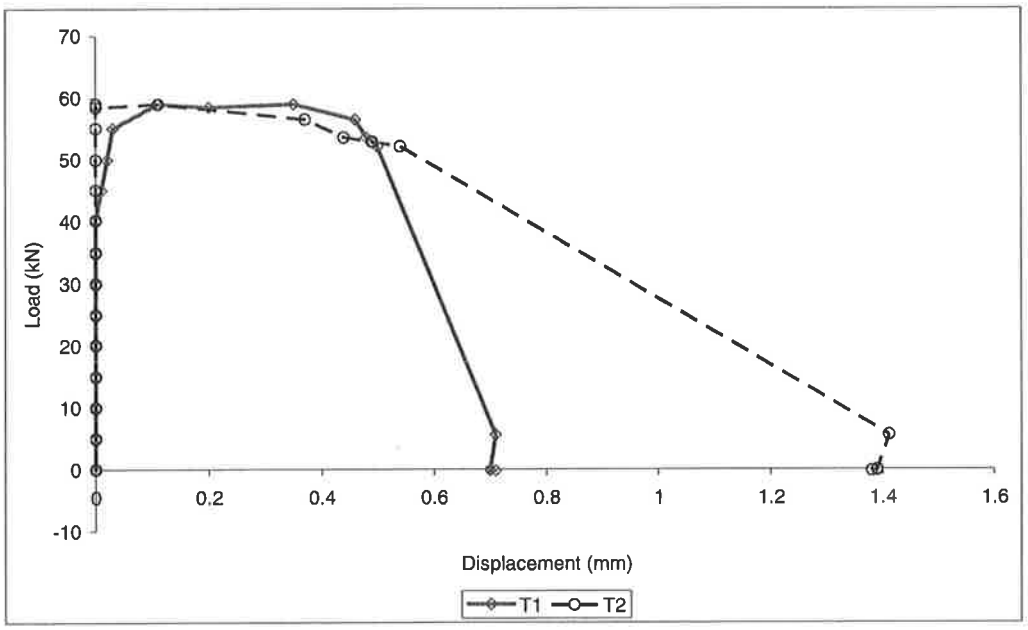

Figure 5.6.43: Load displacement graph for C60NSMa.

5.6.18 Pull Test C85NSMa

The failure load for this test was 75.7 kN with typical failure of concrete peeling off on the outer side of the concrete block shown in Figure 5.6.44 with the lateral displacement in Figure 5.6.45. It can be seen that the lateral displacement are much smaller than in previous test suggesting that the cover remain intact so that this cover is suitable.

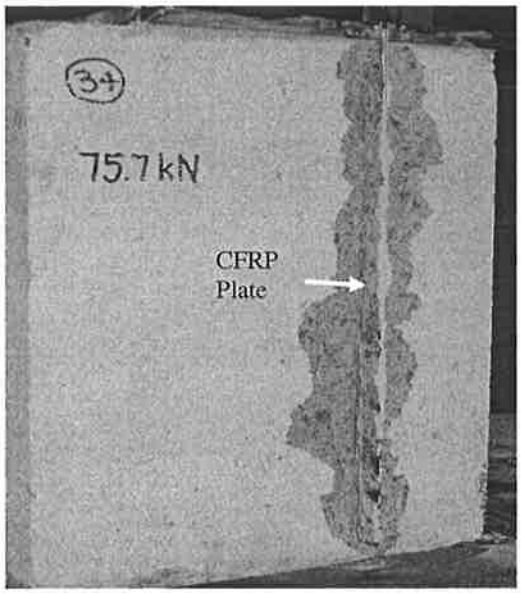

Figure 5.6.44: Failure for pull test C85NSMa.

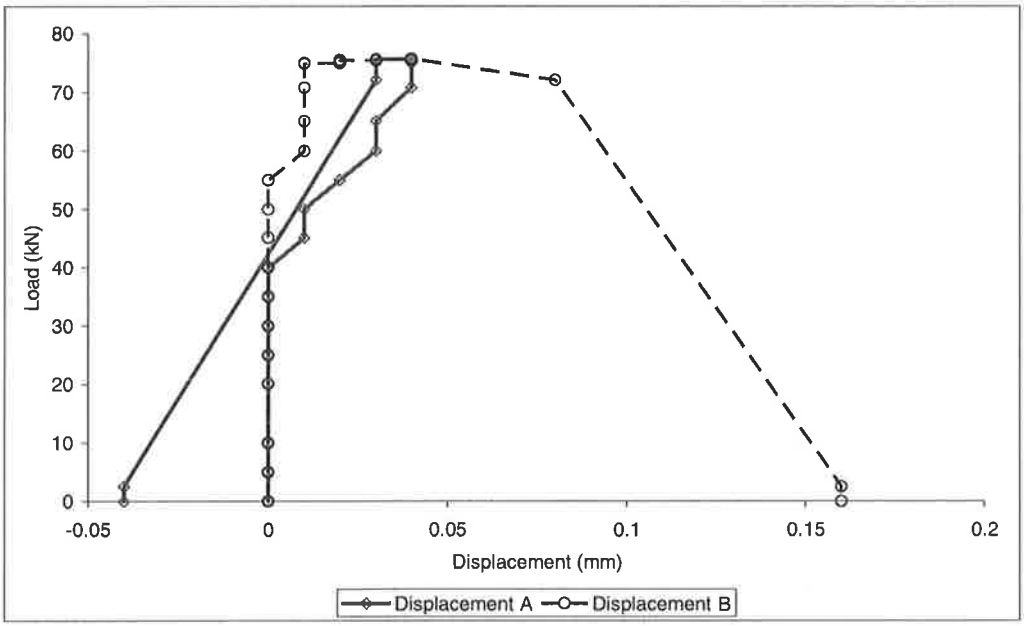

Figure 5.6.45: Load displacement graph for C85NSMa.

5.6.19 Pull Test C150NSMb

The pull test series 2 experiments continues using 40 mm x 2.4 mm plate dimensions to look into the plate size effect on the edge effect. In this test, the plate is located 150 mm from the edge of the concrete block. This is considered to be the reference pull test for this plate size. The failure load for this test was 205.1 kN with the typical plate debonding associated with of 'herring bone' cracks shown in Figure 5.6.46. However in this test, the concrete block split into two pieces which did not happen in other previous tests. The reason of this happening was because this was a pull push test with plate depth of 40 mm and a high debonding load of 205.1 kN; the impact to the test rig base cause by the release or debonding; split the concrete block into two (Figure 5.6.47).

In Figure 5.6.48 and similarly to the previous tests, not much lateral displacement occurred prior to failure. Figure 5.6.48 confirms that the splitting of concrete block happened immediately after failure. Next using the same plate size, the cover is decreased to 50mm.

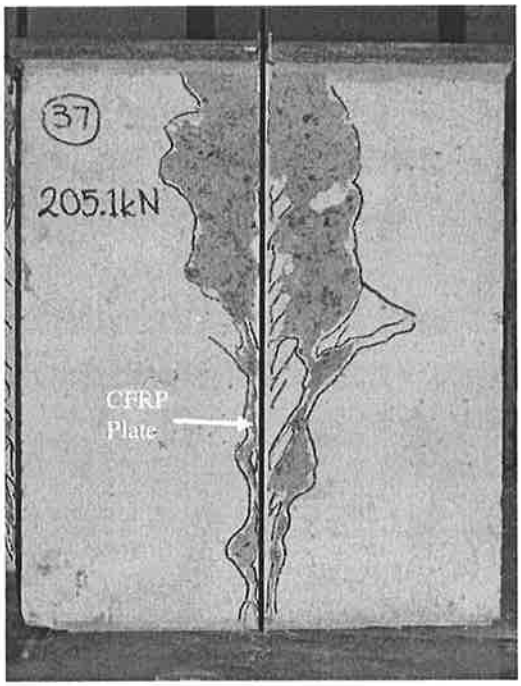

Figure 5.6.46: Failure for pull test C150NSMb.

Figure 5.6.47: Splitting of concrete block.

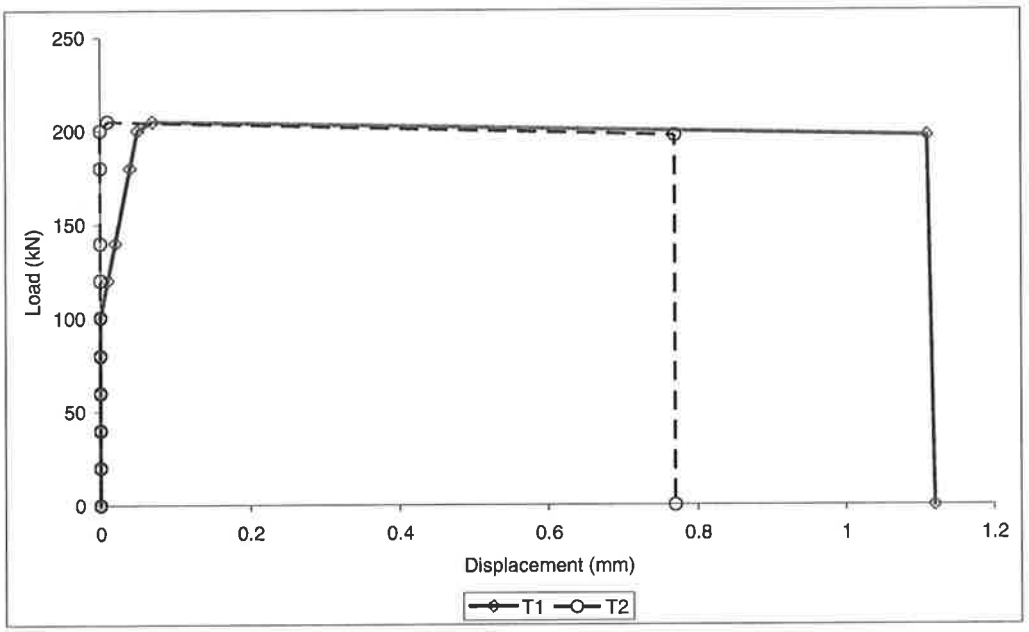

Figure 5.6.48: Load displacement graph for C150NSMb.

5.6.20 Pull Test C50NSMb

The failure load for this test was 119.9 kN with typical failure of concrete by peeling off on the outer side of the concrete block with the appearance of 'herring bone' cracks as shown in Figure 5.6.49. The lateral displacement is given in Figure 5.6.50.

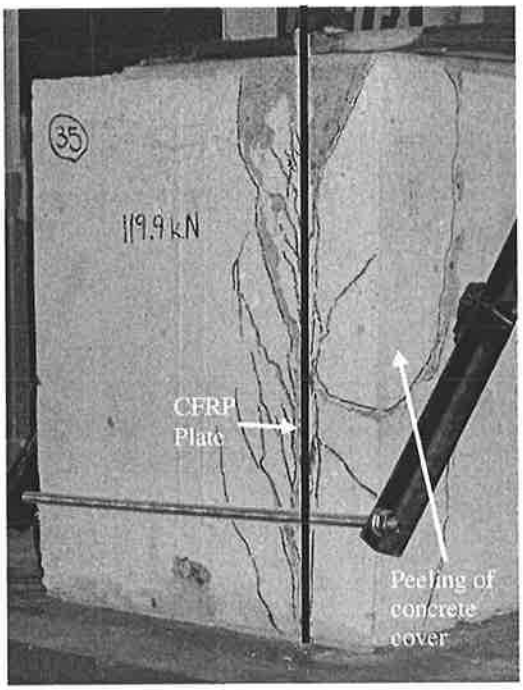

Figure 5.6.49: Failure for pull test C50NSMb.

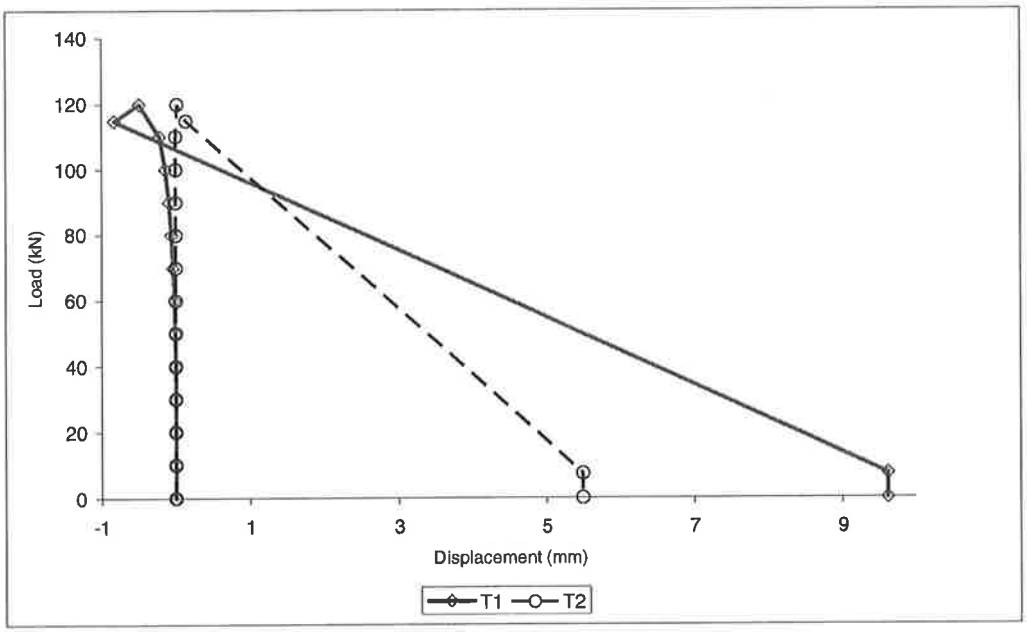

Figure 5.6.50: Load displacement graph for C50NSMb.

5.6.21 Pull Test C75NSMb

The failure load for this test was 170.9 kN with typical failure of concrete by peeling off on the outer side of the concrete block with the appearance of 'herring bone' cracks shown in Figure 5.6.51. The lateral displacement is shown in Figure 5.6.52.

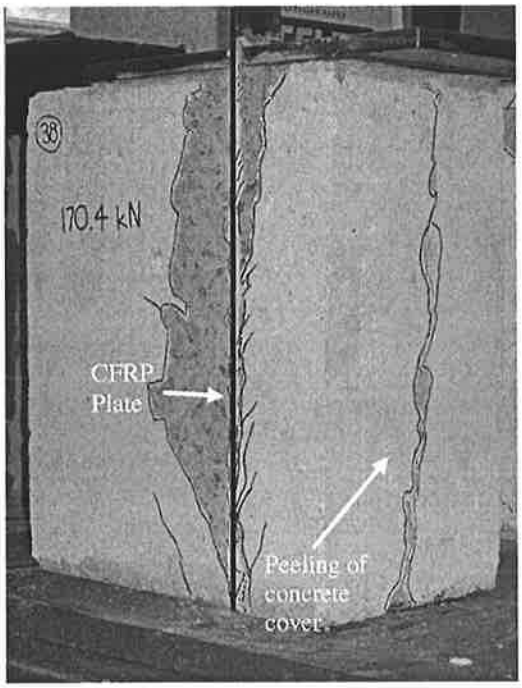

Figure 5.6.51: Failure for pull test C75NSMb.

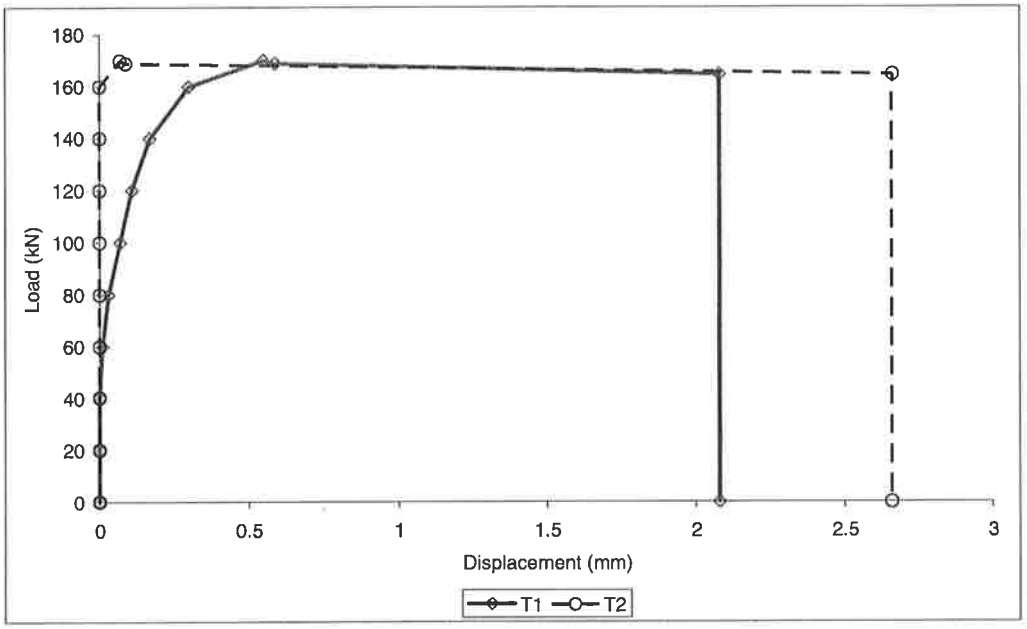

Figure 5.6.52: Load displacement graph for C75NSMb.

5.6.22 Pull Test C100NSM

The failure load for this test was 194.9 kN with typical failure of concrete by peeling off on the outer side of the concrete block with the appearance of 'herring bone' cracks shown in

Figure 5.6.53. However in this test, the concrete block split into two pieces as in Figure 5.6.53 similarly to the reference pull test in Figure 5.6.47. Furthermore the plate split as in Figure 5.6.54. The lateral displacement is shown in Figure 5.6.56.

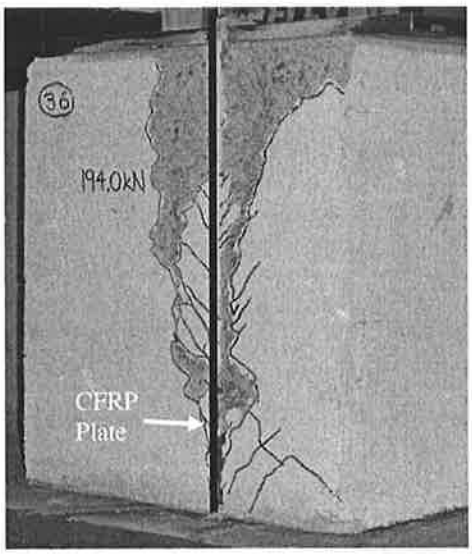

Figure 5.6.53: Failure for pull test C100NSMb.

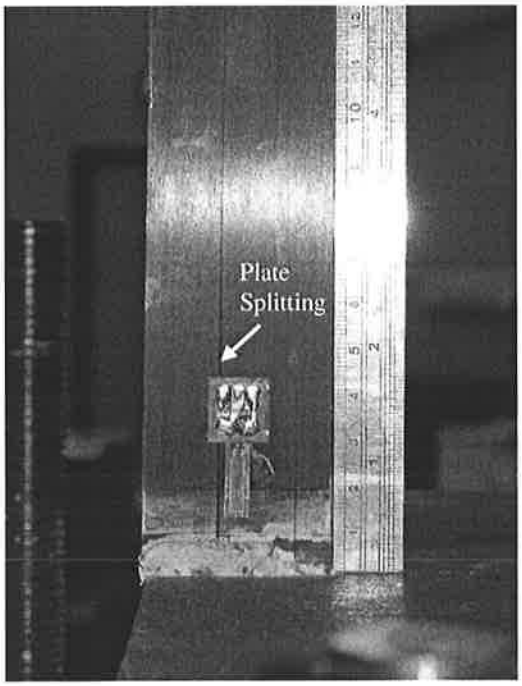

Figure 5.6.54: Splitting of plate for 100mm edge.

Figure 5.6.55: Splitting of concrete block for 100mm edge.

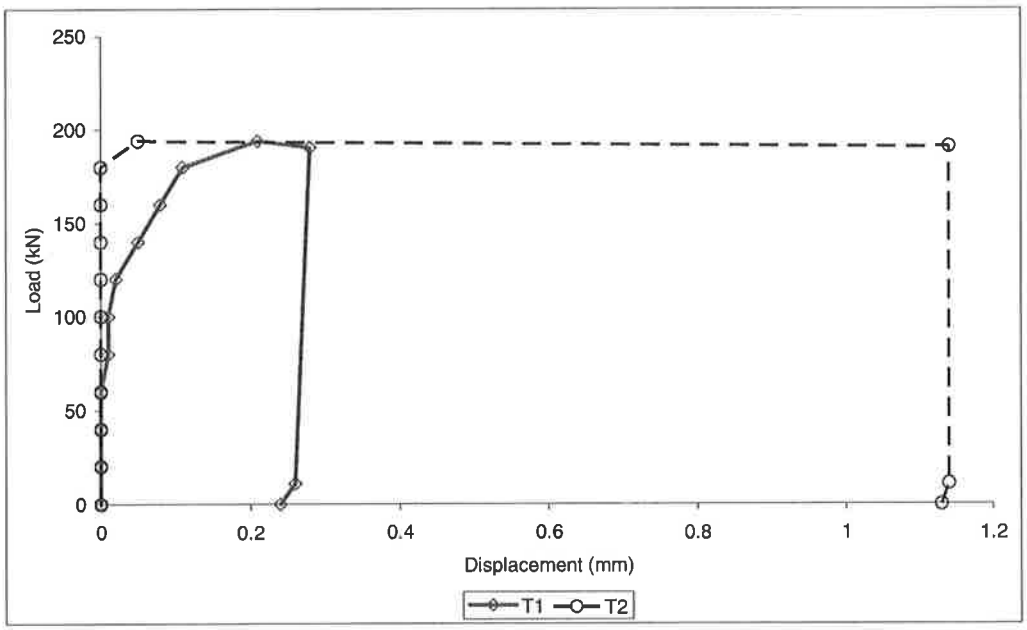

Figure 5.6.56: Load displacement graph for C100NSMb.

5.7 Discussion of Test Results

This section summarises all the pull tests beginning with the NSM plate specimens. The single pull test result plotted on Figure 5.7.1 is the average from two pull tests and this result is consider as a reference test. As mentioned previously, a pull test that reaches more than double the single plate failure indicates that the plates have failed as individual plates. Figure 5.7.1 shows that NSM plates with gaps greater than 53 mm measured from side to side, fail individually that is without any interaction between the plates.

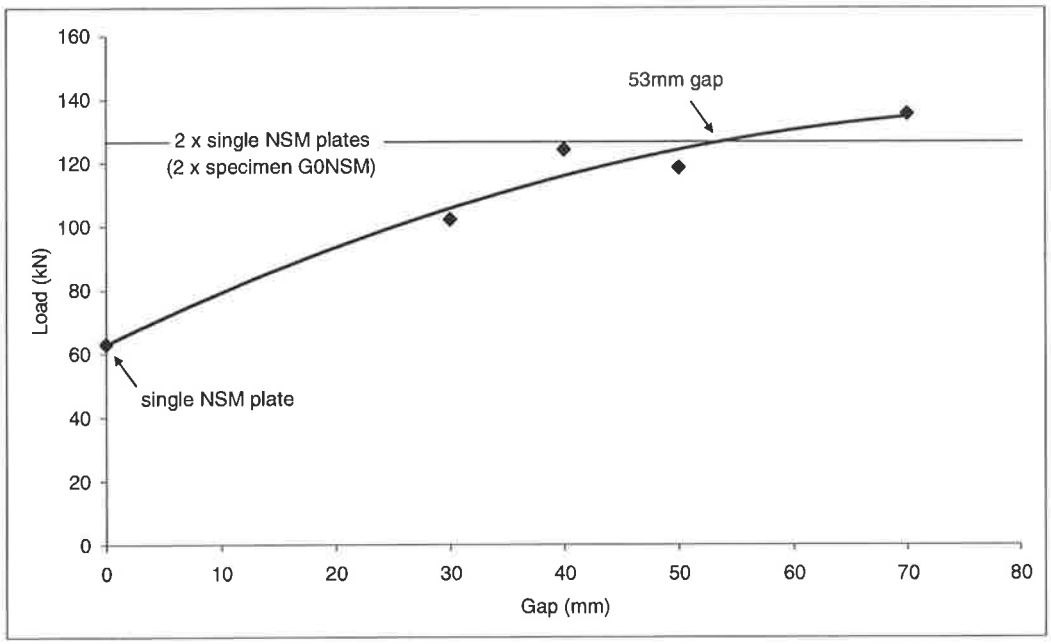

Figure 5.7.1: Summaries of NSM interaction results in series 1.

Similarly for the EB plate interaction pull tests, the single plate result is also used as a reference result. Also mentioned previously, two pull tests were done for the 30 mm gap with and without restraining the specimen, only GEB30r were plotted in Figure 5.7.2. It can be seen that plates with any gap distance is considered to fail as single plate without any interaction.

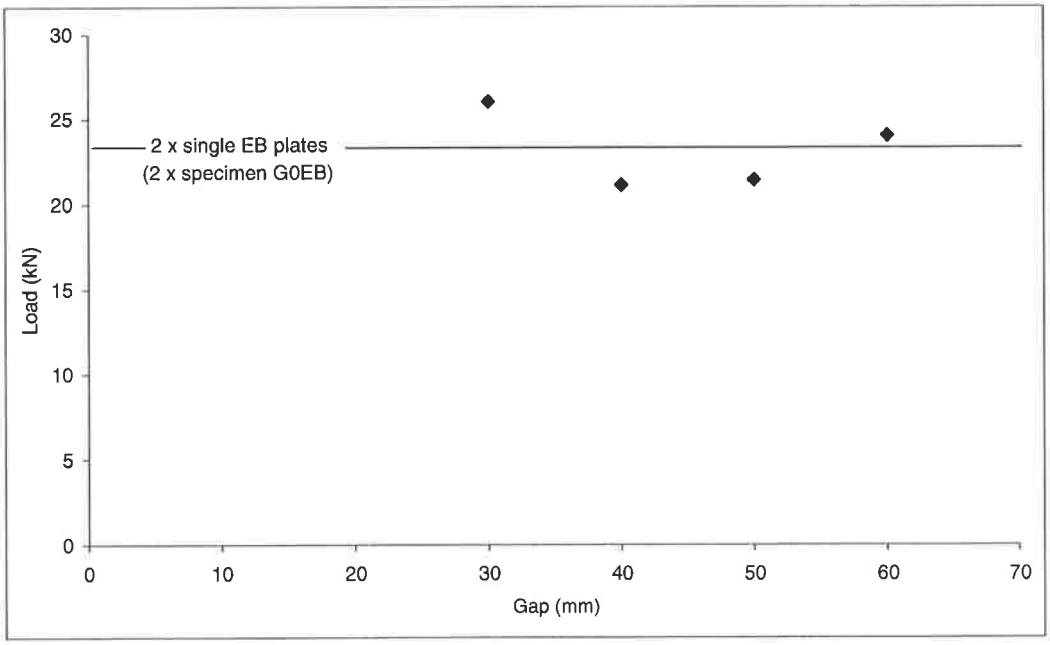

Figure 5.7.2: Summaries of EB interaction results in series 1.

Figure 5.7.3 shows results for the cover series 2 for the 20 mm x 1.4mm CFRP NSM plate. All of the tests are compared with the pull test located at the centre of the concrete block that is with 150 mm cover. From Figure 5.7.3, it can be seen that a cover of 68 mm ensures that the full strength is reached.

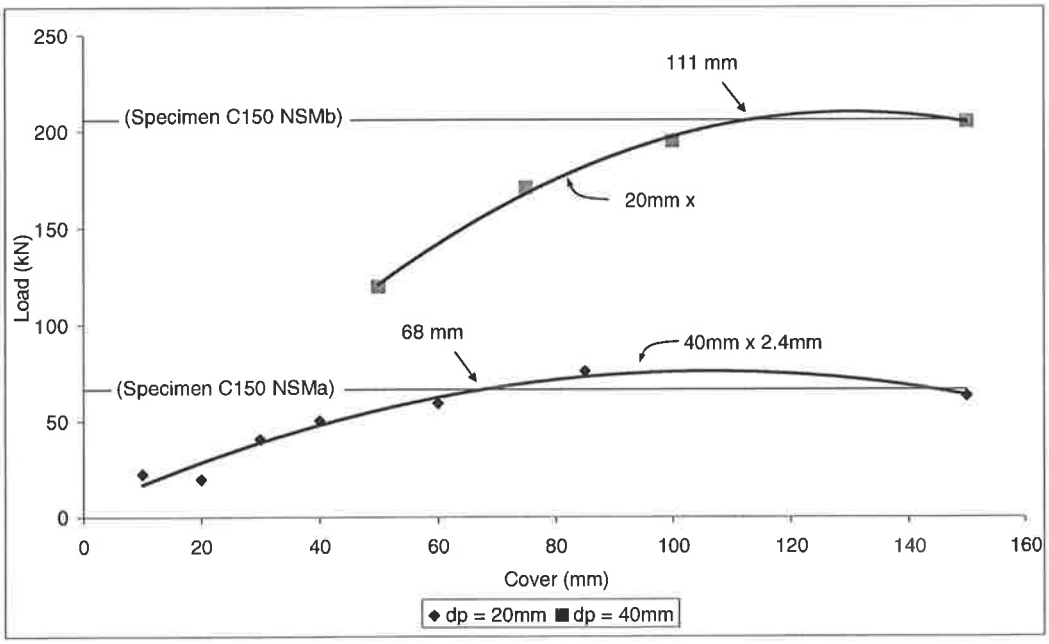

Figure 5.7.3: Cover interaction for 20 mm by 1.2 mm and 40 mm by 2.4 mm CFRP NSM plates.

Also in Figure 5.7.3 shows the results for the cover series 2 for the 40 mm x 2.4mm CFRP NSM plates. All of the tests are compared to the pull test with the NSM plate located on the centre of the concrete block that is 150 mm cover. From Figure 5.7.3, a 111 mm cover ensures full strength.

The results in Figure 5.7.3 are plotted non-dimensionally in Figure 5.7.4 with the cover c in terms of the depth of the plate d_p and the reduced IC debonding resistance with cover $(P_{IC})_{cover}$ in terms of the standard IC debonding resistance $(P_{IC})_{stand}$ associated with NSM plates with plenty of cover. The reduced strength due to lack of cover would appear to vary linearly with a mean value of

$$(P_{IC})_{cover} = (P_{IC})_{stand}\left[0.283\frac{c}{d_p} + 0.196\right] \tag{5.7.1}$$

where the 95% characteristic value can be determined by substituting the coefficient 0.196 with 0.0006 and which for all intents and purposes is zero. Based on the characteristic value, a cover greater than $3.5d_p$ should prevent any reduction in strength.

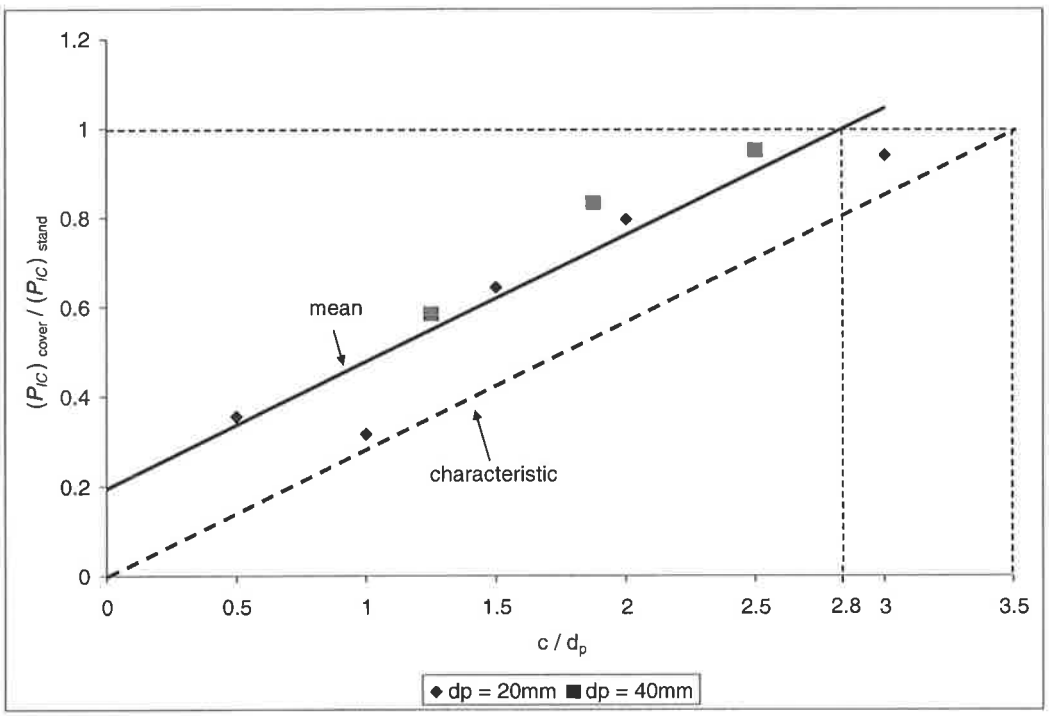

Figure 5.7.4: Reduction in IC debonding resistance.

5.8 Conclusion

A total of 22 pull tests were done in this series of pull tests which included 3 reference tests for each plating method and 2 tests that failed prematurely due to grip failure.

The conclusions that can be made from all of these tests is that for the NSM plating method, the minimum gap between plates was found to be 53 mm and that the for any gap distance EB plates was found to be failing individually.

Meanwhile for the interaction with cover; for 20 mm x 1.4 mm NSM plates the minimum cover was 62 mm and for the 40 mm x 2.4 mm NSM plate the minimum cover was 144 mm.

As a rule of thumb, the cover distance can be simplified as $3.1d_p$ for the 20 mm x 1.4mm CFRP NSM plate and $2.8d_p$ for the 40 mm x 2.4mm CFRP NSM plate as shown in Figure 5.8.1 and Figure 5.8.2.

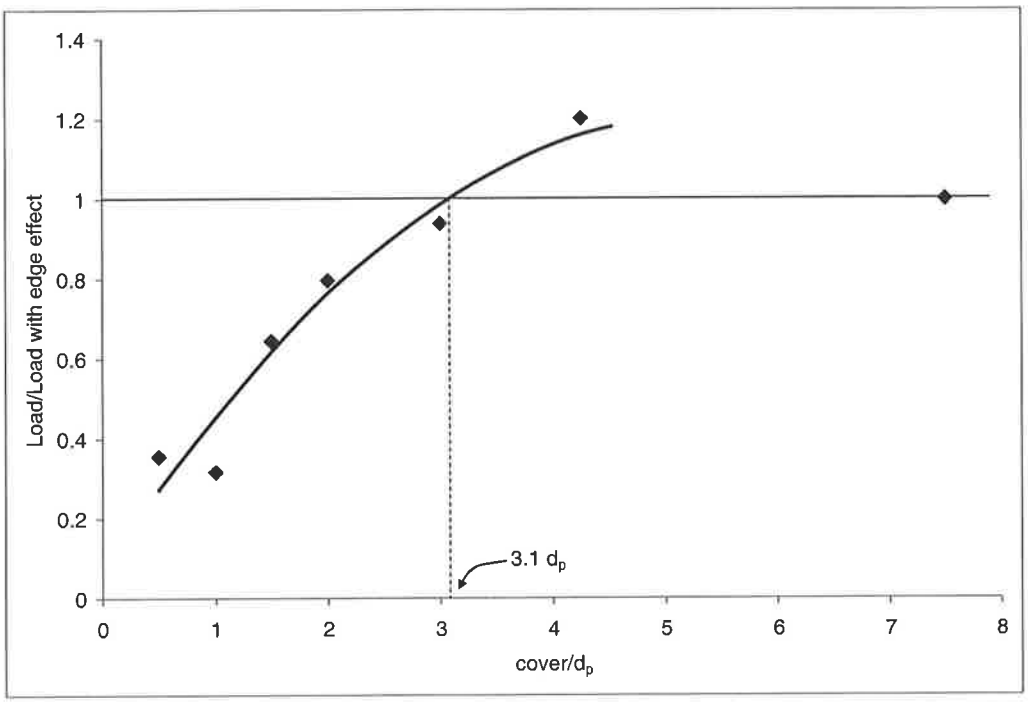

Figure 5.8.1: Summaries of edge effect for 20 mm x 1.4 mm plate in series 2.

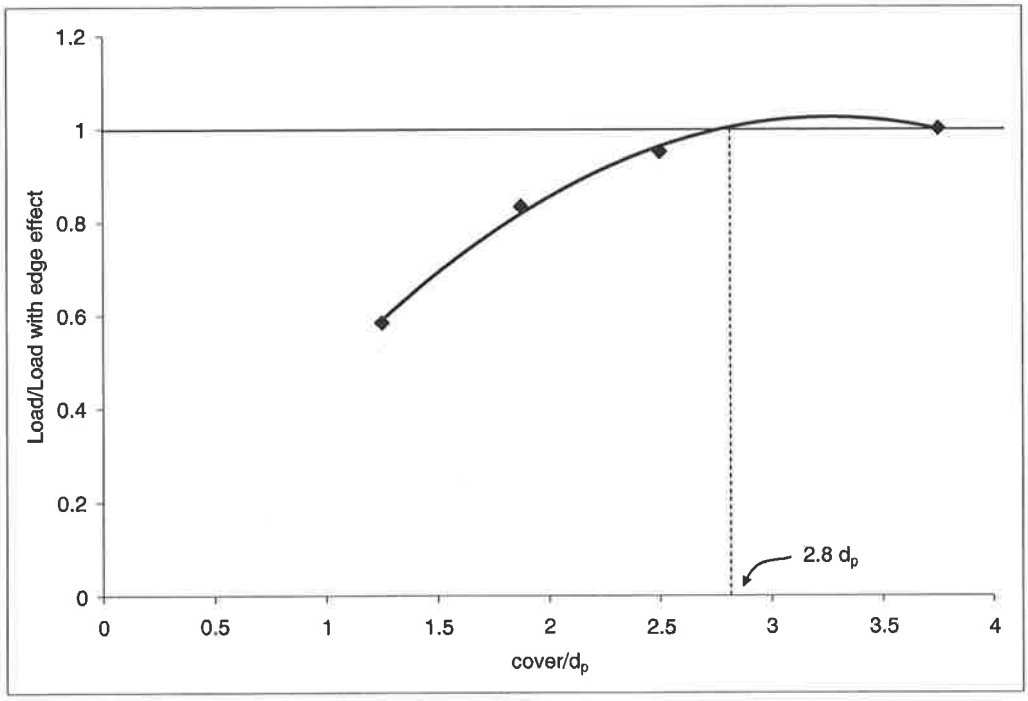

Figure 5.8.2 Summaries of edge effect for 20 mm x 1.4 mm plate in series 2.

5.9 Reference

1. Jones, N. (2004). Investigation into the use of FRP NSMR in Strengthening RC beams. Adelaide, School of Civil and Environmental Engineering, University of Adelaide.: 1-24.

Chapter

6 ANALYSIS OF PULL TEST – PLATE INTERACTION

6 ANALYSIS OF PULL TEST – PLATE INTERACTION

6.1 Introduction

This chapter will elaborate on the analysis of the double Near Surface Mounted (NSM) plated pull tests. Only NSM plates are analysed because of the huge amount of concrete detached when groups of plates fail as a single failure plane as compared to EB plates which usually fail individually.

The next section of this chapter will cover the tests results and the analysis of the results. Then, conclusions made from all the test results are discussed.

6.2 Test Results

Table 6.2.1: Summaries of test results.

Test	Gap (mm)	Type of Plating	E_p (MPa)	E_c (MPa)	d_p (mm)	b_p (mm)	f_c (MPa)	Ave. Max. Strain ε_u ($\mu\varepsilon$)	Ult. Load P_u (kN)
G30NSM	30	NSM	161455	37354	20	1.4	36.7	11143	102.3
G40NSM	40	NSM	161455	37354	20	1.4	36.7	13445	124.3
G50NSM	50	NSM	161455	37354	20	1.4	36.7	12686	118.5
G70NSM	70	NSM	161455	37354	20	1.4	36.7	15297	135.5
NB_F2	73	NSM	173501	30537	15.2	1.24	36.4	10236	66.8
NB_F3	71	NSM	140141	30537	15.0	2.77	36.4	8235	97.2
NS_F1	62	NSM	173501	38578	20.46	1.22	37.1	7441	161.1
NS_F2	124	NSM	173501	38578	15.54	1.24	37.1	14590	97.6

The test results available for the analysis in Table 6.2.1 are from the double plate pull tests in Chapter 5 and previous beam tests by Liu (2005). In Table 6.2.1, average maximum strain is the average of maximum strain in the plates while the ultimate load is the ultimate load per plate.

Observations from the experiments (chapter 5) showed that test G70NSM did not fail as a single failure plane. Furthermore for the slab NS_F2 test, comparison between the calculated strain (14383 microstrain) and experimental strain (Table 6.2.1) clearly showed that the plates failed individually. Hence, pull test G70NSM and slab NS_F2 test are not included in the analysis as both plates in these tests failed individually.

6.3 Analysis of Results

The generic equation (Eq. 6.3.1) for the intermediate crack debonding resistance of individual NSM plate was derived and described in chapter 3. It can be seen from the generic equation (Eq. 6.3.1) that the intermediate crack debonding load (P_{IC}) is proportional to the axial rigidity of the plate alone for a single plate (E_pA_p) without any contribution from the concrete axial rigidity of the small area of concrete attached to the plate. However, for two or more plates that fail in a single failure plane, the total axial rigidity encompassed by the failure plane depends on the number of plates (n), the plate axial rigidity and concrete axial rigidity. Hence adding the concrete axial rigidity, the generic equation for 'n' plates is now as shown in Eq. 6.3.2 where the term 'k' represents the reduction of the concrete axial rigidity due to cracking and interface slip. Figure 6.3.1 gives details of the parameters involved in the analysis. Next, each individual analysis of each test result is described.

$$P_{IC} = \sqrt{\tau_f \delta_f}\sqrt{L_{per}(EA)_p} \tag{6.3.1}$$

$$P_{IC} = \sqrt{\tau_f \delta_f L_{per}}\sqrt{n(EA)_p + (k(EA)_c)} \tag{6.3.2}$$

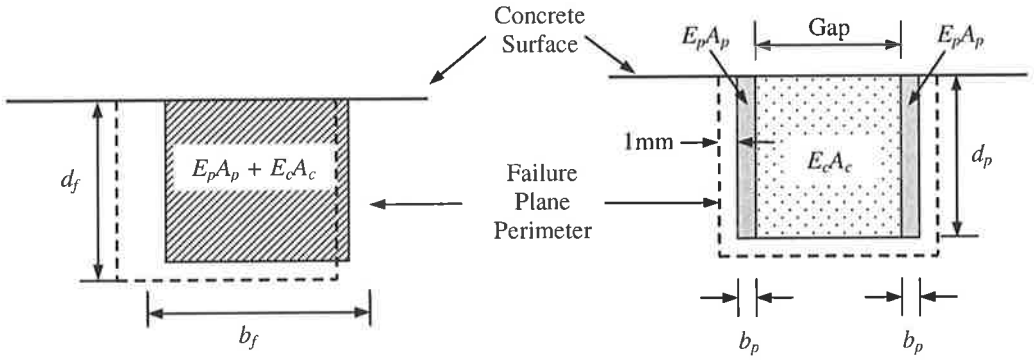

Figure 6.3.1: Details of parameters for the analysis.

6.3.1 Analysis of pull test G30NSM

The analysis begins with pull test G30NSM in Table 6.2.1 which failed at 102.3kN. Figure 6.3.2 shows the analysis from Eq. 6.3.2 where the theoretical value of P_{IC} divided with number of plates is drawn with 'k' ranging from 0 to 1 in increment of 0.05. The value of 51.15 kN shown in Figure 6.3.2, that is the experiment failure load line, intercept at a value

of '*k*' of 0.46 and the result is shown in Table 6.3.1. Next pull test G40NSM analysis is described.

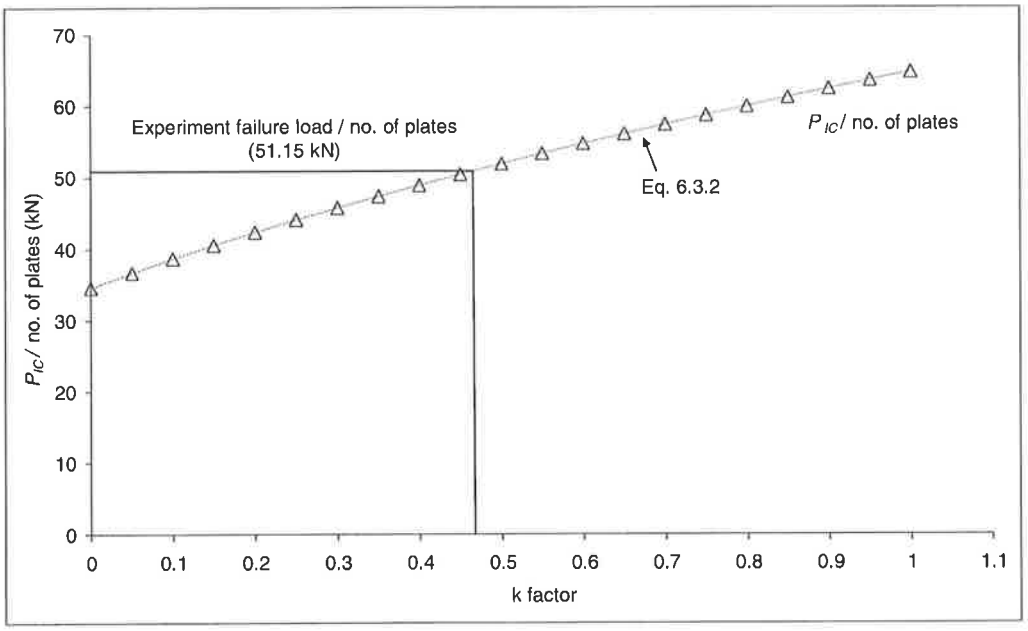

Figure 6.3.2: Analysis of pull test G30NSM.

Table 6.3.1: Summaries of the analysis.

Test	Number of plates	Gap (mm)	k	M_u	M_{cr}	M_u/M_{cr}
G30NSM	2	30	0.46	0	-	0
G40NSM	2	40	0.65	0	-	0
G50NSM	2	50	0.39	0	-	0
NS_F1	5	62	0.07	24.95	3.28	7.61
NB_F2	2	73	0.10	73.11	7.60	9.62
NB_F3	2	71	0.30	79.50	7.60	10.46

6.3.2 Analysis of pull test G40NSM

The failure load for this test in Table 6.2.1 is 124.3 kN. The method of analysis in Figure 6.3.3 is the same as for pull test G30NSM and gives a value of '*k*' of 0.65. Next, the analysis of pull test G50NSM is described.

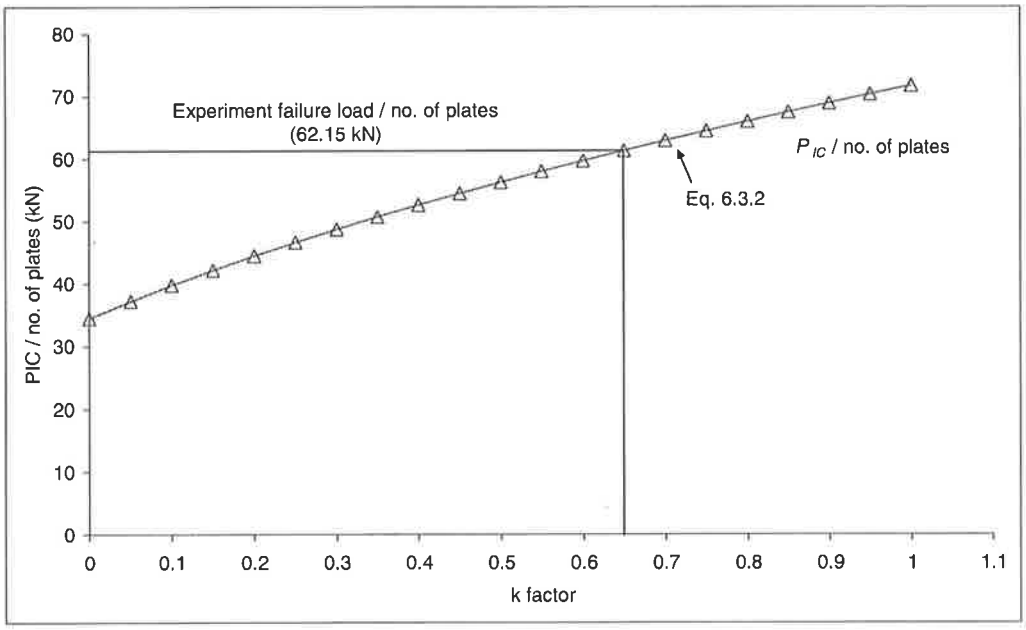

Figure 6.3.3: Analysis of pull test G40NSM.

6.3.3 Analysis of pull test G50NSM

The failure load for this test is 118.5 kN. Again, the method of analysis is the same as for pull tests G30NSM and G40NSM giving a value of '*k*' of 0.39 in shown in Figure 6.3.4. Next, the analysis of beam test NB_F2 in Table 6.2.1 is described.

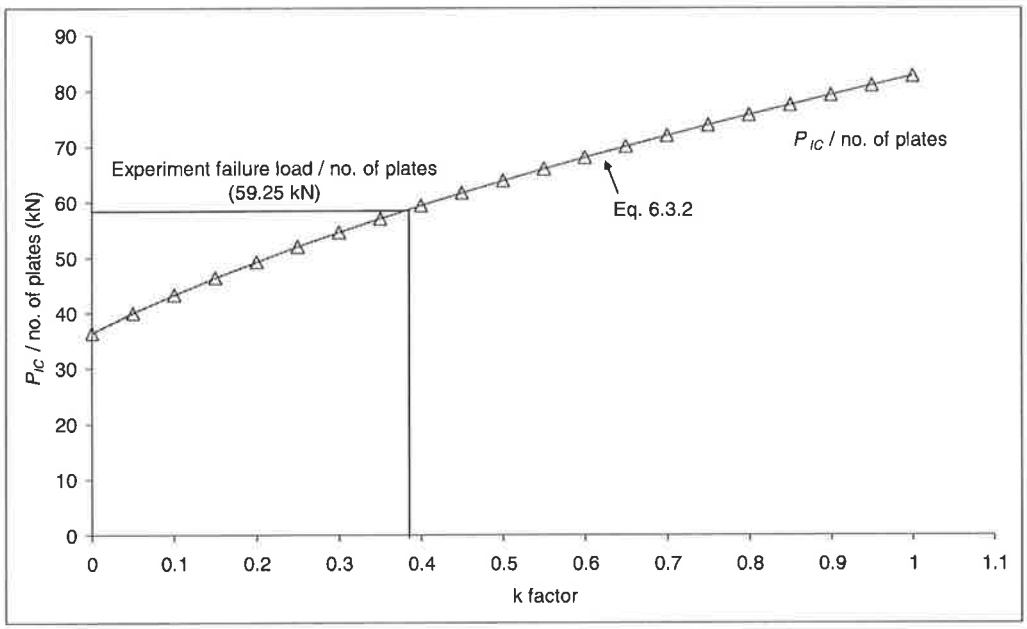

Figure 6.3.4: Analysis of pull test G50NSM.

6.3.4 Analysis of beam test NB_F2

The failure load for this test is 66.81 kN. The method of analysis is the same as for all the pull tests G30NSM, G40NSM and G50NSM giving a value of '*k*' of 0.10 as shown in Figure 6.3.5. Next the analysis of beam test NB_F3 is described.

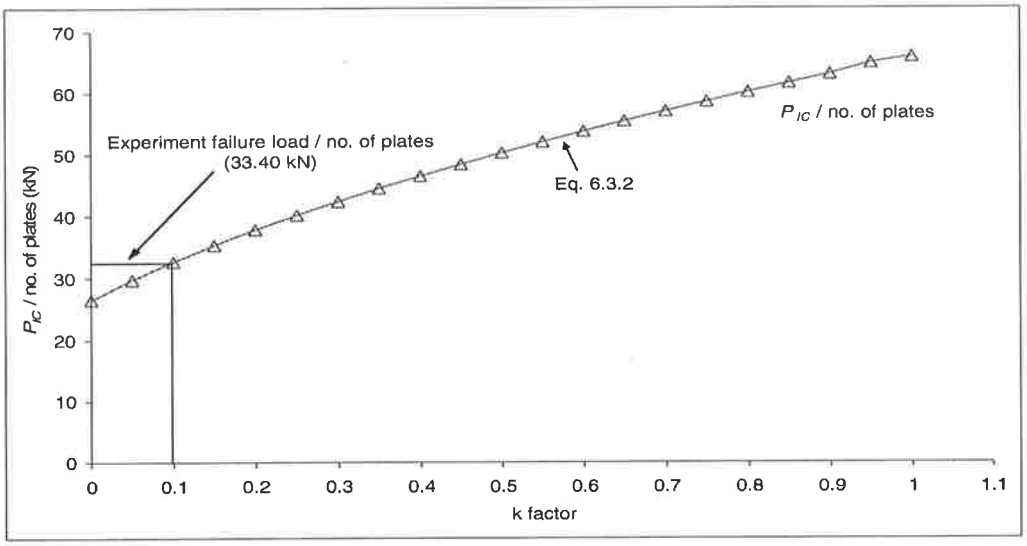

Figure 6.3.5: Analysis of beam test NB_F2.

6.3.5 Analysis of beam test NB_F3

The failure load for this test was 97.20 kN which gives k = 0.30 as shown in Figure 6.3.6. The plate gap for this beam test is 71 mm. Next, the analysis of slab test NS_F1 is described.

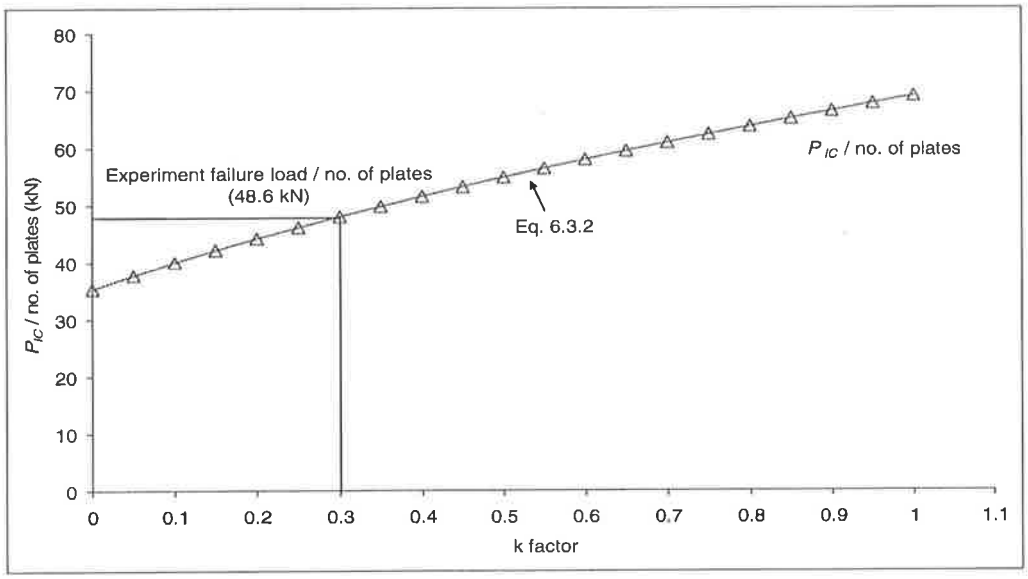

Figure 6.3.6: Analysis of beam test NB_F3.

6.3.6 Analysis of slab test NS_F1

The failure load for this test is 161.20 kN. The plate gap for this beam test is 62 mm with failure plane for number of plates is as shown in Figure 6.3.7. In Figure 6.3.8, the P_{IC} divide by the number of plates is shown. The single plate experimental gives '*k*' value of 0.07 shown in Figure 6.3.8. Looking at Figure 6.3.8, the lowest curve is for the 5 plate curve and hence this controls the debonding load, however this may not always be the case as it depended on the spacings or gaps. The intercept occurs at k = 0.07.

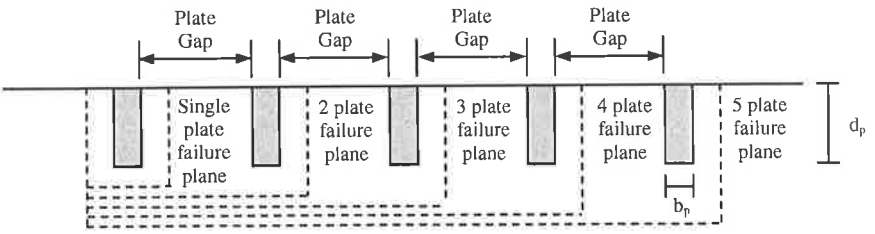

Figure 6.3.7: Failure plane diagram.

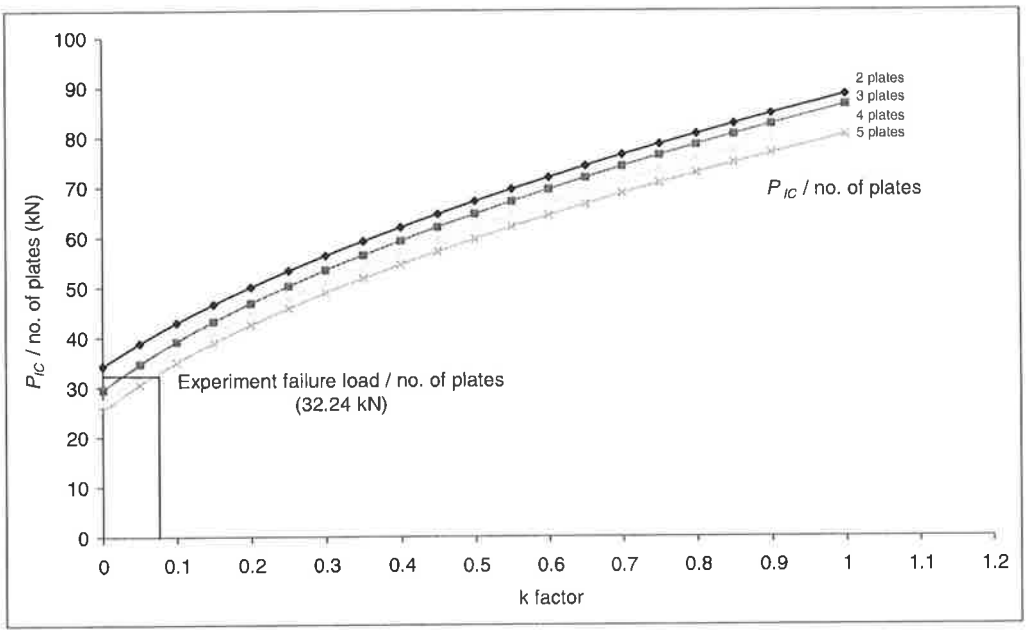

Figure 6.3.8: Analysis of slab test NS_F1.

6.4 Analysis of all test results

The six '*k*' values in Table 6.2.1 are plotted against the non-dimensional moment parameter *Mu/Mcr* in Figure 6.3.1 where M_u is the moment in the specimen at debonding which is

intermediate cracks resistant and M_{cr} is the moment to cause the specimen to crack as shown in Eq. 6.4.1. M_u and M_{cr} are given in Table 6.2.1. The reason for doing this is to determine whether k is affected by flexural cracking and flexural forces. Moment at hogging is being considered as this is where the plate is located and fails. Moment at hogging region (M_{hog}) in Table 6.3.1 calculated from experiments results [Liu (2005)] was divided by the moment to cause cracking M_{cr} (Eq. 6.4.1) to give the non-dimensional moment resistance (M_u/M_{cr}).

$$M_{cr} = 0.6\sqrt{f_c}\left(\frac{dD^2}{6}\right) \tag{6.4.1}$$

In Figure 6.4.1, increasing M_u/M_{cr} it reduces the concrete axial rigidity i.e. *'k'*. However, in the beam test number 2 (B2), the beam failed due to critical diagonal crack (CDC) debonding failure making the results in Figure 6.4.1 a lower bound result. Figure 6.4.2 shows the analysis without B2.

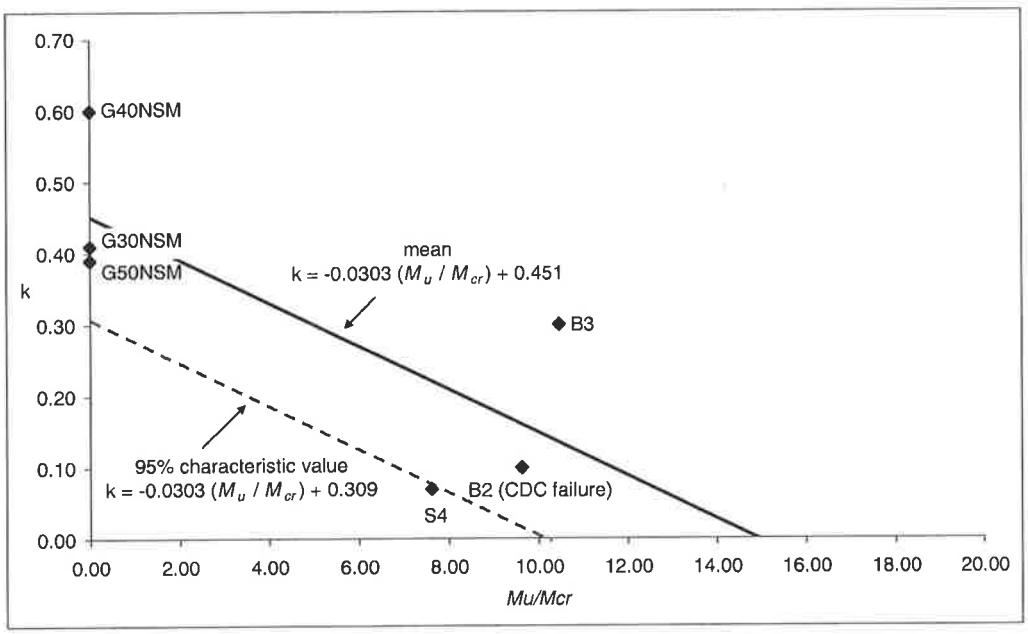

Figure 6.4.1: Summaries of *'k'* compared to moment.

Looking at Figure 6.4.1 and Figure 6.4.2 for the pull test analysis, the reduction of *'k'* was due to the interface slip between the plate and concrete, whilst for the beams and slab, the reduction was due to increase of moment capacity or increase of flexural cracking.

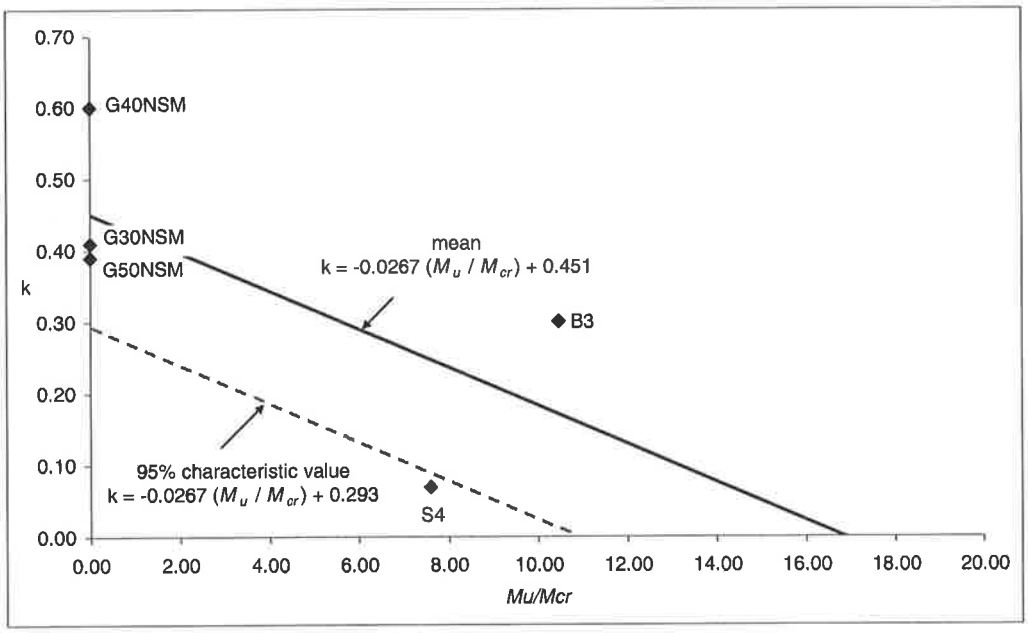

Figure 6.4.2: Summaries of '*k*' compared to moment without CDC failure beam.

The variation of k in Figure 6.4.1 and Figure 6.4.2 as given below;

Figure 6.4.1

$$k = -0.0303(M_u / M_{cr}) + 0.451 \tag{6.4.2}$$

and the 95% characteristic value

$$k = -0.0303(M_u / M_{cr}) + 0.309 \tag{6.4.3}$$

and from Figure 6.4.2

$$k = -0.0267(M_u / M_{cr}) + 0.451 \tag{6.4.4}$$

and the 95% characteristic value

$$k = -0.0267(M_u / M_{cr}) + 0.293 \tag{6.4.5}$$

6.5 Parametric study

A parametric study using Eq. 6.3.2 was done to look into the relationship between calculated failure load and k. In Figure 6.5.1 it is showing that as the number of plates increases with spacing of 50mm, the calculated failure load (P_{IC}) tend to reach a plateau value. Figure 6.5.1 also shows the plate fails as a group with all the k value ranging from 0.0 to 1.0.

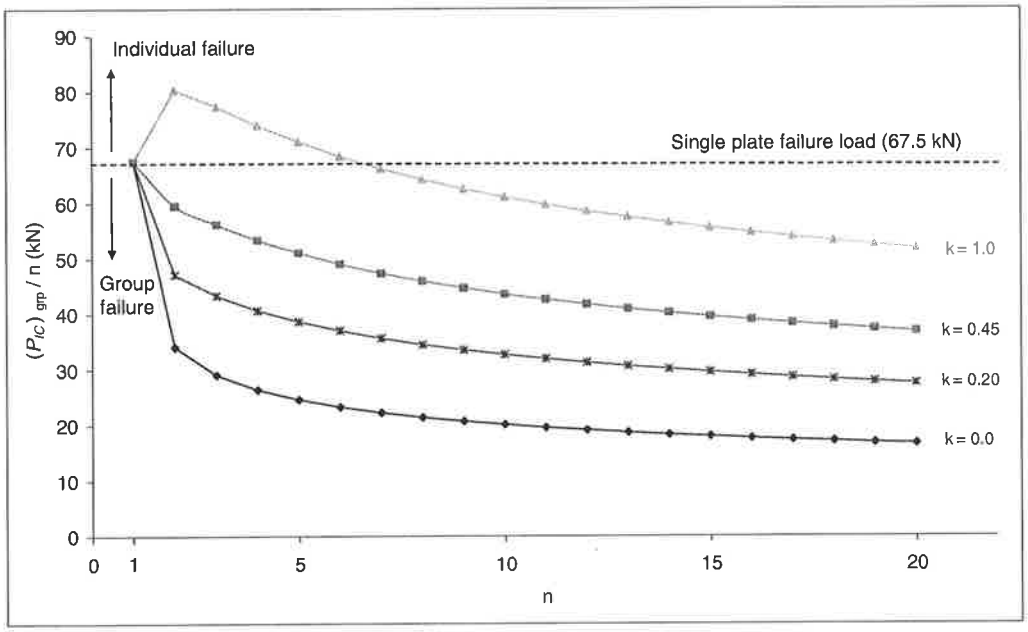

Figure 6.5.1: Relationship between calculated failure load and *'k'* with 50 mm spacing.

The same parametric study continues with a wider plate spacing of 100mm between plates. Figure 6.5.2 shows that a single plate failure will occur from k = 0.50 to 1.0. Meanwhile in Figure 6.5.3, with plate spacing of 150 mm; a single plate failure will occur when k is ranging 0.25 to 1.0. Finally, plate spacing of 200mm is shown in Figure 6.5.4 with a lower value of k ranging from k = 0.20 to 1.0 will give a single plate failure. These shows as the plate spacing is wider, the k value is getting smaller due to the reduction of contribution of concrete axial rigidity in Eq. 6.3.2. As a summary of this analysis, relationship between plate spacing and P_{IC} is shown in Figure 6.5.5 with the tendency of wider plate spacing will fails as a single plate failure. Next the summary is described.

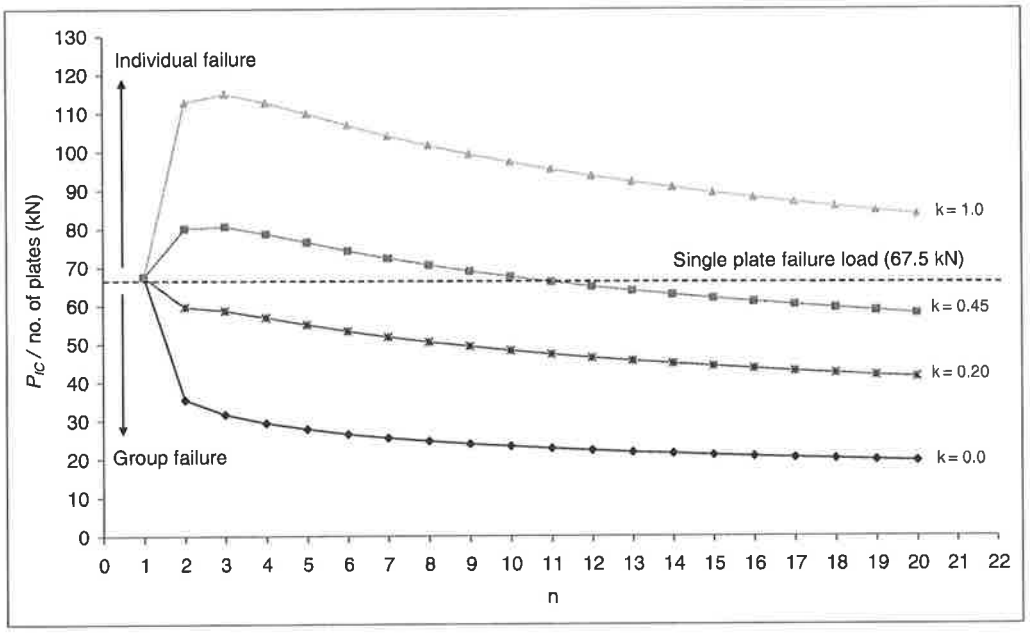

Figure 6.5.2: Relationship between calculated failure load and *'k'* with 100 mm spacing.

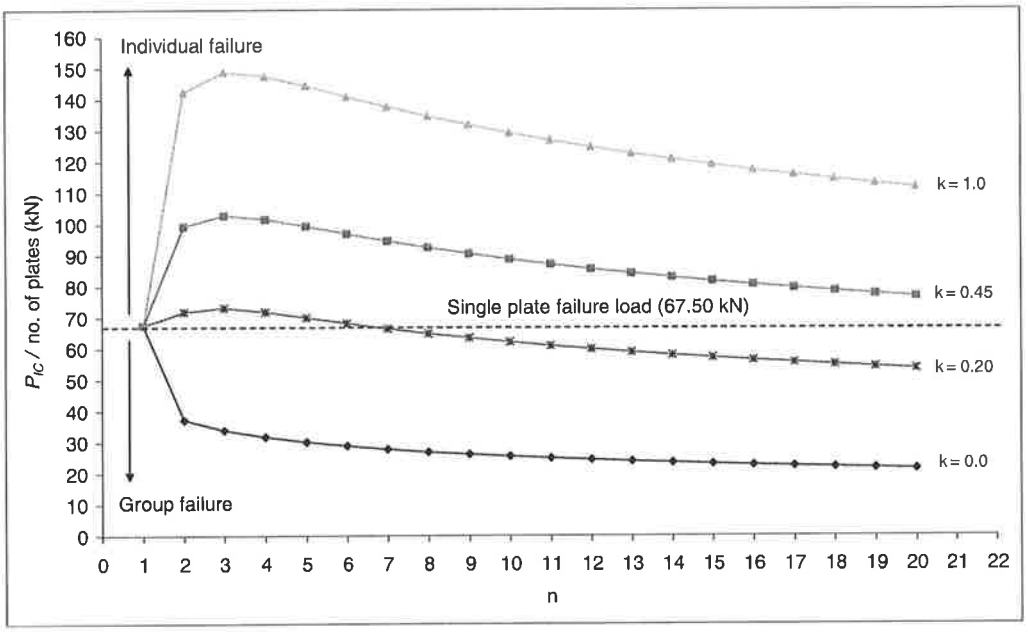

Figure 6.5.3: Relationship between calculated failure load and *'k'* with 150 mm spacing.

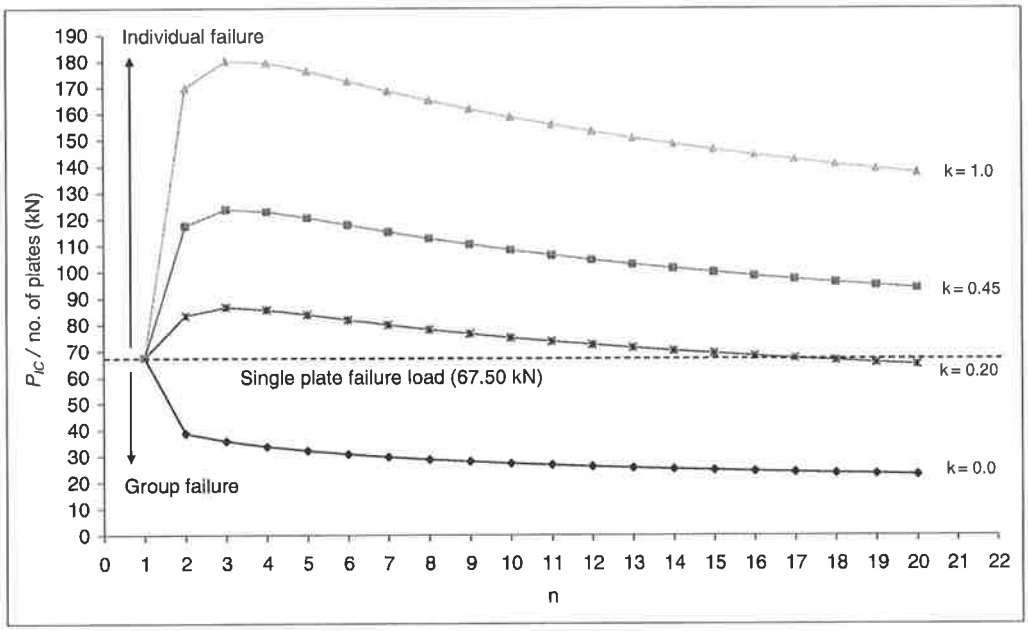

Figure 6.5.4: Relationship between calculated failure load and *'k'* with 200 mm spacing.

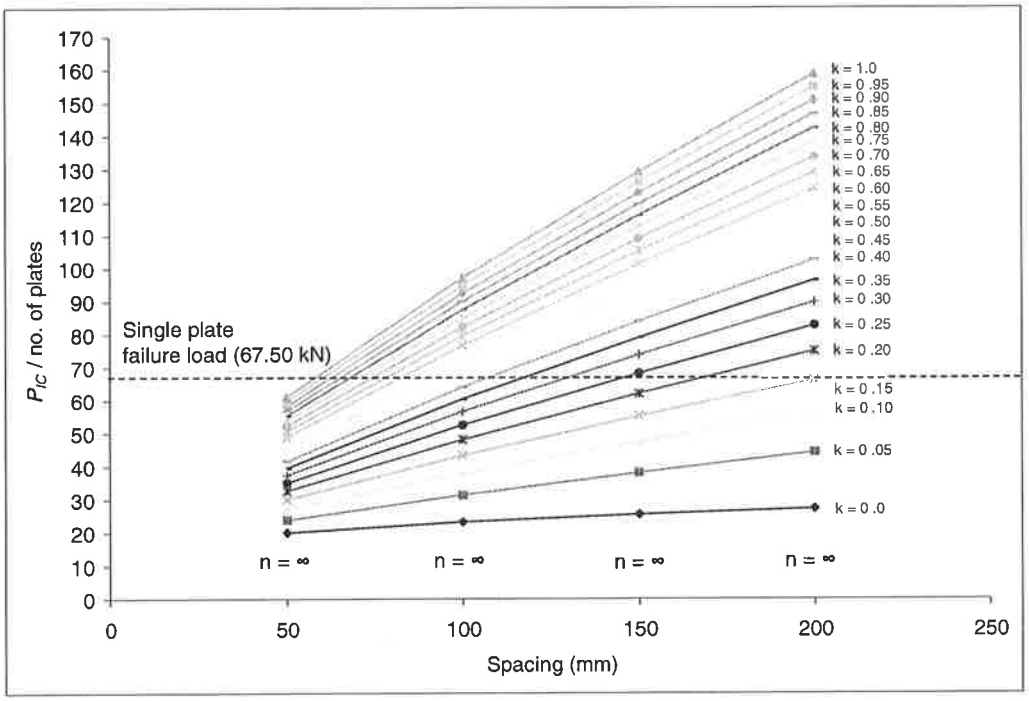

Figure 6.5.5: Relationship between calculated failure load and spacing.

6.6 Conclusion

The Intermediate crack debonding resistance for group of NSM plate is shown by Eq. 6.3.2 with k shown in Eq. 6.4.2 to 6.4.5. It was also found that the reduction of 'k' was due to the interface slip between the plate and concrete for the pull test, whilst for the beams and slab, the reduction was due to increase of moment capacity or increase of flexural cracking.

Parametric study varying the plate spacing shows as the plate spacing getting wider, transaction from failing as a group to a single plate failure is shown in Figures 6.5.1 to 6.5.4.

6.7 Notation

EB	Externally Bonded
NSM	Near Surface Mounted
IC	Intermediate Crack
τ_f	Maximum shear capacity
δ_f	Maximum slip
$\tau_f \delta_f$	Fracture energy
$(EA)_p$	Plate axial rigidity
$(EA)_c$	Concrete axial rigidity
P_{IC}	Intermediate crack debonding resistance
L_{per}	Failure plane perimeter
b_p	Plate width
d_p	Plate depth
f_c	Concrete compressive strength
P_{exp}	Experiment intermediate crack debonding resistance
d_f	Failure plane depth
b_f	Failure plane width
E_p	Plate Young's Modulus
E_c	Concrete Young's Modulus
A_p	Area of plate
A_c	Area of concrete
M_u	Ultimate moment
M_{cr}	Moment to cause cracking

6.8 Reference

1. Liu, I. (2005). Intermediate Crack Debonding of Plated Reinforced Concrete Beams. Department of Civil and Environmental Engineering. Adelaide, University of Adelaide: 610.

Chapter

7 BEAM TEST – TRANSVERSE NSM PLATED BEAM TESTS

7.1 Introduction

The experiments presented earlier (Chapter 3 and 5) were used to develop a generic equation for Intermediate Crack (IC) debonding resistance of a plate bonded to a concrete surface. In this chapter, the generic equation will be used in the prediction of the increase in shear capacity for beams with Carbon Fiber Reinforced Polymer (CFRP) Near Surface Mounted (NSM) plates. Parameters varied in these test were the plate orientation (longitudinal, inclined and vertical) and the presence of internal steel stirrups within the shear span. The behaviour of the plated beams is also compared with that of the corresponding unplated beam.

The specimens, test set-up and the material properties are described first. Then, the observations from each test are described and finally, the conclusions made from all the test results are discussed.

7.2 Specimen Geometries

Four beams were tested; with two tests per beam, one for each half, that is, one half with internal stirrups and the other half without internal stirrups shown in Figure 7.2.1. The beam dimensions were 500 mm deep, 180 mm wide and 5000 mm long as shown in Figure 7.2.2. The nominal plates used in these tests were 20 mm (d_p) x 1.4 mm (b_p) or 10 mm (d_p) x 1.4mm (b_p). The actual plates dimensions for each test are given in Table 7.2.1. The tests begin by testing the control beam (without any plate) which will provide the shear capacity of the concrete and internal steel stirrups. Details of the internal reinforcement are shown in Figure 7.2.2. Meanwhile, details of these three NSM plating orientations are shown in Figures 7.2.3 to 7.2.5.

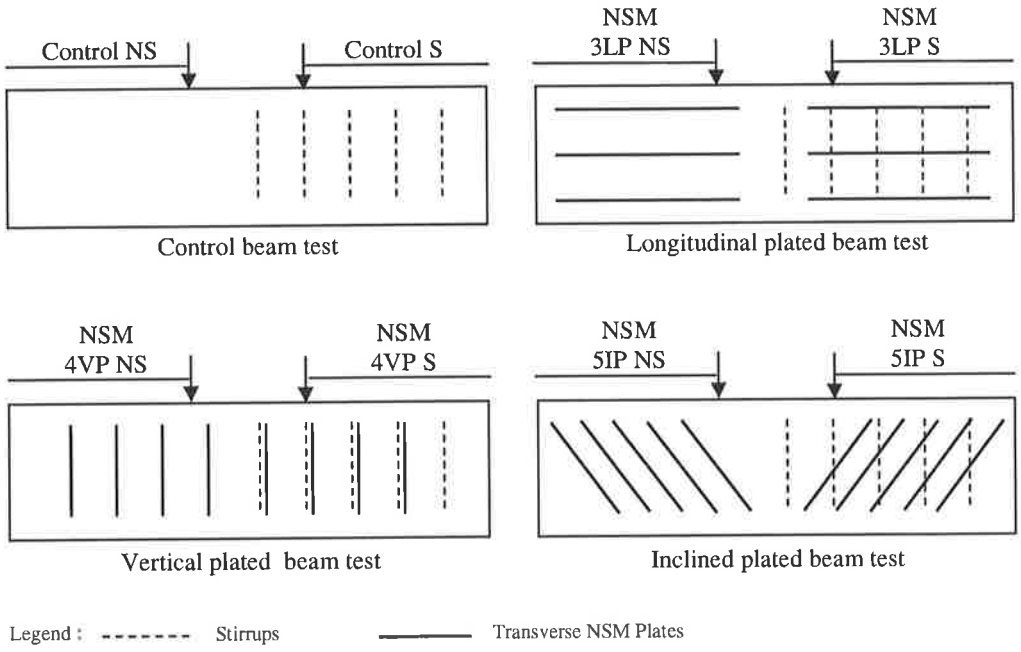

Figure 7.2.1: Beam tests experiments.

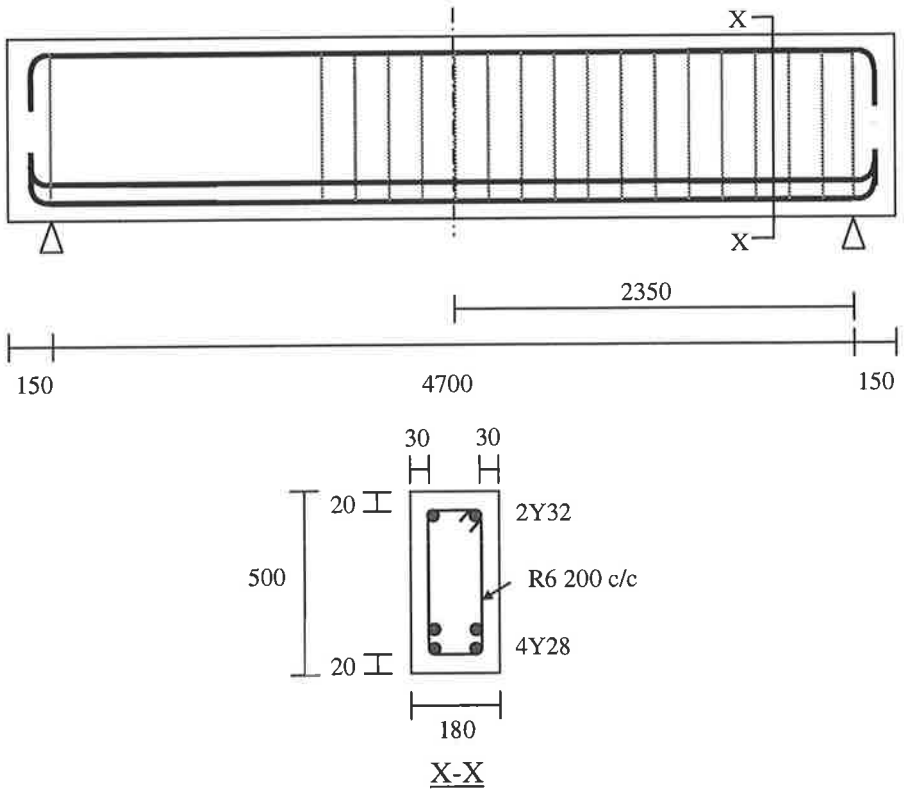

Figure 7.2.2: Beam geometries.

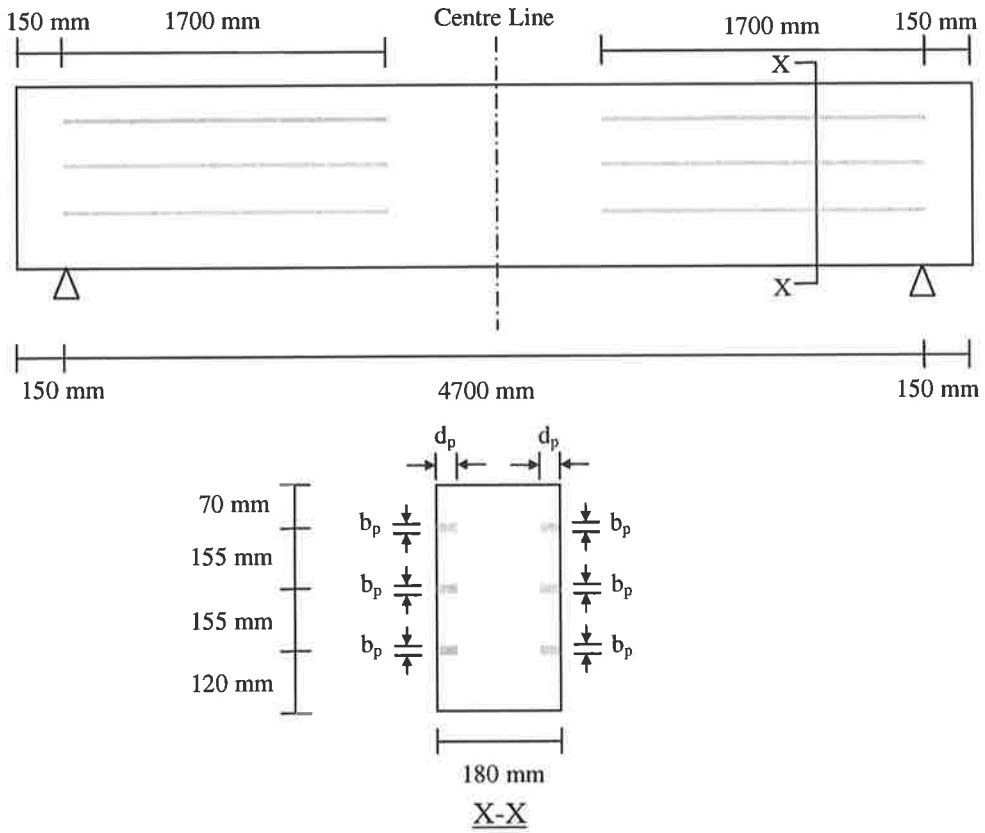

Figure 7.2.3: Longitudinal plate geometries (test 3LP NS and 3LP S).

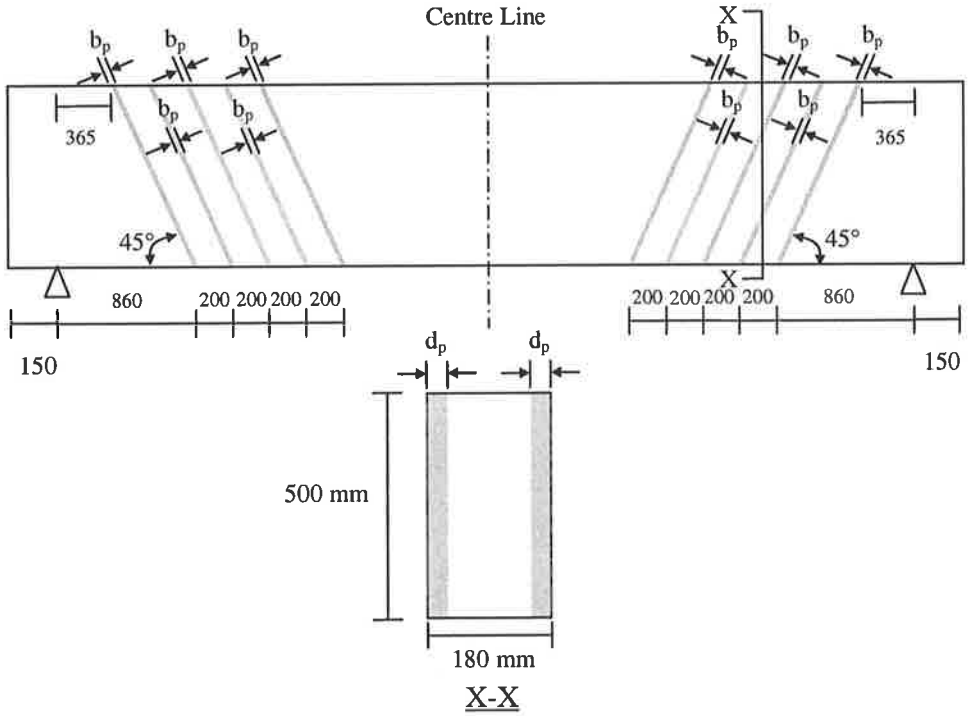

Figure 7.2.4: Inclined plate geometries (test 5IP NS and 5IP S).

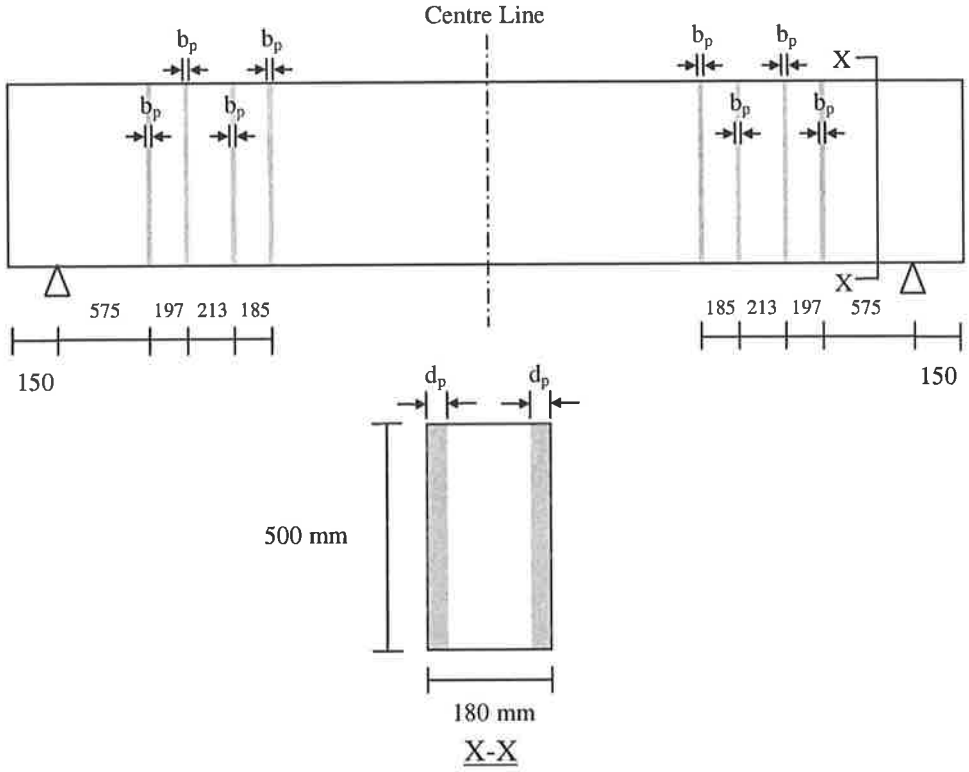

Figure 7.2.5: Vertical plate geometries (test 4VP NS and 4VP S).

Table 7.2.1: Plate dimensions.

	Plates Dimensions	
Specimen	d_p (mm)	b_p (mm)
Control NS	-	-
Control S	-	-
NSM3LP NS	20	1.4
NSM3LP S	20	1.4
NSM5IP NS	10	1.4
NSM5IP S	10	1.4
NSM4VP NS	10	1.4
NSM4VP NS	10	1.4

7.3 Test Setup

The setup for each test is shown in Figure 7.3.1. Each beam shear span was tested separately with the other half of the beam braced (Figure 7.3.1) to avoid failure. A steel reaction frame was assembled as shown Figure 7.3.1 to accommodate the location of the hydraulic jack, 1500 mm from the support. The ratio of the shear span (1500 mm) to the beam depth (500 mm) was kept at 3 to avoid the increase in shear strength due to short span tied arching action.

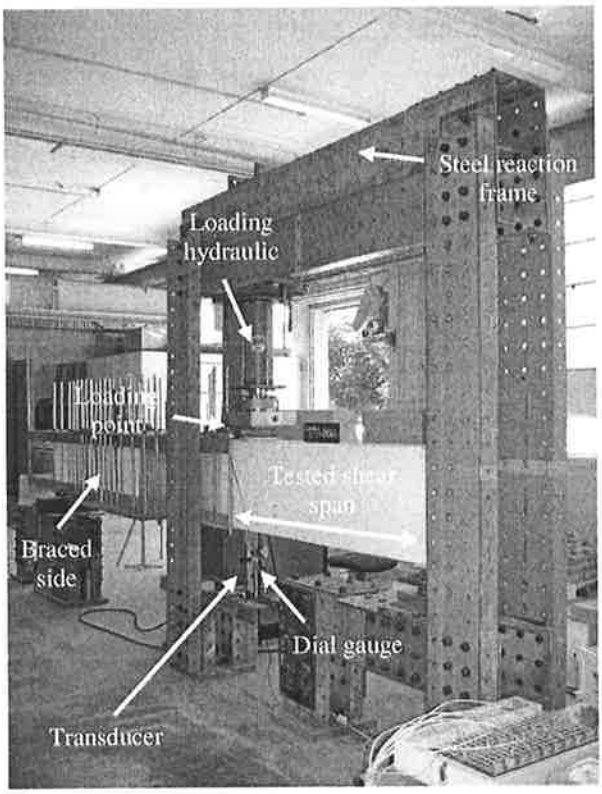

Figure 7.3.1: Typical test setup for the beam tests.

7.4 Instrumentation

Strain gauges were attached to only one plate surface (d_p surface) and also on the steel stirrups to monitor the debonding of the plates and yielding of steel stirrups. The strain gauges used were Kyowa Strain Gauges with Gauge Length of 5mm, Type KFG-5-120-C1-11. The strain gauge layout and numbering are shown in Figures 7.4.1 to 7.4.4 for all four beams. A transducer and dial gauge was placed under the beam at the load point to record the displacement while loading.

The instrumentation for control beam is as shown in Figure 7.4.1. This instrumentation of the stirrups is for all the beam tested. Only one leg of the stirrups side was strain gauged shown in Figure 7.4.1 with the assumption that stirrups on both side behave similarly. All beam were tested with three points loading on both ends of the beams with untested load point is shown shaded (Figure 7.4.1). In Figures 7.4.1 to 7.4.4; the beams are noted with side A and B on both side of the beam for easy reference when analysing the tests data.

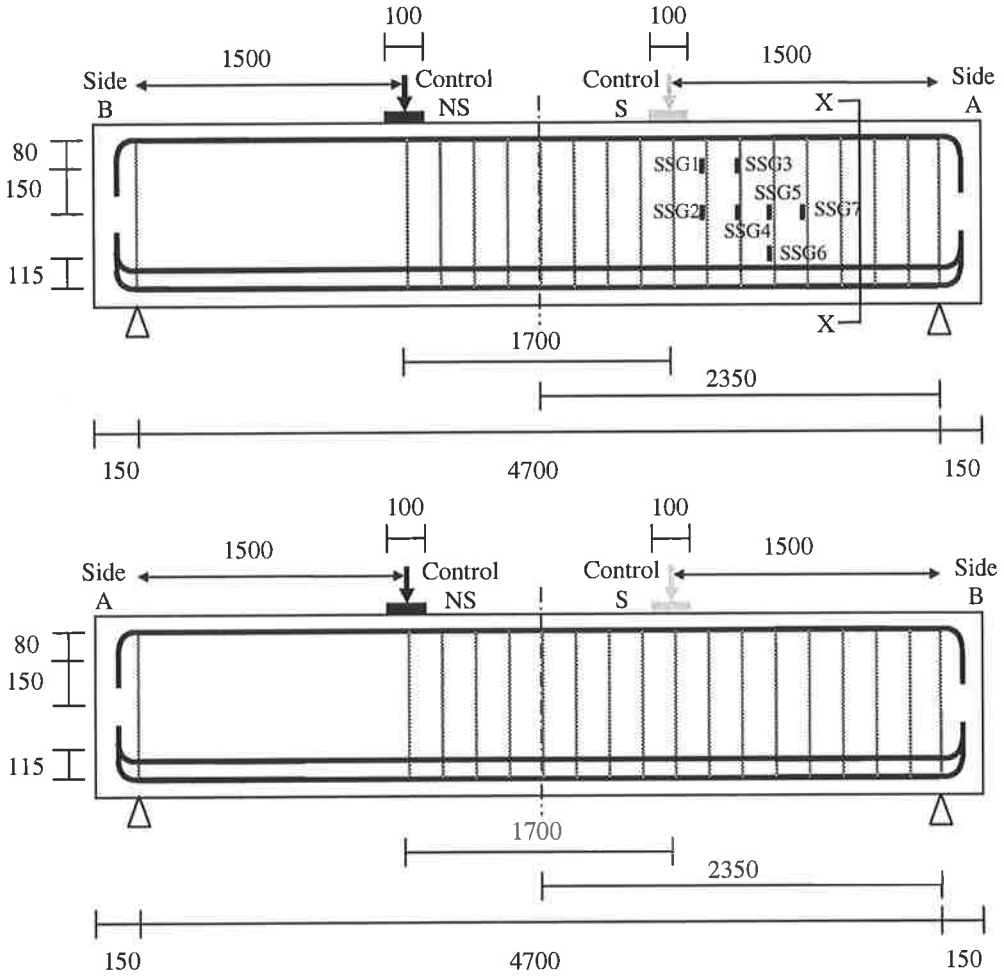

All dimensions are in mm.
NS = Non Stirrups
S = Stirrups
SSG = Stirrup Strain Gauge

Figure 7.4.1: Strain gauge layout for control beam.

Figure 7.4.2 shows the instrumentation for the longitudinal plating beam. Although the numbering and location of strain gauge similar on side A (Figure 7.4.2) but each is for difference test, NSM 3LP NS and NSM 3LP S. For example, test NSM 3LP NS, has fifteen strain gauge on side A with three is on side B and same as for test NSM 3LP S.

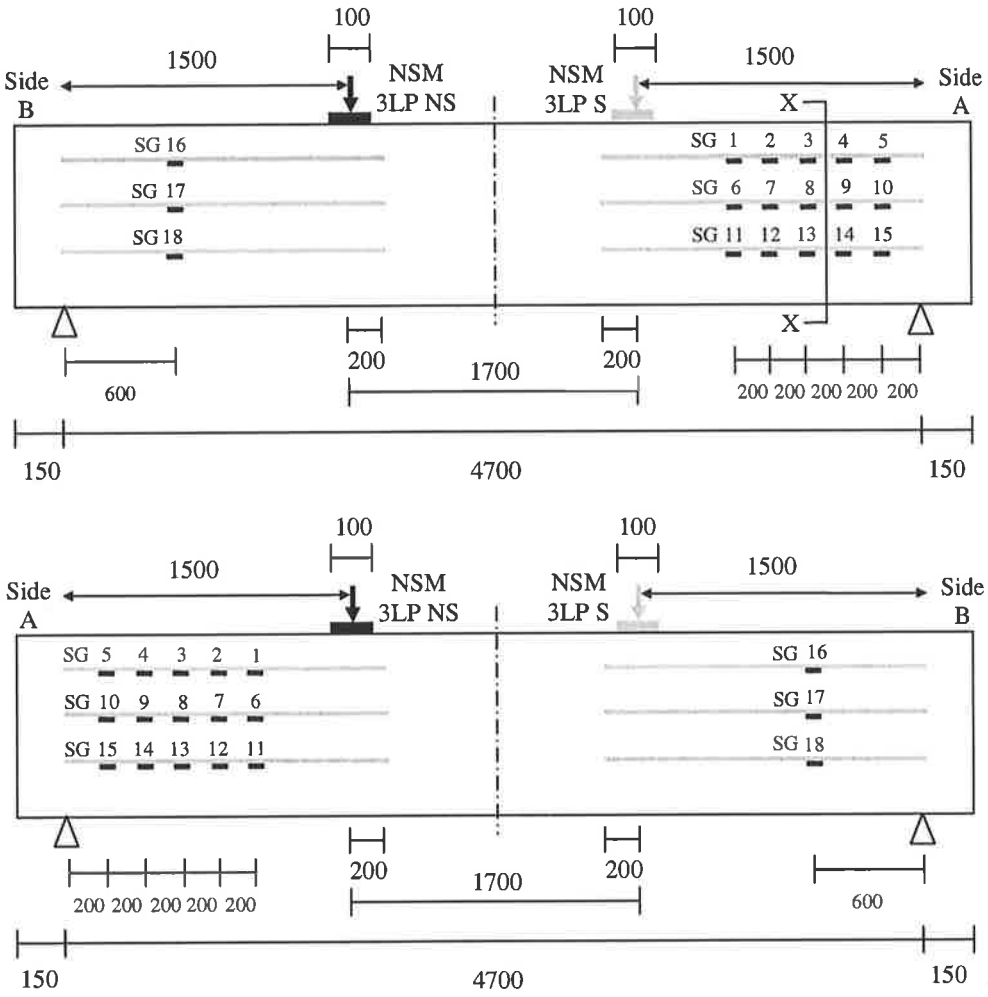

All dimensions are in mm.
NS = Non Stirrups
S = Stirrups
SG = Strain Gauge

Figure 7.4.2: Strain gauge layout for longitudinal plating beam.

Figure 7.4.3 shows the instrumentation for the inclined plating beam. Again similar to previous beam, although the numbering and location of strain gauge similar on side A (Figure 7.4.3) but each numbering is for difference test, NSM 5IP NS and NSM 5IP S. The distance between strain gauges was measured vertically.

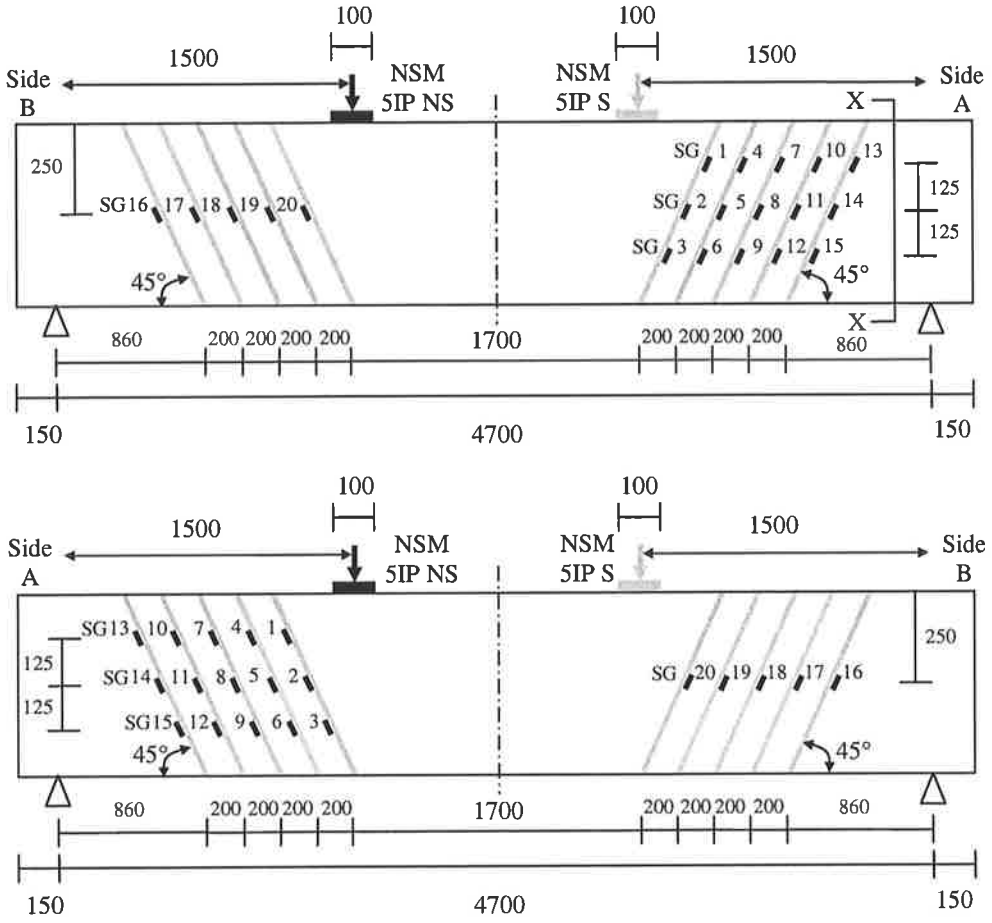

All dimensions are in mm.
NS = Non Stirrups
S = Stirrups

Figure 7.4.3: Strain gauge layout for Inclined plating beam.

Figure 7.4.4 shows the instrumentation for the vertical plating beam. Similar to previous beam tests, although the numbering and location of strain gauge similar on side A (Figure 7.4.4) but each is for difference test, NSM 4VP NS and NSM 4VP S. The distance between strain gauges was measured vertically.

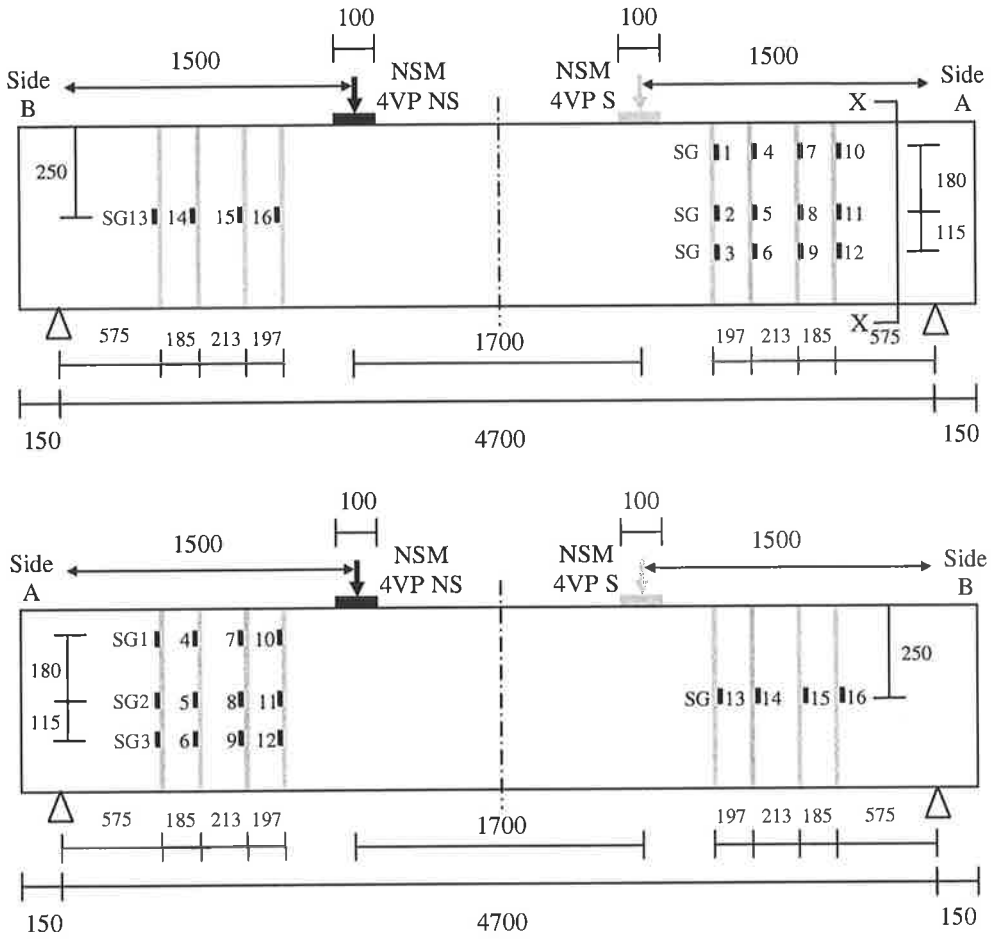

All dimensions are in mm.
NS = Non Stirrups
S = Stirrups

Figure 7.4.4: Strain gauge layout for vertical plating beam.

7.5 Material Properties

The concrete materials properties are shown in Table 7.5.1 which provides the average Young's Modulus (E_c) and compressive strength (f_c). All the beams are with 284 days concrete material properties.

Table 7.5.1: Material properties of the concrete.

Concrete Cylinder Age (days)	E_c (MPa)		f_c (MPa)	
186	Test	Average	Test	Average
	1. 30081	31256	1. 38.0	38.3
	2. 31321		2. 39.8	
	3. 32365		3. 37.1	
284	Test	Average	Tests	Average
	1. 32145	32446	1. 37.8	38.0
	2. 32748		2. 38.2	

The material properties for the steel reinforcement are shown in Table 7.5.2 and that of the NSM plate in Table 7.5.3. Although plate size of 20 mm x 1.4 mm is shown in Table 7.5.3, plate 10 mm x 1.4 mm has the same properties which were fabricated by cutting the 20 mm x 1.4 mm plate into two.

The adhesive properties are presented in Table 7.5.4 which provides the manufactures data except for Young's Modulus which was tested. The Young's Modulus (E_g) of the adhesive was obtained from tensile test with 3 specimens and the average is considered.

Table 7.5.2: Materials properties of the steel reinforcement.

Steel Reinforcement	Yield strength, f_y. (MPa)		Ultimate strength, f_u. (MPa)		Young's Modulus, E_s. (MPa)	
Stirrups (R6)	Tests	Average	Tests	Average	Tests	Average
	1. -	-	1. 708.8	689.0	1. 206552	201069
	2. -		2. 669.0		2. 195586	
Tension Reinforcement (Y28)	Test	Average	Test	Average	Tests	Average
	1. 641.5	637.1	1. 745.3	743.7	1. 209034	208102
	2. 639.1		2. 742.5		2. 207768	
	3. 630.7		3. 743.4		3. 207504	
Tension Reinforcement (Y32)	Test	Average	Test	Average	Tests	Average
	1. 584.2	583.7	1. 700.7	697.2	1. 211320	211214
	2. 580.9		2. 696.6		2. 209485	
	3. 586.1		3. 694.3		3. 212838	

Table 7.5.3: Material properties of the plate specimens.

Specimen	d_p (mm)	b_p (mm)	E_p (MPa)		ε_{rup} (microstrain)	
			Test	Average	Test	Average
20x1.4	20.9	1.37	1. 161663	161455	1. 17896	17703
	20.5	1.36	2. 161041		2. 17801	
	19.7	1.38	3. 161663		3. 17413	

Table 7.5.4: Materials properties of the adhesive.

Adhesive	Tested		Provided by the manufacturer	
	E_g (MPa)		Compression Strength (MPa)	Flexural Strength (MPa)
	Tests	Average		
MBrace Laminate Adhesive	1. 5669	5954	> 60	> 30
	2. 6091			
	3. 6102			

7.6 Test Results

In this section, all the beam tests are described individually starting with the control beam. Table 7.6.1 are summarizes the beam test results.

Table 7.6.1: Summary of the beams test results.

Beam Test	Failure Shear Load (kN)	Maximum Deflection Prior to failure. (mm)	CFRP Maximum Strain ($\mu\varepsilon$)	Stirrups Maximum Strain ($\mu\varepsilon$)	Notes
Control S	219.0	18.18	-	3507	Stop at $V = 219.0$ kN to avoid failure on the non-stirrups side. Retest and fails at $V = 208.1$ kN.
Control NS	114.2	6.28	-	-	-
NSM 3LP NS	119.0	6.65	2438	-	No plate debonding. No increase in shear capacity.
NSM 3LP S	196.5	14.88	4806	4128	No plate debonding. No increase in shear capacity.
NSM 5IP NS	183.6	15.03	12100	-	Plate debonded. Increased the shear capacity.
NSM 5IP S	304.0	25.24	11375	3751	Plate debonded. Increased the shear capacity.
NSM 4VP NS	136	10.25	12668	-	Plate debonded. Increased the shear capacity.
NSM 4VP S	283.6	23.49	11910	3927	Plate debonded. Increased the shear capacity.

7.6.1 Test Control S

The objective this test was to determine the shear strength of the unplated reinforced concrete beam with steel stirrups that is concrete shear capacity (V_c) with steel reinforcement shear capacity (V_s). This half of the beam was loaded twice. The first test stopped because of applied load was affecting the untested end with the appearance of shear crack. The test was stopped at a shear load (V) of 219 kN corresponding to an applied load to (P) of 322 kN. The crack pattern at this load is shown in Figures 7.6.1 and 7.6.2. The second test was done after the Control NS test finished and the failure shear load was 208.1 kN (P = 306 kN) that is lower than the final shear load reached in the first test. This shows that when the first test was stopped, it was near failure and with this finding, the shear load and applied load for this test is $V = 219$ kN and $P = 322$ kN. This failure load was 52.7 kN (31.7%) more compared to AS3600 prediction (166.3 kN). The failure pattern for the second is shown in Figures 7.6.3 and 7.6.4.

Figure 7.6.5 show the strains of the stirrups, where SG 5 gives the maximum strain reading. As the stirrup yield strain was at 3427 microstrain. Figures 7.6.1 and 7.6.3 clearly shows that SG 5 (Stirrup 3) is the only strain reading exceeding the yield strain due to interception of the shear crack. It is worth mentioning here that the measured strain depends on strain gauge location relative to the crack. Figure 7.6.6 shows the load deflection recorded in the first test.

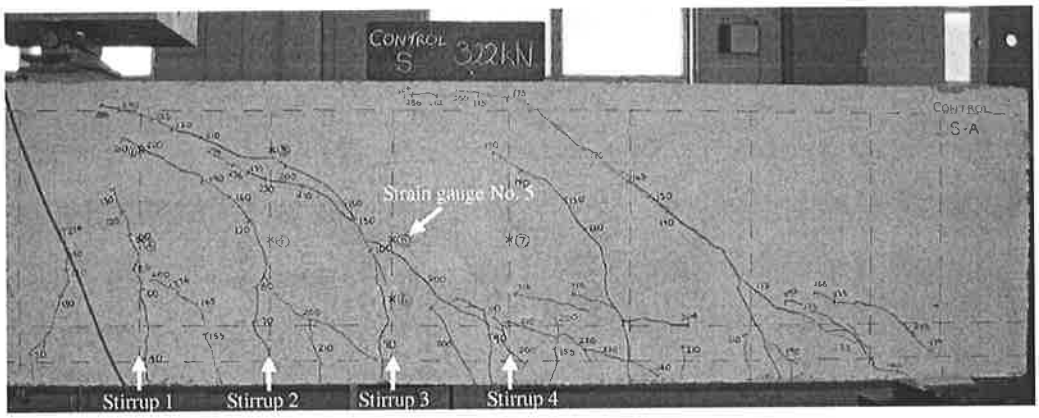

Figure 7.6.1: First test Control S at V = 219kN (P = 322 kN) on Side A.

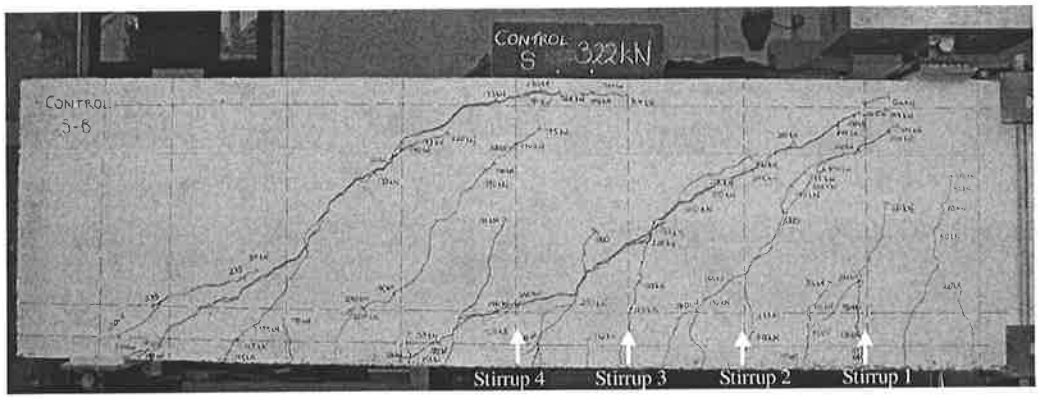

Figure 7.6.2: First test Control S at V = 219kN (P = 322 kN) on Side B.

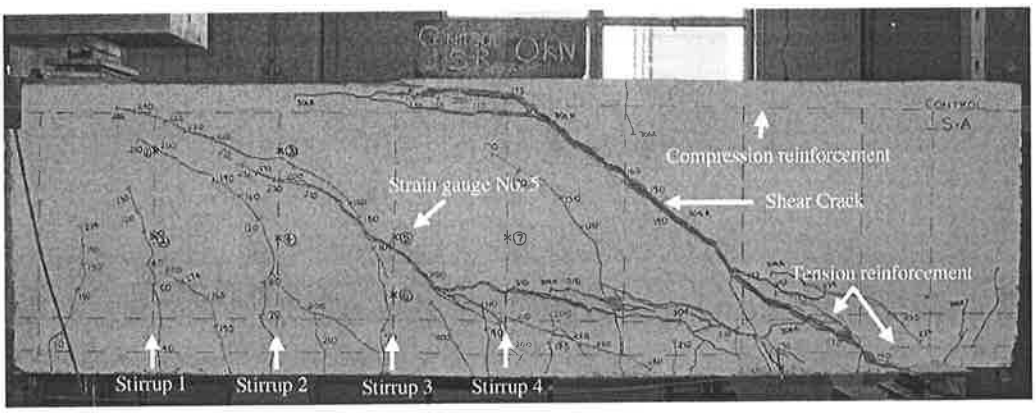

Figure 7.6.3: Failure of Control S (retest) on Side A.

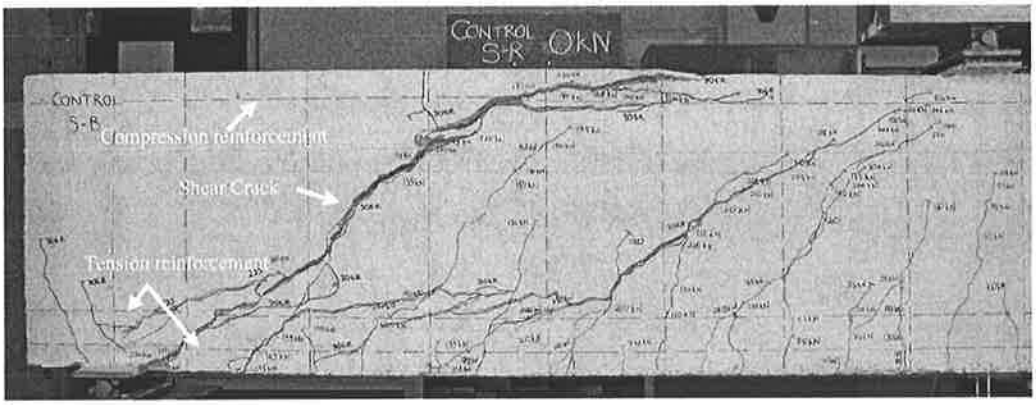

Figure 7.6.4: Failure of Control S (retest) on Side B.

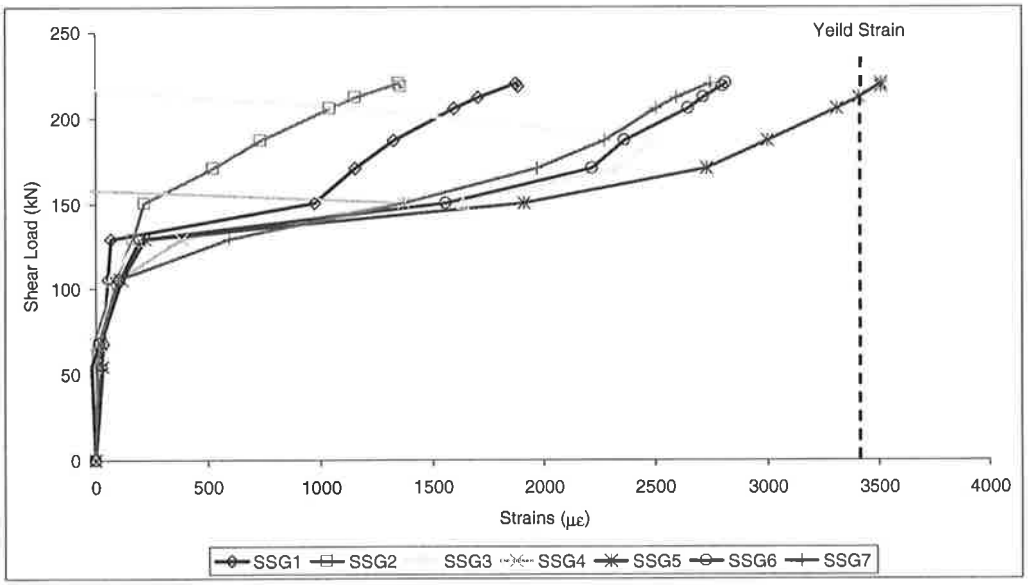

Figure 7.6.5: Strain reading for the stirrups.

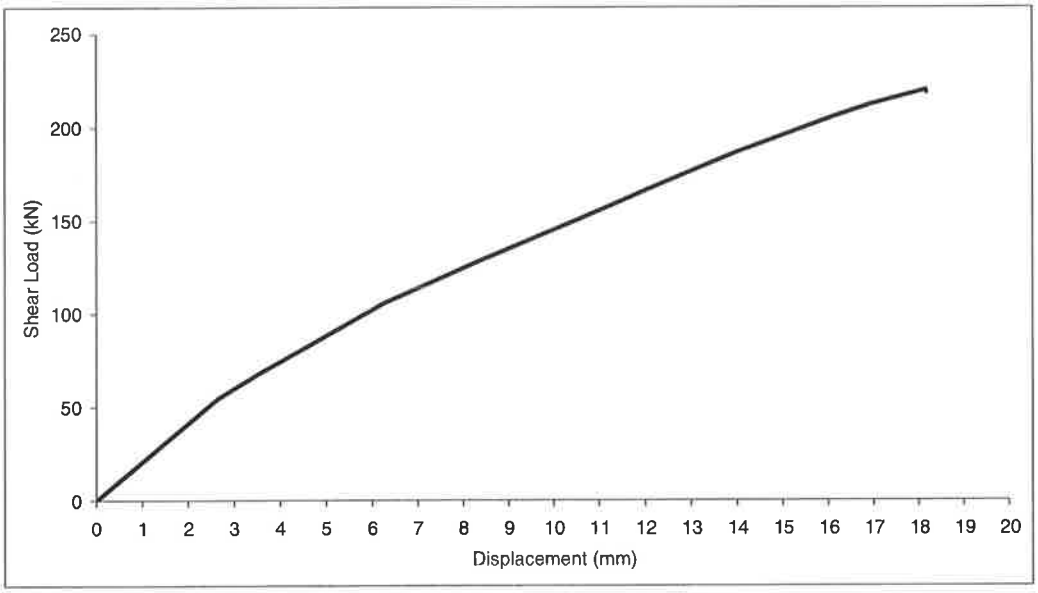

Figure 7.6.6: Deflection of beam test Control S.

7.6.2 Test Control NS

This test was done to determine the shear strength of unplated reinforced concrete beam without steel stirrups. The first flexural cracks appeared at a shear load (V) of 34 kN with an applied load (P) of 50 kN. As the applied load increased, more flexural cracks developed along the shear span. The beam failed at V = 114.2 kN (P = 168 kN) when a critical diagonal shear crack (CDC) suddenly developed. This failure load was 8.9 kN (8.5%) more compared to AS3600 prediction (105.3 kN). Figures 7.6.7 and 7.6.8 show the critical diagonal crack pattern originating the mid-height of the beam and extending to the support and the load cell along the compression and tension reinforcement. The beam failed in shear at which time the shear load V dropped to 47.0 kN (P = 69.2 kN), as shown in Figure 7.6.9.

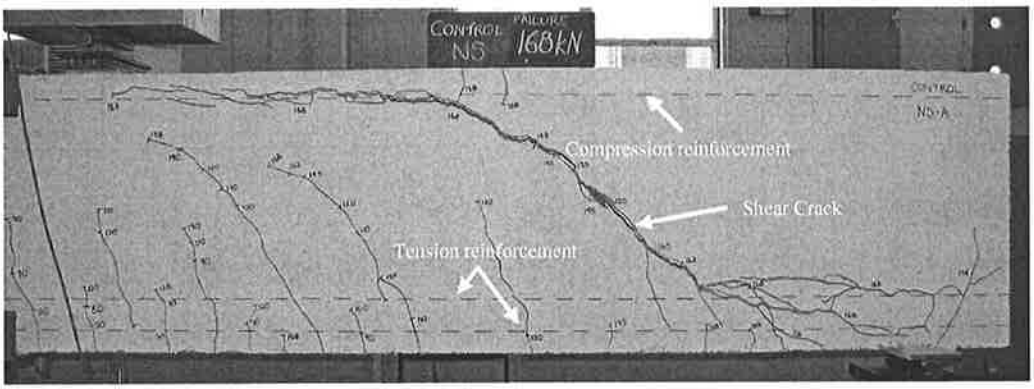

Figure 7.6.7: Failure of Test Control NS at V = 114.2 kN (P = 168 kN) on Side A.

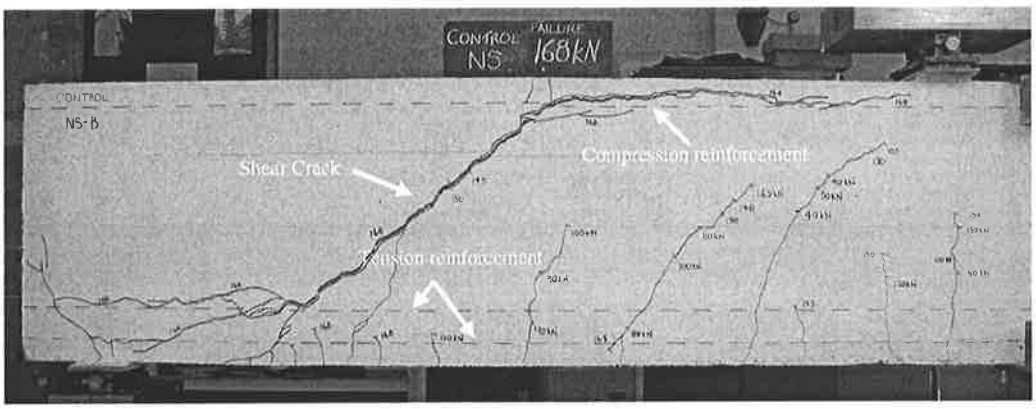

Figure 7.6.8: Failure of Test Control NS at V = 114.2 kN (P = 168 kN) on Side B.

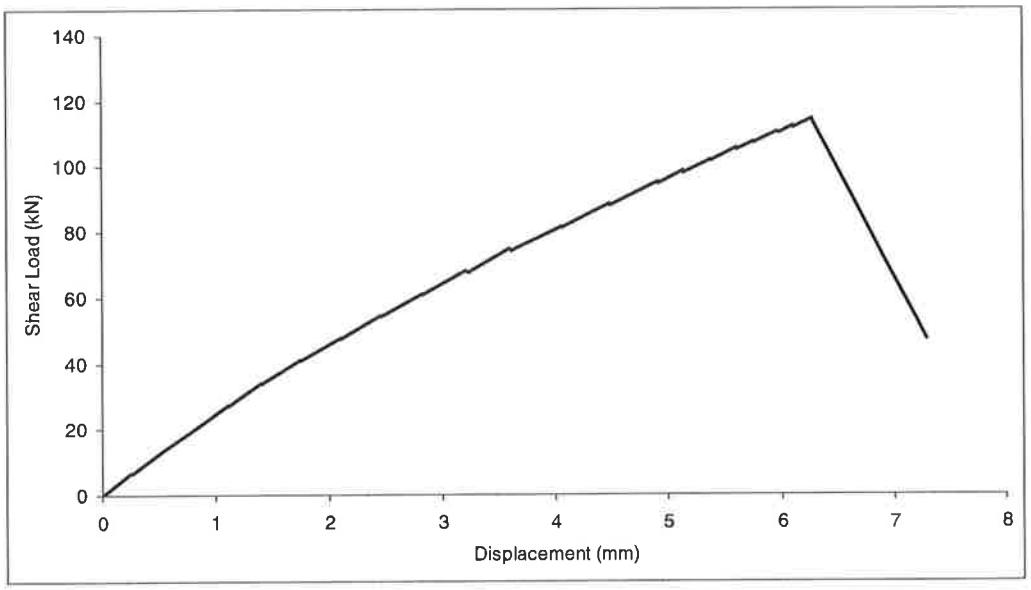

Figure 7.6.9: Deflection of beam test Control NS.

7.6.3 Test NSM 3LP NS

This test was designed to determine the increase of shear strength using longitudinal NSM plates without steel stirrups. Figures 7.6.10 and 7.6.11 show the propagation of flexural cracks without any shear cracks up to a shear load of 115.6 kN (P = 170 kN). As the shear load increased to 119.0 kN (P = 175 kN), a CDC appeared immediately intercepting all three longitudinal plates (Figures 7.6.12 and 7.6.13). However, the CDC did not cause the plates to debond from the concrete beam as shown in Figures 7.6.14 to 7.6.16 which shows the cracks propagating along the longitudinal plates.

Figure 7.6.17 shows that the strains in the plates located on sides A and B of the beam are similar where SG 3 and SG 16 are for the top plates, SG 8 and SG 17 are for the middle plates and SG 13 and SG 18 are for the lower plates. From Figure 7.6.17 the maximum strain recorded was 2438 microstrain in the lower plate (SG 18) and it is considered low compared to the debonding strain recorded in the pull tests discussed in chapter 3 and 5 (13364 microstrain). Strains for the middle plates were close to zero as it is located near the neutral axis. With strain gauge close to cracking shown in Figure 7.6.16 higher strain reading for bottom plates is shown in Figure 7.6.17.

Figure 7.6.18 shows the load deflection recorded where the increase in strength of test NSM 3LP NS compared to Control NS (dashed line) is small at only 4.8 kN (4.2 %). This was expected due to small strain developed in plate that would not do much in increasing V_c.

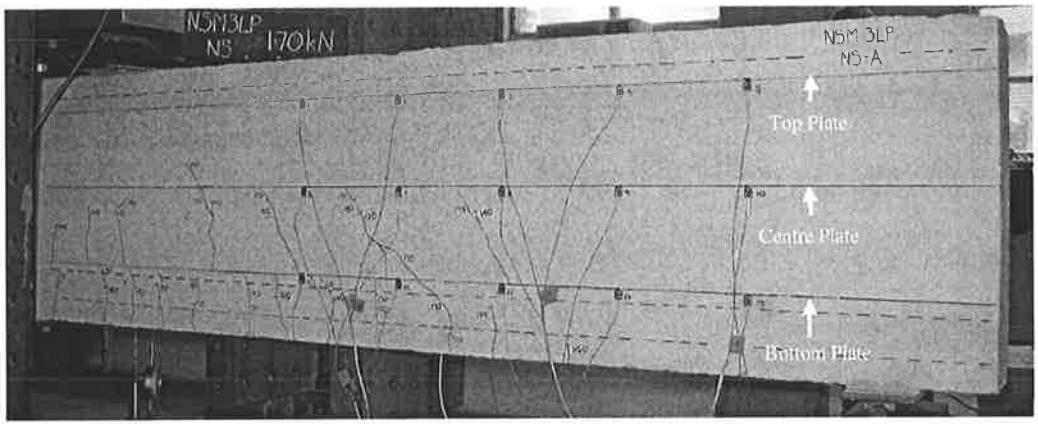

Figure 7.6.10: Propagation of flexural cracks at V = 115.6 kN (P = 170 kN) on side A.

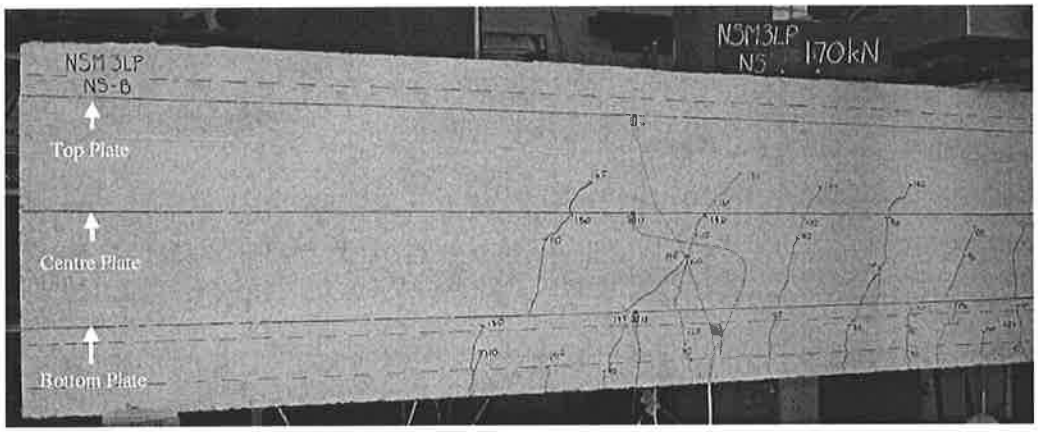

Figure 7.6.11: Propagation of flexural cracks at V = 115.6 kN (P = 170 kN) on side B.

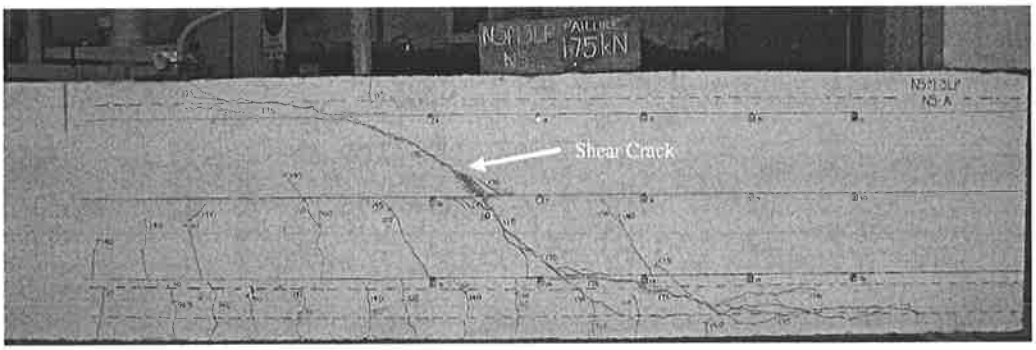

Figure 7.6.12: Failure of test NSM 3LP NS at V = 119 kN (P = 175 kN) on Side A.

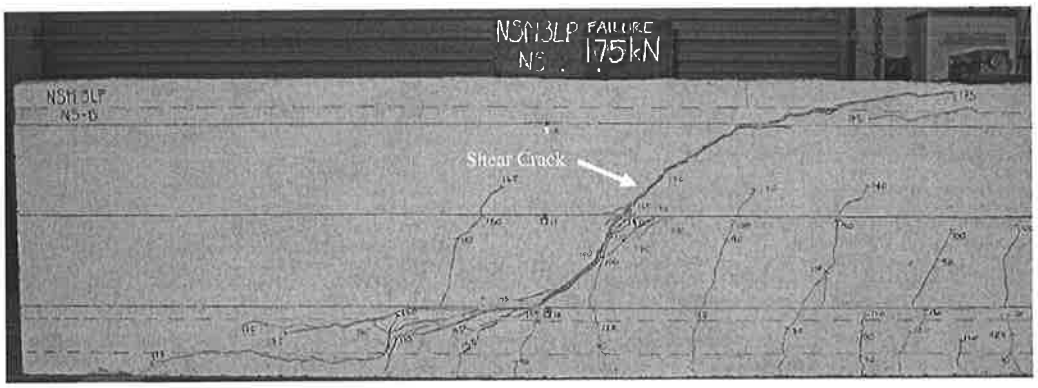

Figure 7.6.13: Failure of test NSM 3LP NS at $V = 119$ kN ($P = 175$ kN) on Side B.

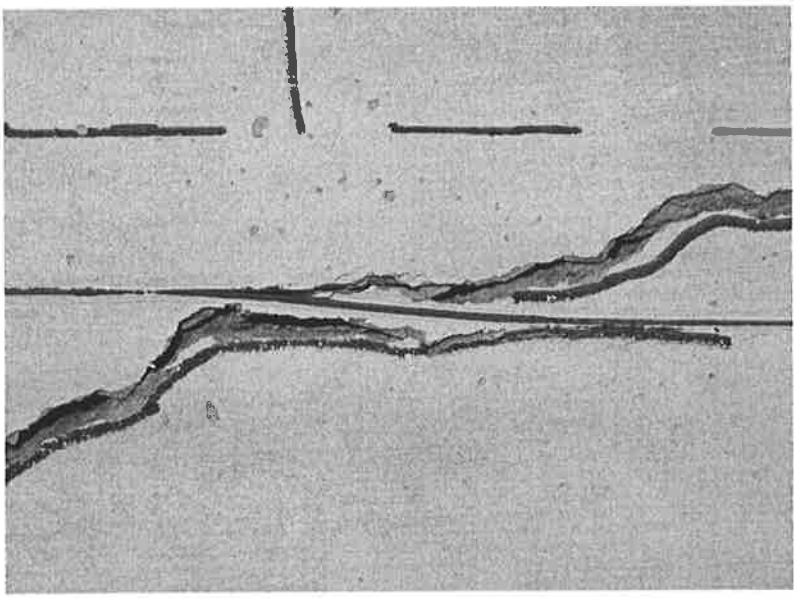

Figure 7.6.14: Propagation of CDC along the top plate.

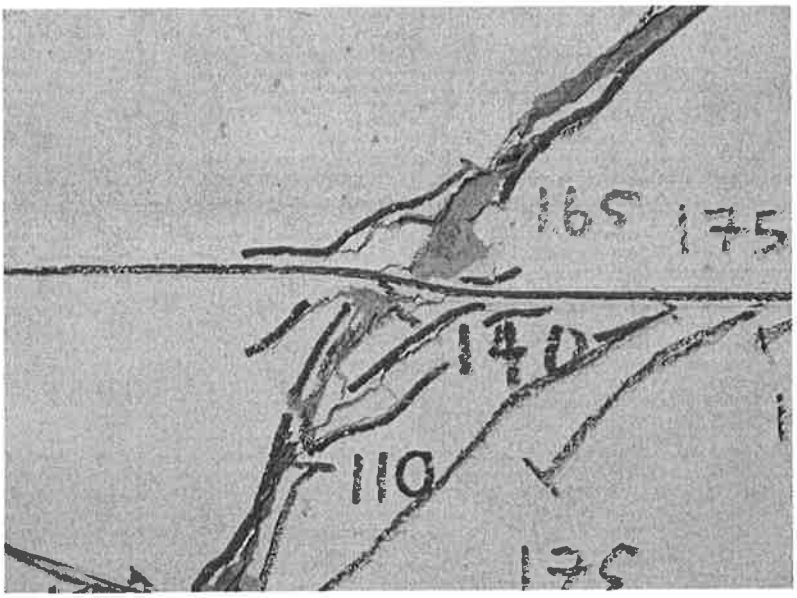

Figure 7.6.15: Propagation of CDC along the centre plate.

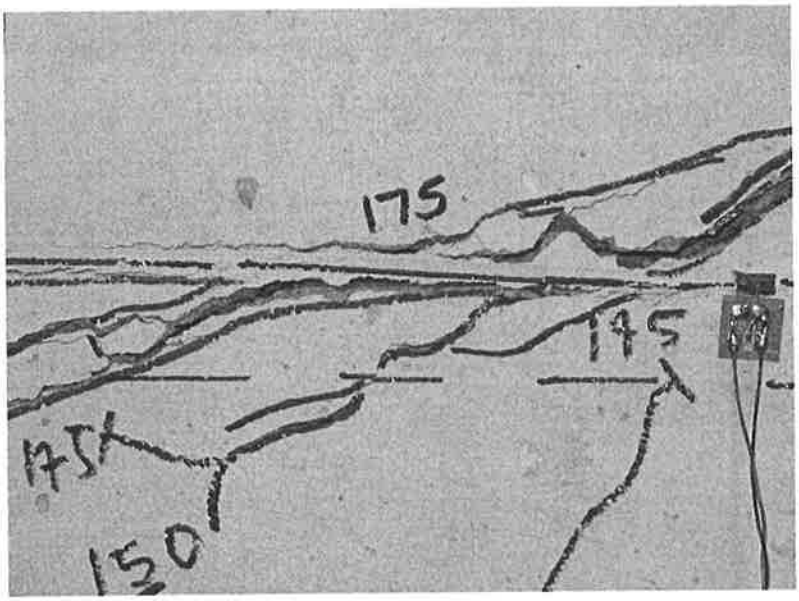

Figure 7.6.16: Propagation of CDC along the bottom plate.

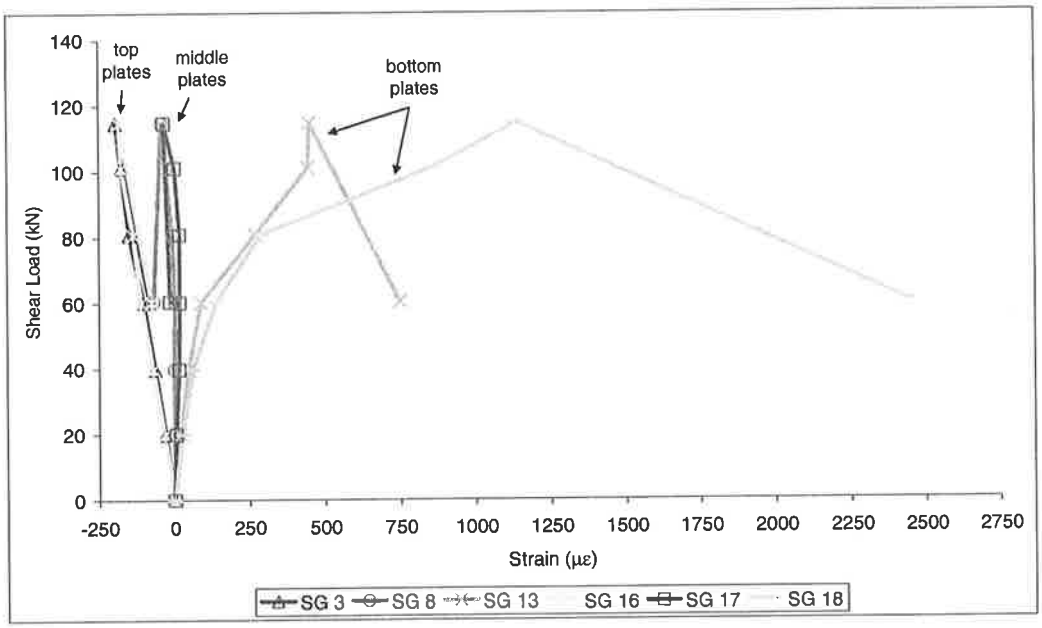

Figure 7.6.17: Strain reading for the longitudinal plates as load increases.

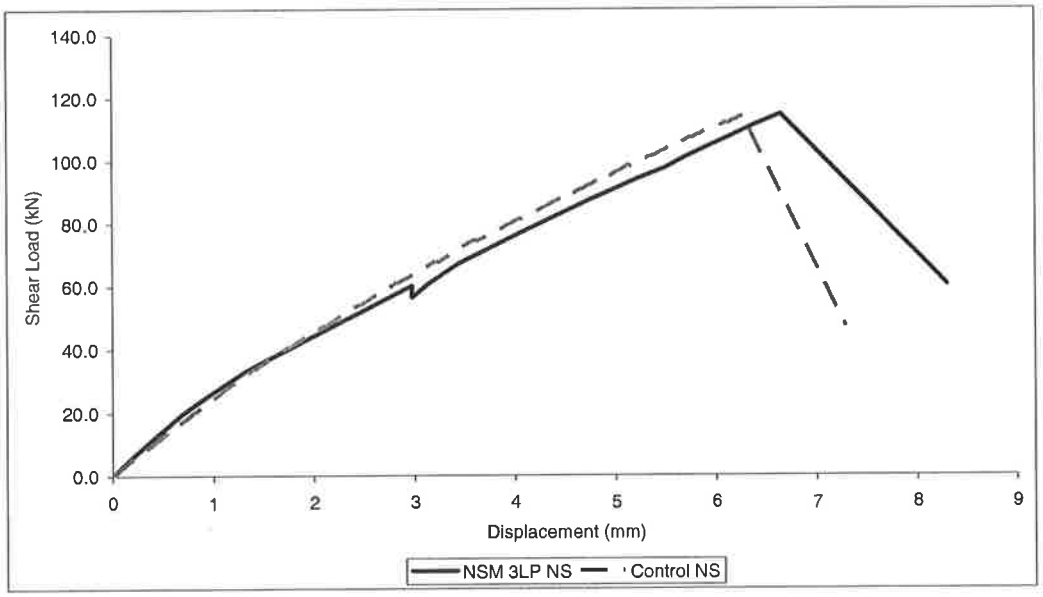

Figure 7.6.18: Deflection of beam test NSM 3LP NS.

7.6.4 Test NSM 3LP S

The increase of shear strength using longitudinal NSM plates when steel stirrups are present was determined in this test. Figures 7.6.19 and 7.6.20 show the propagation of shear cracks as the shear load increases to 117.6 kN (P = 173 kN). As the shear load increased to 125.8 kN (P = 185 kN), another shear crack appeared intercepting the centre and bottom longitudinal plates shown in Figures 7.6.21 and 7.6.22. The beam failed in shear when the shear load reached 196.5 kN (P = 289 kN). The failure crack pattern of this beam is shown in Figures 7.6.23 and 7.6.24 where as before, the shear cracks do not cause the plates to debond. Again, cracks propagate along the longitudinal plates as shown in Figures 7.6.25 to 7.6.27 as in test NSM 3LP NS. Figures 7.6.25 to 7.6.27 also shows the shear deformation of the plate cause by the CDC interception.

Figure 7.6.28 shows that the strains in the plates located on sides A and B of the beam are similar where SG 3 and SG 16 are for the top plates, SG 8 and SG 17 are for the middle plates and SG 13 and SG 18 are for the lower plates. From Figure 7.6.28 the maximum strain recorded was 3743 microstrain in the lower plate (SG 8) and it is considered low compared to the debonding strain recorded in the pull tests discussed in chapter 3 and 5 (13364 microstrain). The strain recorded for the internal steel stirrups given in Figure 7.6.29 shows that stirrups 2, 3 and 4 all yielded. Figure 7.6.30 gives the deflection recorded with applied shear load. Test NSM 3LP S fails lower than Control S (V = 219 kN and P = 322 kN),

comparison between these two tests shows reduction in shear strength (10.3% reduction). The reduced failure load is likely due to experimental scatter.

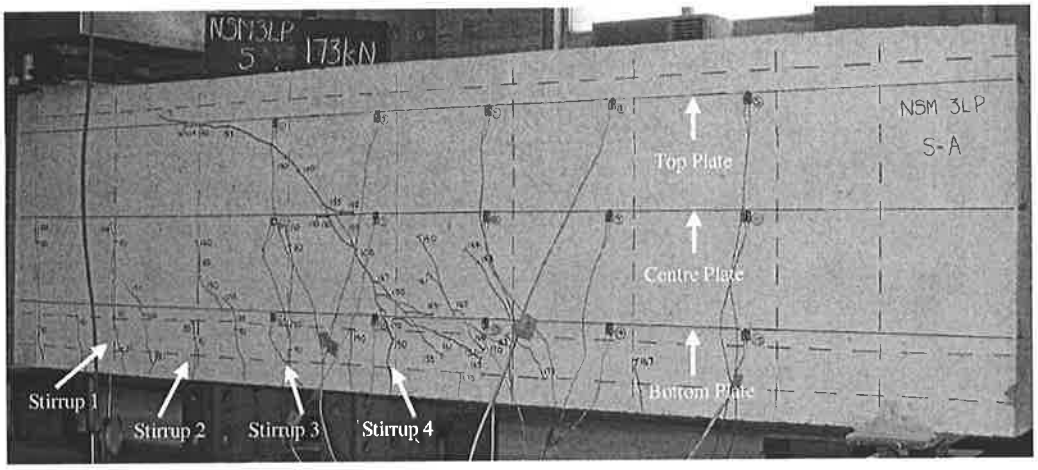

Figure 7.6.19: Test NSM 3LP S at V = 117.6 kN (P = 173 kN) on Side A.

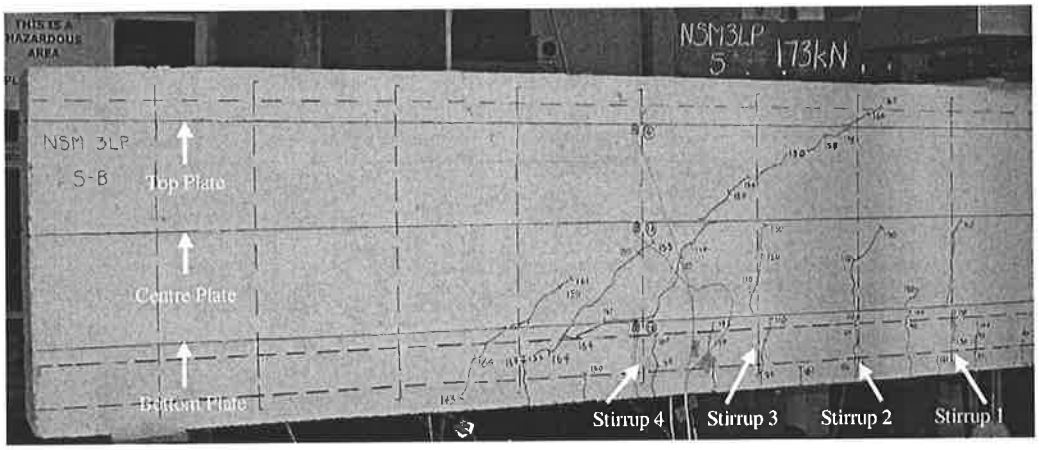

Figure 7.6.20: Test NSM 3LP S at V = 117.6 kN (P = 173 kN) on Side B.

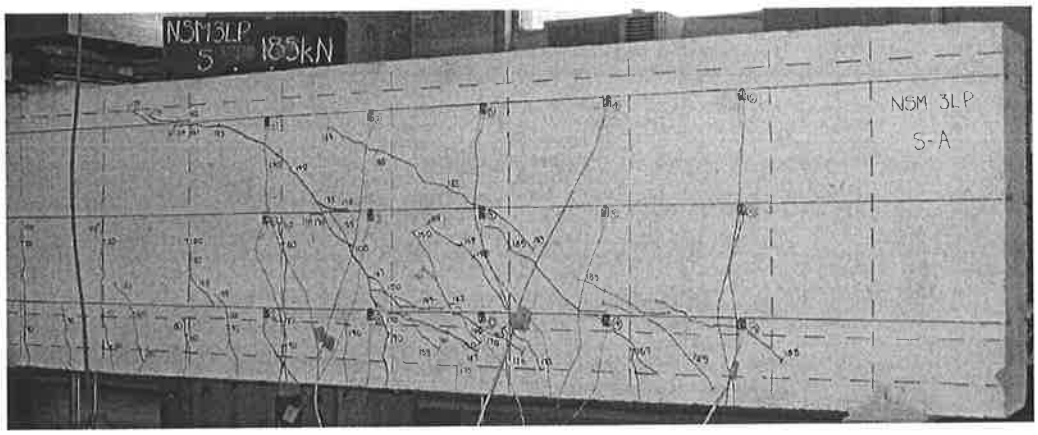

Figure 7.6.21: Test NSM 3LP S at V = 125.8 kN (P = 185 kN) on Side A.

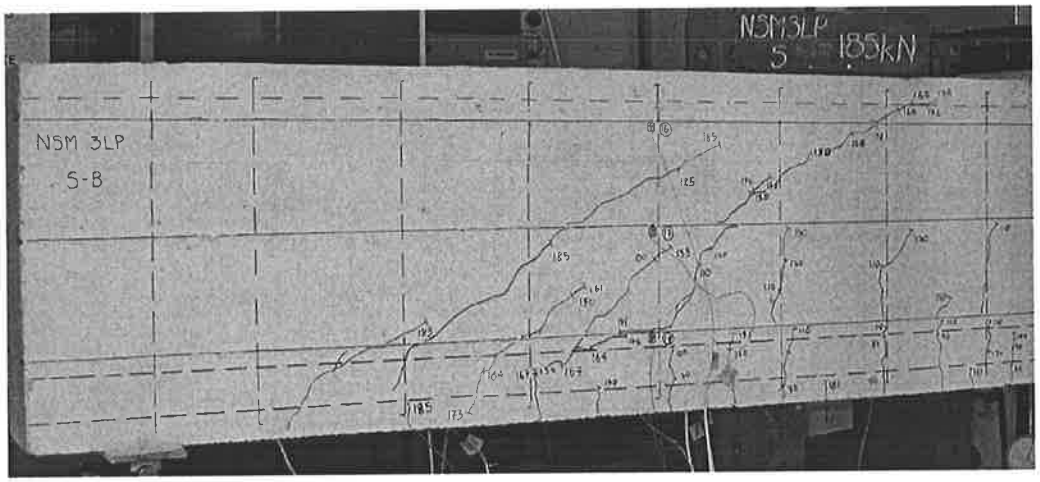

Figure 7.6.22: Test NSM 3LP S at V = 125.8 kN (P = 185 kN) on Side B.

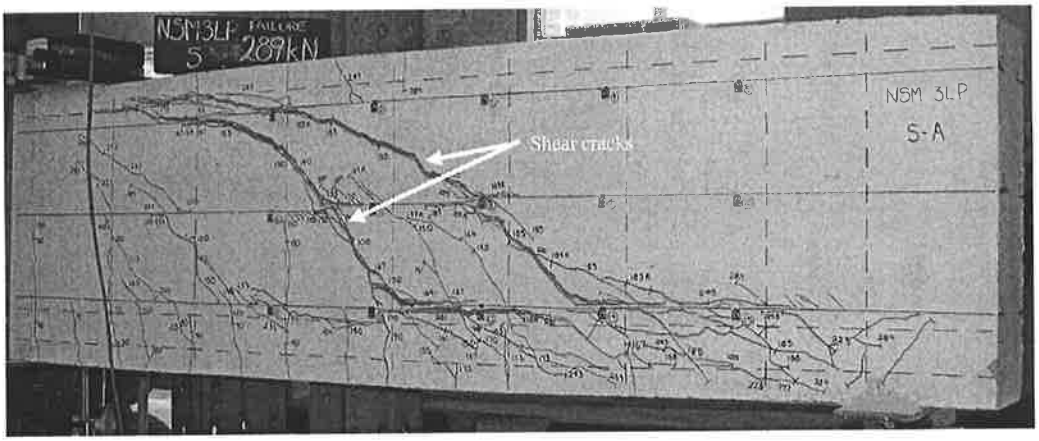

Figure 7.6.23: Failure of test NSM 3LP S at V = 196.5 kN (P = 289 kN) on side A.

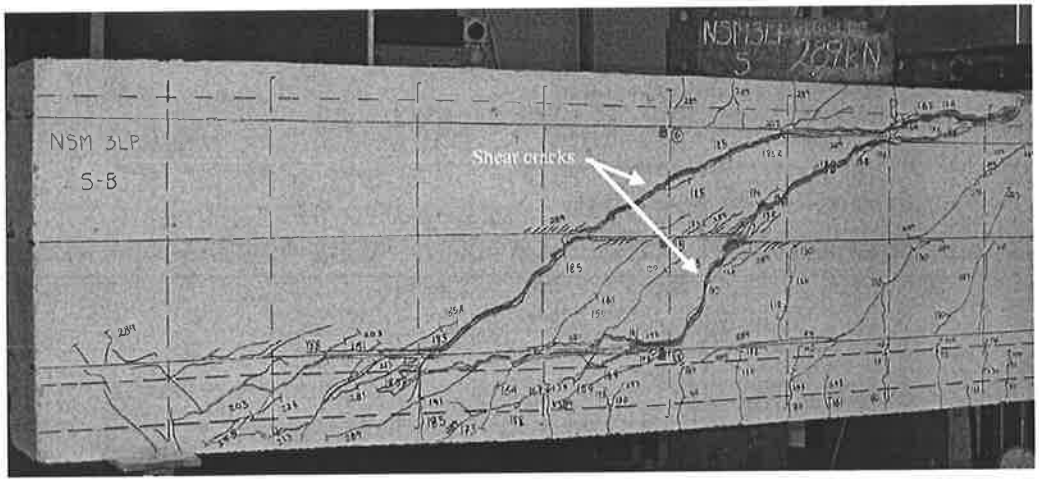

Figure 7.6.24: Failure of test NSM 3LP S at V = 196.5 kN (P = 289 kN) on side B.

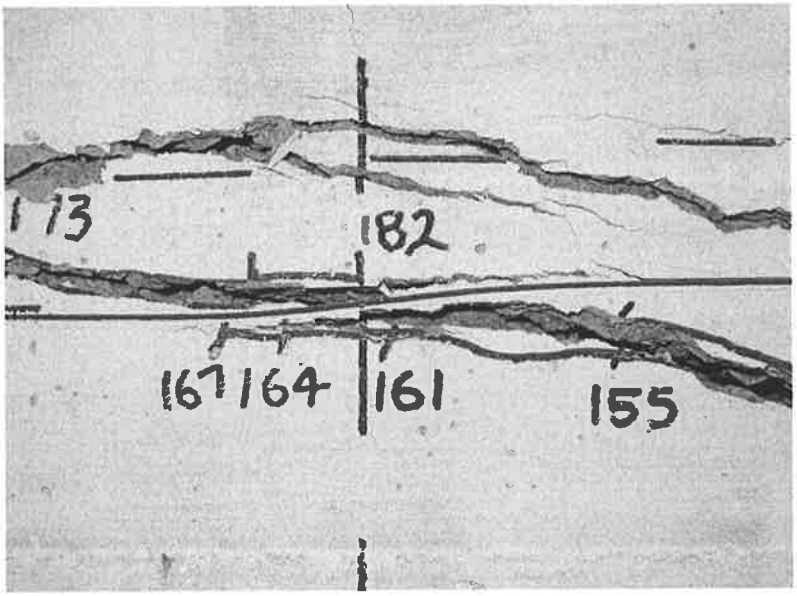

Figure 7.6.25: Propagation of CDC along the top plate.

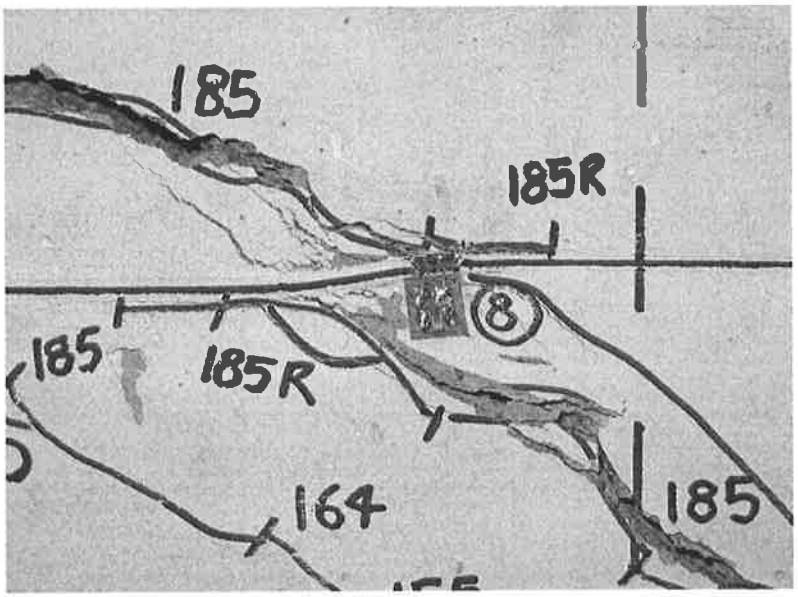

Figure 7.6.26: Propagation of CDC along the centre plate.

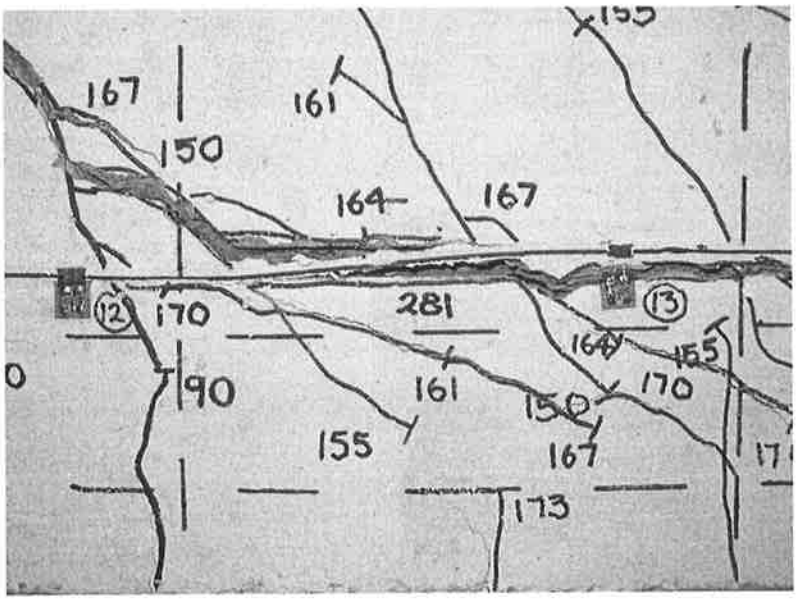

Figure 7.6.27: Propagation of CDC along the bottom plate.

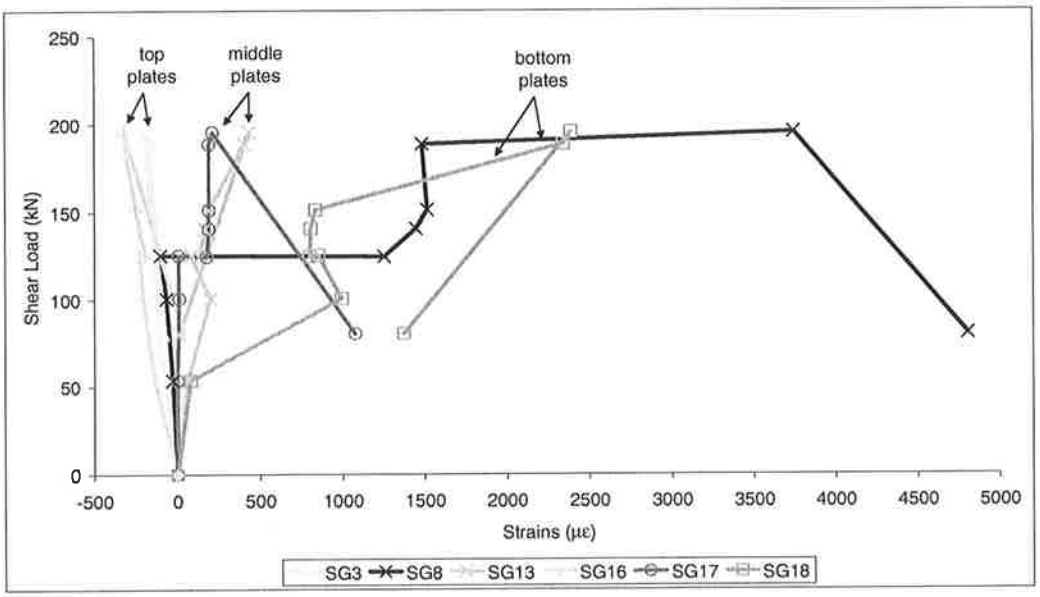

Figure 7.6.28: Strain reading for the longitudinal plates as load increases.

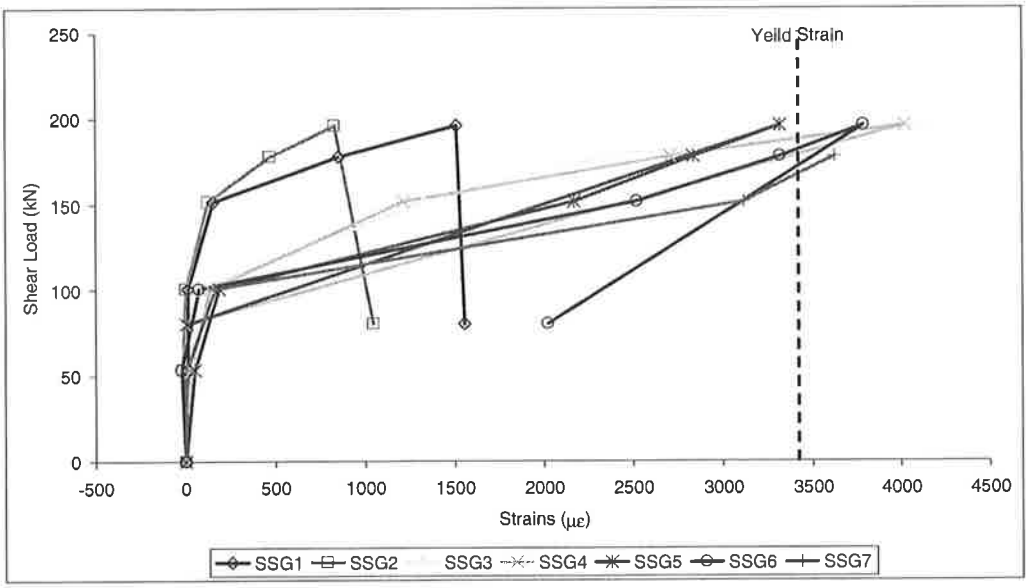

Figure 7.6.29: Strain reading for the internal steel stirrups.

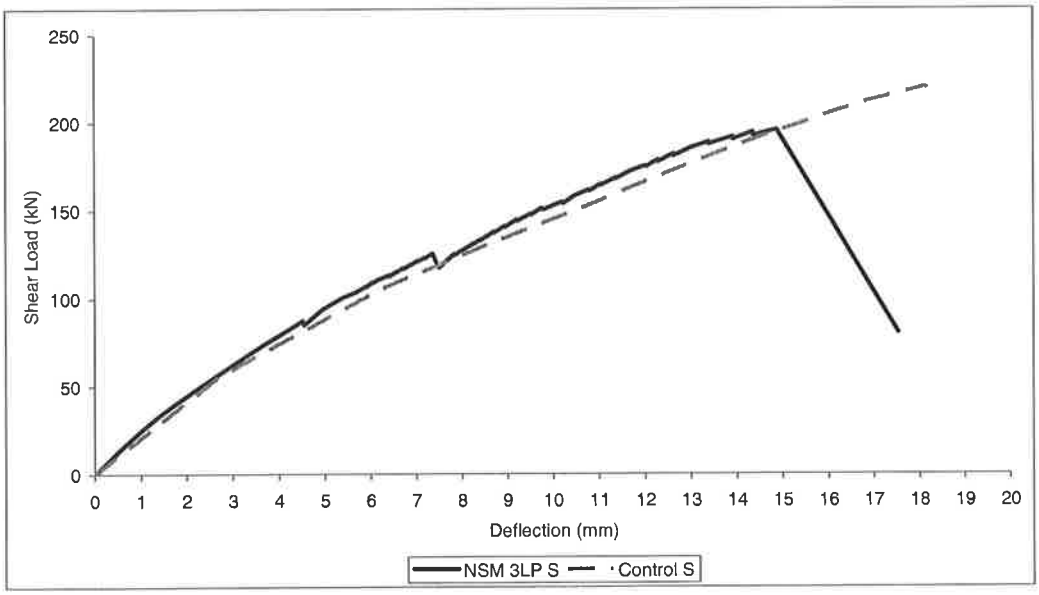

Figure 7.6.30: Deflection of beam test NSM 3LP S.

7.6.5 Test NSM 5IP NS

This test investigates the increase of shear strength using NSM plates inclined at 45° without steel stirrups. Figures 7.6.31 and 7.6.32 show the propagation of flexural and shear cracks as the shear load increased to 125.8 kN (P = 185 kN). As the shear load increased to 136.0 kN (P = 200 kN), intermediate crack (IC) debonding begins to appear in plates C,R and S on side A as shown in Figure 7.6.33 and plates T,U and D on side B as shown in Figure 7.6.34.

At shear load of 178.8 kN (P = 263 kN) more shear cracks form and IC debonding cracks develop further. The beam failed in shear when the shear load reached 183.6 kN (P = 270 kN). The failure crack pattern of this beam is shown in Figures 7.6.37 and 7.6.38 with interception of the shear cracks causing IC debonding of the plates (Figure 7.6.39). The path of this crack is on the weakest part of the strengthened beam. It is worth noting that the debonding was occurring at the shorter bond length of plates.

The strain readings for all the inclined plates are shown in Figure 7.6.40. From Figure 7.6.40 the maximum debonding strain recorded was 12100 microstrain (SG 10) close to the debonding strain of a pull test (13364 microstrain). Figure 7.6.40 also shows a significant axial force develop in the inclined strips leading to IC debonding which was not present in the longitudinal plated beams. Figure 7.6.41 shows the deflection recorded with applied shear load. Comparing test NSM 5IP NS with Control NS shows a large increase in shear strength of 69.4 kN (or 60.7%).

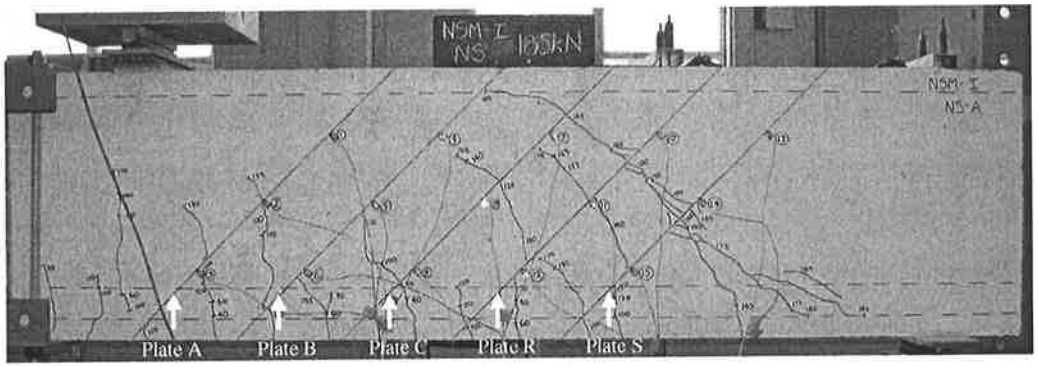

Figure 7.6.31: Test NSM 5IP NS at V = 125.8 kN (P = 185 kN) on Side A.

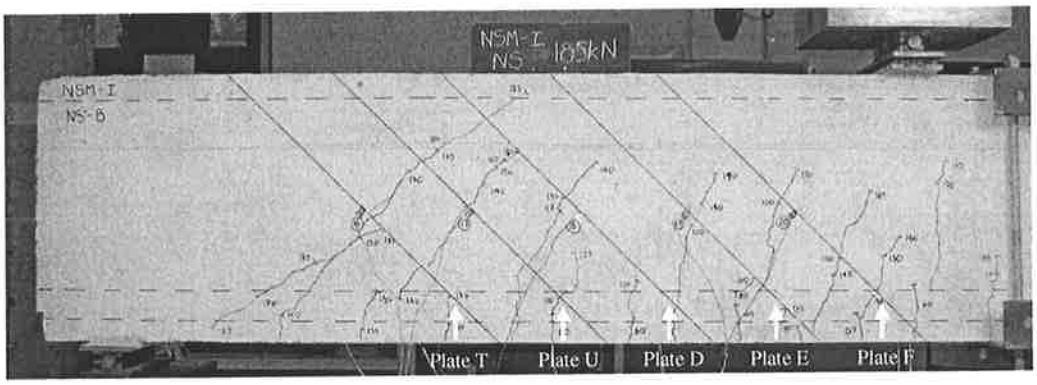

Figure 7.6.32: Test NSM 5IP NS at V = 125.8 kN (P = 185 kN) on Side B.

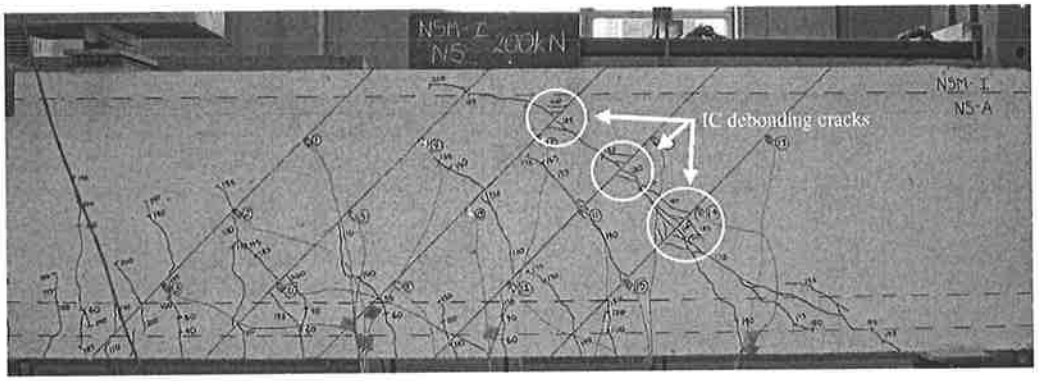

Figure 7.6.33: Test NSM 5IP NS at V = 136.0 kN (P = 200 kN) on Side A.

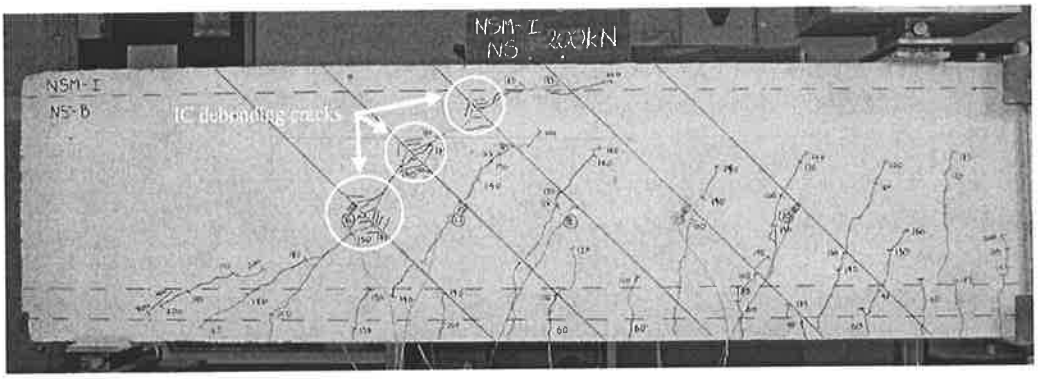

Figure 7.6.34: Test NSM 5IP NS at V = 136.0 kN (P = 200 kN) on Side B.

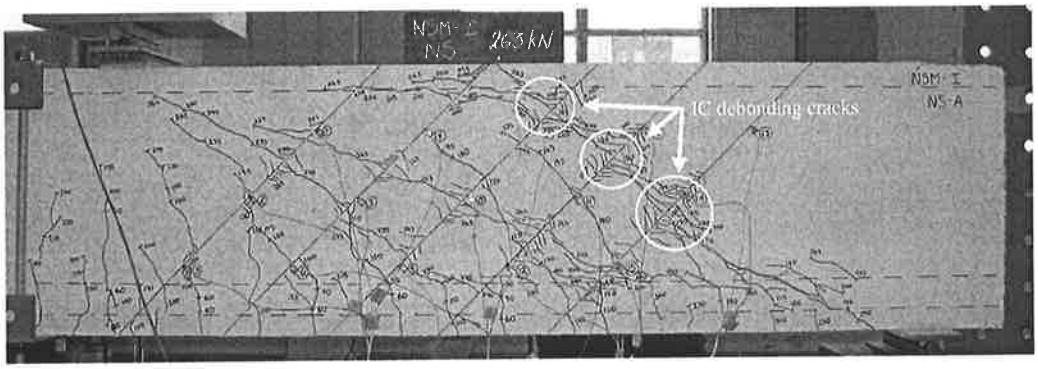

Figure 7.6.35: Test NSM 5IP NS at V = 178.8 kN (P = 263 kN) on Side A.

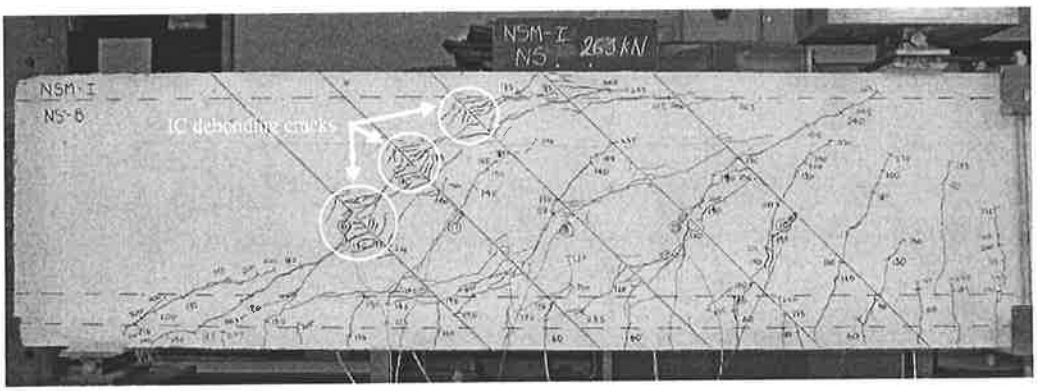

Figure 7.6.36: Test NSM 5IP NS at V = 178.8 kN (P = 263 kN) on Side B.

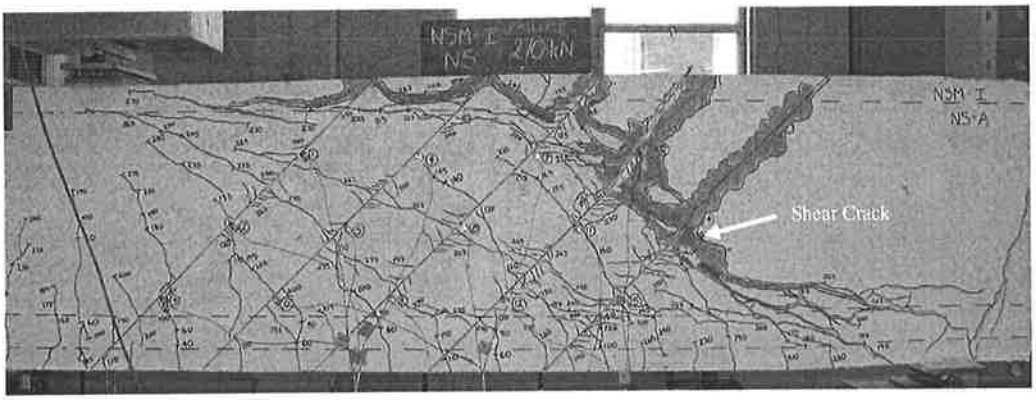

Figure 7.6.37: Failure of test NSM 5IP NS at V = 183.6 kN (P = 270 kN) on side A.

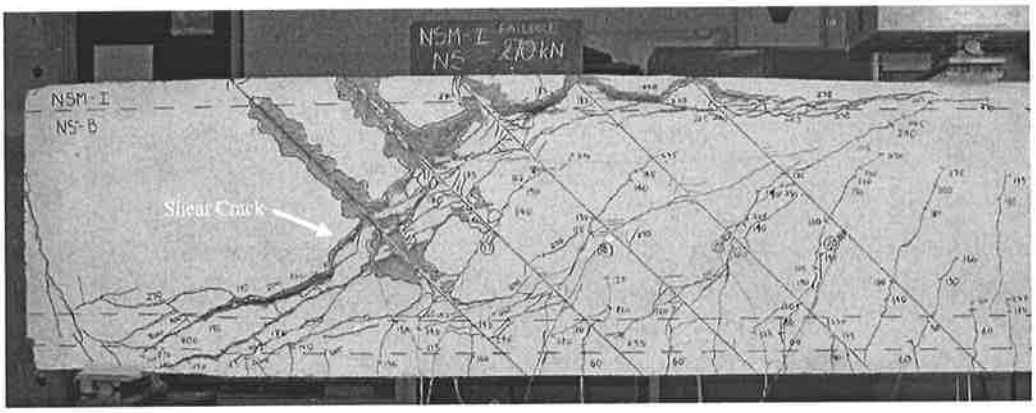

Figure 7.6.38: Failure of test NSM 5IP NS at V = 183.6 kN (P = 270 kN) on side B.

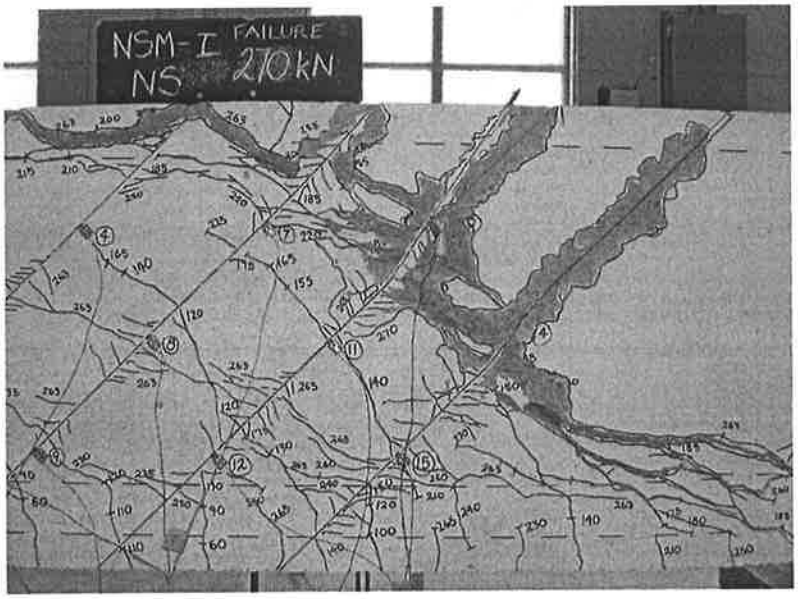

Figure 7.6.39: IC debonding of inclined plates.

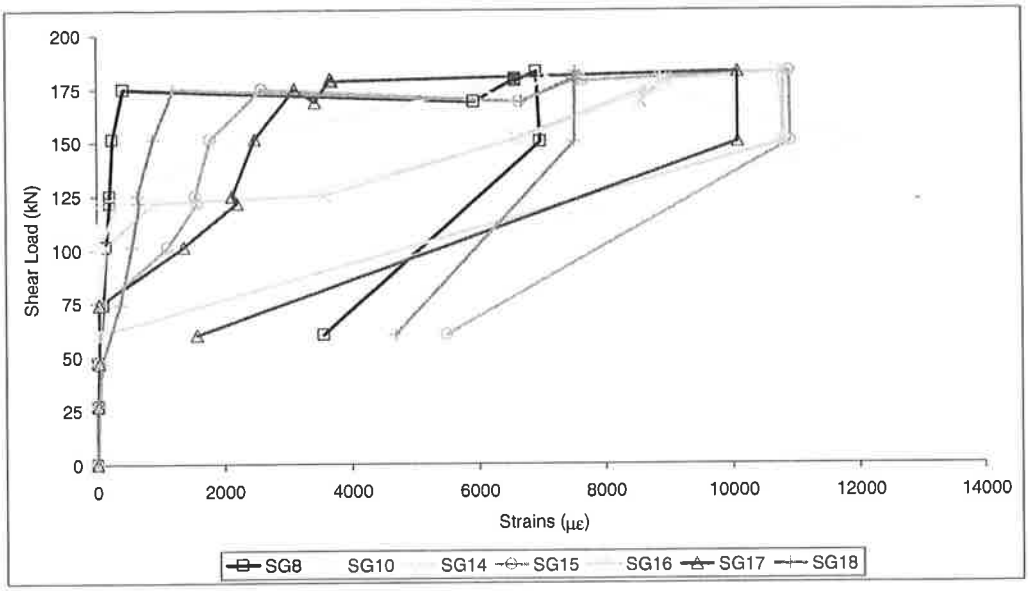

Figure 7.6.40: Strain reading for the inclined plates as load increases.

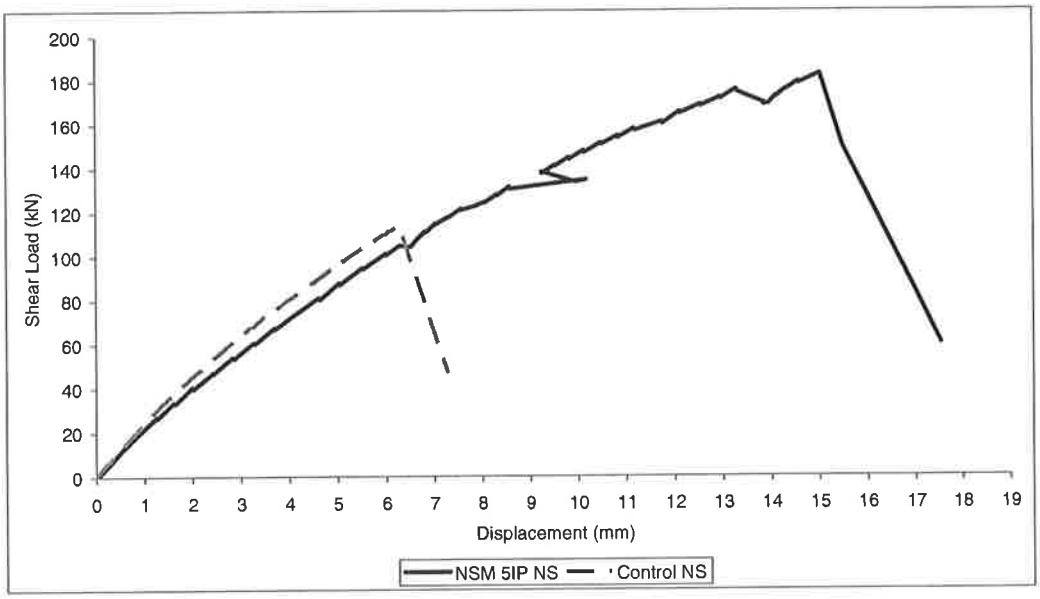

Figure 7.6.41: Deflection of beam test NSM 5IP NS.

7.6.6 Test NSM 5IP S

The test continued by determining the increase of shear strength using inclined NSM plates with steel stirrups. Figures 7.6.42 and 7.6.43 show propagation of flexural and shear cracks as the shear load increased to 95.2 kN (P= 140 kN). As the shear load increased to 142.8 kN (P = 210 kN), intermediate crack (IC) debonding begins to appear on all the plates shown in Figures 7.6.44 and 7.6.45. At shear load of 244.8 kN (P = 360 kN) more shear cracks form and IC debonding cracks develop further (Figures 7.6.46 and 7.6.47). The beam failed in

shear when the shear load reached 304 kN (P = 447 kN). The failure crack pattern of this beam is shown in Figures 7.6.48 and 7.6.49 with interception of the shear cracks causing IC debonding of the plates (Figure 7.6.50). Similar to test NSM 5IP NS, the path of this crack is on the weakest part of the strengthened beam and debonding was occurring at the shorter bond length of plates.

The strain readings for all the inclined plates are shown in Figure 7.6.51. From Figure 7.6.51 the maximum debonding strain recorded was 11375 microstrain (SG 14) close to the debonding strain of a pull test (13364 microstrain). Figure 7.6.51 also shows a significant axial force develop in the inclined strips leading to IC debonding which was not present in the longitudinal plated beams. The strains recorded for the internal steel stirrups (Figure 7.6.52) shows that stirrups 2, 3 and 4 all yielded. Figure 7.6.53 shows the deflection recorded with applied shear load. Comparing test NSM 5IP S and Control S shows a large increase in shear strength of 85 kN (or 38.8%).

In this test, the crack width were measured at 8 different locations (a,b,c,d,e,f,g and h) as shown in Figure 7.6.54. The measurement was taken using a crack measurement microscope by Pika Japan with magnification of 100 times and with one division equal to 0.01mm. The measurement was taken with load increment shown in Table 7.6.2 along the shear crack. From these observations the maximum crack width (0.7mm) was at location g, on the side B shown in Table 7.6.2. These measurements were stopped at a shear load of 244.8 kN for safety reasons.

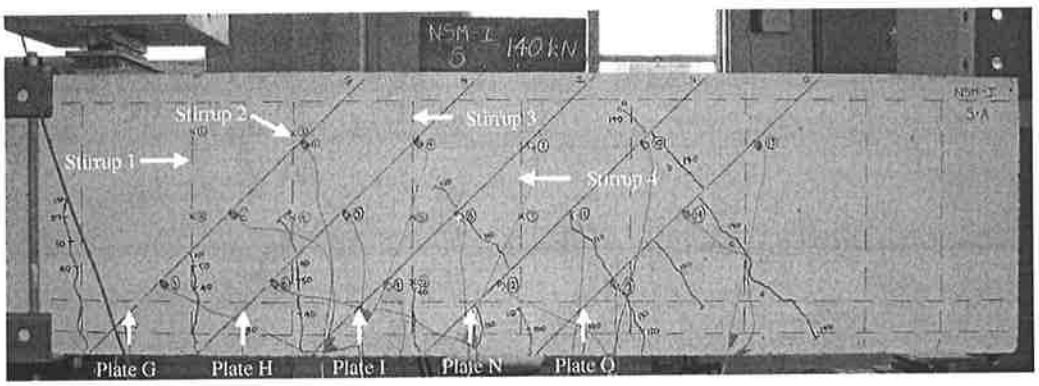

Figure 7.6.42: Test NSM 5IP S at V = 95.2 kN (P = 140 kN) on Side A.

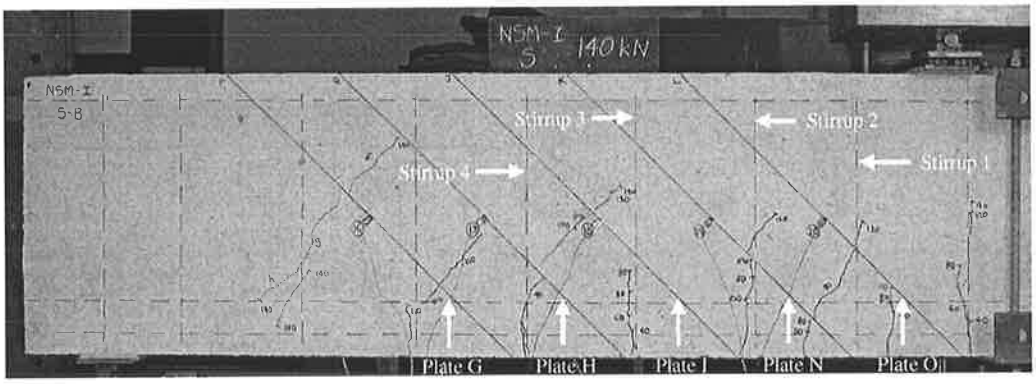

Figure 7.6.43: Test NSM 5IP S at V = 95.2 kN (P = 140 kN) on Side B.

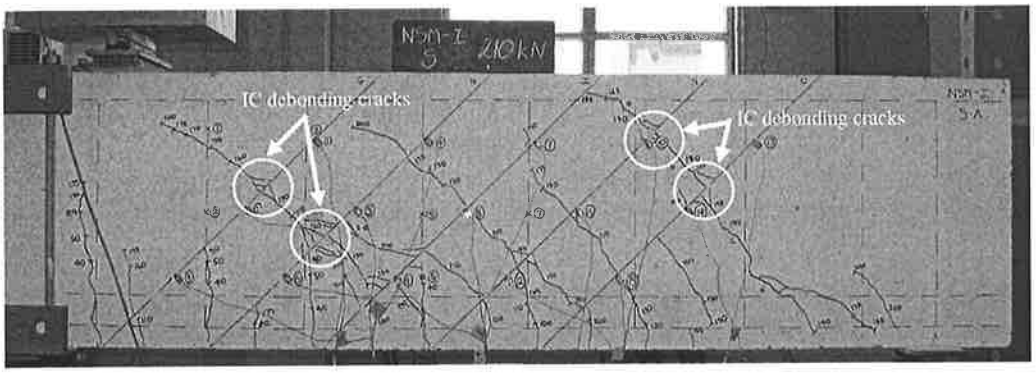

Figure 7.6.44: Test NSM 5IP S at V = 142.8 kN (P = 210 kN) on Side A.

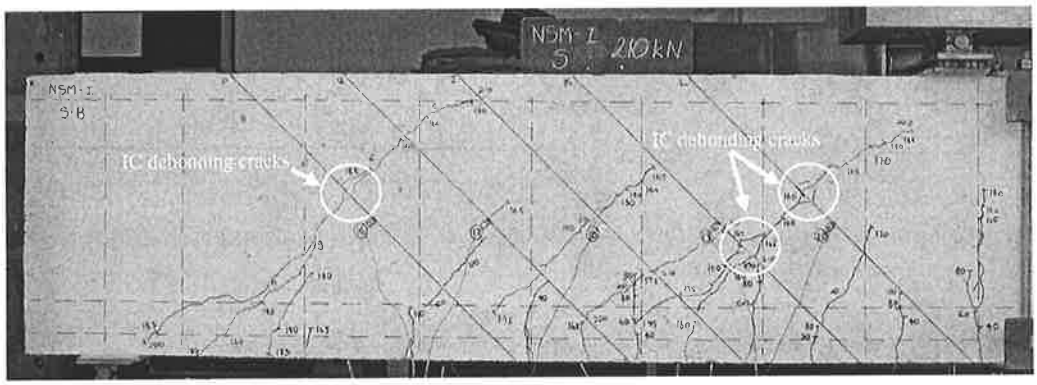

Figure 7.6.45: Test NSM 5IP S at V = 142.8 kN (P = 210 kN) on Side B.

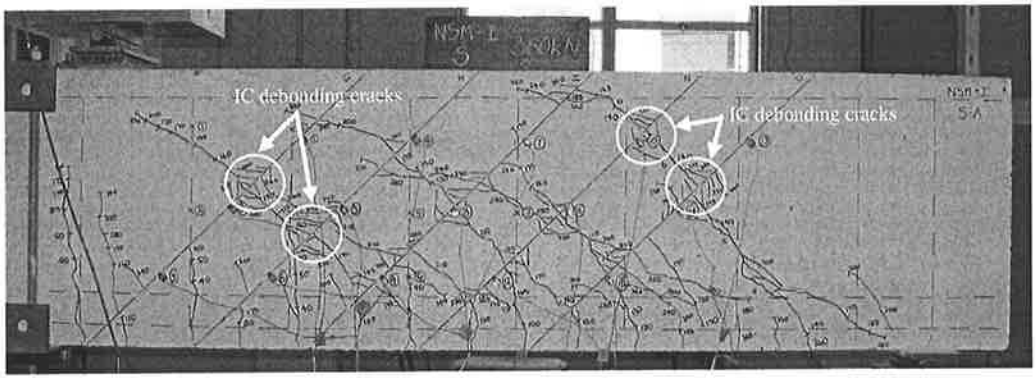

Figure 7.6.46: Test NSM 5IP S at V = 244.8 kN (P = 360 kN) on Side A.

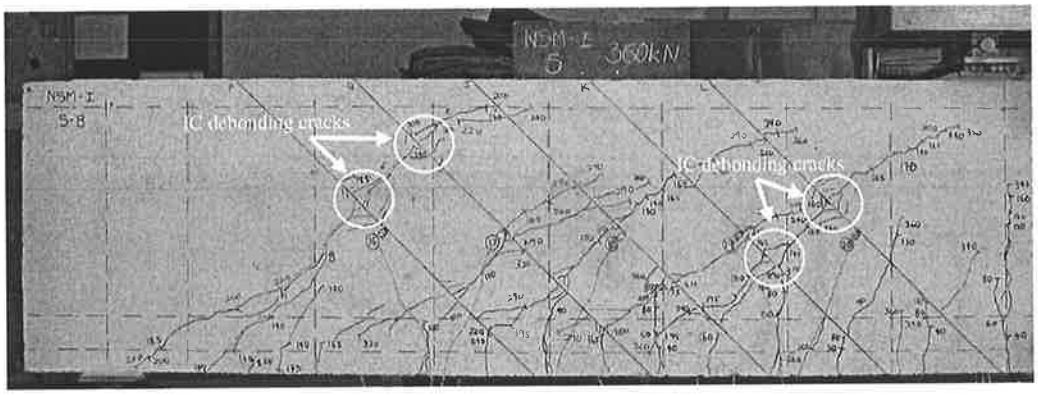

Figure 7.6.47: Test NSM 5IP S at V = 244.8 kN (P = 360 kN) on Side B.

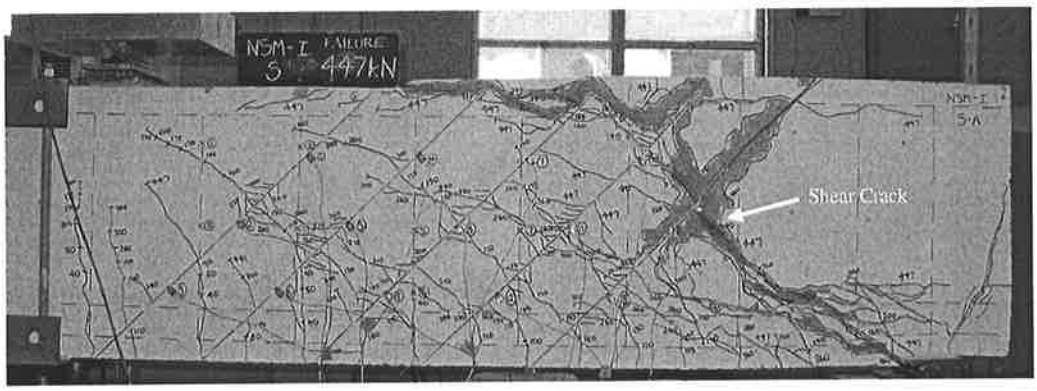

Figure 7.6.48: Failure of test NSM 5IP S at V = 304 kN (P = 447 kN) on side A.

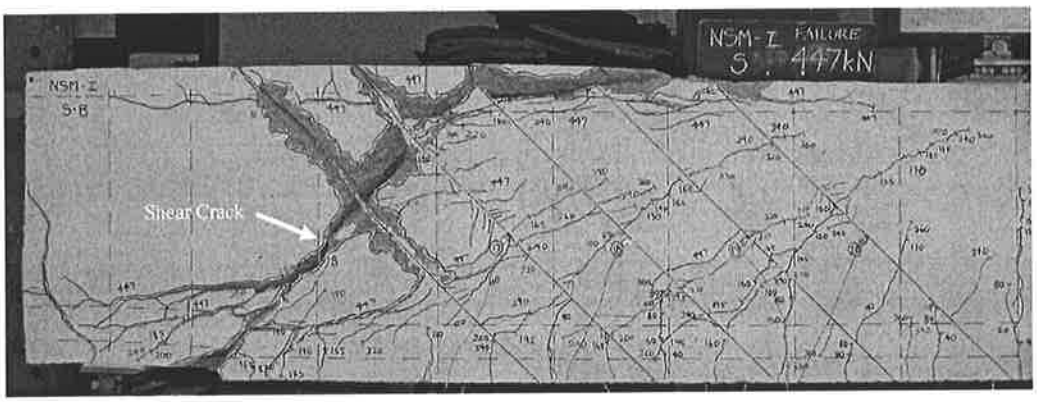

Figure 7.6.49: Failure of test NSM 5IP S at V = 304 kN (P = 447 kN) on side B.

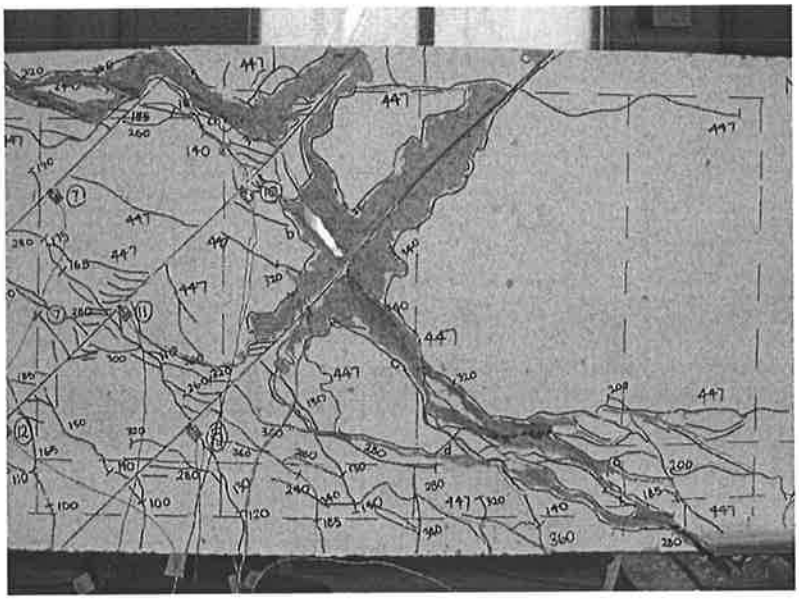

Figure 7.6.50: IC debonding of inclined plates.

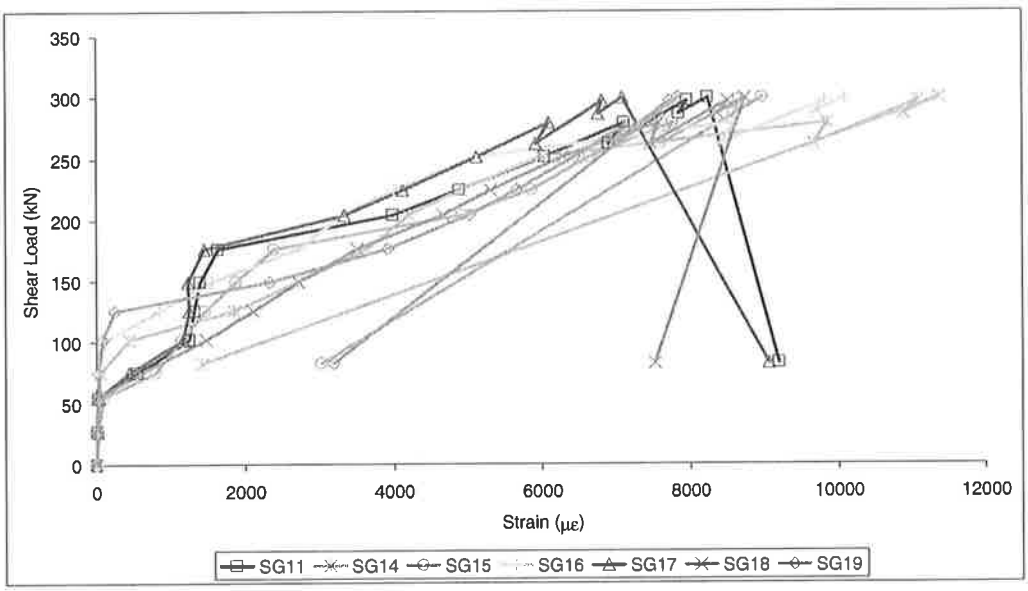

Figure 7.6.51: Strain reading for the inclined plates as load increases.

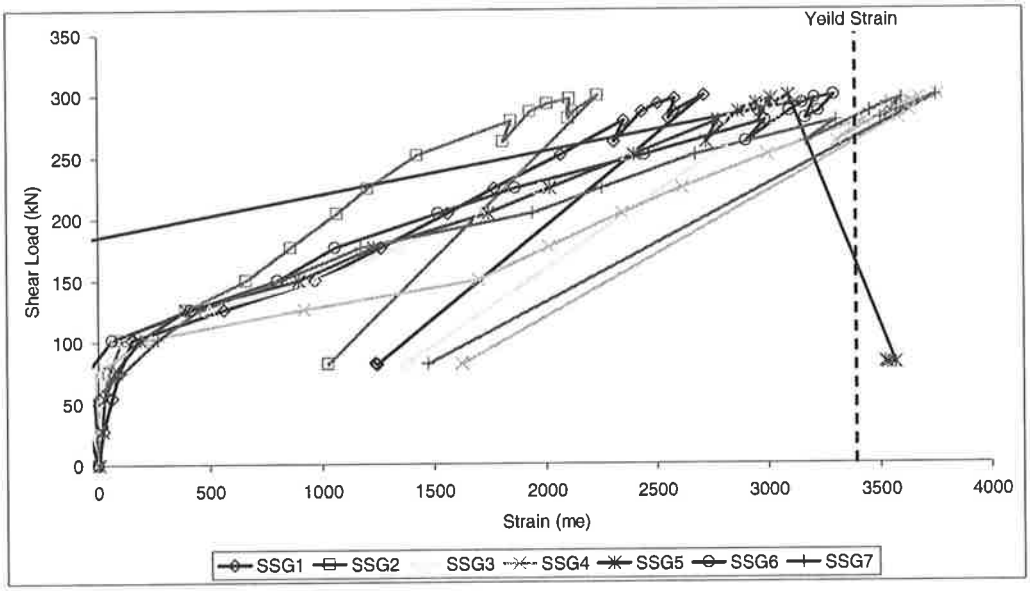

Figure 7.6.52: Strain reading for the internal steel stirrups.

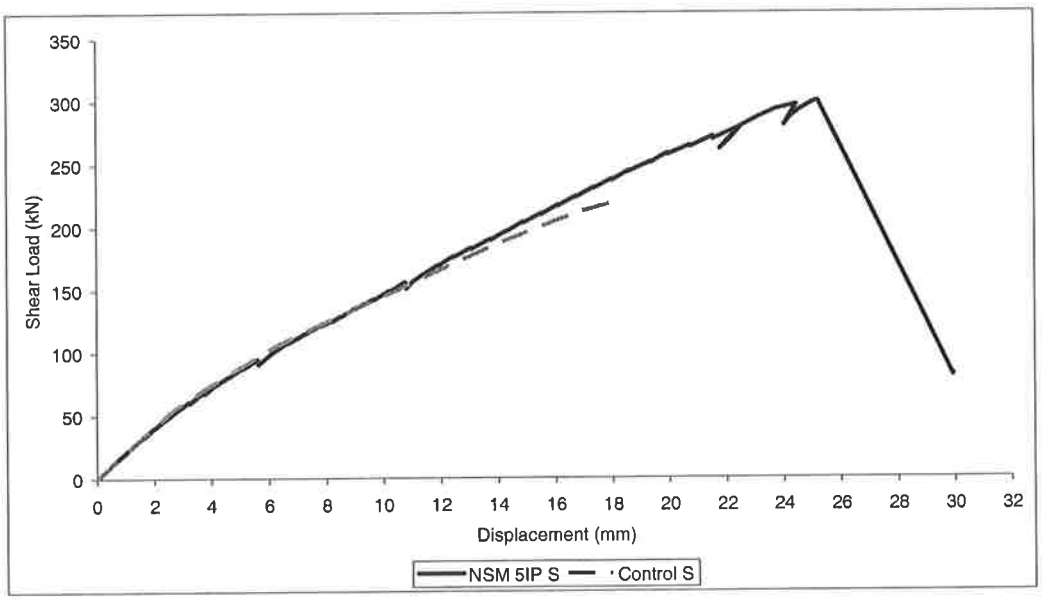

Figure 7.6.53: Deflection of beam test NSM 5IP S.

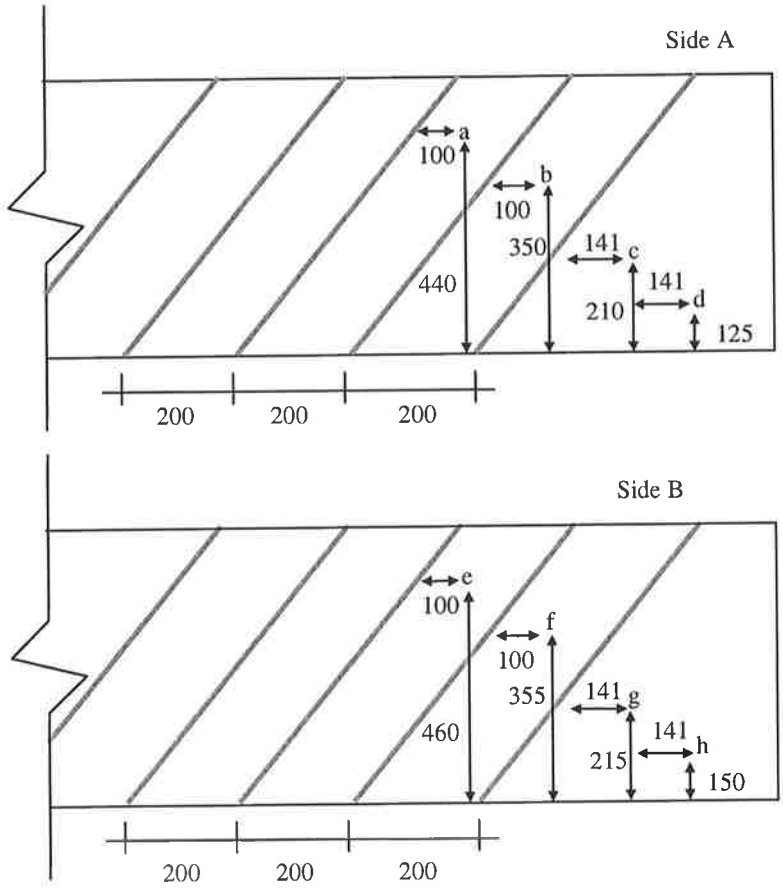

All dimensions are in mm.

Figure 7.6.54: Crack width measurements locations along the shear crack.

Table 7.6.2: Test NSM 5IP S cracks width measurement.

Shear Load (kN)	Crack width measurement (mm)							
	a	b	c	d	e	f	g	h
95.2	-	0.10	0.10	0.09	-	0.05	0.05	0.10
108.8	0.03	0.13	0.13	0.10	-	0.07	0.06	0.11
122.4	0.10	0.14	0.37	0.04	0.05	0.10	0.15	0.05
136.0	0.10	0.15	0.45	0.02	0.10	0.15	0.40	0.10
149.6	0.10	0.15	0.49	0.01	0.20	0.20	0.20	0.05
163.2	0.08	0.14	0.55	0.01	0.25	0.25	0.30	0.05
183.6	0.09	0.16	0.60	0.01	0.25	0.25	0.45	0.05
204.0	0.08	0.19	0.57	0.01	0.30	0.35	0.40	0.03
224.4	0.08	0.14	0.60	0.01	0.30	0.50	0.60	0.03
244.8	0.08	0.13	0.60	0.01	0.35	0.50	0.70	0.03

7.6.7 Test NSM 4VP NS

The aim of this test investigates the increase of shear strength using vertical NSM plates. Figures 7.6.55 and 7.6.56 show the propagation of flexural and shear cracks as the shear load increased to 108.8 kN (P= 160 kN). As the shear load increased to 112.2 kN (P=165 kN), intermediate crack (IC) debonding begins to appear on plate D and N shown in Figures 7.6.57 and 7.6.58. At shear load of 136 kN (P = 200 kN) more IC appearing along plates D,K,L,M and N.

After reaching V = 136 kN (P = 200 kN), the shear load dropped to 126.3 kN (P = 185.8 kN). The beam was reload back to V = 132.6R kN (P = 195R kN) shown in Figures 7.6.61 and 7.6.62, which later again dropping back to V = 115.7 kN (P = 170.2 kN). Finally the beam was reload to V = 124.4R kN (P = 183R kN) and fail in shear. The failure pattern of this beam is shown Figures 7.6.63 and 7.6.64 with interception of the CDC debonded the plate from the concrete beam (Figure 7.6.65) where the cracks propagate along the vertical plates. Similar to the previous tests, the path of this crack is on the weakest part of the strengthened beam and that the debonding was occurring at the shorter bond length of plates. The strains reading for all the vertical plates are shown in Figure 7.6.66, which the maximum debonding strain recorded was 12668 microstrain (SG 14) again close to the debonding strain of a pull test (13364 microstrain). Figure 7.6.67 shows the deflection recorded with applied shear load. Comparing test NSM 4VP NS with Control NS shows increase in shear strength of 21.8 kN (or 19.1%).

Also in this test, the crack widths were measured at 6 different locations (a,b,c,d,e and f) as shown in Figure 7.6.68. From these observation the maximum crack width (1.2 mm) was at location a, on the side A of beam (Table 7.6.3). These measurements were stopped at a shear load of 136 kN also for safety reason.

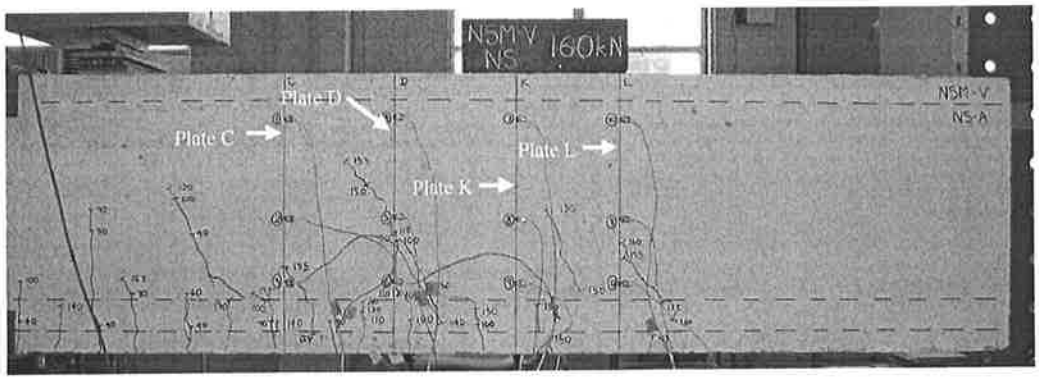

Figure 7.6.55: Test NSM 4VP NS at V = 108.8 kN (P = 160 kN) on Side A.

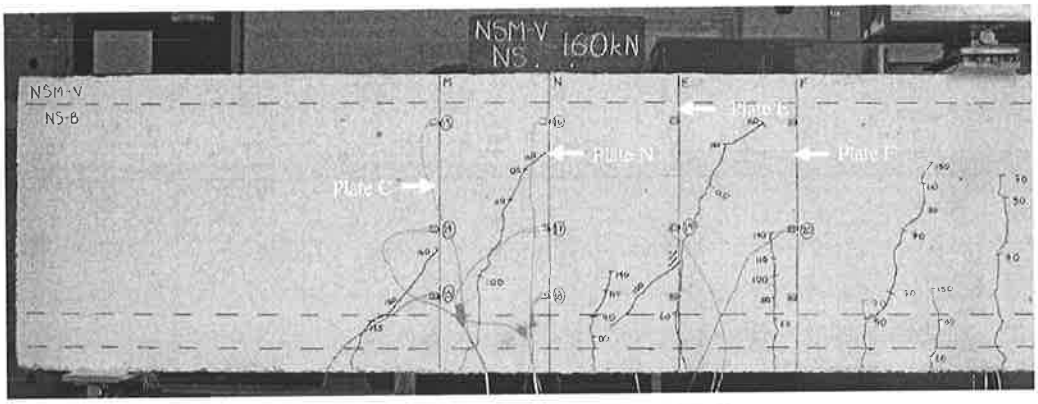

Figure 7.6.56: Test NSM 4VP NS at V = 108.8 kN (P = 160 kN) on Side B.

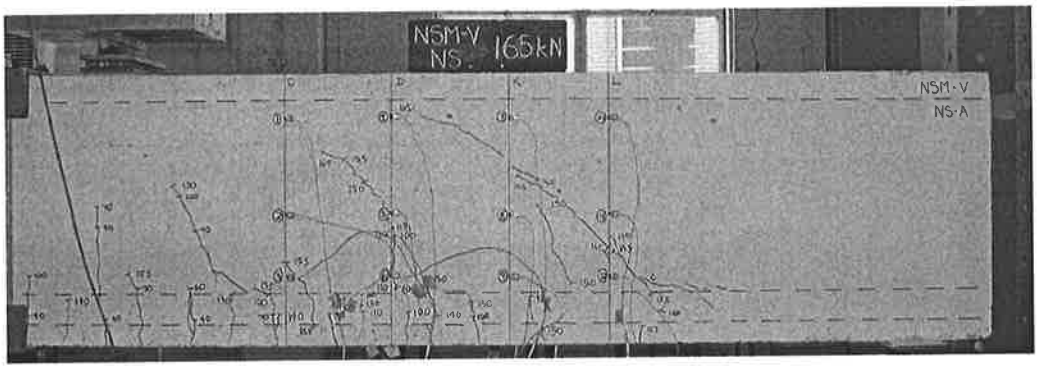

Figure 7.6.57: Test NSM 4VP NS at V = 112.2 kN (P = 165 kN) on Side A.

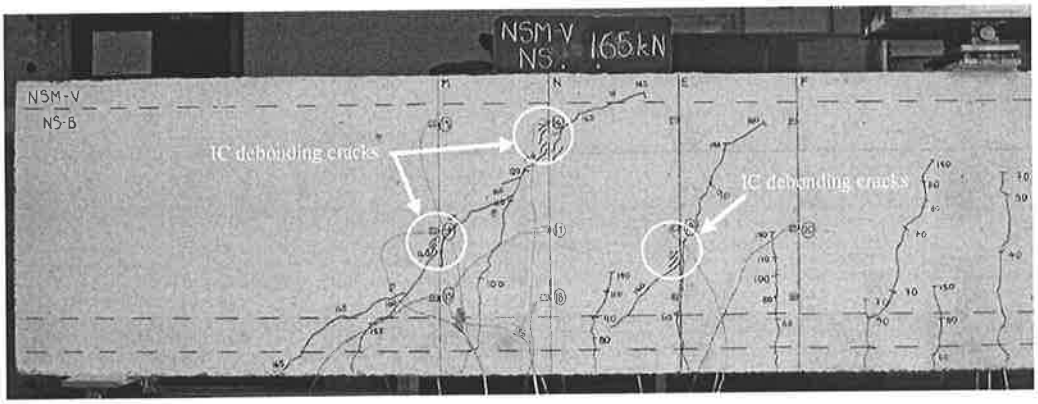

Figure 7.6.58: Test NSM 4VP NS at V = 112.2 kN (P = 165 kN) on Side B.

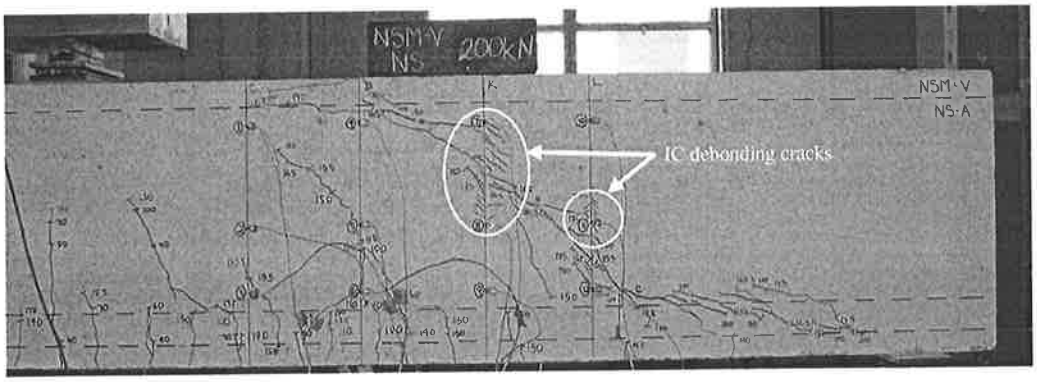

Figure 7.6.59: Test NSM 4VP NS at V = 136 kN (P = 200 kN) on Side A.

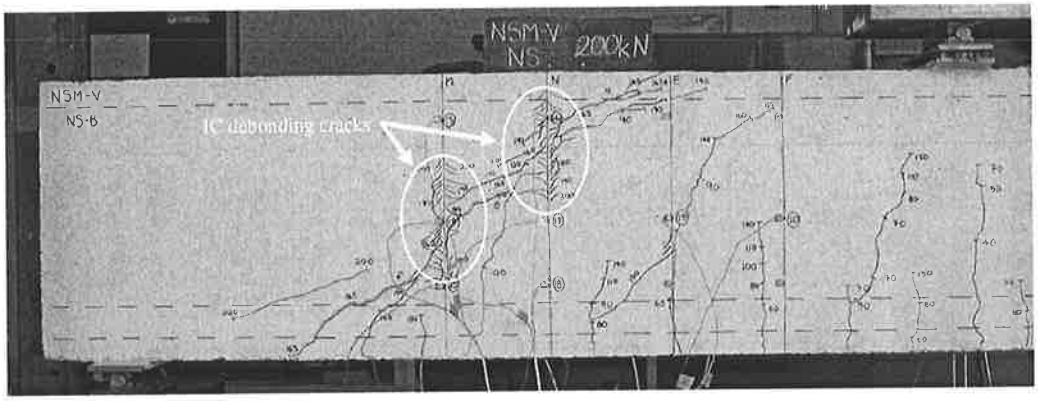

Figure 7.6.60: Test NSM 4VP NS at V = 136 kN (P = 200 kN) on Side B.

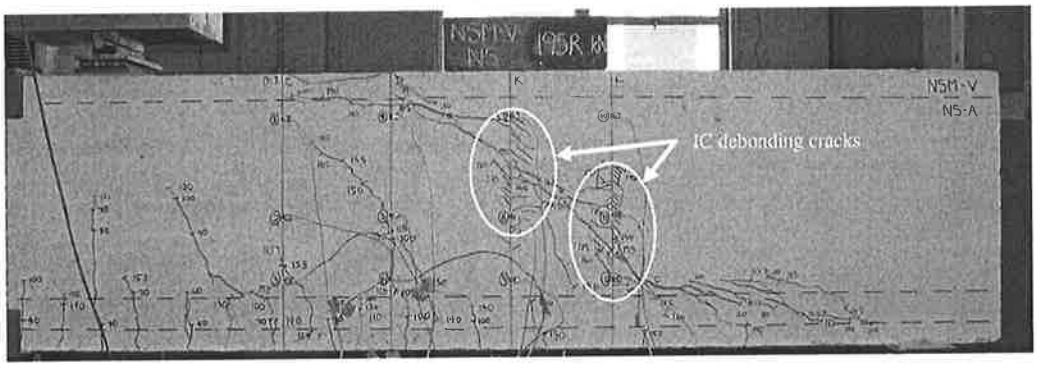

Figure 7.6.61: Test NSM 4VP NS at V = 132.6R kN (P = 195R kN) on Side A.

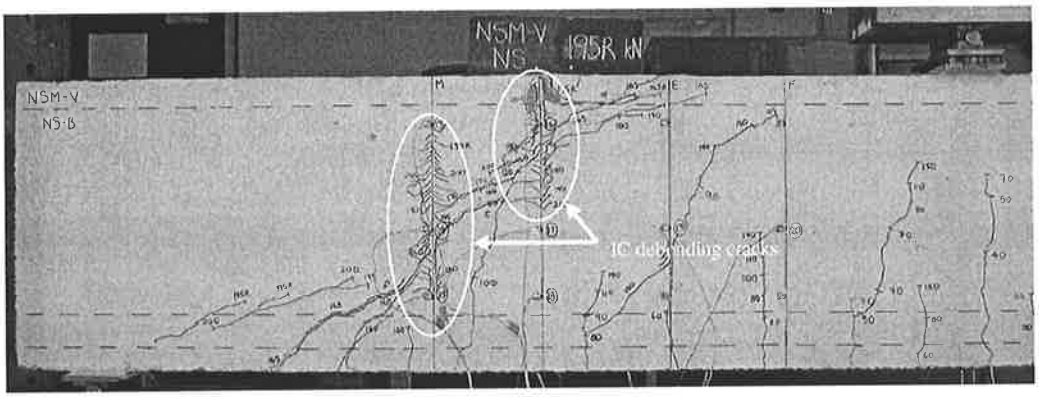

Figure 7.6.62: Test NSM 4VP NS at V = 132.6R kN (P = 195R kN) on Side B.

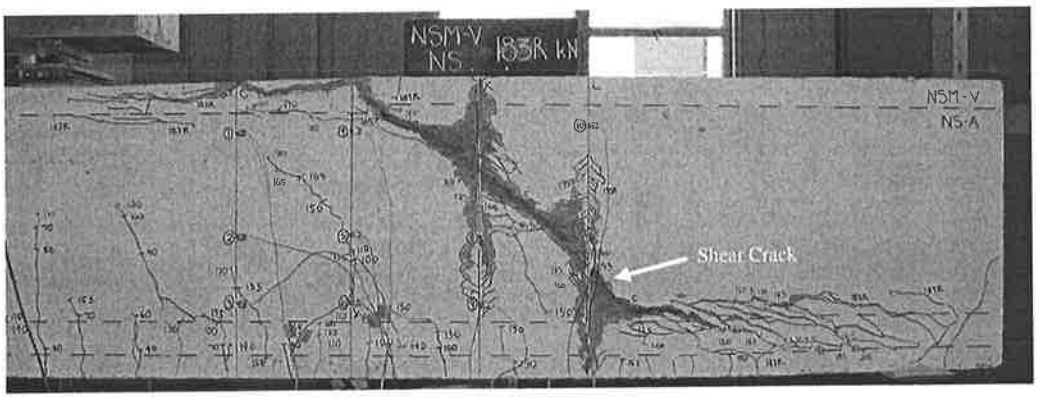

Figure 7.6.63: Failure of test NSM 4VP NS at V = 124.4R kN (P = 183R kN) on side A.

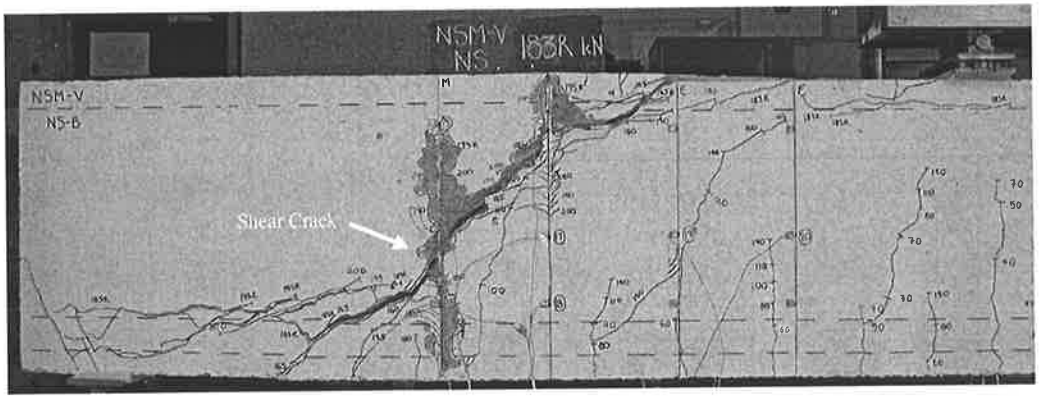

Figure 7.6.64: Failure of test NSM 4VP NS at V = 124.4R kN (P = 183R kN) on side B.

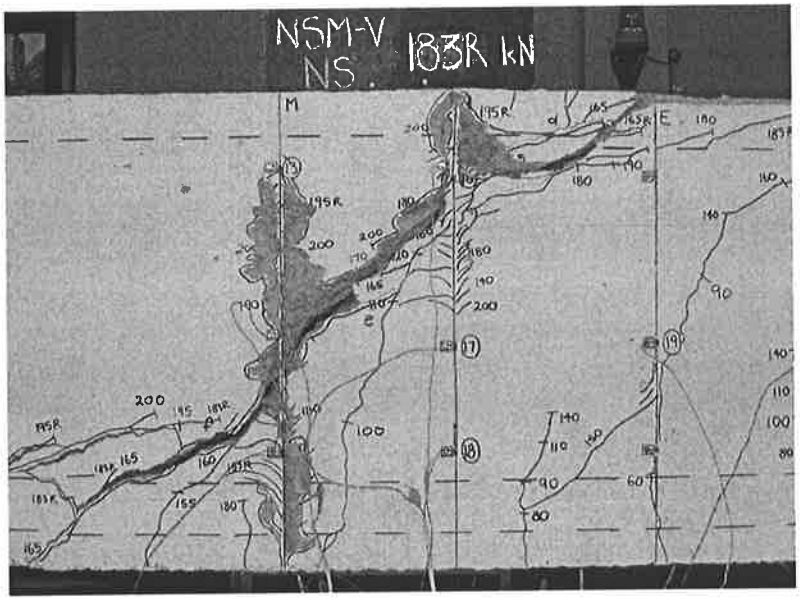

Figure 7.6.65: IC debonding of vertical plates.

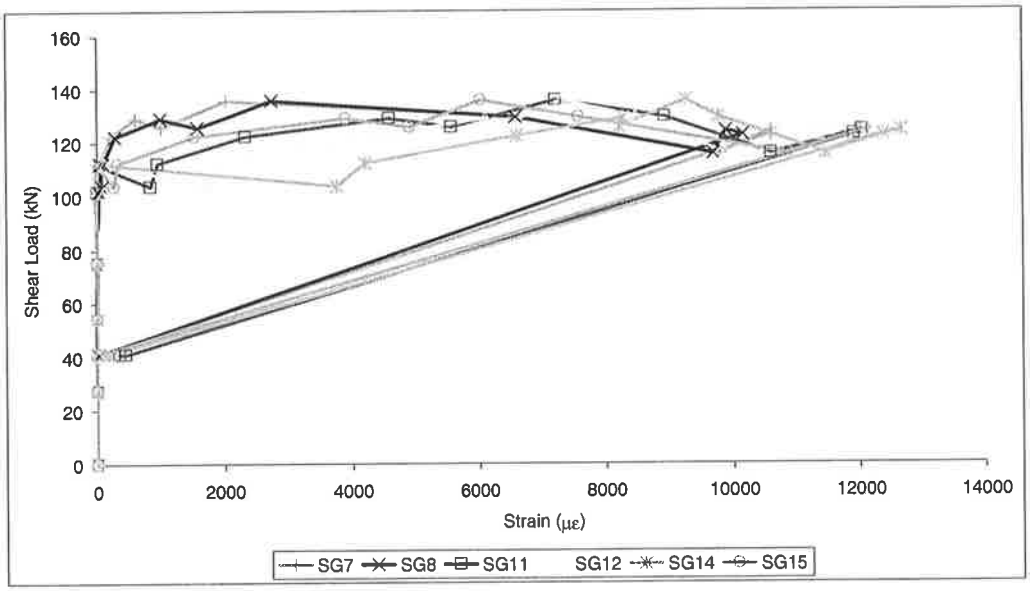

Figure 7.6.66: Strain reading for the inclined plates as load increases.

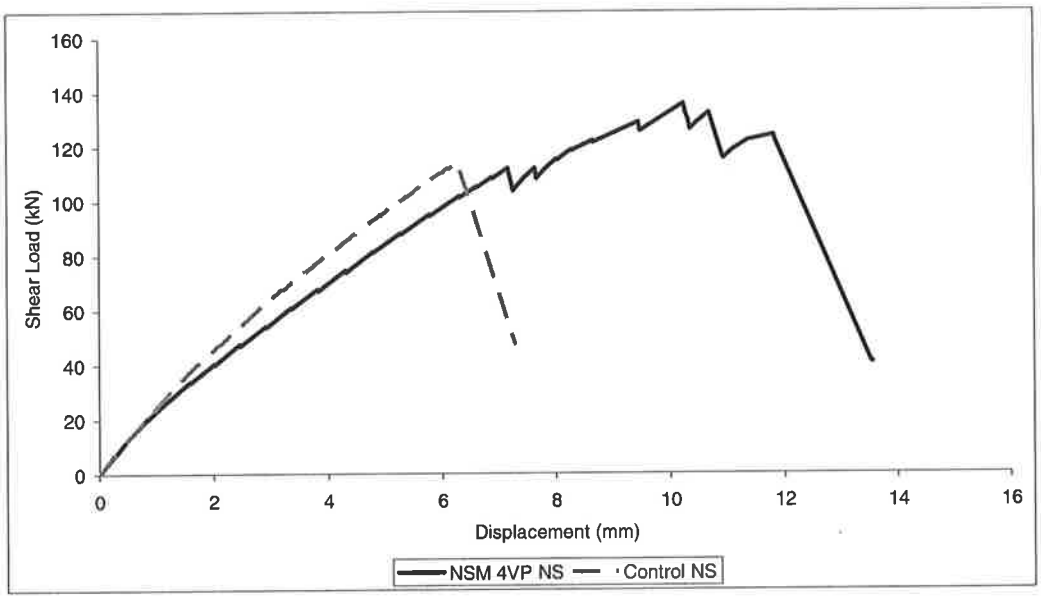

Figure 7.6.67: Deflection of beam test NSM 4VP NS.

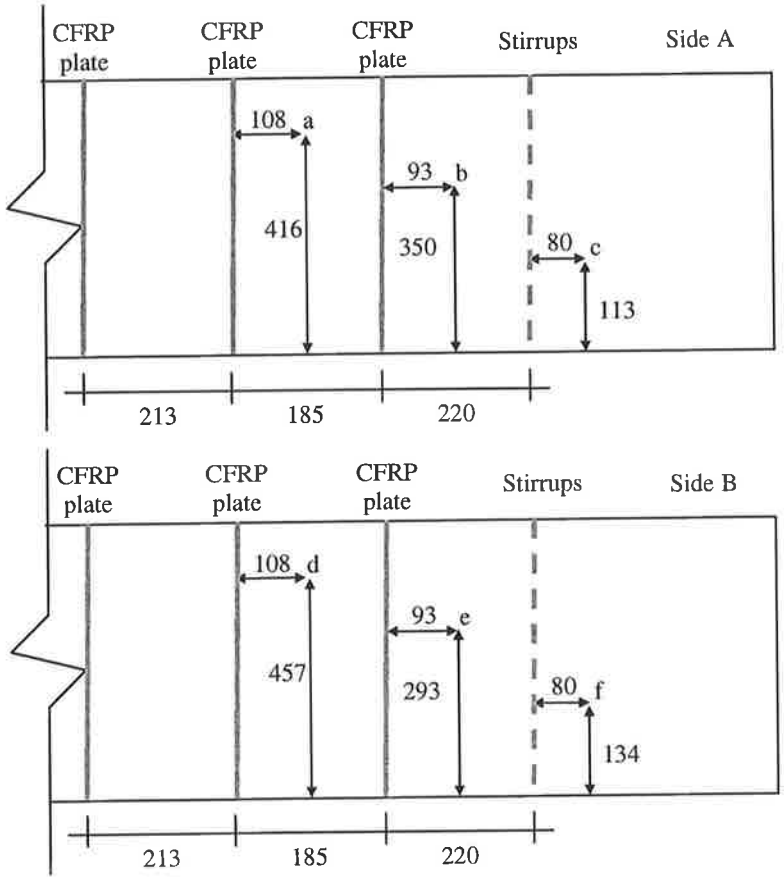

All dimensions are in mm.

Figure 7.6.68: Crack width measurements locations along the shear crack.

Table 7.6.3: Test NSM 4VP NS cracks width measurement.

Shear Load (kN)	Crack width measurement (mm)					
	a	b	c	d	e	f
112.2	0.05	0.30	0.20	0.05	0.20	0.10
108.8R	0.15	0.40	0.30	0.10	0.30	0.20
122.4	0.15	0.80	0.70	0.40	0.60	0.60
136.0	1.20	-	-	0.30	0.70	-

7.6.8 Test NSM 4VP S

This final test investigates the increase of shear strength using vertical NSM plates with the existence of steel stirrups. Figures 7.6.69 and 7.6.70 show the propagation of flexural and shear cracks as the shear load increased to 136 kN (P = 200 kN). As the shear load increased

to 231.2 kN (P = 340 kN), intermediate crack (IC) debonding begins to appear in plates I,J,O and P shown in Figures 7.6.71 and 7.6.72.

After reaching V = 282 kN (P = 414.8 kN), the shear load dropped to 271.5 kN (P = 399.3 kN). The beam was reloaded until it reached V = 283.6 kN (P = 417 kN) and then failed in shear. The failure crack pattern of this beam is shown in Figures 7.6.73 and 7.6.74 with interception of the shear cracks causing IC debonding of plate (Figure 7.6.75) and rupture the internal stirrups (Figure 7.6.76). Also, similar to the previous tests, the path of this crack is on the weakest part of the strengthened beam and that the debonding was occurring at the shorter bond length of plates.

The strain readings for all the vertical plates is shown in Figure 7.6.77, which the maximum debonding strain recorded was 11910 microstrain (SG 14) again close to the debonding strain of a pull test (13364 microstrain). The strain recorded for the internal steel stirrups (Figure 7.6.78) shows that steel stirrups number 3 and 4 were all yielded. Figure 7.6.79 shows the deflection recorded with applied shear load. Comparing test NSM 4VP S with Control S shows increase in shear strength of 64.6 kN (or 29.5%).

In this test, the crack widths were measured at 6 different location (a,b,c,d,e and f) as shown in Figure 7.6.80. From these observations the maximum crack width (> 1.25 mm) was at location e, on the side B of the beam (Table 7.6.4). Again these measurements were stopped at a shear load of 204 kN for safety.

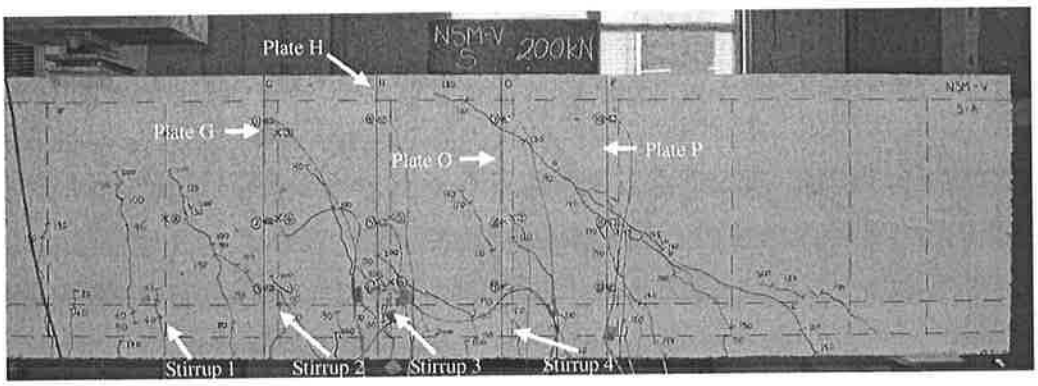

Figure 7.6.69: Test NSM 4VP S at V = 136 kN (P = 200 kN) on Side A.

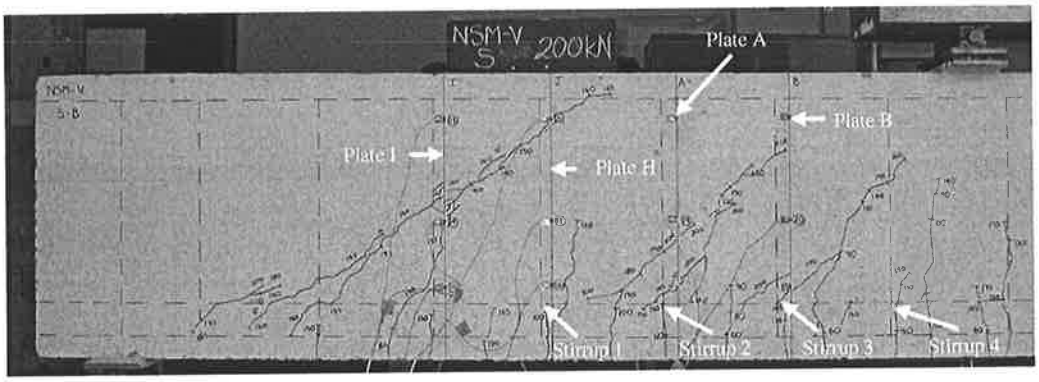

Figure 7.6.70: Test NSM 4VP S at V = 136 kN (P = 200 kN) on Side B.

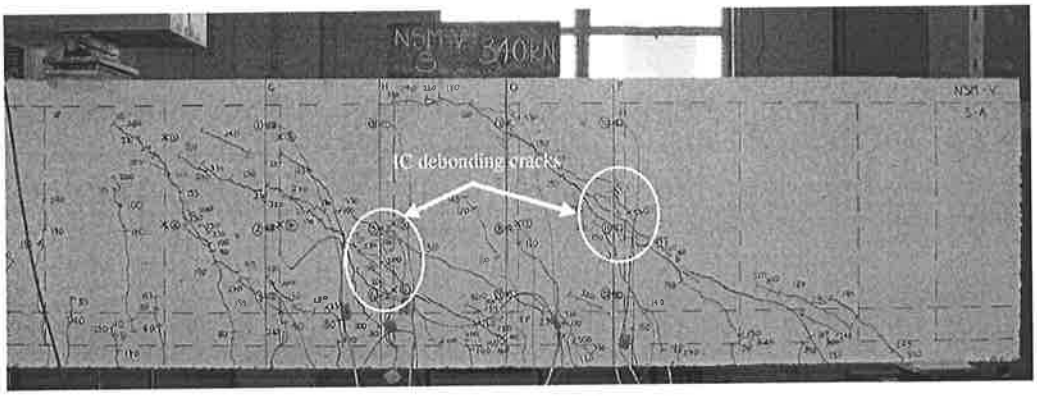

Figure 7.6.71: Test NSM 4VP S at V = 231.2 kN (P = 340 kN) on Side A.

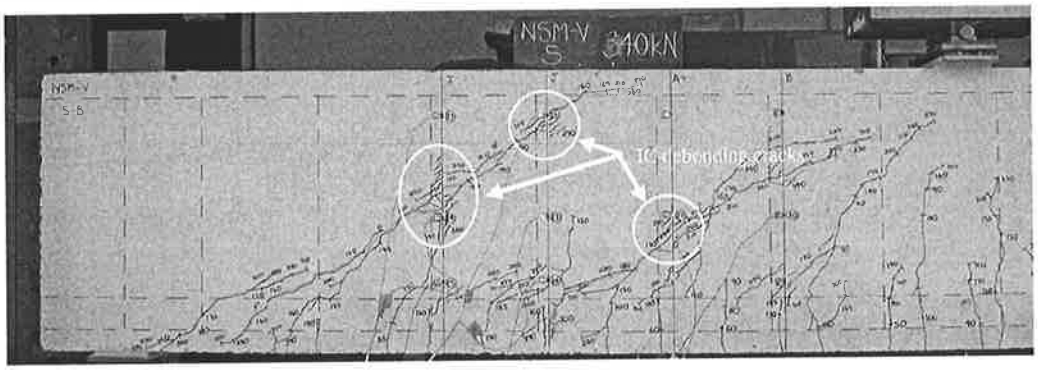

Figure 7.6.72: Test NSM 4VP S at V = 231.2 kN (P = 340 kN) on Side B.

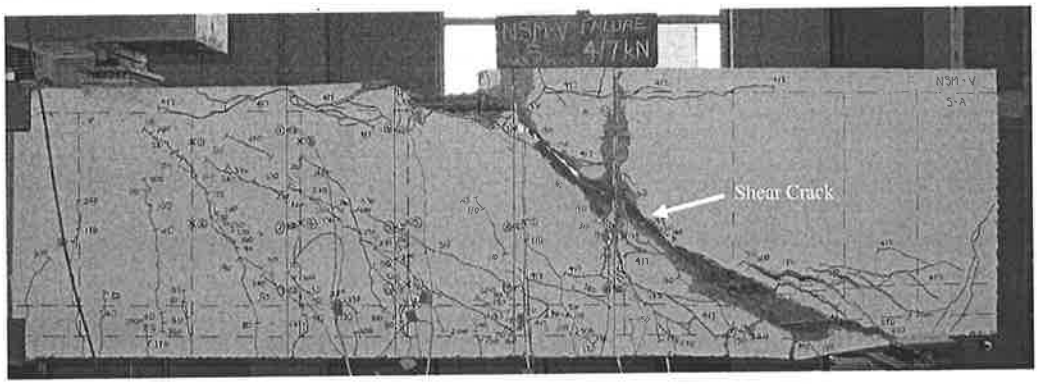

Figure 7.6.73: Failure of test NSM 4VP S at V = 283.6 kN (P = 417 kN) on side A.

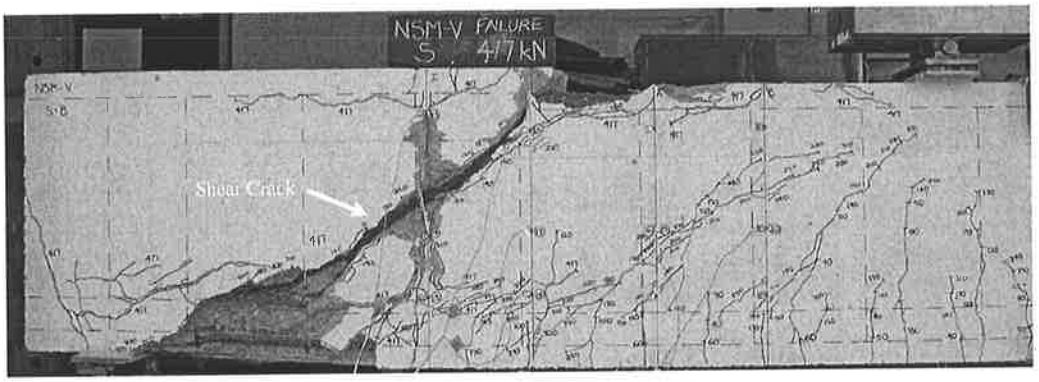

Figure 7.6.74: Failure of test NSM 4VP S at V = 283.6 kN (P = 417 kN) on side B.

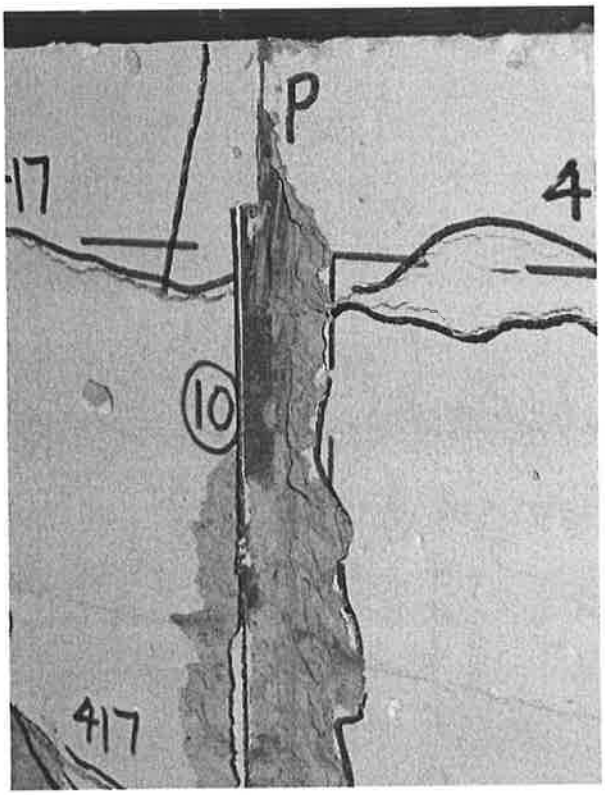

Figure 7.6.75: IC debonding of vertical plates.

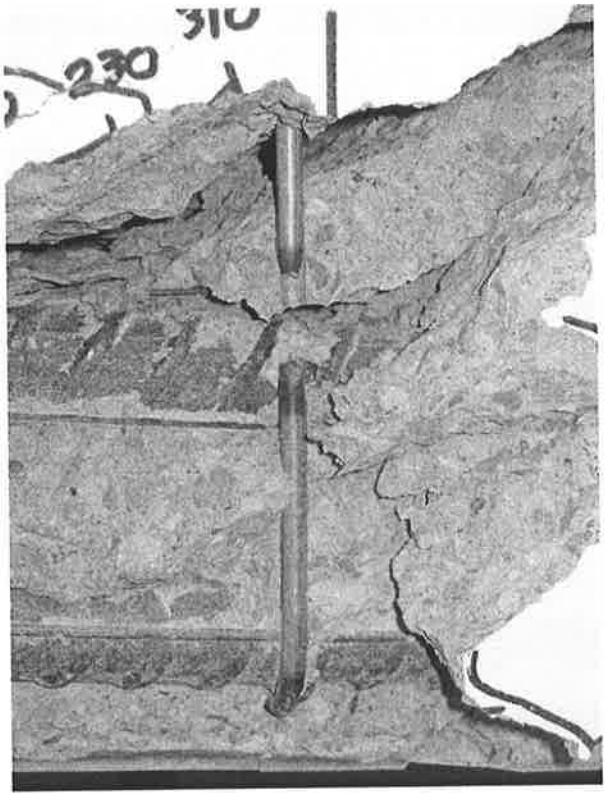

Figure 7.6.76: Rupture of the steel stirrup.

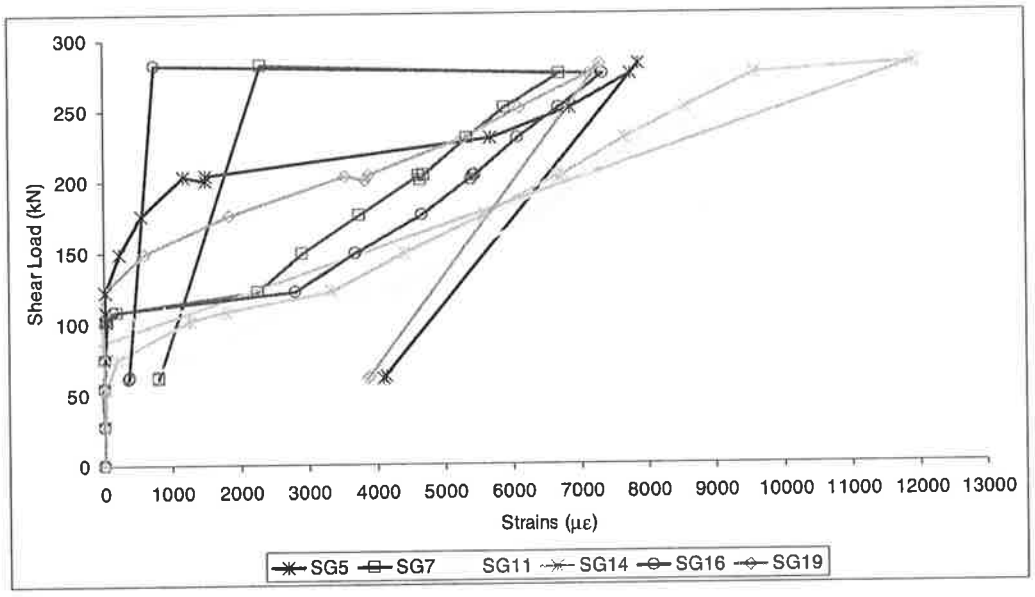

Figure 7.6.77: Strain reading for the inclined plates as load increases.

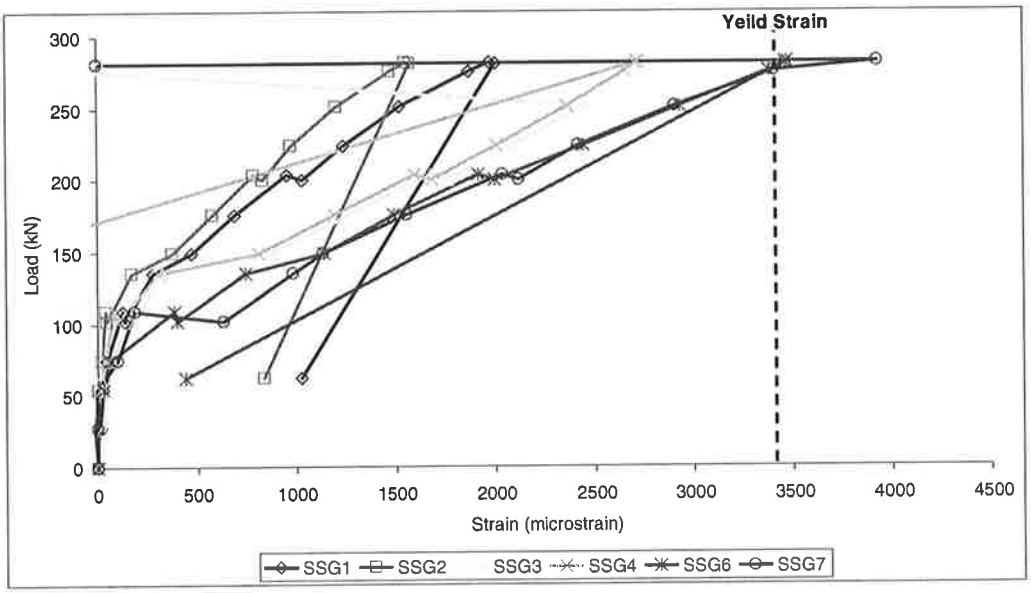

Figure 7.6.78: Strain reading for the internal steel stirrups.

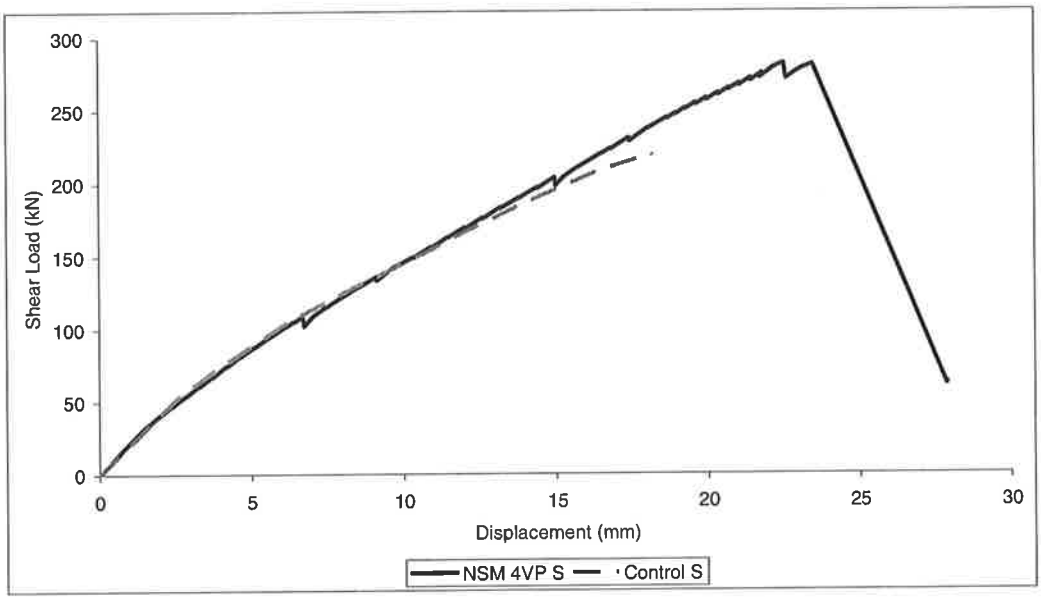

Figure 7.6.79: Deflection of beam test NSM 4VP S.

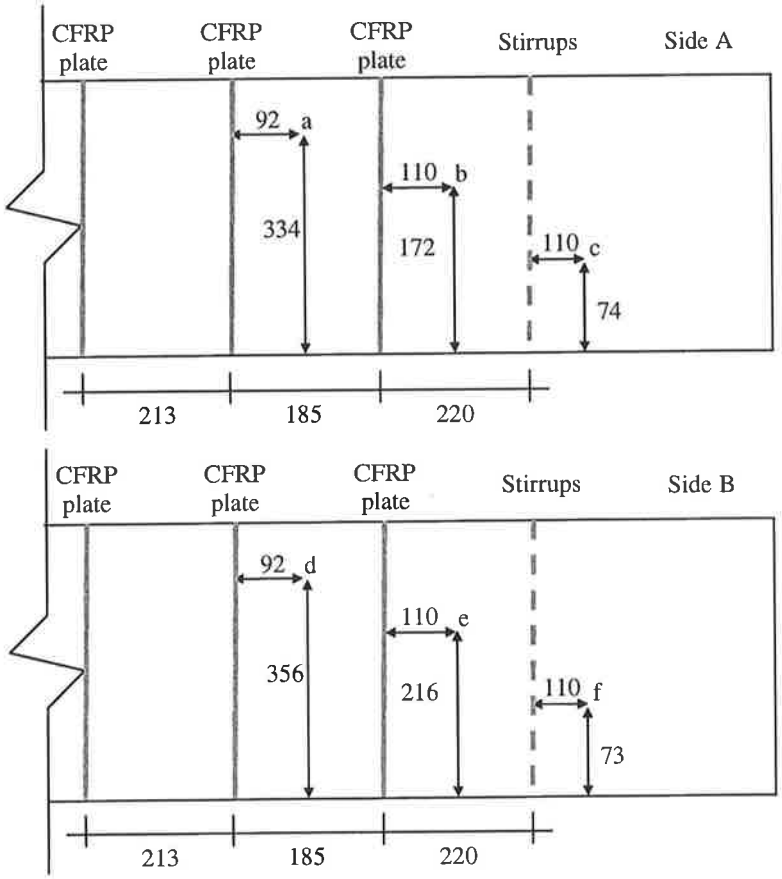

Figure 7.6.80: Crack width measurements locations along the shear crack.

Table 7.6.4: Test NSM 4VP S cracks width measurement.

	Crack width measurement (mm)					
Load (kN)	a	b	c	d	e	f
108.8	0.20	0.32	0.02	0.10	0.20	0.00
122.4	0.40	0.40	0.05	0.20	0.40	0.00
136.0	0.50	0.35	0.05	0.30	0.50	0.00
149.6	0.60	0.70	0.05	0.40	0.55	0.00
163.2	0.60	0.60	0.05	0.60	0.65	0.00
176.8	0.65	0.75	0.03	0.55	1.00	0.00
190.4	0.80	0.85	0.03	0.50	0.90	0.00
204.0	0.73	0.90	0.03	0.80	> 1.25	0.00

7.7 Discussion of Test Results

All the observation from the experiments was explained in the earlier text. Now, the analysis for each beams test is discussed to quantify the contribution of steel stirrups, FRP plates and concrete. In Table 7.7.1, each column is numbered for easy reference in describing the analysis. Column 1 is the plate angle of the FRP plate used in the beam test. The 0, 45 and 90 degrees represent the longitudinal, inclined and vertical FRP plates used in the beam tests. Column 2 represents the shear failure from the experiments. The contribution of the steel stirrups (V_s) towards the total shear load is shown in column 3 and 4. In column 3, V_s is calculated from the experiments by subtracting V_{exp} for Control S with Control NS which is the concrete shear capacity (V_c). Meanwhile in column 4, V_s is calculated using the AS3600 with 45 degree critical diagonal crack (shear crack) intercepting particular numbers of steel stirrups. Observation from experiments shows 2 steel stirrups were intercepted in each beams test which gives value of 122kN calculated using AS3600.

Table 7.7.1 also shows the contribution of FRP plates (V_{frp}) towards the total shear load in columns 5 to 10. The experimental V_{frp} contribution as calculated from strain gauge readings which gives the force in each plates and it is compared with calculated V_{frp} using Intermediate crack resistance equation P_{IC} (chapter 4).

Table 7.7.1 shows the difference between these two reading was not much (except for longitudinal plating); any difference is likely due to the strain gauge on the plate not located at the interception of the shear crack.

All three types of plating contribute differently towards V_{frp}. The longitudinal plated beams does not have any contribution to V_{frp} (vertical component), however it increases the concrete shear capacity (ΔV_c) [Mohamed Ali (2000)]. Forces in the longitudinal plates are shown in columns 7 and 8. The inclined plated beams contributed to both the V_{frp} (vertical) and ΔV_c (horizontal), which were derived from the resultant force in columns 9 and 10. Finally, the vertical plated which solely contributes to the V_{frp} (vertical component) is shown in columns 5 and 6.

Table 7.7.1: Beam experiments analysis.

	Plate Angel (1)	V exp (2)	Vs exp (3)	Vs (4)	Vfrp (kN)						Vc + ΔVc		ΔVc (0.156P)		Vc	
					Vertical		Horizontal		Resultant		SG (11)	P_{IC} (12)	SG (13)	P_{IC} (14)	SG (15)	P_{IC} (16)
					SG (5)	P_{IC} (6)	SG (7)	P_{IC} (8)	SG (9)	P_{IC} (10)						
Control NS	-	114	-	-	-	-	-	-	-	-	-	-	-	-	114	
Control S	-	219	105	122	-	-	-	-	-	-	-	-	-	-	114	
NSM 3LP NS	0	119	-	-	0.0	0.0	6.2	168.0	0.0	0.0	119.0	119.0	1.0	26.2	118.0	92.8
NSM 3LP S	0	197	105	122	0.0	0.0	19.8	168.0	0.0	0.0	92.0	92.0	3.1	26.2	88.9	65.8
NSM 5IP NS	45	184	-	-	85.9	96.0	85.9	96.0	121.5	135.8	98.1	88.0	13.4	15.0	84.7	73.0
NSM 5IP S	45	304	105	122	58.7	68.9	58.7	68.9	83.0	97.4	140.3	130.1	9.2	10.7	131.1	119.4
NSM 4VP NS	90	124	-	-	83.0	91.5	0.0	0.0	0.0	0.0	41.0	32.5	0	0	41.0	32.5
NSM 4VP S	90	284	105	122	77.4	86.8	0.0	0.0	0.0	0.0	101.6	92.2	0	0	101.6	92.2

The only component unknown at this stage is the concrete shear capacity V_c and ΔV_c (column 11 and 12) which varies depending on type of plating. Results in column 11 was calculated with V_{exp} (column 2) subtracting with $V_{s\,exp}$ (column 3) and V_{frp} (column 5) or as Eq. 7.7.1.

$$V_c + \Delta V_c = V_{exp} - V_{s\,exp} - V_{frp,SG} \tag{7.7.1}$$

Meanwhile results in column 12 was calculated the same way as column 11 but using $V_{s\,cdc}$ - (column 4).Column 13 and 14 is the calculation of ΔV_c which is 15.6% from the horizontal force acting in the plates [Oehlers and Seracino (2004)].

Finally with ΔV_c known, the concrete shear capacity is shown in column 15 and 16 from strain gauges reading and IC resistance equation. Table 7.7.1 shows much detail calculation in predicting V_c. Simplified analysis is shown in Table 7.7.2 with V_s and V_{frp} is the average of 3,4 and 5,6. All the graph discussed later in the text are based from this table.

Table 7.7.2: Summary of beam analysis.

	Plate Angel	V (exp)	V_s (average)	V_{frp} (average)	$V_c + \Delta V_c$	ΔV_c (0.156P)	V_c	V_{total}
Control NS	0	114	0	0.0	114.0	0.0	114.0	114.0
Control S	0	219	113.4	0.0	105.6	0.0	105.6	219.0
NSM 3LP NS	0	119	0	0.0	119.0	13.6	105.4	105.4
NSM 3LP S	0	197	113.4	0.0	83.6	14.7	69.0	182.4
NSM 5IP NS	45	184	0	91.0	93.1	14.2	78.9	169.9
NSM 5IP S	45	304	113.4	63.8	126.8	10.0	116.8	294.0
NSM 4VP NS	90	124	0	87.3	36.8	0	36.8	124.0
NSM 4VP S	90	284	113.4	82.1	88.5	0	82.1	284.0

Figure 7.2.1 shows the concrete shear capacity for each plated beams from data in Table 7.7.2. Concrete shear capacity with steel stirrups show that only for the longitudinal plated beam fails below the experiment V_c (Control NS) assuming this is one of the scatter. Meanwhile for non stirrups beam, all three plated beams fail below the experiment concrete shear capacity. It is clearly showing that the concrete shear capacity reduce dramatically for beam without any steel stirrups. However this is not a concern to this research due to all the beams used in the construction are with steel stirrups.

Figure 7.7.2 shows the contribution of FRP towards the shear capacity. FRP plates increase dramatically the shear resistance of beams without any steel stirrups compared to the stirrups beams due to the FRP plates trying to close the crack opening. Figure 7.7.3 shows the contribution of steel reinforcement is the same for all three plated beams.

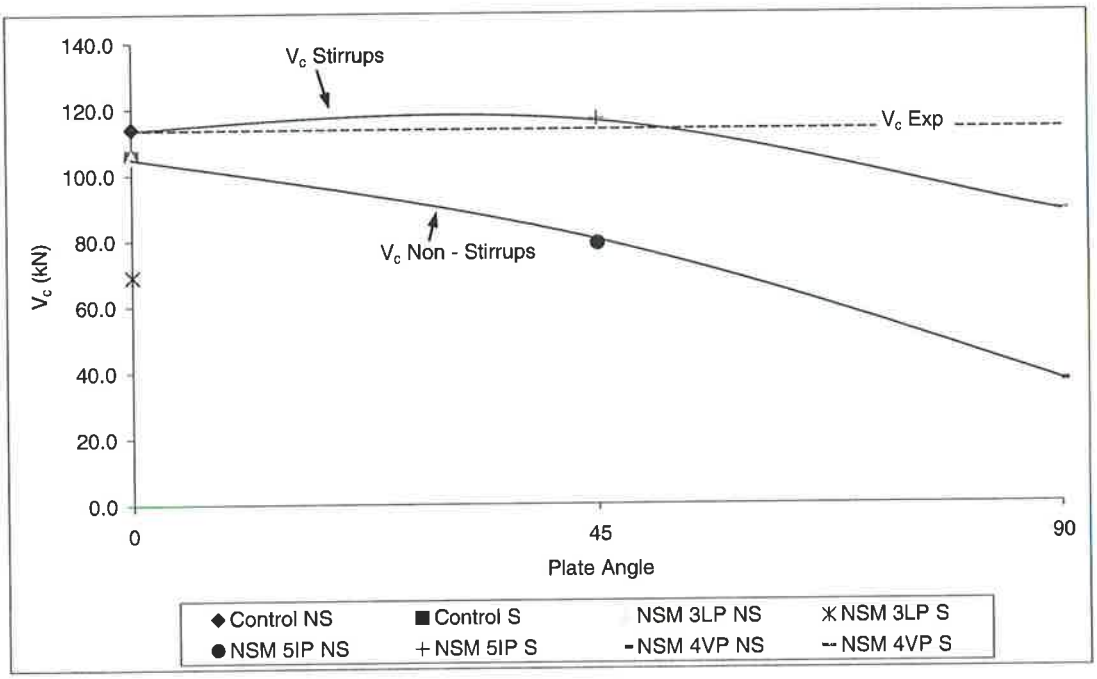

Figure 7.7.1: Reduction of concrete shear capacity.

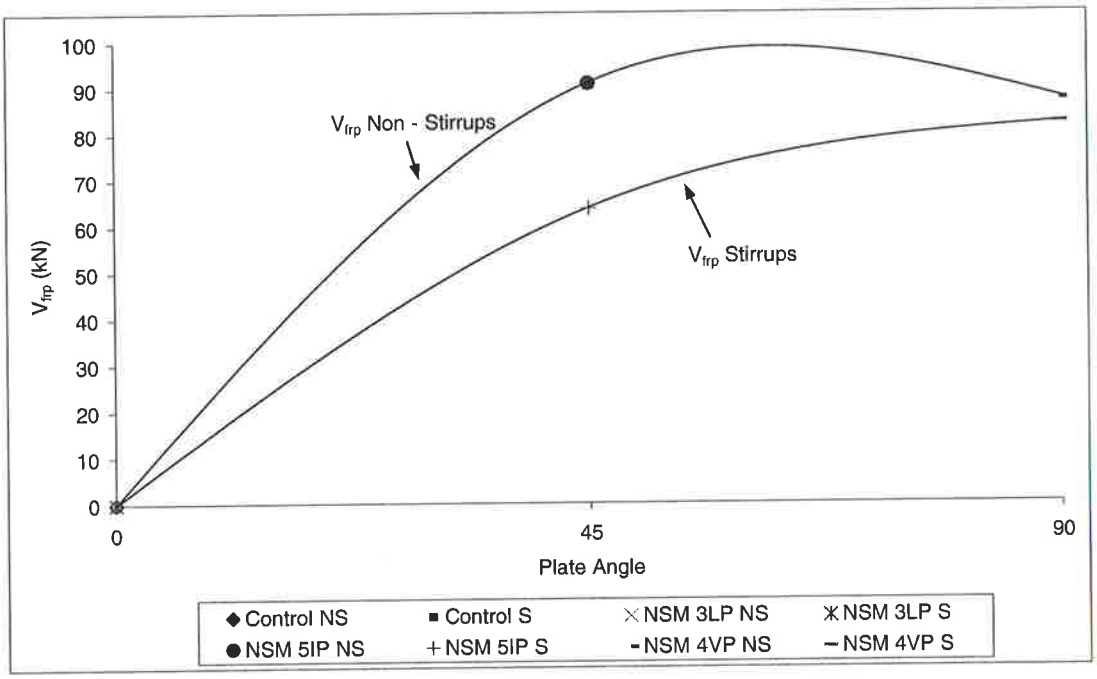

Figure 7.7.2: Contribution of FRP plates towards the shear capacity.

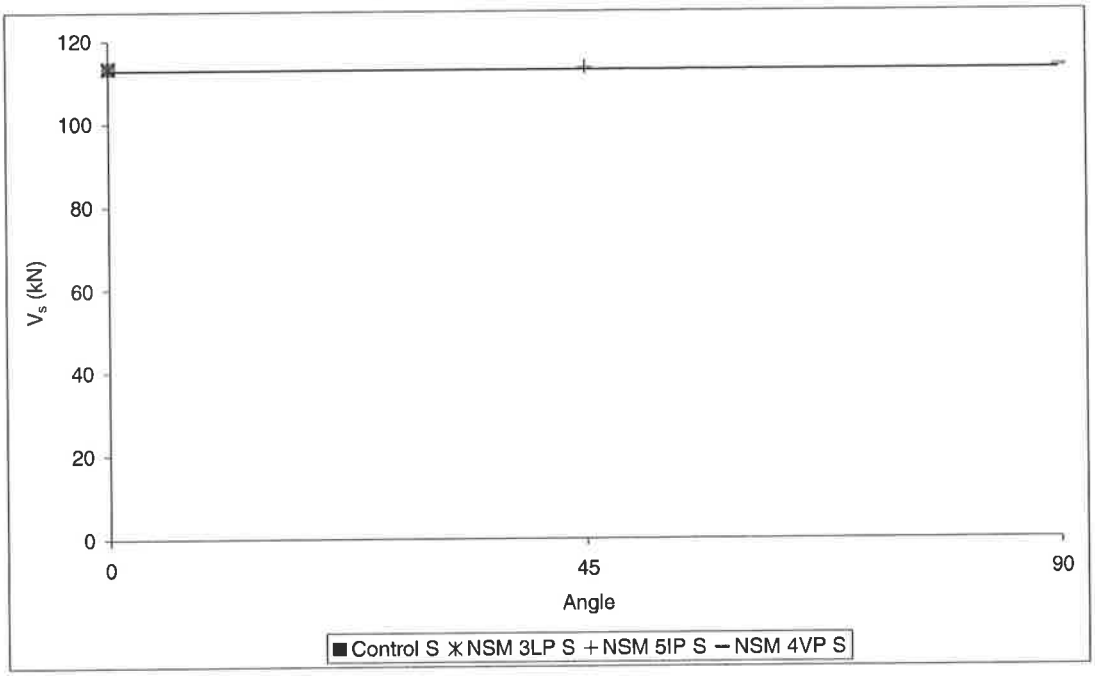

Figure 7.7.3: Contribution of steel stirrups towards the shear capacity.

Figure 7.7.4 shows the contribution of each component towards the total shear load. With V_s as the baseline, vertical plated beam contribute the highest for FRP plate. Longitudinal plated beam does increase the ΔV_c. Meanwhile V_c contributes the most with incline plated beam.

Figure 7.7.5 shows the contribution of each component towards the total shear load. Again with V_s is the baseline, inclined plated beam contribute the highest for FRP plate. Again longitudinal plated beam does increase the ΔV_c. Meanwhile V_c contributes the most with horizontal plated beam.

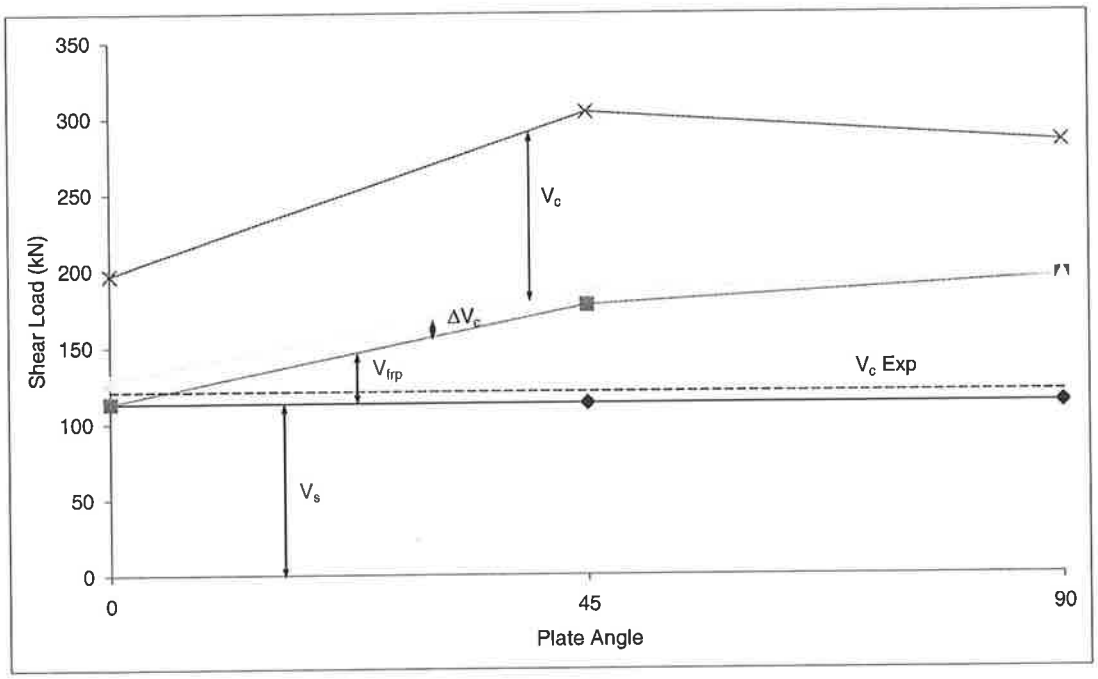

Figure 7.7.4: Contribution of each component towards total shear load test with stirrups.

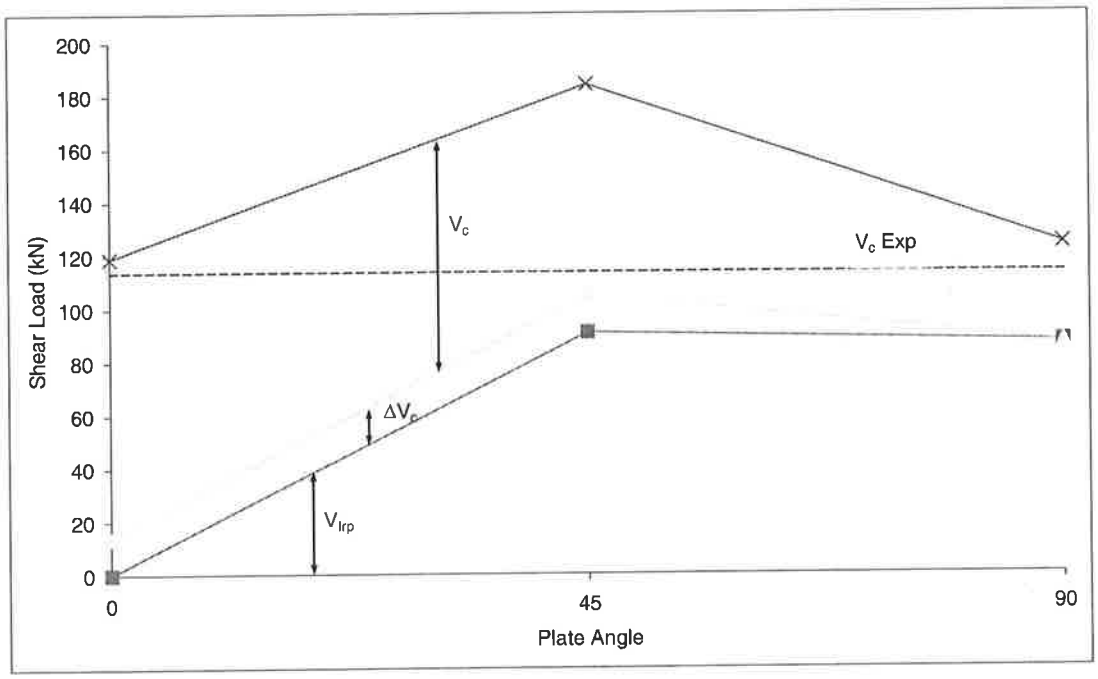

Figure 7.7.5: Contribution of each component towards total shear load test without stirrups.

Finally, Figure 7.7.6 and Figure 7.7.7 show the increase of ΔV_c for plated beams with and without steel stirrups. Longitudinal plated beam increases ΔV_c the most compared to the three methods of plating.

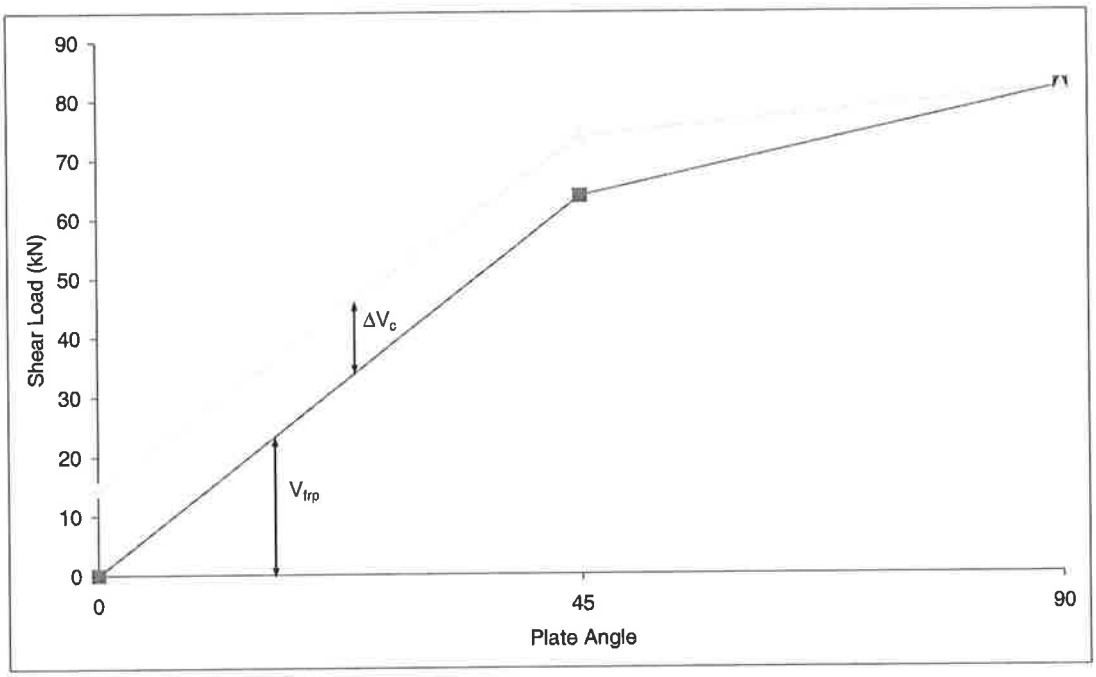

Figure 7.7.6: Increase of concrete shear capacity beam with stirrups.

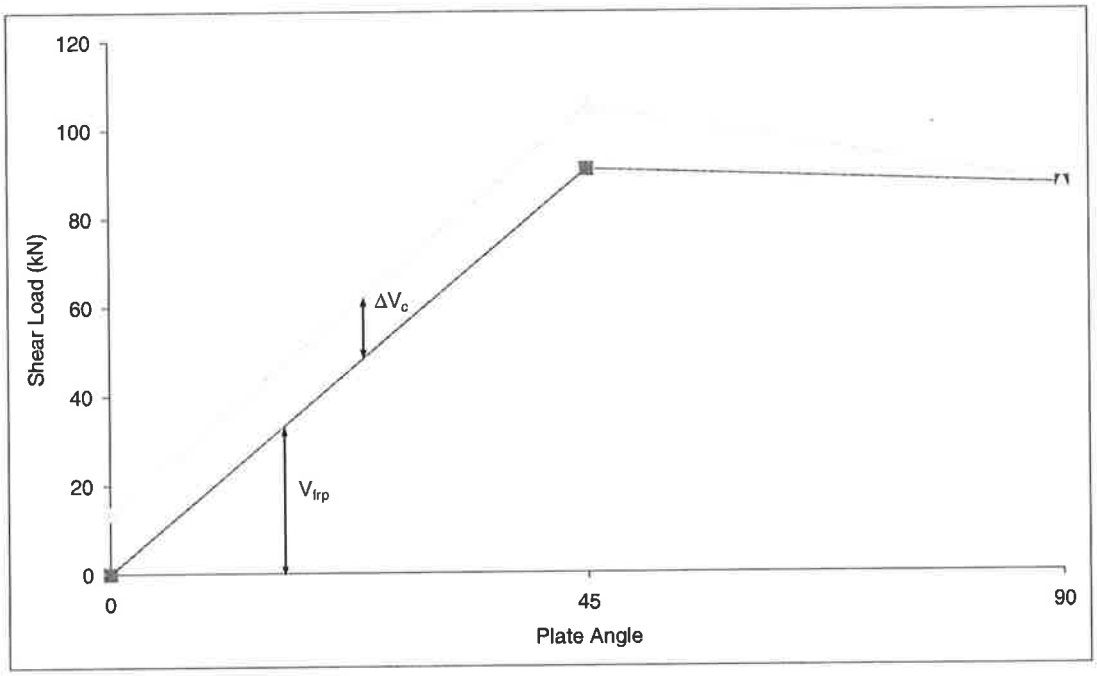

Figure 7.7.7: Increase of concrete shear capacity beam without stirrups.

7.8 Test Results Summaries

This section summarises all the beams tests to identify the increase of shear capacity using NSM CFRP plates. In Figure 7.8.1, without internal steel stirrups; the increase of shear capacity using longitudinal plating compare to the control beam is the lowest. The highest increment of shear capacity is achieved using the inclined plates.

Meanwhile, the lowest increase of shear capacity with internal steel stirrups is also given by longitudinal plated beam (Figure 7.8.1) which was highlighted earlier fails below test Control S. The highest increment of shear capacity with internal stirrups is given again by the inclined plates. Comparison between the control beams also shows with existence of internal steel stirrups, the shear capacity of the control beam increases (Figure 7.8.1).

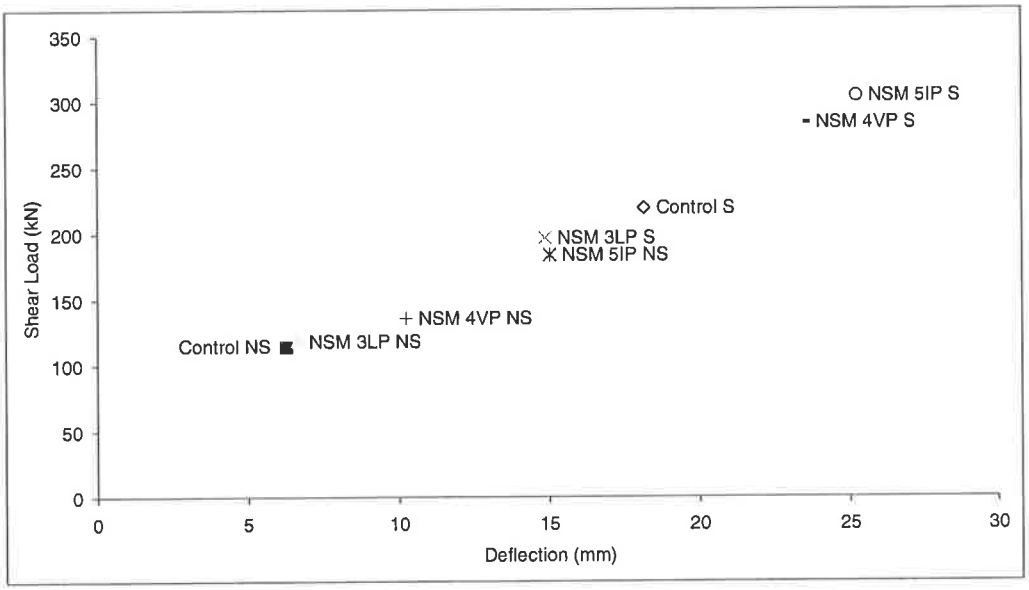

Figure 7.8.1: Summaries of all the beam test results.

7.9 Conclusion

The conclusions that can be made from all these beam tests is that for shear strengthening using NSM plates, the most efficient method is to use inclined plates and the most ineffective method is by longitudinal plating. Another conclusion that can be made from these tests is that in a plated beam, each element (concrete, internal steel stirrups and CFRP plates) contributes towards increasing the shear capacity as described in section 7.7.

7.10 Notation

b_p	Plate width
CDC	Critical Diagonal Crack
CFRP	Carbon Fiber Reinforced Polymer
d_p	Plate depth
EB	Externally Bonded
E_c	Concrete Young's Modulus
E_g	Adhesive Young's Modulus
E_p	Plate Young's Modulus
E_s	Steel Young's Modulus
f_c	Concrete compressive strength
f_u	Steel Ultimate Strength
f_y	Steel Yield Strength
IP	Incline Plating
LP	Longitudinal Plating
NS	Non Stirrups
NSM	Near Surface Mounted
P	Applied Load
S	Stirrups
SG	Strain Gauge
SSG	Stirrups Strain Gauge
V	Shear Load
VP	Vertical Plating

7.11 Reference

1. Australian Standard : Concrete Structures (AS3600-2001) (2001). Australia: 176.

2. Mohamed Ali, M. S. (2000). Peeling of Plates Adhesively Bonded to Reinforced Concrete Beams. Department of Civil and Environmental Engineering. Adelaide, University of Adelaide: 593.

3. Oehlers, D. J. and Seracino, R. (2004). "Design of FRP and Steel Plated RC Structures." 222.

Chapter

8.1 Introduction

The major findings contained within this thesis are explained in this chapter. In this study, the aspects relating to debonding of NSM FRP plates and to the increase in the shear capacity of RC beams are critically investigated.

8.2 Shear Capacity of Transversely Plated Beams

A mathematical model for the shear capacity of beams with transverse plates was developed in the form shown in Eq. 8.2.1 where the k factors were derived empirically and quantify the interaction between the different components of the shear capacity.

$$V_n = k_c V_c + (\Delta V_c + k_{frp} V_{frp}) + k_s V_s \qquad (8.2.1)$$

where

V_c is the concrete component of the shear capacity calculated using codes

k_c is the concrete shear capacity factor that allows for failure before the full capacity of V_c is achieved

ΔV_c is the increase of V_c due to the longitudinal component of the plate

V_{frp} is the transverse component of the contribution of FRP plating to the shear capacity

k_{frp} is the FRP plating shear capacity factor that allows for shear failure prior to the full theoretical capacity of V_{frp} being achieved

V_s is the contribution of internal steel stirrups to shear capacity calculated using the codes

k_s is the internal steel reinforcement shear capacity factor that allows for shear failure prior to all the stirrups being fully yielded

8.3 Generic IC debonding resistance

Sixteen pull tests were done with different materials and dimensions and with various aspect ratios to investigate the maximum failure load, shear stress, slip, strain, material stiffness and crack patterns.

The following generic equation for the Intermediate Crack (IC) debonding resistance was developed. It is the first of it kind, combining EB plates and NSM plates in one equation.

The model is only a function of the geometric and material properties and is applicable to any type of plate material. It is derived using an idealized linear softening bond-slip model and is a function of: the aspect ratio d_f/b_f of the interface debonding crack, which is a measure of the confinement effect of the cover concrete; the concrete compressive strength; and the axial rigidity of the plate alone. The generic equation is shown in Eq. 8.3.1 below.

$$P_{IC} = \eta 0.85 \frac{d_f}{b_f}^{0.25} f_c^{0.33} \sqrt{L_{per}(EA)_p} < \begin{cases} f_{rupt} A_p & \textit{for FRP plates} \\ f_y A_p & \textit{for metallic plates} \end{cases} \quad (8.3.1)$$

where units of N and mm are used, f_{rupt} is the rupture stress of an FRP plate, and f_y is the yield stress of a metallic plate and

$$\eta = \begin{cases} 1.0 & \textit{mean} \\ 0.85 & \textit{characteristic} \end{cases} \quad (8.3.2)$$

Finally, the generic equation was validated by comparison with existing push-pull data and a well-known existing model of Chen and Teng's (2002). An empirical model for the fundamental bond-slip relationship, suitable for use in numerical simulations, was also developed

8.4 Pull tests – Understanding plate and cover interaction

A total of 22 pull tests were done in this series of pull tests. The conclusions that can be made from all of these tests is that for the NSM plating method, the minimum gap between plates was found to be 53 mm and that for any gap distance EB plates were found to fail individually. Meanwhile for the interaction with cover; for 20 mm x 1.4 mm NSM plates the minimum cover was 62 mm and for the 40 mm x 2.4 mm NSM plate the minimum cover was 144 mm. As a rule of thumb, the minimum cover distance can be simplified as $3d_p$.

8.5 Plate interaction

The Intermediate crack debonding resistance for groups of NSM plates is shown by Eq. 8.5.1 with mean and 95% characteristic value of k shown in Eq. 8.6.2 and 8.6.3

$$P_{IC} = \sqrt{\tau_f \delta_f L_{per}} \sqrt{n(EA)_p + (k(EA)_c)} \quad (8.5.1)$$

$$k = -0.0303(M_u / M_{cr}) + 0.451 \quad (8.5.2)$$

$$k = -0.0267(M_u / M_{cr}) + 0.451 \quad (8.5.3)$$

8.6 Transverse NSM Plated beam tests

The conclusions that can be made from all the beam tests is that for shear strengthening using NSM plates, the most efficient method is to use inclined plates and the most ineffective method is by using longitudinal plating.

8.7 Summary

The major contribution of this thesis is towards the development of a generic equation for the Intermediate Crack (IC) debonding resistance of a plate bonded to a concrete surface. This generic equation was also used to calculate the increase of the shear capacity provided by FRP plates and to quantify the interaction between the transverse plates, internal steel stirrups and the concrete component.

Appendix A

APPENDIX A

		Author	Berset	Uji	Al-Sulaimani	Chajes	Sato	Miyauchi	Taerwe	Sato	Umezu	Funakawa	Araki	Ono	Taljsten	Chaallal	Mitsui	Triantafillou	Khalifa	Khalifa	Kachlakev	Deniaud	Li	Khalifa	Pellegrino	Chaallal
		Year	1992	1992	1994	1995	1996	1997	1997	1997	1997	1997	1997	1997	1997	1998	1998	1998	1999	2000	2000	2001	2001	2002	2002	2002
		Number of valid tests	2	4	2	4	4	3	4	2	15	3	8	5	3	4	6	9	2	4	1	9	4	4	9	20
Properties And Parameters	Geometry	Rectangular section	■	■	■		■	■	■		■	■	■	■	■	■	■	■	■		■		■	■	■	
		T – section				■				■										■		■				■
		Beam with L < 2m	■	■	■	■		■		■			■	■		■		■					■			
		Beam with 2m < L < 4m					■				■						■		■	■		■		■	■	
		Beam with L > 4m							■			■			■						■					■
	Type of beam	Normal beam (a/d > 2.5)	■	■	■	■	■	■	■	■	■	■		■	■	■		■	■	■	■	■		■	■	
		Deep beams						■					■	■			■						■			■
		Scale effect																				■				
		Precracked			■										■		■									
	Concrete and Steel	Concrete strength																				■				
		Longitudinal reinforcement									■															
		Transverse reinforcement									■											■			■	■
	Type of FRP	Carbon		■		■	■	■	■	■	■	■	■	■	■	■	■	■	■	■		■	■	■	■	■
		Aramid			■						■		■													
		Glass	■		■	■															■	■				
	Strengthening Scheme	Side plates	■	■	■		■								■	■		■			■		■		■	
		U - wrap				■	■		■	■									■	■		■		■		■
		Wrapped		■				■	■		■	■	■	■			■									
		Continuous	■	■	■	■	■			■	■	■	■	■	■		■		■	■	■	■	■	■	■	■
		Strips			■		■	■	■		■		■		■	■		■		■		■		■		
		90º strips		■	■	■	■	■	■	■	■	■	■	■		■	■		■	■	■	■	■	■	■	■
		Inclines strips	■	■		■									■	■		■				■				

L = Beam length , a = shear span and d = beam effective depth

Appendix B

APPENDIX B
ANALYSIS

TAYLOR, H.P.J. (1972)

Beam Designation	exp	Eurocode2			AS 3600-2001			CDC analysis		a/d	a	d	fc'	Area of steel (mm^2)	
		code	Vexp/Vcode	Vcdc/Vcode	code	Vexp/Vcode	Vcdc/Vcode	cdc	Vexp/Vcdc					Tension	Compression
B1	104.25	91.88	1.13	0.90	83.03	1.26	1.00	83.08	1.25	3.00	1400	462.0	27.2	1256.64	0
B2	87.30	89.09	0.98	0.89	80.51	1.08	0.98	78.92	1.11	3.00	1400	462.0	24.8	1256.64	0
B3	85.30	96.99	0.88	0.94	87.65	0.97	1.04	91.06	0.94	3.00	1400	462.0	32.0	1256.64	0
C1	22.50	26.04	0.86	0.96	24.29	0.93	1.02	24.87	0.90	3.00	700	227.5	25.6	314.16	0
C2	24.00	26.04	0.92	0.96	24.29	0.99	1.02	24.87	0.97	3.00	700	227.5	25.6	314.16	0
C3	27.50	26.68	1.03	0.97	24.88	1.11	1.04	25.92	1.06	3.00	700	227.5	27.5	314.16	0
C4	22.50	24.30	0.93	0.91	22.66	0.99	0.98	22.11	1.02	3.00	700	227.5	20.8	314.16	0
C5	27.00	24.91	1.08	0.93	23.23	1.16	0.99	23.07	1.17	3.00	700	227.5	22.4	314.16	0
C6	27.50	27.08	1.02	0.98	25.26	1.09	1.05	26.56	1.04	3.00	700	227.5	28.8	314.16	0
D1	11.60	10.01	1.16	1.20	9.70	1.20	1.24	12.02	0.97	3.00	420	128.5	32.0	113.10	0
D2	12.10	10.01	1.21	1.20	9.70	1.25	1.24	12.02	1.01	3.00	420	128.5	32.0	113.10	0
D3	10.60	10.01	1.06	1.20	9.70	1.09	1.24	12.02	0.88	3.00	420	128.5	32.0	113.10	0
D4	11.40	10.01	1.14	1.20	9.70	1.18	1.24	12.02	0.95	3.00	420	128.5	32.0	113.10	0

KIM, J.K. and PARK, Y.-D (1994)

Beam Designation	exp	Eurocode2			AS 3600-2001			CDC analysis		a/d	a	d	fc'	Area of steel (mm^2)	
		code	Vexp/Vcode	Vzhang/Vcode	code	Vexp/Vcode	Vzhang/Vcode	cdc	Vexp/Vzhang					Tension	Compression
A4.5-1	74.00	71.50	1.03	0.94	67.29	1.10	1.00	67.20	1.10	4.50	1215	270.0	53.7	860.00	0
A4.5-2	70.90	71.50	0.99	0.94	67.29	1.05	1.00	67.20	1.06	4.50	1215	270.0	53.7	860.00	0
A6.0-1	65.80	71.50	0.92	0.85	67.29	0.98	0.90	60.62	1.09	6.00	1620	270.0	53.7	860.00	0
A6,0-2	67.80	71.50	0.95	0.85	67.29	1.01	0.90	60.62	1.12	6.00	1620	270.0	53.7	860.00	0
CTL-1	78.50	71.50	1.10	1.08	67.29	1.17	1.15	77.19	1.02	3.00	810	270.0	53.7	860.00	0
CTL-2	79.60	71.50	1.11	1.08	67.29	1.18	1.15	77.19	1.03	3.00	810	270.0	53.7	860.00	0
P1.0-1	64.30	58.56	1.10	1.20	55.12	1.17	1.27	70.12	0.92	3.00	816	272.0	53.7	468.00	0
P1.0-2	62.20	58.56	1.06	1.20	55.12	1.13	1.27	70.12	0.89	3.00	816	272.0	53.7	468.00	0
P3.4-1	78.07	72.45	1.08	1.22	80.93	0.96	1.10	88.74	0.88	3.00	801	267.0	53.7	1520.00	0
P3.4-2	78.52	72.45	1.08	1.22	80.93	0.97	1.10	88.74	0.88	3.00	801	267.0	53.7	1520.00	0
D142-1	49.13	40.41	1.22	1.32	38.79	1.27	1.37	53.19	0.92	3.00	426	142.0	53.7	452.00	0
D142-2	47.10	40.41	1.17	1.32	38.79	1.21	1.37	53.19	0.89	3.00	426	142.0	53.7	452.00	0

APPENDIX B
ANALYSIS

B.TALJSTEN and L.ELFGREN (2000)

Beam Designation	exp	Eurocode2			AS 3600-2001			CDC analysis		a/d	a	d	fc'	Area of steel (mm^2)	
		code	Vexp/Vcode	Vcdc/Vcode	code	Vexp/Vcode	Vcdc/Vcode	cdc	Vexp/Vcdc					Tension	Compression
R1	113.00	113.73	0.99	1.03	104.16	1.08	1.12	116.87	0.97	3.63	1600	441.0	53.8	1608.50	402
R2	120.50	112.95	1.07	1.19	103.44	1.16	1.24	128.16	0.94	2.72	1200	441.0	52.7	1608.50	402

MOHAMED ALI, M.S. (2000)

Beam Designation	exp	Eurocode2			AS 3600-2001			CDC analysis		a/d	a	d	fc'	Area of steel (mm^2)	
		code	Vexp/Vcode	Vcdc/Vcode	code	Vexp/Vcode	Vcdc/Vcode	cdc	Vexp/Vcdc					Tension	Compression
SPREF	85.60	87.59	0.98	1.04	82.30	1.04	1.11	91.28	0.94	3.58	1200	335.0	29.1	942.48	157

AHMED KHALIFA, GUSTAVO TUMIALAN, et al. (1999)

Beam Designation	exp	Eurocode2			AS 3600-2001			CDC analysis		a/d	a	d	fc'	Area of steel (mm^2)	
		code	Vexp/Vcode	Vcdc/Vcode	code	Vexp/Vcode	Vcdc/Vcode	cdc	Vexp/Vcdc					Tension	Compression
CF	76.00	63.52	1.20	1.20	59.81	1.27	1.27	76.12	1.00	3.39	940	277.0	50.0	804.25	804

AHMED KHALIFA and A. NANNI (2002)

Beam Designation	exp	Eurocode2			AS 3600-2001			CDC analysis		a/d	a	d	fc'	Area of steel (mm^2)	
		code	Vexp/Vcode	Vcdc/Vcode	code	Vexp/Vcode	Vcdc/Vcode	cdc	Vexp/Vcdc					Tension	Compression
SO	45.00	49.12	0.92	1.54	59.21	0.76	1.27	75.46	0.60	3.00	760	253.3	27.5	1608.50	1609

KULKARNI, SHRIKRISHNA M. SHAH, et al. (1998)

Beam Designation	exp	Eurocode2			AS 3600-2001			CDC analysis		a/d	a	d	fc'	Area of steel (mm^2)	
		code	Vexp/Vcode	Vcdc/Vcode	code	Vexp/Vcode	Vcdc/Vcode	cdc	Vexp/Vcdc					Tension	Compression
B4JL20-S	19.52	22.29	0.88	1.04	21.25	0.92	1.09	23.10	0.85	5.00	760	152.0	41.9	235.62	0
B3SE03-S	23.02	22.82	1.01	1.09	21.76	1.06	1.14	24.90	0.92	4.50	684	152.0	45.0	235.62	0
B3NO15-S	22.66	22.48	1.01	1.13	21.43	1.06	1.18	25.37	0.89	4.00	608	152.0	43.0	235.62	0
B3NO30-S	24.24	22.48	1.08	1.16	21.43	1.13	1.22	26.06	0.93	3.50	532	152.0	43.0	235.62	0
B3NO30-H	27.36	22.82	1.20	1.19	21.76	1.26	1.25	27.22	1.01	3.50	532	152.0	45.0	235.62	0

APPENDIX B
ANALYSIS

SALANDRA, M.A. and S.H. AHMAD (1989)

Beam Designation	exp	Eurocode2			AS 3600-2001			CDC analysis		a/d	a	d	fc'	Area of steel (mm^2)	
		code	Vexp/Vcode	Vcdc/Vcode	code	Vexp/Vcode	Vcdc/Vcode	cdc	Vexp/Vcdc					Tension	Compression
LR-2.59-NS	26.70	26.88	0.99	1.36	25.27	1.06	1.45	36.64	0.73	2.59	444	171.5	53.7	253.35	0
LR-3.63`-NS	21.79	26.61	1.07	1.19	25.02	0.87	1.27	31.72	0.69	3.63	623	171.5	52.1	253.35	0

XIE, S.H. AHMAD, et al. (1994)

Beam Designation	exp	Eurocode2			AS 3600-2001			CDC analysis		a/d	a	d	fc'	Area of steel (mm^2)	
		code	Vexp/Vcode	Vcdc/Vcode	code	Vexp/Vcode	Vcdc/Vcode	cdc	Vexp/Vcdc					Tension	Compression
NNN-3	36.68	40.93	0.90	1.08	39.77	0.92	1.12	44.37	0.83	3.00	648	216.0	37.7	628.32	0

ADEBAR, PERRY COLLINS, et al. (1996)

Beam Designation	exp	Eurocode2			AS 3600-2001			CDC analysis		a/d	a	d	fc'	Area of steel (mm^2)	
		code	Vexp/Vcode	Vcdc/Vcode	code	Vexp/Vcode	Vcdc/Vcode	cdc	Vexp/Vcdc					Tension	Compression
ST1	128.00	157.07	0.81	1.21	171.91	0.74	1.10	189.68	0.67	2.88	801	278.0	52.5	3141.60	0
ST2	119.00	157.07	0.76	1.21	171.91	0.69	1.10	189.68	0.63	2.88	801	278.0	52.5	3141.60	0
ST3	108.00	123.90	0.87	1.27	145.74	0.74	1.08	156.89	0.69	2.88	801	278.0	49.3	3141.60	0
ST8	81.00	121.25	0.67	1.25	142.62	0.57	1.06	151.47	0.53	2.88	801	278.0	46.2	3141.60	0
ST16	74.30	87.11	0.85	1.41	118.17	0.63	1.04	122.65	0.61	4.49	799	178.0	51.5	3141.60	0
ST23	90.00	102.88	0.87	1.37	96.89	0.93	1.46	141.31	0.64	2.88	801	278.0	58.9	3141.60	0

M.S. ISLAM, H.J. PAM, et al. (1998)

Beam Designation	exp	Eurocode2			AS 3600-2001			CDC analysis		a/d	a	d	fc'	Area of steel (mm^2)	
		code	Vexp/Vcode	Vcdc/Vcode	code	Vexp/Vcode	Vcdc/Vcode	cdc	Vexp/Vcdc					Tension	Compression
M25-SO	47.50	41.68	1.14	1.09	48.76	0.97	0.93	45.43	1.05	3.86	799	207.0	26.6	628.32	628
M40-SO	47.50	45.41	0.99	1.21	61.65	0.77	0.94	61.15	0.82	3.86	799	207.0	34.4	628.32	628
M60-SO	45.50	51.71	0.73	1.04	60.50	0.75	1.08	65.10	0.70	3.86	799	207.0	50.8	628.32	628

APPENDIX B
ANALYSIS

BAZANT, ZDENEK P., et al. (1991)

Beam Designation	exp	Eurocode2			AS 3600-2001			CDC analysis		a/d	a	d	fc'	Area of steel (mm^2)	
		code	Vexp/Vcode	Vcdc/Vcode	code	Vexp/Vcode	Vcdc/Vcode	cdc	Vexp/Vcdc					Tension	Compression
I7	5.49	4.74	1.16	1.65	4.74	1.16	1.65	7.82	0.70	3.00	244	81.2	46.8	51.00	0
I8	5.58	4.74	1.18	1.65	4.74	1.18	1.65	7.82	0.71	3.00	244	81.2	46.8	51.00	0
I9	5.18	4.74	1.09	1.65	4.74	1.09	1.65	7.82	0.66	3.00	244	81.2	46.8	51.00	0
I10	9.07	9.49	0.96	1.28	8.98	1.01	1.35	12.13	0.75	3.00	488	162.5	46.8	100.00	0
I11	9.78	9.49	1.03	1.28	8.98	1.09	1.35	12.13	0.81	3.00	488	162.5	46.8	100.00	0
I12	10.14	9.49	1.07	1.30	8.98	1.13	1.37	12.33	0.82	3.00	488	162.5	46.8	100.00	0
II7	5.40	4.77	1.13	1.61	4.76	1.13	1.61	7.69	0.70	3.00	248	82.5	46.1	51.00	0
II8	5.02	4.77	1.05	1.61	4.76	1.05	1.61	7.69	0.65	3.00	248	82.5	46.1	51.00	0
II9	4.44	4.77	0.93	1.61	4.76	0.93	1.61	7.69	0.58	3.00	248	82.5	46.1	51.00	0
II10	7.29	9.48	0.77	1.29	8.95	0.81	1.36	12.20	0.60	3.00	495	165.1	46.1	100.00	0
II11	8.38	9.48	0.88	1.29	8.95	0.94	1.36	12.20	0.69	3.00	495	165.1	46.1	100.00	0
II12	8.20	9.48	0.87	1.29	8.95	0.92	1.36	12.20	0.67	3.00	495	165.1	46.1	100.00	0

KANI, G.N.J. (1967)

Beam Designation	exp	Eurocode2			AS 3600-2001			CDC analysis		a/d	a	d	fc'	Area of steel (mm^2)	
		code	Vexp/Vcode	Vcdc/Vcode	code	Vexp/Vcode	Vcdc/Vcode	cdc	Vexp/Vcdc					Tension	Compression
40	32.00	28.61	1.12	0.89	29.98	1.07	0.85	25.50	1.25	5.35	747	139.7	26.4	548.39	0
41	51.40	29.29	1.75	1.19	30.76	1.67	1.13	34.78	1.48	2.41	340	141.2	27.2	561.29	0
43	29.10	28.60	1.02	0.90	30.56	0.95	0.84	25.79	1.13	5.93	813	137.2	28.0	567.74	0
47	28.20	26.39	1.07	0.98	28.67	0.98	0.90	25.74	1.10	5.13	678	132.1	24.75	567.74	0
48	27.10	26.64	1.02	0.97	28.83	0.94	0.89	25.74	1.05	5.09	678	133.4	24.8	567.74	0
52	28.90	27.91	1.04	1.00	29.65	0.97	0.94	27.84	1.04	3.93	544	138.4	24.82	567.74	0
55	32.60	26.88	1.21	1.29	29.03	1.12	1.19	34.61	0.94	3.02	406	134.6	25.1	567.74	0
56	28.00	28.20	0.99	1.23	30.17	1.05	0.87	34.61	0.81	3.46	476	137.4	27.2	561.29	0
57	31.60	28.69	1.10	0.91	30.17	1.05	0.87	26.16	1.21	5.39	747	138.7	26.4	554.84	0
58	28.90	28.72	1.01	1.07	30.23	0.96	1.01	30.67	0.94	3.44	476	138.4	27.24	551.29	0
59	50.00	29.13	1.72	1.16	30.72	1.63	1.10	33.90	1.48	2.67	373	139.7	26.6	567.74	0
60	39.30	29.16	1.35	1.14	30.77	1.28	1.08	33.13	1.19	2.93	407	138.7	26.8	567.74	0

APPENDIX B
ANALYSIS

ELZANATY, A.H., A.H.NILSON, et al. (1986)

Beam Designation	exp	Eurocode2			AS 3600-2001			CDC analysis		a/d	a	d	fc'	Area of steel (mm^2)	
		code	Vexp/Vcode	Vcdc/Vcode	code	Vexp/Vcode	Vcdc/Vcode	cdc	Vexp/Vcdc					Tension	Compression
F11	44.81	47.31	0.95	0.85	44.54	1.01	0.90	40.20	1.11	4.00	1092	273.0	20.7	582.47	0
F12	54.48	56.10	0.97	0.82	56.88	0.96	0.81	46.14	1.18	4.00	1092	273.0	20.7	1213.48	0
F8	45.97	55.46	0.83	1.02	52.20	0.88	1.09	56.69	0.81	4.00	1092	273.0	40.0	485.39	0
F13	46.35	58.93	0.79	0.99	55.48	0.84	1.05	58.39	0.79	4.00	1092	273.0	40.0	582.47	0
F14	64.93	69.87	0.93	0.96	70.85	0.92	0.95	67.06	0.97	4.00	1092	273.0	40.0	1213.48	0

KANI, M.W., M.W. HUGGINS, et al. (1979)

Beam Designation	exp	Eurocode2			AS 3600-2001			CDC analysis		a/d	a	d	fc'	Area of steel (mm^2)	
		code	Vexp/Vcode	Vcdc/Vcode	code	Vexp/Vcode	Vcdc/Vcode	cdc	Vexp/Vcdc					Tension	Compression
1	28.70	28.30	1.01	0.91	30.31	0.95	0.85	25.72	1.12	5.93	812	137.0	28.0	565.13	0
2	28.60	27.25	1.05	1.02	29.12	0.98	0.95	27.81	1.03	3.93	538	137.0	25.0	561.02	0
3	32.70	27.25	1.20	1.12	29.36	1.11	1.04	30.55	1.07	3.02	414	137.0	25.0	575.40	0
4	65.10	53.32	1.22	1.00	55.73	1.17	0.96	53.38	1.22	3.00	810	270.0	27.0	1154.09	0
5	55.40	51.61	1.07	0.91	54.59	1.01	0.86	47.04	1.18	4.00	1080	270.0	27.0	1157.87	0
6	53.60	54.87	0.98	0.92	56.79	0.94	0.89	50.44	1.06	4.00	1080	270.0	30.0	1113.21	0
7	93.10	91.45	1.02	0.84	88.28	1.05	0.87	76.67	1.21	4.00	2172	543.0	26.0	2346.41	0
8	107.80	92.61	1.16	0.92	89.40	1.21	0.96	85.48	1.26	3.12	1694	543.0	27.0	2346.41	0
9	84.60	91.45	0.93	0.69	87.75	0.96	0.72	63.22	1.34	6.84	3714	543.0	26.0	2304.06	0

TUREYEN, A. and R.FROSH (2002)

Beam Designation	exp	Eurocode2			AS 3600-2001			CDC analysis		a/d	a	d	fc'	Area of steel (mm^2)	
		code	Vexp/Vcode	Vcdc/Vcode	code	Vexp/Vcode	Vcdc/Vcode	cdc	Vexp/Vcdc					Tension	Compression
V-S-1	179.30	172.92	1.04	1.02	161.73	1.11	1.09	176.01	1.02	3.40	1225	360.4	34.5	1782.86	0
V-S-2	203.70	212.19	0.96	0.93	203.77	1.00	0.97	197.67	1.03	3.40	1225	360.4	34.5	3565.72	0

APPENDIX B
ANALYSIS

COLLINS, M.P. and D.KUCHMA (1999)

Beam Designation	exp	Eurocode2			AS 3600-2001			CDC analysis		a/d	a	d	fc'	Area of steel (mm^2)	
		code	Vexp/Vcode	Vcdc/Vcode	code	Vexp/Vcode	Vcdc/Vcode	cdc	Vexp/Vcdc					Tension	Compression
BN50	131.70	125.80	1.05	1.11	114.28	1.15	1.22	139.83	0.94	3.00	1350	450.0	37.0	1093.50	0
BN25	72.90	75.38	0.97	1.16	70.24	1.04	1.24	87.08	0.84	3.00	675	225.0	37.0	594.00	0
BN12	40.00	38.22	1.05	1.43	37.49	1.07	1.46	54.58	0.73	3.07	338	110.0	37.0	297.00	0
SE50A-45	68.60	87.93	0.78	1.16	79.57	0.86	1.28	101.89	0.67	2.72	1248	459.0	53.0	799.00	0
SE50A-45-R	80.50	87.93	0.92	1.16	79.57	1.01	1.28	101.89	0.79	2.72	1248	459.0	53.0	799.00	0

MPHONDE, A.G. and G.C. FRANTZ (1984)

Beam Designation	exp	Eurocode2			AS 3600-2001			CDC analysis		a/d	a	d	fc'	Area of steel (mm^2)	
		code	Vexp/Vcode	Vcdc/Vcode	code	Vexp/Vcode	Vcdc/Vcode	cdc	Vexp/Vcdc					Tension	Compression
A0-3-3b	64.60	52.84	1.22	0.94	59.19	1.09	0.84	49.91	1.29	3.60	1073	298.0	22.6	1521.94	0
A0-3-3c	66.80	57.74	1.16	0.91	57.17	1.17	0.92	52.69	1.27	3.60	1073	298.0	29.5	1050.86	0
A0-7-3a	82.16	64.39	1.28	1.07	72.12	1.14	0.96	69.21	1.19	3.60	1073	298.0	40.9	1521.94	0
A0-7-3b	82.79	66.57	1.24	1.10	74.57	1.11	0.98	73.36	1.13	3.60	1073	298.0	45.2	1521.94	0
A0-3-2	77.77	52.68	1.48	1.07	59.01	1.32	0.95	56.76	1.38	2.50	745	298.0	22.4	1521.94	0
A0-7-2	117.90	68.43	1.72	1.28	76.65	1.54	1.15	86.98	1.34	2.50	745	298.0	49.1	1521.94	0

AHMAD, S.H., A.R. KHALOO, et al. (1986)

Beam Designation	exp	Eurocode2			AS 3600-2001			CDC analysis		a/d	a	d	fc'	Area of steel (mm^2)	
		code	Vexp/Vcode	Vcdc/Vcode	code	Vexp/Vcode	Vcdc/Vcode	cdc	Vexp/Vcdc					Tension	Compression
A8	77.77	52.68	1.48	1.07	59.01	1.32	0.95	56.76	1.38	2.50	745	298.0	22.4	1521.94	0

AHMED KHALIFA and A. NANNI (2000)

Beam Designation	exp	Eurocode2			AS 3600-2001			CDC analysis		a/d	a	d	fc'	Area of steel (mm^2)	
		code	Vexp/Vcode	Vcdc/Vcode	code	Vexp/Vcode	Vcdc/Vcode	cdc	Vexp/Vcdc					Tension	Compression
BT1	90.00	74.47	1.21	0.95	75.05	1.20	0.94	70.42	1.28	3.00	1170	390.0	35.0	1231.50	265

Mean	**1.02**	**1.08**
Standard Deviation	**0.15**	**0.16**
Coefficient Of Variance	**14.70**	**14.66**

1.03	**1.07**
0.16	**0.17**
15.77	**16.28**

0.96
0.22
22.41

Appendix C

APPENDIX C
ANALYSIS

AHMED KHALIFA and A. NANNI (2000)

Specimen	Concrete strength f'_c (Mpa)	Web thickness b_w(mm)	Depth h (mm)	Effective depth d(mm)	Area of steel (mm^2)		FRP type	FRP thickness t_{frp} (mm)	FRP effective height $h_{frp,e}$ (mm)	Young's modulus E_{frp}(Mpa)	Tensile strength f_{frp}(Mpa)	Strengthening scheme	*Wfrp/Sfrp*	Crack angle θ (°)	V_{frp} Exp. (kN)	V_{frp} Cal. (kN)	$\frac{V_{frp}(Exp)}{V_{frp}(Cal)}$
					Tension	Compression											
BT2	35	150	405	390	1231.50	265.46	CFRP	0.165	224	228000.0	3790	SP90	0.71	45	65	60.13	1.08
BT3	35	150	405	390	1231.50	265.46	CFRP	0.165	224	228000.0	3790	SP90	0.71	45	67.5	52.93	1.28
BT5	35	150	405	390	1231.50	265.46	CFRP	0.165	224	228000.0	3790	SS90	0.40	45	31.5	36.70	0.86

AHMED KHALIFA, GUSTAVO TUMIALAN, et al. (1999)

Specimen	Concrete strength f'_c (Mpa)	Web thickness b_w(mm)	Depth h (mm)	Effective depth d(mm)	Area of steel (mm^2)		FRP type	FRP thickness t_{frp} (mm)	FRP effective height $h_{frp,e}$ (mm)	Young's modulus E_{frp}(Mpa)	Tensile strength f_{frp}(Mpa)	Strengthening scheme	*Wfrp/Sfrp*	Crack angle θ (°)	V_{frp} Exp. (kN)	V_{frp} Cal. (kN)	$\frac{V_{frp}(Exp)}{V_{frp}(Cal)}$
					Tension	Compression											
CO2	20.5	150	305	264	1231.50	265.46	CFRP	0.165	237.6	228000.0	3500	US90	0.40	35	40	44.00	0.91
CO3	35	150	405	390	1231.50	265.46	CFRP	0.165	224	228000.0	3790	SP90	0.71	45	67.5	63.50	1.06

S.Y. PARK, A.E. NAAMAN, et al. (2001)

Specimen	Concrete strength f'_c (Mpa)	Web thickness b_w(mm)	Depth h (mm)	Effective depth d(mm)	Area of steel (mm^2)		FRP type	FRP thickness t_{frp} (mm)	FRP effective height $h_{frp,e}$ (mm)	Young's modulus E_{frp}(Mpa)	Tensile strength f_{frp}(Mpa)	Strengthening scheme	$\frac{w_{frp}}{s_{frp}\sin\beta}$	Crack angle θ (°)	V_{frp} Exp. (kN)	V_{frp} Cal. (kN)	$\frac{V_{frp}(Exp)}{V_{frp}(Cal)}$
					Tension	Compression											
2	25.4	100	250	204	422.54	157.08	CFRP	0.3	250	38500.0	574	UP90	1.00	40	39.35	32.58	1.21

Mean	1.06
Standard Deviation	0.163
Coefficient Of Variance	15.32

Appendix D

APPENDIX D
ANALYSIS

DENIAUD, C and J.J. ROGER CHENG (2001)

Specimen	Concrete strength f'_c (Mpa)	Web thickness b_w(mm)	Depth h (mm)	Effective depth d(mm)	s/d	Area of steel (mm^2)			FRP type	FRP thickness t_{frp} (mm)	FRP effective height $h_{frp,e}$ (mm)	Young's modulus E_{frp}(Mpa)	Tensile strength f_{frp}(Mpa)	Strengthening scheme	*Wfrp/Sfrp*	Crack angle θ (°)
						Tension	Compression	Internal Stirrups								
T4S2-G90	29	150	400	367	0.54	1061.86	157.08	56.54	GFRP	1.8	217	17700.0	250	SP90	0.71	45
T6S4-C90	44	150	600	541	0.74	2123.72	157.08	56.54	CFRP	0.11	391	230000.0	3400	SS90	1.00	45
T6S4-G90	44	150	600	541	0.74	2123.72	157.08	56.54	GFRP	1.8	391	17700.0	250	SP90	0.71	45

PELLEGRINO, C and MODENA, C (2002)

Specimen	Concrete strength f'_c (Mpa)	Web thickness b_w(mm)	Depth h (mm)	Effective depth d(mm)	s/d	Area of steel (mm^2)			FRP type	FRP thickness t_{frp} (mm)	FRP effective height $h_{frp,e}$ (mm)	Young's modulus E_{frp}(Mpa)	Tensile strength f_{frp}(Mpa)	Strengthening scheme	*Wfrp/Sfrp*	Crack angle θ (°)
						Tension	Compression	Internal Stirrups								
TR30D10	31.4	150	300	250	0.80	N.A.	N.A.	100.53	CFRP	0.33	270.0	233600	3550	SP90	0.71	45
TR30D2	31.4	150	300	250	0.80	398.20	398.20	100.53	CFRP	0.495	270.0	233600	3550	SP90	0.71	45
TR30D20	31.4	150	300	250	0.80	398.20	398.20	100.53	CFRP	0.495	270.0	233600	3550	SP90	0.71	45
TR30D3	31.4	150	300	250	0.80	398.20	398.20	100.53	CFRP	0.165	270.0	233600	3550	SP90	0.71	45
TR30D4	31.4	150	300	250	0.80	398.20	398.20	100.53	CFRP	0.33	270.0	233600	3550	SP90	0.71	45
TR30D40	31.4	150	300	250	0.80	398.20	398.20	100.53	CFRP	0.33	270.0	233600	3550	SP90	0.71	45

A.LI, C. DIAGANA, et al. (2003)

Specimen	Concrete strength f'_c (Mpa)	Web thickness b_w(mm)	Depth h (mm)	Effective depth d(mm)	s/d	Area of steel (mm^2)			FRP type	FRP thickness t_{frp} (mm)	FRP effective height $h_{frp,e}$ (mm)	Young's modulus E_{frp}(Mpa)	Tensile strength f_{frp}(Mpa)	Strengthening scheme	*Wfrp/Sfrp*	Crack angle θ (°)
						Tension	Compression	Internal Stirrups								
PU1	38	130	450	425	0.71	1325.75	100.53	56.55	CFRP	0.43	382.5	105000	1400	US90	0.20	45
PU2	38	130	450	425	0.71	1325.75	100.53	56.55	CFRP	0.43	382.5	105000	1400	US90	0.16	45
PC1	38	130	450	425	0.71	1325.75	100.53	56.55	CFRP	0.43	382.5	105000	1400	WS90	0.20	45
PC2	38	130	450	425	0.71	1325.75	100.53	56.55	CFRP	0.43	382.5	105000	1400	WS90	0.16	45

Appendix E

APPENDIX E
ANALYSIS

	$(V_{exp}-V_{theory}) / P_{plate}$								
Specimen	$k_{0.12}$	$k_{0.13}$	$k_{0.14}$	$k_{0.15}$	$k_{0.16}$	$k_{0.17}$	$k_{0.18}$	$k_{0.19}$	$k_{0.20}$
SP01	1.96	1.81	1.68	1.57	1.47	1.38	1.30	1.24	1.17
SP-T6	1.22	1.13	1.05	0.98	0.92	0.86	0.81	0.77	0.73
SP-T12	1.22	1.13	1.05	0.98	0.92	0.86	0.81	0.77	0.73
MB01	0.92	0.85	0.79	0.74	0.69	0.65	0.62	0.58	0.55
SP21	1.61	1.49	1.38	1.29	1.21	1.14	1.08	1.02	0.97
SP22	1.73	1.60	1.48	1.38	1.30	1.22	1.15	1.09	1.04
SP31	1.86	1.72	1.60	1.49	1.40	1.31	1.24	1.18	1.12
SP32	1.80	1.66	1.54	1.44	1.35	1.27	1.20	1.13	1.08
SP42	1.05	0.97	0.90	0.84	0.78	0.74	0.70	0.66	0.63
SP-S5	1.69	1.56	1.44	1.35	1.26	1.19	1.12	1.06	1.01
SP-S8	1.76	1.62	1.51	1.41	1.32	1.24	1.17	1.11	1.05
2n1	0.92	0.85	0.79	0.74	0.69	0.65	0.62	0.58	0.55
2n2	2.10	1.94	1.80	1.68	1.58	1.48	1.40	1.33	1.26
2n3	0.97	0.90	0.83	0.78	0.73	0.69	0.65	0.61	0.58
2n4	1.70	1.57	1.46	1.36	1.28	1.20	1.14	1.08	1.02
3c1N	0.77	0.71	0.66	0.62	0.58	0.54	0.51	0.49	0.46
3c2N	0.81	0.75	0.70	0.65	0.61	0.57	0.54	0.51	0.49
Shear-01	0.94	0.87	0.81	0.75	0.70	0.66	0.63	0.59	0.56
Shear-02	0.87	0.80	0.75	0.70	0.65	0.61	0.58	0.55	0.52
Shear-03	0.99	0.92	0.85	0.79	0.74	0.70	0.66	0.63	0.60
Shear-04	1.03	0.95	0.88	0.83	0.77	0.73	0.69	0.65	0.62
SPC6	1.78	1.64	1.52	1.42	1.33	1.25	1.18	1.12	1.07
SPC12	1.01	0.93	0.86	0.80	0.75	0.71	0.67	0.64	0.60
mean	1.28	1.18	1.10	1.02	0.96	0.90	0.85	0.81	0.77
Stand. Dev.	0.4364	0.4028	0.3741	0.3491	0.3273	0.3081	0.2909	0.2756	0.2618
Coe. Of Var.	34.1066	34.1066	34.1066	34.1066	34.1066	34.1066	34.1066	34.1066	34.1066
Characteristic value (95%)	0.56	0.52	0.48	0.45	0.42	0.40	0.38	0.36	0.34

Appendix F

APPENDIX F
ANALYSIS

Specimen	Concrete strength f'_c (Mpa)	bc	Depth h (mm)	Plating	Le	Plate thickness t(mm)	Young's modulus E_s(Mpa)	fy	Strengthening scheme	bp	a	4	x	Vexp	3.5	4.5	5.5	6.0	6.5	7.5	Vexp/Vcal						
																					3.50	4.00	4.50	5.50	6.00	6.50	7.00
SP01	48.9	200	370	Steel	548.0	10	210000	330	Tension	200	1150	135	662	140.0	132.4	136.8	140.2	142.4	144.1	147.6	1.06	1.03	1.02	1.00	0.98	0.97	0.95
SP-T6	35.3	200	370	Steel	460.5	6	210000	365	Tension	200	1200	110	758	113.0	108.2	111.2	114.4	116.0	117.5	120.5	1.04	1.03	1.02	0.99	0.97	0.96	0.94
SP-T12	35.3	200	370	Steel	651.3	12	210000	306	Tension	200	1200	129	678	113.0	126.4	130.8	135.1	137.2	139.7	143.3	0.89	0.88	0.86	0.84	0.82	0.81	0.79
MB01	52.0	200	370	Steel	418.0	6	210000	365	Tension	200	1150	120	725	112.0	118.7	120.8	122.9	123.8	124.8	126.5	0.94	0.94	0.93	0.91	0.90	0.90	0.89
FP/B2/L	38.1	130	180	Steel	315.7	3	205000	321	Tension	130	500	49	368	46.8	48.3	49.4	50.6	50.8	51.5	52.5	0.97	0.96	0.95	0.92	0.92	0.91	0.89
FP/B2/R	39.1	130	180	Steel	313.6	3	205000	321	Tension	130	500	49	368	50.0	48.3	49.4	50.6	50.8	51.5	52.5	1.03	1.03	1.01	0.99	0.98	0.97	0.95
FP/B3/L	40.1	130	180	Steel	407.2	5	210000	317	Tension	130	500	54	345	64.2	54.2	55.7	56.9	56.6	57.2	59.0	1.18	1.18	1.15	1.13	1.13	1.12	1.09
FP/B3/R	41.1	130	180	Steel	404.7	5	210000	317	Tension	130	500	54	345	70.8	54.2	55.7	56.9	56.6	57.2	59.0	1.31	1.30	1.27	1.24	1.25	1.24	1.20
FP/B4/L	42.1	130	180	Steel	568.9	10	210000	293	Tension	130	500	65	300	85.0	64.5	66.5	69.1	69.7	70.3	72.4	1.32	1.30	1.28	1.23	1.22	1.21	1.17
FP/B4/R	42.1	130	180	Steel	568.9	10	210000	293	Tension	130	500	65	300	78.7	64.5	66.5	69.1	69.7	70.3	72.4	1.22	1.20	1.18	1.14	1.13	1.12	1.09
SP21	48.9	200	370	Steel	548.0	10	210000	330	Side	130	1150	133	783	157.0	129.5	135.8	142.3	143.3	146.4	151.9	1.21	1.18	1.16	1.10	1.10	1.07	1.03
SP22	48.9	200	370	Steel	548.0	10	210000	330	Side	130	1150	133	783	162.0	129.5	135.8	142.3	143.3	146.4	151.9	1.25	1.22	1.19	1.14	1.13	1.11	1.07
SP31	48.9	200	370	Steel	548.0	10	210000	330	Side	130	1150	127	819	169.0	124.5	130.0	136.5	138.4	141.4	146.8	1.36	1.33	1.30	1.24	1.22	1.20	1.15
SP32	48.9	200	370	Steel	548.0	10	210000	330	Side	130	1150	127	819	166.0	124.5	130.0	136.5	138.4	141.4	146.8	1.33	1.31	1.28	1.22	1.20	1.17	1.13
SP42	48.9	200	370	Steel	548.0	10	210000	330	Side	130	1150	121	859	132.0	119.2	125.0	131.0	132.3	134.8	140.1	1.11	1.09	1.06	1.01	1.00	0.98	0.94
SP-S5	20.9	150	250	Steel	467.7	5	200000	321	Side	75	663	63	646	66.7	61.8	63.8	64.8	65.4	66.2	68.0	1.08	1.07	1.05	1.03	1.02	1.01	0.98
SP-S8	20.9	150	250	Steel	591.6	8	200000	321	Side	75	663	67	622	72.8	66.0	68.3	69.3	70.8	71.1	72.7	1.10	1.09	1.07	1.05	1.03	1.02	1.00
2n1	58.0	200	300	Steel	371.3	5	210000	311	Side	65	1150	114	743	103.0	112.3	115.1	118.1	119.3	120.8	123.8	0.92	0.90	0.89	0.87	0.86	0.85	0.83
2n2	58.0	200	300	Steel	371.3	5	210000	311	Side	65	1150	114	743	126.0	112.3	115.1	118.1	119.3	120.8	123.8	1.12	1.11	1.09	1.07	1.06	1.04	1.02
2n3	58.0	200	300	Steel	469.7	8	210000	301	Side	65	1150	119	738	109.0	110.0	113.6	117.5	126.9	128.7	132.3	0.99	0.91	0.96	0.93	0.86	0.85	0.82
2n4	58.0	200	300	Steel	469.7	8	210000	301	Side	65	1150	119	738	127.0	110.0	113.6	117.5	126.9	128.7	132.3	1.15	1.06	1.12	1.08	1.00	0.99	0.96
3c1N	52.4	200	300	Steel	481.8	8	210000	308	Side	65	1350	107	798	103.0	98.6	102.0	105.4	113.4	115.2	118.0	1.04	0.96	1.01	0.98	0.91	0.89	0.87
3c2N	52.4	200	300	Steel	481.8	8	210000	308	Side	65	1350	107	798	104.0	98.6	102.0	105.4	113.4	115.2	118.0	1.06	0.97	1.02	0.99	0.92	0.90	0.88
Shear-01	50.0	200	300	Steel	475.7	8	200000	360	Angle	167	1150	137	725	138.0	134.5	142.8	150.6	151.5	154.7	161.2	1.03	1.01	0.97	0.92	0.91	0.89	0.86
Shear-02	50.0	200	300	Steel	475.7	8	200000	360	Angle	167	1150	137	725	134.0	134.5	142.8	150.6	151.5	154.7	161.2	1.00	0.98	0.94	0.89	0.88	0.87	0.83
Shear-03	50.0	200	300	Steel	475.7	8	200000	360	Angle	232	1150	153	725	159.0	147.3	158.0	167.5	171.7	176.1	184.6	1.08	1.04	1.01	0.95	0.93	0.90	0.86
Shear-04	50.0	200	300	Steel	475.7	8	200000	360	Angle	232	1150	153	725	162.0	147.3	158.0	167.5	171.7	176.1	184.6	1.10	1.06	1.03	0.97	0.94	0.92	0.88
SPC6	35.3	200	370	Steel	461.0	6	210000	365	Compression	200	1200	89	755	124.0	88.4	90.2	93.0	93.3	93.7	95.0	1.40	1.39	1.37	1.33	1.33	1.32	1.31
SPC12	35.3	200	370	Steel	651.0	12	210000	306	Compression	200	1200	90	680	117.0	89.0	91.3	93.0	93.6	94.8	96.1	1.31	1.30	1.28	1.26	1.25	1.23	1.22
SPC20	35.3	200	370	Steel	841.0	20	210000	433	Compression	200	1200	92	913	94.0	90.4	92.7	94.8	96.3	96.8	98.6	1.04	1.02	1.01	0.99	0.98	0.97	0.95
														mean							1.12	1.09	1.08	1.05	1.03	1.01	0.98
														St. Dev.							0.139	0.143	0.135	0.131	0.137	0.137	0.134
														Coe.Of.Var							12.38	13.03	12.50	12.50	13.31	13.49	13.64
														Characteristic (95%)							0.89	0.86	0.86	0.83	0.80	0.79	0.76

Appendix G

Appendix G

Specimen	Numbers of Plates	Plate Dimension (Depth x Width)	Average	Groove Dimension (Depth x Width)	Average
12mm x 12mm (Steel)	1	1. 11.94mm x 11.93mm 2. 11.92mm x 11.92mm 3. 11.88mm x 11.92mm	11.91mm x 11.92mm	1. 13.42mm x 13.33mm 2. 12.85mm x 13.30mm 3. 12.74mm x 13.34mm	13.00mm x 13.32mm
12mm x 12mm (Aluminium)	1	1. 12.42mm x 12.41mm 2. 12.42mm x 12.41mm 3. 12.42mm x 12.39mm	12.42mm x 12.40mm	1. 13.24mm x 13.61mm 2. 12.98mm x 13.75mm 3. 12.90mm x 13.61mm	13.04mm x 13.66mm
12mm x 12mm (CFRP)	8	1. 12.80mm x 11.79mm 2. 12.86mm x 11.92mm 3. 12.63mm x 11.94mm	12.76mm x 11.88mm	1. 14.21mm x 14.04mm 2. 14.23mm x 13.86mm 3. 14.41mm x 13.84mm	14.28mm x 13.91mm
12mm x 3mm (CFRP)	2	1. 13.80mm x 3.73mm 2. 13.78mm x 4.02mm 3. 14.04mm x 3.75mm	12.37mm x 2.76mm	1. 13.80mm x 3.73mm 2. 13.78mm x 4.02mm 3. 14.04mm x 3.75mm	13.87mm x 3.83mm
12mm x 4mm (CFRP)	3	1. 12.60mm x 4.36mm 2. 12.70mm x 4.20mm 3. 12.90mm x 4.29mm	12.73mm x 4.28mm	1. 13.81mm x 4.91mm 2. 13.66mm x 4.91mm 3. 13.70mm x 4.94mm	13.72mm x 4.92mm
12mm x 6mm (CFRP)	4	1. 12.50mm x 5.76mm 2. 12.47mm x 5.79mm 3. 12.56mm x 5.79mm	12.51mm x 5.78mm	1. 12.96mm x 7.80mm 2. 13.25mm x 8.63mm 3. 13.70mm x 8.40mm	13.30mm x 8.27mm
24mm x 4mm (CFRP)	3	1. 24.44mm x 4.25mm 2. 24.07mm x 4.35mm 3. 23.91mm x 4.52mm	24.14mm x 4.37mm	1. 24.52mm x 5.55mm 2. 24.44mm x 5.60mm 3. 25.15mm x 5.74mm	24.70mm x 5.63mm
30mm x 7mm (CFRP)	5	1. 30.33mm x 7.45mm 2. 30.56mm x 7.31mm 3. 30.77mm x 7.41mm	30.55mm x 7.39mm	1. 30.64mm x 9.41mm 2. 30.63mm x 9.40mm 3. 31.08mm x 9.38mm	40.78mm x 9.39mm
12mm x 5mm (Steel)	1	N.A.	N.A.	N.A.	N.A.
20mm x 26mm (CFRP)	17	1. 25.26mm x 20.64mm 2. 25.41mm x 20.68mm 3. 25.11mm x 20.48mm	25.26mm x 20.60mm	1. 27.64mm x 22.58mm 2. 27.73mm x 22.78mm 3. 27.72mm x 23.09mm	27.69mm x 22.82mm

Specimen	Numbers of Plates	Plate Dimension (Depth x Width)	Average	Groove Dimension (Depth x Width)	Average
12mm x 30mm (CFRP)	8	1. 11.95mm x 30.96mm 2. 11.98mm x 30.95mm 3. 12.12mm x 30.84mm	12.02mm x 30.92mm	1. 13.29mm x 33.28mm 2. 13.30mm x 32.95mm 3. 13.43mm x 32.80mm	13.34mm x 33.01mm
12mm x 50mm (CFRP)	8	1. 12.18mm x 50.39mm 2. 12.23mm x 50.36mm 3. 12.18mm x 50.25mm	12.20mm x 50.33mm	1. 13.38mm x 52.22mm 2. 13.11mm x 52.42mm 3. 13.10mm x 52.51mm	13.19mm x 52.38mm
12mm x 60mm (CFRP)	8	1. 11.65mm x 61.02mm 2. 11.84mm x 61.04mm 3. 11.73mm x 61.04mm	11.74mm x 61.03mm	1. 12.70mm x 63.10mm 2. 13.10mm x 63.04mm 3. 13.00mm x 62.89mm	12.93mm x 63.01mm
12mm x 70mm (CFRP)	8	1. 11.90mm x 71.19mm 2. 12.00mm x 71.58mm 3. 11.99mm x 70.98mm	11.93mm x 71.25mm	1. 12.60mm x 72.83mm 2. 12.60mm x 72.88mm 3. 13.10mm x 73.61mm	12.76mm x 73.10mm
12mm x 80mm (CFRP)	8	1. 12.22mm x 80.96mm 2. 12.43mm x 81.13mm 3. 12.20mm x 80.98mm	12.28mm x 81.00mm	1. 13.24mm x 83.06mm 2. 13.44mm x 83.07mm 3. 13.61mm x 82.93mm	13.43mm x 83.02mm
12mm x 100mm (CFRP)	8	1. 12.17mm x 100.82mm 2. 12.26mm x 101.59mm 3. 12.48mm x 100.83mm	12.30mm x 101.08mm	1. 12.84mm x 102.97mm 2. 12.84mm x 103.33mm 3. 12.95mm x 104.07mm	12.87mm x 103.45mm

Notes : Measurement No. 1 is for top of the plates/grooves.
Measurement No. 2 is for centre of the plates/grooves.
Measurement No. 3 is for top of the plates/grooves.

Appendix H

Appendix H

Specimen	Ultimate Load P_u (kN)	Shear Stress τ_f (MPa)	Maximum Slip δ_f (mm)	Maximum Strain ε_{max} ($\mu\varepsilon$)	Strain Prior Debonding ε ($\mu\varepsilon$)	E_{exp} (MPa)	E_{cal} (MPa)	Notes
12mm x 12mm (Mild Steel)	74.10	6.50	0.53	2911	2911	183044	-	Debonding crack appearing along the plate.
12mm x 12mm (Aluminium)	30.40	-	-	27581	-	63819	-	Plate yielded.
12mm x 12mm (CFRP)	85.90	9.16	0.72	4810	4810	131566	129180	Debonding crack appearing along the plate.
12mm x 3mm (CFRP)	59.20	15.00	0.97	11840	11840	146348	139907	Debonding crack appearing along the plate.
12mm x 4mm (CFRP)	54.10	12.50	1.15	7648	7648	134467	136748	Debonding crack appearing along the plate.
12mm x 6mm (CFRP)	47.60	9.93	1.00	5136	5136	130489	134998	Debonding crack appearing along the plate.
24mm x 4mm (CFRP)	110.00	16.94	1.55	8846	8846	141434	134029	Appearance of 'herring bone' crack and wide area of concrete attached.
30mm x 7mm (CFRP)	165.30	15.40	0.70	5522	5522	134562	132567	Appearance of 'herring bone' crack and wide area of concrete attached.
12mm x 5mm (Steel)	29.30	-	-	7200	-	195494	-	Plate yielded.
20mm x 26mm (CFRP)	199.40	10.00	0.40	3800	3788	129837	158504	Appearance of 'herring bone' crack and wide area of concrete attached.
12mm x 30mm (CFRP)	115.80	11.78	0.32	2560	2557	135113	128986	Appearance of 'herring bone' crack and wide area of concrete attached.
12mm x 50mm (CFRP)	110.50	2.93	0.21	1658	1560	132761	127171	Wide area of concrete attached to the plate.

Specimen	Ultimate Load P_u (kN)	Shear Stress τ_f (MPa)	Maximum Slip δ_f (mm)	Maximum Strain ε_{max} ($\mu\varepsilon$)	Strain Prior Debonding ε ($\mu\varepsilon$)	E_{exp} (MPa)	E_{cal} (MPa)	Notes
12mm x 60mm (CFRP)	113.60	5.92	0.2	1892	1875	126511	131920	Wide area of concrete attached to the plate.
12mm x 70mm (CFRP)	144.80	6.46	0.15	1552	1562	135810	129914	Wide area of concrete attached to the plate.
12mm x 80mm (CFRP)	134.60	3.90	0.17	1253	1205	137139	126381	Wide area of concrete attached to the plate.
12mm x 100mm (CFRP)	155.60	4.08	0.10	1326	1229	135000	126185	Wide area of concrete attached to the plate.

Appendix I

Table A1

Chajes et al. (1996)

Specimen	d_p (mm)	b_p (mm)	Materials	Type of Plating	L (mm)	E_p (MpA)	f_c (MpA)	f_t	b_c (mm)	P_u (kN)	L_e (mm)	
C15	1.016	25.40	CFRP	EB	152.4	108478	36.4	-	152.4	11.92	135.16	$L_e < L$
C16	1.016	25.40	CFRP	EB	203.2	108478	36.4	-	152.4	11.57	135.16	$L_e < L$

Taljsten (1997)

Specimen	d_p (mm)	b_p (mm)	Materials	Type of Plating	L (mm)	E_p (MpA)	f_c (MpA)	f_t	b_c (mm)	P_u (kN)	L_e (mm)	
C200 50A	1.25	50	CFRP	EB	200	170000	60.0	4.10	200	27.50	165.61	$L_e < L$
C300 50A	1.25	50	CFRP	EB	300	170000	66.0	4.30	200	35.10	161.71	$L_e < L$
C400 50A	1.25	50	CFRP	EB	400	170000	66.0	4.30	200	26.90	161.71	$L_e < L$

Yao, J et al. (2005)

Specimen	d_p (mm)	b_p (mm)	Materials	Type of Plating	L (mm)	E_p (MpA)	f_c (MpA)	f_t	b_c (mm)	P_u (kN)	L_e (mm)	
III-7	1.27	25.3	GFRP	EB	100	22500	27.7	3.05	100	4.78	73.68	$L_e < L$
III-8	1.27	50.6	GFRP	EB	100	22500	27.7	3.05	100	8.02	73.68	$L_e < L$

Taljsten (1997)

Specimen	d_p (mm)	b_p (mm)	Materials	Type of Plating	L (mm)	E_p (MpA)	f_c (MpA)	f_t	b_c (mm)	P_u (kN)	L_e (mm)	
S400 40A	2.9	40	STEEL	EB	400	205000	66.0	4.30	200	41.10	270.48	$L_e < L$
S400 60A	2.9	60	STEEL	EB	400	205000	66.0	4.30	200	58.40	270.48	$L_e < L$
S400 60B	2.9	60	STEEL	EB	400	205000	60.0	4.10	200	53.00	277.00	$L_e < L$
S300 80C	2.9	80	STEEL	EB	300	205000	60.0	4.10	200	68.00	277.00	$L_e < L$
S500 80C	2.9	80	STEEL	EB	500	205000	69.1	4.40	200	67.30	267.39	$L_e < L$
S600 80B	2.9	80	STEEL	EB	600	205000	60.0	4.10	200	71.40	277.00	$L_e < L$
S800 80A	2.9	80	STEEL	EB	800	205000	60.0	4.10	200	61.60	277.00	$L_e < L$

Page, M et al. (2005)

Specimen	d_p (mm)	b_p (mm)	Materials	Type of Plating	L (mm)	E_p (MpA)	f_c (MpA)	f_t	b_c (mm)	P_u (kN)	L_e (mm)	
30MPa-200-10	10.48	1.22	CFRP	NSM	200	161800	30	3.1	300	27.9	200	$L_e < L$
30MPa-250-10	10.29	1.22	CFRP	NSM	250	161800	30	3.1	300	26.6	200	$L_e < L$
30MPa-300-10	10.38	1.22	CFRP	NSM	300	161800	30	3.1	300	26	200	$L_e < L$
30MPa-350-10	10.35	1.22	CFRP	NSM	350	161800	30	3.1	300	23	200	$L_e < L$
30MPa-200-15	15.65	1.26	CFRP	NSM	200	162050	30	3.1	300	47.1	200	$L_e < L$
30MPa-300-15	15.31	1.26	CFRP	NSM	300	162050	30	3.1	300	51.6	200	$L_e < L$
30MPa-200-20	20.00	1.20	CFRP	NSM	200	162300	30	3.1	300	52.4	200	$L_e < L$
30MPa-300-20	19.85	1.24	CFRP	NSM	300	162300	30	3.1	300	67.8	200	$L_e < L$
42MPa-200-10	10.29	1.27	CFRP	NSM	200	161800	42	3.1	300	30.6	200	$L_e < L$
48MPa-200-10	10.10	1.28	CFRP	NSM	200	161800	48	3.7	300	33.7	200	$L_e < L$
50MPa-200-10	10.56	1.26	CFRP	NSM	200	161800	50	3.7	300	33.3	200	$L_e < L$
50MPa-200-20	20.43	1.28	CFRP	NSM	200	162300	50	3.7	300	71.5	200	$L_e < L$
50MPa-200-20	20.22	1.28	CFRP	NSM	200	162300	50	3.7	300	75	200	$L_e < L$
50MPa-300-20	19.27	1.24	CFRP	NSM	300	162300	50	3.7	300	68.1	200	$L_e < L$
53MPa-200-10	10.43	1.30	CFRP	NSM	200	161800	53	4.0	300	34	200	$L_e < L$
53MPa-200-10	10.23	1.24	CFRP	NSM	200	161800	53	4.0	300	31.9	200	$L_e < L$
53MPa-300-10	10.30	1.27	CFRP	NSM	300	161800	53	4.0	300	37.9	200	$L_e < L$
53MPa-200-20	20.10	1.27	CFRP	NSM	200	162300	53	4.0	300	72.5	200	$L_e < L$
53MPa-200-20	20.47	1.26	CFRP	NSM	200	162300	53	4.0	300	77.9	200	$L_e < L$
53MPa-300-20	20.15	1.25	CFRP	NSM	300	162300	53	4.0	300	66.3	200	$L_e < L$
65MPa-200-10	9.95	2.90	CFRP	NSM	200	144600	65	4.9	300	45.1	200	$L_e < L$

Table A2

Yao, J et al. (2005)

Specimen	d_p (mm)	b_p (mm)	Materials	Type of Plating	L (mm)	E_p (MpA)	f_c (MpA)	f_t	b_c (mm)	P_u (kN)	L_e (mm)		t_g	E_g (MpA)
I2	0.165	25	CFRP	Wet lay up	85	256000	23	3.23	150	5.69	64.88	$L_e < L$	1	6500
I3	0.165	25	CFRP	Wet lay up	95	256000	23	3.23	150	5.76	64.88	$L_e < L$	1	6500
I4	0.165	25	CFRP	Wet lay up	95	256000	23	3.23	150	5.76	64.88	$L_e < L$	1	6500
I5	0.165	25	CFRP	Wet lay up	95	256000	23	3.23	150	6.17	64.88	$L_e < L$	1	6500
I6	0.165	25	CFRP	Wet lay up	115	256000	23	3.23	150	5.96	64.88	$L_e < L$	1	6500
I7	0.165	25	CFRP	Wet lay up	145	256000	23	3.23	150	5.95	64.88	$L_e < L$	1	6500
I8	0.165	25	CFRP	Wet lay up	190	256000	23	3.23	150	6.68	64.88	$L_e < L$	1	6500
I9	0.165	25	CFRP	Wet lay up	190	256000	23	3.23	150	6.35	64.88	$L_e < L$	1	6500
I10	0.165	25	CFRP	Wet lay up	95	256000	23	3.23	150	6.17	64.88	$L_e < L$	1	6500
I12	0.165	25	CFRP	Wet lay up	85	256000	23	3.23	150	6	64.88	$L_e < L$	1	6500
I13	0.165	25	CFRP	Wet lay up	95	256000	23	3.23	150	6.14	64.88	$L_e < L$	1	6500
I14	0.165	25	CFRP	Wet lay up	115	256000	23	3.23	150	6.19	64.88	$L_e < L$	1	6500
I15	0.165	25	CFRP	Wet lay up	145	256000	23	3.23	150	6.27	64.88	$L_e < L$	1	6500
I16	0.165	25	CFRP	Wet lay up	190	256000	23	3.23	150	7.03	64.88	$L_e < L$	1	6500
II-2	0.165	25	CFRP	Wet lay up	95	256000	22.9	3.02	150	6.75	64.97	$L_e < L$	1	6500
II-5	0.165	25	CFRP	Wet lay up	190	256000	22.9	3.02	150	7.07	64.97	$L_e < L$	1	6500
III-1	0.165	25	CFRP	Wet lay up	100	256000	27.1	3.05	150	5.94	61.77	$L_e < L$	1	6500
III-2	0.165	50	CFRP	Wet lay up	100	256000	27.1	3.05	150	11.66	53.98	$L_e < L$	1	6500
III-3	0.165	75	CFRP	Wet lay up	100	256000	27.1	3.05	150	14.63	49.33	$L_e < L$	1	6500
III-4	0.165	100	CFRP	Wet lay up	100	256000	27.1	3.05	150	19.07	46.12	$L_e < L$	1	6500
IV-1	0.165	25	CFRP	Wet lay up	95	256000	18.9	2.81	150	5.86	68.82	$L_e < L$	1	6500
IV-2	0.165	25	CFRP	Wet lay up	95	256000	18.9	2.81	150	5.9	68.82	$L_e < L$	1	6500
IV-3	0.165	25	CFRP	Wet lay up	95	256000	19.8	2.81	150	5.43	67.87	$L_e < L$	1	6500
IV-4	0.165	25	CFRP	Wet lay up	95	256000	19.8	2.81	150	5.76	67.87	$L_e < L$	1	6500
IV-5	0.165	25	CFRP	Wet lay up	95	256000	18.9	2.81	150	5	68.82	$L_e < L$	1	6500
IV-6	0.165	25	CFRP	Wet lay up	95	256000	19.8	2.81	150	7.08	67.87	$L_e < L$	1	6500
IV-7	0.165	25	CFRP	Wet lay up	95	256000	18.9	2.81	150	5.5	68.82	$L_e < L$	1	6500
IV-8	0.165	25	CFRP	Wet lay up	95	256000	19.8	2.81	150	5.93	67.87	$L_e < L$	1	6500
IV-9	0.165	25	CFRP	Wet lay up	95	256000	18.9	2.81	150	5.38	68.82	$L_e < L$	1	6500
IV-10	0.165	25	CFRP	Wet lay up	95	256000	19.8	2.81	150	6.6	67.87	$L_e < L$	1	6500
IV-11	0.165	25	CFRP	Wet lay up	95	256000	18.9	2.81	150	5.51	68.82	$L_e < L$	1	6500
IV-12	0.165	25	CFRP	Wet lay up	95	256000	19.8	2.81	150	5.67	67.87	$L_e < L$	1	6500
IV-13	0.165	25	CFRP	Wet lay up	95	256000	18.9	2.81	150	6.31	68.82	$L_e < L$	1	6500
IV-14	0.165	25	CFRP	Wet lay up	95	256000	19.8	2.81	150	6.19	67.87	$L_e < L$	1	6500
V-1	0.165	15	CFRP	Wet lay up	95	256000	21.1	3.01	150	3.81	71.81	$L_e < L$	1	6500
V-2	0.165	15	CFRP	Wet lay up	95	256000	21.1	3.01	150	4.41	71.81	$L_e < L$	1	6500
V-3	0.165	25	CFRP	Wet lay up	95	256000	21.1	3.01	150	6.26	66.58	$L_e < L$	1	6500
V-4	0.165	50	CFRP	Wet lay up	95	256000	21.1	3.01	150	12.22	58.19	$L_e < L$	1	6500
V-5	0.165	75	CFRP	Wet lay up	95	256000	21.1	3.01	150	14.29	53.18	$L_e < L$	1	6500
V-6	0.165	100	CFRP	Wet lay up	95	256000	21.1	3.01	150	15.58	49.72	$L_e < L$	1	6500
VII-1	0.165	25	CFRP	Wet lay up	95	256000	24.9	3.51	150	6.8	63.36	$L_e < L$	1	6500
VII-2	0.165	25	CFRP	Wet lay up	95	256000	24.9	3.51	150	6.62	63.36	$L_e < L$	1	6500
VII-3	0.165	25	CFRP	Wet lay up	145	256000	24.9	3.51	150	7.33	63.36	$L_e < L$	1	6500
VII-4	0.165	25	CFRP	Wet lay up	145	256000	24.9	3.51	150	6.49	63.36	$L_e < L$	1	6500
VII-5	0.165	25	CFRP	Wet lay up	190	256000	24.9	3.51	150	7.07	63.36	$L_e < L$	1	6500
VII-6	0.165	25	CFRP	Wet lay up	190	256000	24.9	3.51	150	7.44	63.36	$L_e < L$	1	6500
VII-7	0.165	25	CFRP	Wet lay up	240	256000	24.9	3.51	150	7.16	63.36	$L_e < L$	1	6500
VII-8	0.165	25	CFRP	Wet lay up	240	256000	24.9	3.51	150	6.24	63.36	$L_e < L$	1	6500

Table A3

Specimen	d_p (mm)	b_p (mm)	Materials	Type of Plating	L (mm)	E_p (MpA)	f_c (MpA)	f_l	b_c (mm)	P_u (kN)	L_e (mm)	
12x12	12.00	12.00	STEEL	NSM	350	183044	36.7	3.78	300	74.1	552.69	$L_e > L$
12x12	12.00	12.00	CFRP	NSM	350	131566	36.7	3.78	300	85.9	443.12	$L_e > L$
12x12	12.00	12.00	Aluminium	NSM	350	63819	36.7	3.78	300	30.4	308.63	$L_e < L$
12x3	12.37	2.76	CFRP	NSM	350	146348	36.7	3.78	300	59.3	269.42	$L_e < L$
12x4	12.47	4.24	CFRP	NSM	350	134467	36.7	3.78	300	54.1	307.48	$L_e < L$
12x6	12.35	5.73	CFRP	NSM	350	130489	36.7	3.78	300	47.6	336.07	$L_e < L$
24x4	24.06	4.33	CFRP	NSM	350	141434	36.7	3.78	300	130	347.69	$L_e < L$
30x7	30.60	7.3	CFRP	NSM	350	134562	36.7	3.78	300	165.3	583.02	$L_e > L$
12x5	12.00	5.00	STEEL	NSM	350	195494	36.7	3.78	300	24.3	460.58	$L_e > L$
26x20	25.26	20.6	CFRP	NSM	350	129837	36.7	3.78	300	199.4	647.70	$L_e > L$
12x30	12.01	30.75	CFRP	NSM	350	135113	36.7	3.78	300	115.8	474.65	$L_e > L$
12x50	12.19	50.33	CFRP	NSM	350	132761	36.7	3.78	300	110.5	464.96	$L_e > L$
12x60	11.74	61.03	CFRP	NSM	350	126511	36.7	3.78	300	133.6	436.48	$L_e > L$
12x70	11.93	71.25	CFRP	NSM	350	135810	36.7	3.78	300	144.8	449.21	$L_e > L$
12x80	12.28	81.02	CFRP	NSM	350	137139	36.7	3.78	300	134.6	452.58	$L_e > L$
12x100	12.30	101.08	CFRP	NSM	350	135000	36.7	3.78	300	154	436.07	$L_e > L$

Appendix J

Table A1

Page, M et al. (2005)

Specimen	d_p (mm)	b_p (mm)	Materials	Type of Plating	L (mm)	E_p (MpA)	f_c (MpA)	f_t	b_c (mm)	τ_u (kN)
30MPa-200-10	10.48	1.22	CFRP	NSM	200	161800	30	3.1	300	9.00
30MPa-250-10	10.29	1.22	CFRP	NSM	250	161800	30	3.1	300	9.00
30MPa-300-10	10.38	1.22	CFRP	NSM	300	161800	30	3.1	300	7.00
30MPa-350-10	10.35	1.22	CFRP	NSM	350	161800	30	3.1	300	9.00
30MPa-200-15	15.65	1.26	CFRP	NSM	200	162050	30	3.1	300	9.00
30MPa-300-15	15.31	1.26	CFRP	NSM	300	162050	30	3.1	300	8.50
30MPa-200-20	20.00	1.20	CFRP	NSM	200	162300	30	3.1	300	9.00
30MPa-300-20	19.85	1.24	CFRP	NSM	300	162300	30	3.1	300	12.00
42MPa-200-10	10.29	1.27	CFRP	NSM	200	161800	42	3.1	300	10.50
48MPa-200-10	10.10	1.28	CFRP	NSM	200	161800	48	3.7	300	12.00
50MPa-200-10	10.56	1.26	CFRP	NSM	200	161800	50	3.7	300	11.00
50MPa-200-20	20.43	1.28	CFRP	NSM	200	162300	50	3.7	300	13.00
50MPa-200-20	20.22	1.28	CFRP	NSM	200	162300	50	3.7	300	12.00
50MPa-300-20	19.27	1.24	CFRP	NSM	300	162300	50	3.7	300	13.00
53MPa-200-10	10.43	1.30	CFRP	NSM	200	161800	53	4.0	300	12.50
53MPa-200-10	10.23	1.24	CFRP	NSM	200	161800	53	4.0	300	10.00
53MPa-300-10	10.30	1.27	CFRP	NSM	200	161800	53	4.0	300	10.00
53MPa-200-20	20.10	1.27	CFRP	NSM	200	162300	53	4.0	300	15.00
53MPa-200-20	20.47	1.26	CFRP	NSM	200	162300	53	4.0	300	14.40
53MPa-300-20	20.15	1.25	CFRP	NSM	300	162300	53	4.0	300	15.00
65MPa-200-10	9.95	2.90	CFRP	NSM	200	144600	65	4.9	300	14.00

Wu Z. et al. (2001)

Specimen	d_p (mm)	b_p (mm)	Materials	Type of Plating	L (mm)	E_p (MpA)	f_c (MpA)	f_t	b_c (mm)	τ_u (kN)
S-CFS-400-25	1.00	80.00	CFRP	EB	250	138000	57.6	-	300	8.00